Mechanistic Studies on *Retinitis Pigmentosa* for Gene Therapy Approaches

Dissertation der Fakultät für Biologie

der Ludwig-Maximilians-Universität München

Lena Isabelle Zobel

München, 2022

Diese Dissertation wurde angefertigt
unter der Leitung von Herrn Prof. Dr. Stylianos Michalakis
im Bereich der Pharmakologie für Naturwissenschaften
an der Ludwig-Maximilians-Universität München

Erstgutachter/in:	Prof. Dr. Stylianos Michalakis
Zweitgutachter/in:	Prof. Dr. Christof Osman
Tag der Abgabe:	05.05.2022
Tag der mündlichen Prüfung:	29.06.2022

Erklärung

Ich versichere hiermit an Eides statt, dass ich meine Dissertation selbständig und ohne unerlaubte Hilfsmittel angefertigt habe.
Die vorliegende Dissertation wurde weder ganz noch teilweise bei einer anderen Prüfungskommission vorgelegt.
Ich habe noch zu keinem früheren Zeitpunkt versucht, eine Dissertation einzureichen oder an einer Doktorprüfung teilzunehmen.

München, den 01.07.2022

_____

Lena Isabelle Zobel

Table of Contents

This is ten percent luck

Twenty percent skill

Fifteen percent concentrated power of will

Five percent pleasure

Fifty percent pain

And a hundred percent reason to remember the name

Abstract

Retinitis pigmentosa (RP) is a group of severe hereditary blindness diseases usually caused by mutations in genes necessary for the process of phototransduction. RP is characterized by progressive retinal degeneration affecting rod photoreceptors and subsequently cone photoreceptors. Gene augmentation therapy using recombinant adeno-associated virus (rAAV) vectors represents a promising and potentially curative therapeutic option.

In this study, a novel *Cnga1*^{MUT} mouse model was characterized by *in vivo* analysis of retinal morphology and function over an observation period of 12 months, followed by immunohistochemical analysis. The *Cnga1*^{MUT} mouse carries a c.1526A>G missense mutation in the *Cnga1* gene encoding the A1 subunit of the cyclic-nucleotide gated (CNG) channel. This mutation leads to substitution of Tyr509 within the cyclic nucleotide-binding domain (CNBD) by cysteine resulting in degradation of the CNGA1 but also the CNGB1 protein, which together form the heterotetrameric channel complex in rod photoreceptors. Loss of the CNG channel results in impaired retinal function and progressive degeneration of photoreceptors. These phenotypic observations excellently mimic key findings in patients with *CNGA1*-linked RP (RP49) and qualify *Cnga1*^{MUT} mice as a valid preclinical model for this disease.

To shed light into the mechanisms underlying photoreceptor degeneration, proteomic analysis of different animal models of RP was performed and revealed the involvement of endoplasmic reticulum (ER) stress, autophagy, and metabolic and oxidative stress.

Two novel gene therapy approaches based on rAAV-vector mediated gene augmentation for *CNGB1*- or *CNGA1*-linked RP were developed and tested in the respective mouse models. Therapeutic effects after intraocular injections of rAAVs were assessed *in vivo* by using spectral-domain optical coherence tomography (SD-OCT) and electroretinography (ERG). Transgene expression was investigated via immunohistochemistry. It was shown that both vectors had beneficial effects on retinal morphology and retinal function. In summary, these results demonstrate gene augmentation therapy as a promising approach to treat RP.

1 Introduction

1.1 The Mammalian Retina

1.1.1 Anatomy of the Retina

The retina is a layered neuronal tissue that lines the back of the eye and resembles a neuronal network, enabling vision by detecting light stimuli and converting them into electrical signals. (Kolb, 1995; Hoon et al., 2014; Ptito et al., 2021). In mammals, the basic structure of the retina is highly conserved (Wässle and Boycott, 1991; Masland, 1996; Hoon et al., 2014) and consists of five major neuronal cell types: photoreceptors, horizontal cells, bipolar cells, amacrine cells and ganglion cells (Figure 1). Photoreceptor outer segments are attached to retinal pigment epithelial (RPE) cells. In addition, Müller glia, microglia and astrocytes are present supporting metabolic, homeostatic and immunological functions (Reichenbach and Bringmann, 2020). Cell bodies and processes of the cells are aligned in a distinct way forming the neuronal network with the characteristic structure with three nuclear and two synaptic (or plexiform) layers. Remarkably, the retina has an inverse architecture meaning that the light-sensitive photoreceptors are located in the outermost layer facing away from the incident light (Kolb, 1995). The cell bodies of the photoreceptors form the outer nuclear layer (ONL), and their synaptic terminals are connected to the bipolar cells in the adjacent outer plexiform layer (OPL). Here, horizontal cells serve as modulator of synaptic transmission between photoreceptors and bipolar cells (Herrmann et al., 2011). In turn, the cell bodies of the bipolar cells, together with those of the amacrine and horizontal cells, form the inner nuclear layer (INL). In the inner plexiform layer (IPL), bipolar cells are connecting to ganglion cells in order to further process the electrical signal received from the photoreceptors (Euler et al., 2014; Diamond, 2017). Additionally, amacrine cells control ganglion cell responses by connecting to bipolar and ganglion cells (Sandell et al., 1989; Baccus et al., 2008; Grimes et al., 2010; Diamond, 2017). The cell bodies of the ganglion cells finally form the ganglion cell layer (GCL), while their axons gather at the optic disc and form the optic nerve that leaves the eye in order to forward the visual information to the brain.

The photoreceptors can be divided into two classes: rods that mediate dim-light (scotopic) vision and cones that confer vision under daylight (photopic) conditions (Wässle and Boycott, 1991). In the human retina, rods make up approximately 95% of photoreceptors (Curcio et al.,

1990). They have high sensitivity to light and confer monochromatic vision at low light (Rieke, 2000; Sampath and Rieke, 2004). In contrast, the less sensitive cones exist in different subtypes (three in primates, two in most other mammals) with distinct sensitivities to light wavelengths and are responsible for high acuity color vision in bright light (Rieke and Baylor, 2000; Nikonov et al., 2006; Thoreson and Dacey, 2019). In primates, cones are mostly localized in the macula, a central spot in the retina known as the area of high-acuity vision (Molday and Moritz, 2015).

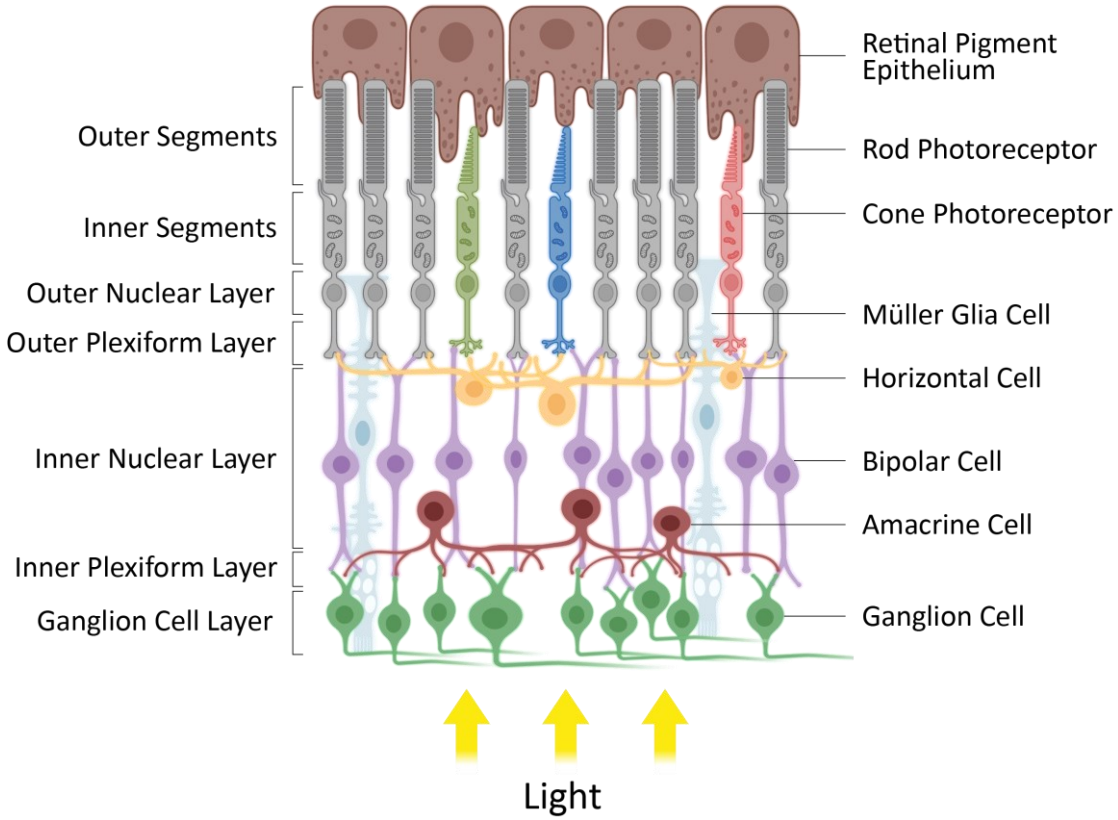

Figure 1. The inverse Structure of the Retina. Light-sensitive photoreceptor outer segments (OS) are embedded in the retinal pigment epithelium (RPE). Photoreceptor cell bodies form the outer nuclear layer (ONL) and their endings synapse with bipolar cells in the outer plexiform layer (OPL). Cell bodies of bipolar cells, horizontal cells and amacrine cells form the inner nuclear layer (INL). Bipolar cells are connected to the ganglion cells in the adjacent inner plexiform layer (IPL). Ganglion cell bodies finally form the ganglion cell layer (GCL).

Rods and cones are highly compartmentalized cells consisting of five principal parts (Figure 2): the synaptic terminal, the cell soma containing the nucleus, the inner segment (IS), the connecting cilium (CC), and the outer segment (OS) (Carter-Dawson and LaVail, 1979). Proteins are produced in the IS, which is the metabolic and biosynthetic machinery containing compartment. The CC connects the OS with the IS and controls protein translocation to the

OS. The RPE has small protrusions (microvilli) which engulf the OS and are involved in OS renewal, restoration of the visual pigment and thus in the maintenance of visual function (Young, 1967; Young and Bok, 1969; van Soest et al., 1999). The OS are filled with multiple stacks of membrane discs formed by invagination of the plasma membrane and contain the photosensitive pigments necessary for phototransduction (Fu, 1995). However, while rod OS discs are separated from the plasma membrane, cone discs are adjacent to the plasma membrane (Pearring et al., 2013).

1.1.2 Phototransduction

The process of absorbing photons in the OS of the photoreceptors in order to generate a visual signal is known as phototransduction. In rods, constant production of cyclic guanosine monophosphate (cGMP) by transmembrane guanylyl cyclases (GCs) causes activation of cyclic nucleotide gated (CNG) channels in the darkness (Yang et al., 1995; Pugh et al., 1997). cGMP-binding to the channel leads to channel opening and permanent influx of sodium (Na^+) and calcium (Ca^{2+}) ions into the cytosol (Hagins et al., 1970; Stryer, 1986). This non-inactivating cation influx is known as the “dark current” which depolarizes the photoreceptor and, in turn, leads to glutamate release at the synaptic terminal (Michalakis et al., 2018).

Upon illumination, a well-characterized G-protein-signaling pathway is initiated (Figure 2). Incoming photons activate the rod-specific photosensitive pigment rhodopsin, a G protein-coupled receptor (GPCR), which causes a conformational change of the 11-*cis*-retinal chromophore to the all-*trans* isomer (Lamb and Pugh, 2006; Arshavsky and Burns, 2012; Palczewski, 2014). Activated rhodopsin, in turn, stimulates the trimeric G protein transducin by exchange of guanosine diphosphate (GDP) with guanosine triphosphate (GTP). Subsequently, the dissociated transducin α-subunit binds to the cGMP-specific phosphodiesterase 6 (PDE6) causing release of the inhibitory constraint of PDE6γ-subunits (Cote, 2021). Enzymatically active PDE6αβ-subunits hydrolyze cGMP resulting in reduction of free cGMP concentration, which in turn leads to CNG channel closure and photoreceptor hyperpolarization. Consequently, the darkness-induced glutamate release is terminated by this hyperpolarization (Molday and Moritz, 2015).

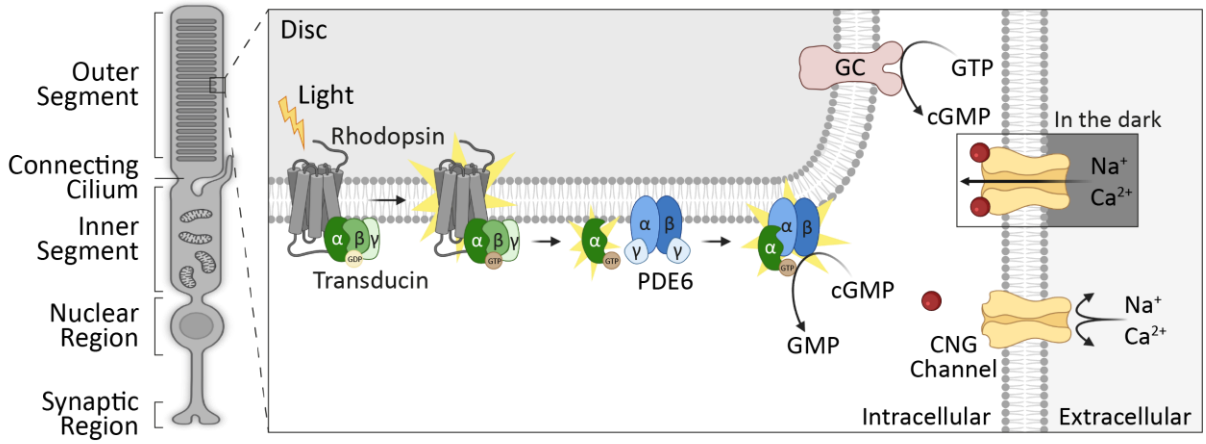

Figure 2. The Rod Phototransduction Process. Compartmentalized rods consist of a synaptic region, a nuclear region, and an inner segment (IS) and outer segment (OS) linked by the connecting cilium. The phototransduction process takes place in the OS: incoming light causes a conformational change of the rod-specific 11-*cis*-retinal chromophore rhodopsin to its all-*trans* isomer. Activated rhodopsin stimulates transducin by exchange of guanosine diphosphate (GDP) with guanosine triphosphate (GTP). The dissociated transducin α-subunit in turn binds to cGMP phosphodiesterase 6 (PDE6) causing release of the inhibitory constraint of PDE6γ-subunits. Cyclic guanosine monophosphate (cGMP) produced by guanylyl cyclases (GCs) is hydrolyzed by activated PDE6 resulting in decrease of free cGMP concentration and, subsequently, in cyclic nucleotide gated (CNG) channel closure. Consequently, the "dark current" cation influx is stopped causing photoreceptor hyperpolarization and finally termination of darkness-mediated glutamate release.

1.1.3 Cyclic Nucleotide-Gated (CNG) Channels

Rod CNG channels are responsible for visual signal transduction during the phototransduction process by controlling the cation influx of Na^+ and Ca^{2+} ions. CNG channels represent a specific class of ion channels within the superfamily of voltage-gated ion channels (VGICs), with which they share a similar structure (Kaupp and Seifert, 2002; Yu et al., 2005; Biel and Michalakis, 2009). The tetrameric native CNG channel complex consists of three α- and one β-subunit (CNGA1 and CNGB1 in rods, CNGA3 and CNGB3 in cones; Figure 3) (Weitz et al., 2002; Zheng et al., 2002; Zhong et al., 2002; Peng et al., 2004; Shuart et al., 2011; Ding et al., 2012; Zheng et al., 2022). Though native CNG channels function as heterotetramers, CNGA-subunits can form functional homotetrameric channels *in vitro* (Chen et al., 1993; Körschen et al., 1995; Finn et al., 1996; Biel et al., 1999b). While general CNG channel structure has been studied extensively, the respective studies focused mainly on homotetrameric CNGA channels including TAX-4 from *C. elegans* (Li et al., 2017; Zheng et al., 2020). Just recently, however, the

first human CNG channel structure was revealed giving new insights into structural mechanisms (Xue et al., 2021a; Xue et al., 2021b). Each subunit is composed of six α-transmembrane helices (S1-S6) and the intracellular N- and C-termini (Figure 3) (Kaupp et al., 1989; Henn et al., 1995). Though S1-S4 helices form the highly conserved so-called voltage-sensitive domain (VSD), CNG channel gating is not voltage-dependent (Craven and Zagotta, 2006; Li et al., 2017; Michalakis et al., 2018). While other members of the VGICs superfamily contain an S4 segment that has regularly distributed positively charged amino acids, the S4 of CNG channels seems to be segmented (Li et al., 2017). This segmentation causes an accumulation of positively charged amino acids at the C-terminal end of S4 and may explain the lacking voltage-dependency of CNG channels. The channel pore is formed by the S5 and S6 helices together with the pore helix and contains the selectivity filter with the sequence motif TIGE within the so-called pore loop (Goulding et al., 1993; Flynn and Zagotta, 2001; Zhou et al., 2001). The cytosolic C-terminus contains the cyclic nucleotide binding domain (CNBD) consisting of four α-helices (A-C and P) and a β-roll between helix A and B. The CNBD is connected to the transmembrane helices by the C-linker which consists of 6 α-helices (A'-F') (Figure 3, right panel).

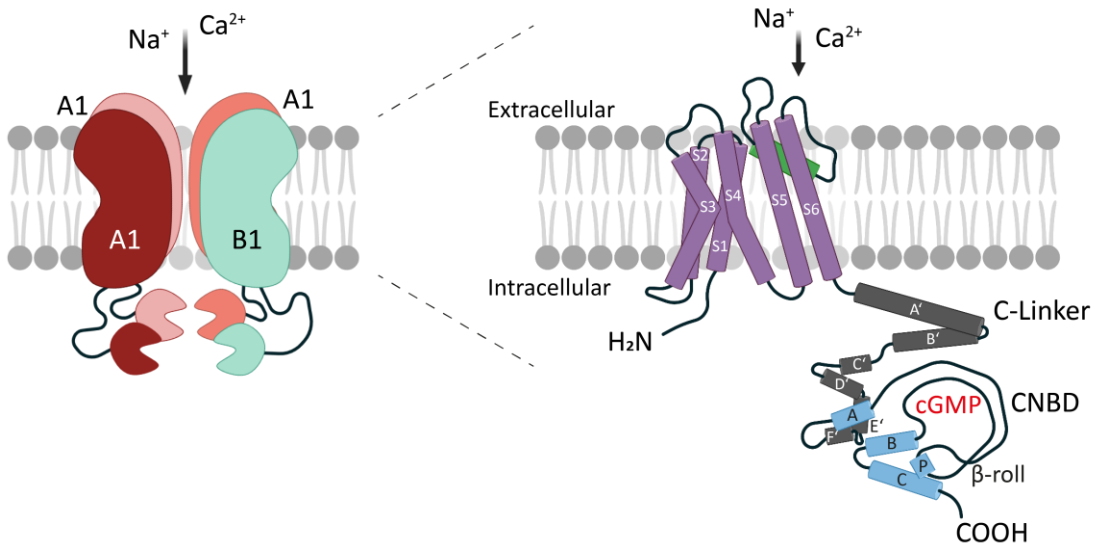

Figure 3. Rod CNG Channel Structure. The tetrameric rod CNG channel consists of three A1- and one B1-subunit. Each subunit is composed of six transmembrane helices (S1-S6) and the intracellular N- and C-termini. The S1-S4 helices form the voltage-sensitive domain (VSD) and the S5 and S6 helices together with the pore helix (green) form the channel pore which contains the selectivity filter in the pore loop. The C-linker located in the C-terminus consists of six α-helices (A'-F') and connects the transmembrane helices to the cyclic nucleotide binding domain (CNBD). The CNBD, in turn, consists of four α-helices (A-C and P) and a β-roll.

The topology of the rod CNG channel subunits is highly conserved throughout the A1- and B1-subtypes (Chen et al., 1993; Körschen et al., 1995; Molday and Molday, 1998; Kaupp and Seifert, 2002).

The most important difference between A1 and B1 subunit, however, is the autoinhibitory N-terminal 571-residue glutamic acid- and proline-rich (GARP) domain in rod B1-subunits (Körschen et al., 1995) which is responsible for CNG channel trafficking to rod OS and controls channel activation by acting as gatekeeper (Poetsch et al., 2001; Michalakis et al., 2011; Pearring et al., 2013; Pearring et al., 2021).

While the A subunits are thought to be responsible for key channel properties, the B subunits appear to contribute specific biophysical properties to the native channel complex in addition to proper localization, such as Ca^{2+}/Calmodulin-dependent modulation, ligand sensitivity and selectivity, and gating (Kaupp and Seifert, 2002; Biel and Michalakis, 2009; Michalakis et al., 2018; Xue et al., 2021a).

1.2 Retinitis Pigmentosa

It is well established that mutations in human CNG channel genes are correlated with inherited diseases (so-called channelopathies) including *retinitis pigmentosa* (RP).

RP is a group of hereditary blinding diseases with a prevalence of 1 in 3.000 - 7.000 that affect more than 1.5 million patients worldwide (Verbakel et al., 2018; Hanany et al., 2020). The term “retinitis pigmentosa” was first introduced by the Dutch ophthalmologist F.C. Donders and refers to the intraretinal pigmentation (“bone spicules”) arising in the mid-periphery and originating from migrating RPE cells (Fahim et al., 1993; Verbakel et al., 2018). RP is characterized by progressive retinal degeneration, that begins with primary demise of rod photoreceptors, followed by the secondary loss of cone photoreceptors (Hamel, 2006; Hartong et al., 2006; Verbakel et al., 2018). Initially, rod degeneration manifests as night blindness, followed by loss of peripheral vision which is known as “tunnel vision” (Figure 4). Since cone survival depends on rod survival, secondary degeneration of cones occurs as gradual visual field constrictions and eventually results in complete blindness. Although the main features are common in all forms of RP, the age of onset, time course of disease progression, and severity of symptoms depend on the genetic defect.

Approximately 50-60% of all patients suffer from an autosomal recessive form, while autosomal dominant and X-chromosomal-linked forms make up 30-40% and 5-15%,

respectively (Hartong et al., 2006). To date, mutations in about 90 genes have been linked to RP (https://sph.uth.edu/RETNET/), but the mechanisms underlying photoreceptor cell death still remain unclear.

Figure 4. Progression of RP. Initial rod degeneration manifests as night blindness followed by loss of peripheral vision in the early stage leading to so-called "tunnel vision". Secondary degeneration of cones leads to a further reduction of the visual field in the intermediate stage. In the late stage, complete blindness eventually occurs.

Several hypotheses have been developed proposing that cell death is usually caused by apoptosis (Sancho-Pelluz et al., 2008; Newton and Megaw, 2020). Apoptosis is known as programmed cell death of dysfunctional cells triggered by the cell itself without damaging surrounding healthy cells (Kerr et al., 1972; Lockshin and Zakeri, 2001). One frequently raised photoreceptor cell death hypothesis involves extensively high cGMP levels and excessive Ca^{2+} influx (Fox et al., 1999; Fiscus, 2002). Indeed, mutations that incite either a nonfunctional cGMP-hydrolyzing PDE6 or overactive cGMP-producing GCs, both of which lead to extremely high levels of cGMP, have been shown to cause some types of RP (McLaughlin et al., 1993; Yan et al., 1998; Tucker et al., 1999). Consistent with this, cGMP-forced activation of CNG channels leading to excessive Ca^{2+} influx is suggested to have an impact on rod photoreceptor cell death (Takano et al., 2004; Wenzel et al., 2005; Paquet-Durand et al., 2011). In contrast, also low Ca^{2+} levels were reported to contribute to cell death mechanisms. Continuous light-induced damage, causing permanent CNG channel closure and, thus, reduction of Ca^{2+} levels, has widely been used for generation of RP models (Hao et al., 2002; Wenzel et al., 2005; Fain, 2006). Moreover, by means of the equivalent-light hypothesis, these findings can be applied to CNG channelopathies. This hypothesis states that the absence of CNG channels is equivalent to permanent CNG channel closure by light overexposure, and thereby also leads to low Ca^{2+} levels (Lisman and Fain, 1995; Pierce, 2001). The low Ca^{2+} hypothesis also supports the assumption that excessive Ca^{2+} levels, as suggested by the high Ca^{2+} hypothesis, appear only secondary to the degeneration process. Furthermore, the excessive Ca^{2+} levels may not

only be caused by CNG channels, but also by dysfunctional voltage-dependent L-type Ca^{2+} channels, mitochondria or endoplasmic reticulum (ER) (Frasson et al., 1999; Fain, 2006; Sancho-Pelluz et al., 2008).

1.2.1 *CNGA1*-linked RP - Type 49

Mutations in the *CNGA1* gene are found to cause the autosomal recessive RP type 49 (RP49) that makes up 1-8% of all autosomal recessive RP cases depending on the genetic background (Dryja et al., 1995; Paloma et al., 2002; Zhang et al., 2004; Chen et al., 2013; Katagiri et al., 2014; Maria et al., 2015; Jin et al., 2016; Wang et al., 2016; Gao et al., 2019; Wang et al., 2020). Several disease-causing mutation patters of CNGA1 are published to date and share a similar phenotype characterized by night blindness from an early age, followed by a slowly progressing age-related loss of peripheral vision and decreased visual acuity by about 30 years of age. The human *CNGA1* gene is located on the shorter arm of chromosome 4 at position 12 (4p12) and consists of at least 11 exons (Dhallan et al., 1992; Griffin et al., 1993). Two transcript variants are known resulting in the expression of two isoforms with a molecular weight of about 80 kDa.

Until recently, only one transgenic mouse model was available, in which overexpression of a CNGA1 antisense mRNA causes a 50% reduction of CNGA1 transcript levels (Leconte and Barnstable, 2000). Although showing progressive retinal degeneration comparable to human patients, possible toxic effects induced by antisense mRNA overexpression that could affect the phenotype cannot be excluded. However, in 2021 a first knockout (KO) mouse model was established using the CRISPR/Cas technique (Liu et al., 2021), in which a 65 bp deletion in exon 2 leads to complete loss of CNGA1 protein. These mice developed a relatively rapid degeneration of rods with a reduction to 50% at 2 months of age, and complete loss at 4 months of age.

In the present study, a second mouse model, rederived from the ENU archive (Sabrautzki et al., 2017), was characterized. These mice carry a missense mutation in the murine *Cnga1* gene leading to the substitution of Tyr509 by Cys (c.1526A>G; p.Tyr509Cys) and therefore to non-functional CNGA1 protein. This mutation affects a residue that is highly conserved in a variety of species, including humans, and which is equivalent to human Tyr513. As it is thus only 4 amino acids away from a mutant residue recently found in human RP patients (Arg509;

(Kandaswamy et al., unpublished) it is well likely that this mutation has similar effects and reflects the phenotype of RP49 patients.

1.2.2 *CNGB1*-linked RP - Type 45

The autosomal recessive RP type 45 (RP45) is caused by mutations in the *CNGB1* gene and represents about 4% of all autosomal recessive RP cases (Hartong et al., 2006). The course of RP45 seems to be very similar to RP49, including night blindness in early childhood and progressive loss of peripheral vision (Bareil et al., 2001; Kondo et al., 2004; Sahel et al., 2010; Azam et al., 2011; Simpson et al., 2011; Song et al., 2011; Bocquet et al., 2013; Fu et al., 2013; Nishiguchi et al., 2013; Schorderet et al., 2013; Tiab et al., 2013; Maranhao et al., 2015; Maria et al., 2015; Saqib et al., 2015; Xu et al., 2015; Fradin et al., 2016; Perez-Carro et al., 2016; Habibi et al., 2017; Hull et al., 2017; Petersen-Jones et al., 2018; Xiang et al., 2018; Ba-Abbad et al., 2019; Rodriguez-Munoz et al., 2020). RP45 is typically diagnosed at around 30 years of age and leads to complete blindness by 60 years of age. The human *CNGB1* gene is located on the longer arm of chromosome 16 at position 21 (16q21). It consists of at least 33 exons (Ardell et al., 1996; Ardell et al., 2000; Bareil et al., 2001) encoding several splicing variants. Rod photoreceptors express the 240 kDa CNGB1a isoform, whereas the shorter CNGB1b isoform is expressed in olfactory neurons (Chen et al., 1993; Körschen et al., 1995; Sautter et al., 1998; Bönigk et al., 1999).

To date, various animal models of *CNGB1*-linked RP have been established (Hüttl et al., 2005; Zhang et al., 2009; Ahonen et al., 2013; Winkler et al., 2013). In this study, *Cngb1*-deficient mice were used as preclinical animal model for the development of new gene therapy approaches. The *Cngb1* KO (*Cngb1*$^{-/-}$) mouse model (Hüttl et al., 2005) lacking exon 26 (*Cngb1*-X26), and thus resulting in premature termination of CNGB1 translation, is characterized by a slow progressive retinal degeneration with an early onset already at postnatal day 15 (P15). By 6 months of age, about 50% of the rods are lost, which subsequently leads to cone degeneration, and by 1 year of age, only 10-20% of the photoreceptors remain.

1.2.3 *PDE6A*-linked RP - Type 43

Moreover, it is known that mutations in the gene encoding the PDE6 β-subunit cause some cases of RP (RP type 40, RP40). As both α- and β-subunits are required for full phosphodiesterase activity, also the *PDE6A* gene was screened for mutations (Huang et al.,

1995). Until today, several mutations were identified causing the autosomal recessive RP type 43 (RP43) (Dryja et al., 1999; Riazuddin et al., 2006; Sakamoto et al., 2009; Corton et al., 2010; Khan et al., 2015; Nair et al., 2017; Mizobuchi et al., 2019; Dawood et al., 2021). Patients with RP43 also share a similar phenotype including slow disease progression in childhood, followed by sudden loss of large visual field areas and subsequent slow progression of degeneration of the remaining visual field (Kuehlewein et al., 2020). The human *PDE6A* gene is located on the longer arm of chromosome 5 spanning the positions 31 to 33 (5q31-q33) (Pittler et al., 1990). It consists of 22 exons and causes the expression of a ~100 kDa protein (Huang et al., 1995). Several animal models have been established representing RP43 (Petersen-Jones et al., 1999; Sakamoto et al., 2009; Tuntivanich et al., 2009; Sothilingam et al., 2015).

In this study, two different *Pde6a*-deficient mouse models were used for the generation of a new crossbred mouse line in order to characterize the mechanisms leading to photoreceptor cell death. For generating this new mouse model, homozygous *Pde6a* mutant ($Pde6a^{MUT}$) mice carrying either the V685M mutation ($Pde6a^{V685M}$) or the R562W mutation ($Pde6a^{R562W}$) (Sakamoto et al., 2009; Sothilingam et al., 2015) were used. The V685M mutation causes an amino acid change in exon 16 resulting in loss of catalytic function of PDE6A. The R562W knock-in mutation leads to skipping of exon 13 and thereby to shortened PDE6A protein (p.541_576del), which lacks the amino-terminal portion of the catalytic domain. Both $Pde6a^{MUT}$ mouse lines exhibit a fast-progressing RP phenotype characterized by reduced photoreceptor layer thickness and reduced response to light. While $Pde6a^{V685M}$ mice have only minor residual PDE6 activity, $Pde6a^{R562W}$ mice still show 10% activity compared to corresponding wild type (WT) mice and therefore represent the less affected mutant. Recently, additional ablation of CNG channels in *rd1* mice, a mouse model of fast-progressing *PDE6B*-linked RP, was shown to result in morphological rescue of rod photoreceptors (Paquet-Durand et al., 2011). For this reason, $Pde6a^{MUT}$ mice were crossbred with $Cngb1^{-/-}$ mice in order to investigate possible rescue effects also in this new double-mutant (DBM) mouse model.

In addition to this new mouse line, the previously described $Pde6a^{-/-}$ dog model was used for further development of a gene augmentation therapy (Petersen-Jones et al., 1999; Tuntivanich et al., 2009; Mowat et al., 2017; Occelli et al., 2017). $Pde6a^{-/-}$ dogs carry a 1 bp adenine deletion in exon 15 resulting in premature termination of translation and, thus, in

absence of PDE6A protein. Similar to *Pde6a*^{MUT} mice, *Pde6a*$^{-/-}$ dogs show an early-onset and fast-progressing phenotype with photoreceptor cell death peaking at postnatal day 21 (P21).

1.3 Therapeutic Interventions for RP: Gene Therapy

To date, no curative treatment option for RP exists. Pharmacological approaches aim to provide supportive and conservative treatment but do not target the underlying mechanisms of RP leading to cell death (Dias et al., 2018). However, several strategies are under investigation including neuroprotection by neurotrophic or anti-apoptotic agents (Buch et al., 2007; Drack et al., 2012; Trifunovic et al., 2012; Guadagni et al., 2015; Jayakody et al., 2015), retinal prostheses (Chow et al., 2004; Yanai et al., 2007) and cell transplantation (Shintani et al., 2009; Jones et al., 2017). One promising approach is the transplantation of autologous mutation-corrected induced pluripotent stem cells (iPSCs). Recently, a CRISPR/Cas9-mediated genome editing strategy was developed to correct retinal mutations in iPSCs (Burnight et al., 2017).

Nevertheless, a growing number of preclinical and clinical trials has successfully demonstrated photoreceptor rescue and preserved vision using gene therapeutic approaches for the therapy of inherited retinal diseases (Petersen-Jones et al., 2009; Komaromy et al., 2010; Michalakis et al., 2010; Carvalho et al., 2011; Black et al., 2014; Beltran et al., 2015; Latella et al., 2016; Hafler, 2017; Mowat et al., 2017; Occelli et al., 2017; Schön et al., 2017; Cideciyan et al., 2018; Ofri et al., 2018; Maeder et al., 2019; Cehajic-Kapetanovic et al., 2020; Garafalo et al., 2020; Wagner et al., 2021). Moreover, in 2018, the first gene therapy product for Leber congenital amaurosis, Luxturna® (voretigen neparvovec, Novartis) (Bainbridge et al., 2008; Jacobson et al., 2012; Maguire et al., 2019), was approved marking the beginning of a new era.

1.3.1 The Eye as a Target for Gene Therapy

Currently, the eye is in the focus of translational gene therapy research, as it offers favorable anatomical and immunological characteristics (Dias et al., 2018; Ziccardi et al., 2019). The main advantages are (1) the accessibility for surgeries and follow-up monitoring; (2) the small size of the retina that allows small amounts of therapeutics; (3) the compartmentalization of the eye that prevents systemic spreading of therapeutics; (4) the immune privilege that reduces immune response and allows good tolerance of therapeutics; and (5) the possibility of treating only one eye and using the contralateral untreated eye as an internal control. Besides,

mammals share a similar eye anatomy, allowing the testing of potential gene therapies in multiple mammalian animal models (Slijkerman et al., 2015).

Gene therapy drugs are mainly administered by intraocular injections (Figure 5) (Dias et al., 2018; Ziccardi et al., 2019; Botto et al., 2021; Ross and Ofri, 2021). To date, most retinal gene therapies require subretinal (SR) delivery of the therapeutic vector. SR injections, although reaching target cells in the outer retina more precisely, are more invasive and require iatrogenic retinal detachment. This can potentially damage the photoreceptors and thus impair remnant vision (Jacobson et al., 2006; Peng et al., 2017). Moreover, only retinal cells are transduced that are in close contact to the subretinal bleb, which is formed by the injection and contains the therapeutic agent. Consequently, the treatment effect is limited to a small area. In contrast, intravitreal (IVT) injections are less invasive, easier to perform and do not damage the retina. However, although a wide retinal area can be reached by IVT injections, delivery to the outer retinal cells seems to be less efficient (Harvey et al., 2002; Dalkara et al., 2009). Despite the limitations of both types of applications, intraocular injections of gene therapy drugs represent a promising treatment option for inherited retinal diseases and are therefore of great scientific interest.

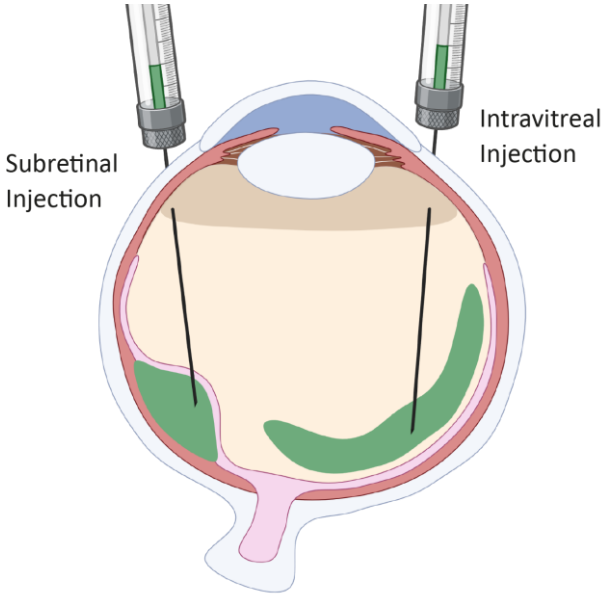

Figure 5. Administration Pathways used for Gene Therapy in the Eye. Subretinal (SR) injections cause retinal detachment by formation of a subretinal bleb that contain the therapeutic agent. In contrast, intravitreal (IVT) injections force the therapeutic agent to spread inside the vitreous.

1.3.2 Recombinant Adeno-Associated Virus-Mediated Gene Augmentation

The wide heterogeneity of RP makes it difficult to provide a single, common gene therapy approach. However, many auspicious gene therapy approaches are currently being investigated. While CRISPR/Cas-mediated genome editing and gene silencing seems to be promising for autosomal dominant mutations, gene augmentation (also called gene replacement or gene supplementation) has so far obtained the best results in the treatment of autosomal recessive RP (Dalkara and Sahel, 2014; Dias et al., 2018; Ziccardi et al., 2019). For this strategy, a healthy copy of the whole mutant gene, under the control of a tissue specific promoter, is delivered to the affected cells to compensate the lack of functional protein (Figure 6). Gene augmentation is therefore exceptionally suitable for the therapy of diseases caused by loss-of-function mutations.

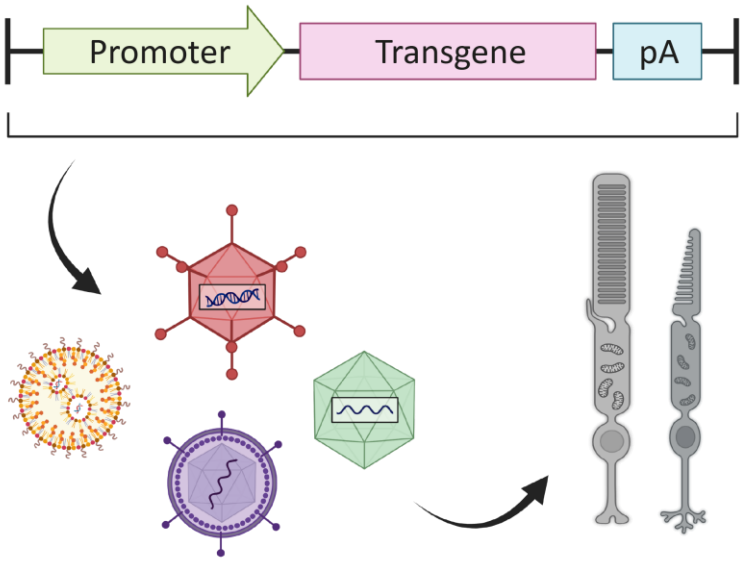

Figure 6. Gene Supplementation Therapy. An entire expression cassette including a tissue specific promoter, the gene of interest (transgene) and a polyadenylation signal (pA) is packaged into specific gene therapeutic vectors and delivered to the target cells.

For the delivery of therapeutic genes (transgenes), viral and non-viral vectors can be used (Lipinski et al., 2013). Retinal gene therapies are mostly based on recombinant viral vectors, of which three types are available (Dias et al., 2018; Ziccardi et al., 2019; Botto et al., 2021): adenoviruses (Ads), lentiviruses (LVs) and adeno-associated viruses (AAVs).

Ads are non-enveloped double-stranded (ds) DNA viruses with a diameter of approximately 90-100 nm. Despite their large cargo capacity of up to 37 kb, and their abilities to transduce a

large number of cell types and to obtain high levels of transgene expression, Ads remain only second choice vectors for retinal gene therapy. This can be attributed to poor transduction of photoreceptor cells (except in early developmental stages), lack of longevity of expression, and high safety risks leading to immune responses and long-term toxicity.

LVs are enveloped single-stranded (ss) RNA retroviruses that can integrate their proviral DNA into the host genome. LVs used for gene therapy are modified to stop their replication and thus are non-pathogenic. They are characterized by a relatively high loading capacity of about 8-10 kb and allow stable transgene expression by genome integration. However, this integration also causes the risk of insertional mutagenesis. In addition, LVs transduce photoreceptor cells only poorly, which is why they are rarely used in retinal gene therapy.

In contrast, AAVs represent a well suitable and the best characterized delivery approach for retinal gene therapy. AAVs are small (~25 nm), non-enveloped and non-pathogenic dependoviruses meaning that they require an AdHelper virus for replication since AAVs themselves are naturally deficient in replication (Hastie and Samulski, 2015). AAVs contain an ssDNA genome which consists of a *rep* gene encoding for replication proteins and a *cap* gene encoding for viral proteins. The *rep* and *cap* genes are flanked by inverted terminal repeats (ITRs) that serve as origins of replication (Barnes et al., 2019). For gene therapy application, *rep/cap* genes have been removed in favor of the transgene resulting in recombinant AAVs (rAAVs).

The major advantages of rAAV-based gene therapy are the low immunogenicity, high transduction efficiency, and ability to maintain sustained transgene levels, and broad tropism by different serotypes (Dalkara et al., 2016; Srivastava, 2016; Ziccardi et al., 2019). To date, more than 100 serotypes have been identified (Gao et al., 2002; Gao et al., 2004; Mori et al., 2004; Schmidt et al., 2006) and AAV serotype 2 (AAV2) has been used as gold standard for retinal gene therapy. In order to combine the advantages of AAV2, such as transduction efficiency with specific tissue tropism, so-called “pseudotyped” AAVs have been developed by fusion of AAV2 *rep* with another serotype’s *cap* gene (Auricchio, 2003; Grimm and Kay, 2003). Moreover, capsid engineering has become of great interest in recent years since there is an unmet need for novel rAAV capsids targeting larger retinal areas or enhancing retinal transduction (Petrs-Silva et al., 2009; Dalkara et al., 2013; Kay et al., 2013; Zinn et al., 2015; Grimm and Buning, 2017; Barnes et al., 2019; Katada et al., 2019; Pavlou et al., 2021; Ross and Ofri, 2021). The major limitation of AAVs, however, is the restricted packaging capacity of only

4.7 kb (Wu et al., 2010), which precludes treatment of diseases caused by mutated genes greater than 4 kb. To overcome this limitation, several strategies including rAAV dual vector technologies have been developed (McClements and MacLaren, 2017; Trapani, 2019). In this process, a transgene is split into at least two parts and packaged into the appropriate number of separate rAAV vectors. The transgene is then reconstituted in full length after co-transduction of the target cells.

Despite the great success of viral vectors in the treatment of inherited retinal diseases, delivery vectors still need to be improved. For this reason, non-viral delivery systems such as nanoparticles or liposomes are increasingly coming into the focus of basic and translational research (Dias et al., 2018; Ziccardi et al., 2019; Botto et al., 2021). Non-viral vectors are superior to viral vectors with respect to their low immunogenicity, easier producibility and lower production costs. However, they show lower transduction efficiency and are currently hardly used in clinical trials.

Nevertheless, regardless of which vectors are used, gene therapy approaches have been investigated in various preclinical and clinical studies and the field has made significant progress in recent years, making gene therapy a promising new strategy for the treatment of inherited retinal diseases.

2 Aim of the Thesis

Most autosomal-recessive forms of RP (arRP) are caused by mutations in genes that are necessary for the phototransduction process. Although great scientific effort has been made, the mechanisms underlying the clinical manifestation of RP still remain unclear. Moreover, currently no approved treatments are available. Since RP is a monogenic disease caused by mutations, gene supplementation approaches have been increasingly investigated in recent years.

In the present study, a multilevel approach was employed aiming to characterize disease mechanisms of RP and to develop novel potentially curative gene therapeutic approaches for specific forms of RP. For this purpose, the following concepts were investigated:

(1) First, the retinal phenotype of a new *Cnga1* mutant (*Cnga1*^{MUT}) mouse line was characterized. *In vivo* and *ex vivo* tests were performed in order to clarify to which extent this mouse line can be used to model the phenotype of human RP patients.

(2) Furthermore, in order to elucidate how signaling pathways are deregulated in RP, proteomic and immunohistochemical analysis of retinal samples from different animal models was performed. For this purpose, four mouse or dog models of RP with effects in different proteins involved in rod phototransduction were analyzed and compared.

(3) The final aim was to develop new gene therapeutic approaches for the therapy of *CNGA1*- or *CNGB1*-linked RP and to test their efficacy in *Cngb1*$^{-/-}$ and *Cnga1*^{MUT} mice, respectively. To this end, rAAV vectors expressing a healthy copy of the affected gene were generated and administered locally to the eye via subretinal or intravitreal injection. Subsequently, treatment effects were analyzed in the living animal or in tissue samples after necropsy to assess therapeutic benefit at the functional and morphological level.

3 Materials and Methods

3.1 Materials

All materials, chemicals, solutions and buffers were purchased from Sigma-Aldrich, VWR, Merck, Thermo Fisher Scientific, Bio-Rad or Roth unless stated otherwise. Their quality was either “pro analysi” or “for molecular biology”. Highly pure deionized water obtained from a Milli-Q Plus System (Millipore) was used for all buffers and reaction mixes.
Schematics were created with Biorender.com and figures were generated using Adobe Illustrator.

3.2 Animals

All animal experiments in this study were carried out in accordance with the ARVO Statement of the Use of Animals in Ophthalmic and Vision Research and were approved by the local authorities (Regierung von Oberbayern, Regierungspräsidium Tübingen, Michigan State University and Charles River Laboratories Institutional Animal Care and Use Committees).
All mice maintained at the mouse facility of the Department of Pharmacy, Ludwig-Maximilians-University Munich were kept in conventional Euro-Standard type III cages under SPF conditions in a 12 h light/dark cycle and received food (Ssniff; regular feed: R/M-H autoclavable V1534/35-3; breeding feed: M-Z Extrudat autoclavable V1124/25-3) and water *ad libitum*. Ear punctures were used for identification.
All dogs were housed in standard laboratory accommodation in the AAALAC approved vivarium at the MSU College of Veterinary Medicine in a 12 h light/dark cycle and fed with a commercial laboratory dog diet.

3.2.1 *Cnga1^{MUT}* mice

The *Cnga1^{MUT}* mouse line was generated by the Institute of Developmental Genetics, Helmholtz Zentrum München, German Research Center for Environmental Health, Neuherberg, Germany. For that purpose, ten-week-old C3HeB/FeJ male mice were injected intraperitoneal with ENU (three doses of 90 mg/kg in weekly intervals) as previously described (Hrabe de Angelis et al., 2000). A DNA archive was generated by cryo-archiving of first generation (F1) founder male mice by their sperm and spleen-derived DNA samples

(Sabrautzki et al., 2017). This DNA archive was screened for mutations in the *Cnga1* gene affecting the cytoplasmic domain using the following primers:

Cnga1Ex9L1: 5´ - TGA GAG AGA AGT CCT GAG ATA CC - 3´
Cnga1Ex9R1: 5´ - TGA GGT CAT CTT TGG AGA GGC - 3´

Cnga1^{MUT} mice were bred on a C57BL6/J-background, without the rd1 and rd8 mutation. The corresponding wild type mice were used as wild type controls.

3.2.2 *Cngb1*$^{-/-}$ mice

The *Cngb1*$^{-/-}$ mouse line was generated as described (Hüttl et al., 2005) and bred on a genetically mixed background of the strains 129/SvJ and C57BL6/N, without the rd8 (Crb111; (Mattapallil et al., 2012) mutation. The corresponding wild type mice were used as wild type controls.

3.2.3 *Pde6a*^{MUT}*xCngb1*$^{-/-}$ mice

Double-mutant *Pde6a*^{MUT}*xCngb1*$^{-/-}$ mice were housed at the animal facility of the Division of Ocular Neurodegeneration, Centre for Ophthalmology, Institute for Ophthalmic Research, University of Tübingen by the group of Dr. Regine Mühlfriedel (Prof. Dr. Mathias Seeliger lab). *Pde6a*^{MUT}*xCngb1*$^{-/-}$ mice were generated by crossbreeding of homozygous *Pde6a* mutant mice, having either the V685M or the R562W mutation, with *Cngb1*$^{-/-}$ mice. The *Pde6a*-V685M (*Pde6a*^{V685M}; A.B6-Tyr+/J-*Pde6a*$^{nmf282/nmf282}$) mouse line was obtained from Jackson Labs (Sakamoto et al., 2009). The *Pde6a*-R562W-knock-in (*Pde6a*^{R562W}) mouse line was generated by GenOway using standard procedures of homologous recombination in murine embryonic stem (ES) cells as described previously (Sothilingam et al., 2015). Double-mutant (DBM) mice that were homozygous for *Pde6a* and *Cngb1* mutations were used for the present study. The corresponding wild type mice were used as wild type controls.

3.2.4 Pde6a$^{-/-}$ dogs

The *Pde6a*$^{-/-}$ dog line was generated as described (Petersen-Jones et al., 1999; Tuntivanich et al., 2009) and all dogs used for this study were homozygous for a mutation in the *Pde6a* gene.

3.3 Genotyping of *Cngb1*$^{-/-}$ and *Cnga1*^{MUT} mice

3.3.1 Genomic DNA Isolation

Tissue for genomic DNA isolation was obtained by ear biopsies and genomic DNA was isolated as follows. Tissue samples were digested in 600 µL NaOH (50 mM) at 95°C for 10 min. Subsequently, 50 µl Tris-HCl (pH 8.0) were added for pH neutralization, the samples were centrifuged for 6 minutes at 13.000 rpm and the DNA containing supernatant was used for polymerase chain reaction (PCR).

3.3.2 Polymerase Chain Reaction (PCR)

PCR was carried out using a ProFlex PCR System Cycler (Applied Biosystems) to amplify DNA fragments with GoTaq polymerase (Promega) in combination with the following primers (Eurofins Genomics Germany GmbH).

Primer	**Sequence 5'-3' (*Cngb1*$^{-/-}$)**	**Sequence 5'-3' (*Cnga1*^{MUT})**
Primer_for	CCT CAT GCA TGC GAC CTG AAA T	TGA GAG AGA AGT CCT GAG ATA CC
Primer_rev 1	GCC CAG ACT AGA ACA CAA GTC	TGA GGT CAT CTT TGG AGA GGC
Primer_rev 2	CAC AGC CAT TAC ACA TAG CAG TG	-

The following reaction mix was prepared for PCR:

Substance	**Volume [µL] (*Cngb1*$^{-/-}$)**	**Volume [µL] (*Cnga1*^{MUT})**
Template DNA	2	2
Primer_for (10 µM)	1.5	1.5
Primer_rev 1 (10 µM)	1.5	1.5
Primer_rev 2 (10 µM)	1.5	-
dNTPs	4	4
5x Green GoTaq® buffer	5	5
GoTaq® DNA polymerase	0.2	0.2
H_2O	ad 25	ad 25

The following PCR cycle protocol was used for amplification of DNA fragments:

Step	Temperature	Duration	Cycles
Initial Denaturation	95°C	5 min	1
Denaturation	95°C	30 s	35
Annealing	60°C (*Cngb1*$^{-/-}$) 59°C (*Cnga1*^{MUT})	30 s	
Elongation	72°C	30 s	
Final Elongation	72°C	5 min	1

3.3.3 Agarose Gel Electrophoresis and Fragment Isolation

For separation and detection of amplified DNA fragments, gel electrophoresis was carried out using 2 % agarose gels. Gels were prepared by dissolving agarose (Genaxxon Bioscience) in Tris/Borate/EDTA (TBE) buffer. PeqGreen (VWR International GmbH) was used to visualize DNA fragments under UV light. The solid gel was placed in an electrophoresis chamber filled with TBE buffer. Pockets were loaded with PCR samples, a molecular weight marker (Gene Ruler 1 kb plus DNA ladder; Thermo Fisher Scientific) was used as a DNA size reference, and electrophoresis was carried out by applying a voltage of 120 – 180 V. Subsequently, separated bands were visualized under UV light (GelDoc 2000 molecular imager, Bio-Rad Laboratories, Inc.). For *Cngb1*$^{-/-}$ mice, wild type (WT) and knockout bands were identified at 480 bp and 415 bp, respectively. For *Cnga1*^{MUT} mice, the resulting 400 bp fragment was isolated using the Qiaquick Gel Extraction Kit (Qiagen) according to the manufacturer's instructions and DNA concentration was measured using the Nanodrop™ 2000c spectrophotometer (Thermo Fisher Scientific).

3.3.4 Restriction Digest

For identifying *Cnga1*^{MUT} mice, the isolated 400 bp fragment was digested using the restriction enzyme FastDigest RsaI (Thermo Fisher Scientific).

The following digestion mix was prepared:

Substance	Volume
DNA sample	200 ng
10x Fast Digest Green Buffer	2 µL
Fast Digest RsaI	0.5 µL
H_2O	ad 20 µL

Digests were incubated for 2 h at 37°C and gel electrophoresis was carried out afterwards as described above. Wild type and mutant bands were identified at 200 bp and 400 bp, respectively.

3.4 Cloning

3.4.1 pGL2.0_hRHO194-hCNGB1a-SV40pA_modified

For generation of pGL2.0_hRHO194-hCNGB1a-SV40pA_modified (Figure 7), an in-house produced version of pGL2.0_hRHO194-hCNGB1a-SV40pA (Wagner et al., 2021) was modified. cDNA sequence of hCNGB1a in in-house pGL2.0_hRHO194-hCNGB1a-SV40pA was based on transcript variant 1 (NCBI Reference Sequence NM_001297.4) with two differences: K404del and K1091Q. For modification of these differences (Q403_L404insK and Q1091K), standard cloning techniques and site-directed mutagenesis were used as described in chapter 3.4.3 and 3.4.4.

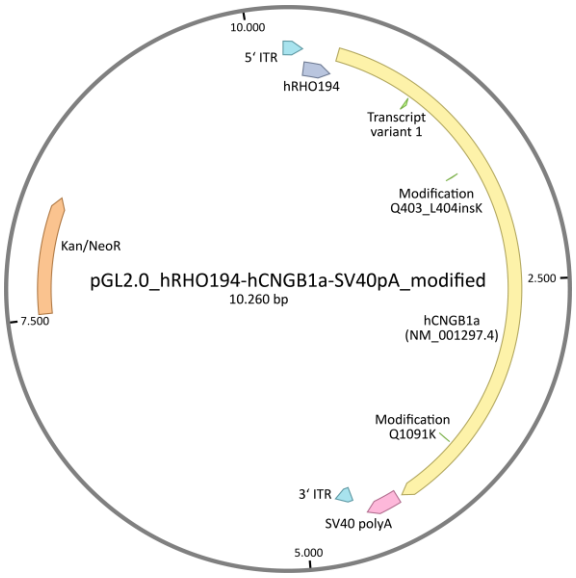

Figure 7. Plasmid Map of pGL2.0_hRHO194-hCNGB1a-SV40pA_modified. The expression cassette consists of a short human rhodopsin promoter (hRHO194), the modified cDNA sequence of hCNGB1a (NM_001297.4), and a SV40 poly A, and is flanked by AAV2 ITRs. The map was designed with benchling.com.

First, the hCNGB1a-fragment was cloned into another backbone (pcDNA^{TM}3.1, Invitrogen, Thermo Fisher Scientific) using the restriction enzymes BamHI and BcuI. Site-directed mutagenesis was performed one after the other for both mutation sites using the following primers (Eurofins Genomics Germany GmbH):

Q403_L404insK_for: 5’ - GCA CTT CAG ATC AGA AGC TGT GGG AGG AAG TTG GGG - 3’
Q403_L404insK_rev: 5’ - CCC CAA CTT CCT CCC ACA GCT TCT GAT CTG AAG TGC - 3’

Q1091K_for: 5’ - GCA ACA ATA AGC CCA AGG AGG AGA AGA GCG TGC - 3'
Q1091K_rev: 5’ - GCA CGC TCT TCT CCT CCT TGG GCT TAT TGT TGC - 3'

After confirmation of sequence modifications by Sanger sequencing (Eurofins Genomics Germany GmbH), hCNGB1a_modified was cloned back into the pGL2.0-backbone by again restriction digest with BamHI and BcuI and ligation.
The final plasmid sequence was again verified by sequencing.

3.4.2 pGL2.1_hRHO-hCNGA1-mWPRE-BGHpA

The plasmid pGL2.1_hRHO-hCNGA1-mWPRE-BGHpA (Figure 8) was produced at LMU by Dr. Victoria Splith (now ViGeneron GmbH). Standard cloning techniques were used for plasmid generation. cDNA sequence of hCNGA1 in pGL2.1_hRHO-hCNGA1-mWPRE-BGHpA was based on transcript variant 2 (NCBI Reference Sequence NM_000087.5).

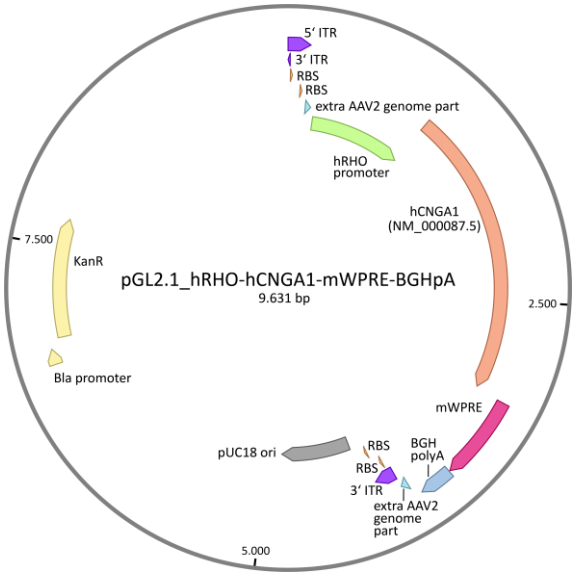

Figure 8. Plasmid Map of pGL2.1_hRHO-hCNGA1-mWPRE-BGHpA. The expression cassette consists of a human rhodopsin promoter (hRHO), the cDNA sequence of hCNGA1 (NM_000087.5), a mouse WPRE, and a BGH poly A, and is flanked by modified AAV2 ITRs. The map was designed with benchling.com.

3.4.3 Standard Cloning Techniques

3.4.3.1 Restriction Digest

For restriction digest, FastDigest restriction enzymes (Thermo Fisher Scientific) were used according to the manufacturer's instructions.

The following digestion mix was prepared:

Substance	Volume
DNA	3 µg
10x Fast Digest Green Buffer	3 µL
FastDigest RE	1 µL each
H_2O	ad 30 µL

Digests were incubated for 2 h at 37°C and gel electrophoresis was carried out afterwards.

3.4.3.2 Agarose Gel Electrophoresis and Fragment Isolation

For separation and isolation of digested DNA fragments, gel electrophoresis was carried out using 0.7 – 2% agarose gels depending on the size of the fragments of interest. Gel electrophoresis and visualization of DNA fragments was performed as described in chapter 3.3.3. Fragments of interest were isolated using the Qiaquick Gel Extraction Kit (Qiagen) according to the manufacturer's instructions and DNA concentration was measured using the Nanodrop™ 2000c spectrophotometer (Thermo Fisher Scientific).

3.4.3.3 Ligation

For ligation of two fragments, T_4-DNA Ligase (Thermo Fisher Scientific) was used according to the manufacturer's instructions.

The following ligation mix was prepared:

Substance	Volume
Backbone	100 ng
Insert	X ng
T_4-Ligase Buffer	4 µL
T_4-Ligase	1 µL
H_2O	ad 20 µL

The amount of insert was calculated using the following equation:

$$X\ [ng] = \text{molar ratio } \left(\frac{\text{insert}}{\text{backbone}}\right) \times 100\ ng \times \frac{\text{length insert [kb]}}{\text{length backbone [kb]}}$$

A molar ratio $\left(\frac{\text{insert}}{\text{backbone}}\right)$ of 1:2 or 1:3 was chosen depending on the size of the fragments. Ligations were incubated for 1 h at RT and used for bacterial transformation afterwards.

3.4.3.4 Bacterial Transformation and Inoculation

For production of plasmid DNA, chemically competent Stbl3 *Escherichia coli* bacteria (One Shot™ Stbl3™ Chemically Competent *E. coli*, Invitrogen, Thermo Fisher Scientific) were used. Bacteria were thawed on ice for 10 min prior to transformation. 3, 5 or 10 µL of the ligation mix were added to the bacteria, gently mixed and chilled on ice for 30 min. The bacteria were heat-shocked at 42°C for 30 s in a Thermomixer compact (Eppendorf) and incubated on ice for 2 min. Subsequently, the bacteria were plated on LB(+) agar plates containing antibiotics (100 µg/mL ampicillin or 200 µg/mL kanamycin, depending on the plasmid's antibiotic resistance). In case of a kanamycin-resistance, bacteria were incubated in 1 mL S.O.C. medium (Invitrogen, Thermo Fisher Scientific) for 1 h at 37°C and 300 rpm prior to plating. Agar plates were incubated overnight at 37°C.

LB(+) Medium*	Volume
Peptone	10 g
Yeast Extract	5 g
NaCl	5 g
D-(+)-Glucose	1 g
H_2O	ad 1 L

* pH adjusted to 7.5 and sterile filtrated

LB(+) Agar Plate	Volume
Agar	15 g
LB(+) Medium	ad 1 L
Antibiotics*	

* Added after autoclaving

The next day, individual bacterial colonies were picked from the agar plates and incubated overnight at 37°C in a shaking incubator (Certomat IS, B. Braun Biotech International) at 225 rpm in LB(+) medium containing antibiotics as described before. The following amounts of LB(+) medium were used: 5 mL for small-scale production, 100 mL for medium-scale production or 200 mL for large-scale production. Plasmid DNA was extracted using alkaline

lysis or the PureLink™ HiPure Midiprep or Maxiprep Kit (Invitrogen, Thermo Fisher Scientific) according to the manufacturer's instructions.

3.4.4 Site-Directed Mutagenesis

All primers were purchased from Eurofins Genomics. Primers for site-directed mutagenesis were designed to span the site-to-be-mutated in forward and reverse direction with the desired changes in the sequence center. The KAPA HiFi HotStart ReadyMix PCR kit (KAPA Biosystems) was used to amplify the complete plasmid with the designed primers to incorporate the mutated sequence.

The following KAPA reaction mix was prepared:

Substance	Volume
Template Plasmid DNA	10-25 ng
2x KAPA Hotstart ReadyMix	12.5 µL
Primer forward (10µM)	1 µL
Primer reverse (10µM)	1 µL
H_2O	ad 25 µL

The following PCR cycle protocol was used for plasmid amplification:

Step	Temperature	Duration	Cycles
Initial Denaturation	95°C	3 min	1
Denaturation	98°C	20 s	
Annealing	60°C – 72°C *	15 s	25
Elongation	72°C	60 s /kb + 60 s	
Final Elongation	72°C	10 min	1
Cooling	10°C	15 min	1

* Annealing temperature was set to the melting point of the respective primers

After amplification of the plasmid containing the desired mutation, template plasmid DNA was degraded using the FastDigest DpnI restriction enzyme (Thermo Fisher Scientific).

The following digestion mix was prepared:

Substance	Volume
Amplified Plasmid DNA	25 µL
10x Fast Digest Green Buffer	3 µL
FastDigest DpnI	1 µL
H_2O	ad 30 µL

The digest was incubated for 2 h at 37°C and the restriction enzyme was inactivated by denaturation at 80°C for 5 min afterwards. 3, 5 or 10 µL of the mix were transformed into competent bacteria as described in chapter 3.4.3.4.

3.5 Production of Recombinant Adeno-Associated Virus Vectors

Recombinant adeno-associated virus (rAAV) vectors using the following combinations of gene of interest (GOI) and capsid were produced:

GOI	GOI Plasmid	Capsid
hCNGB1a (NM_001297.4)	pGL2.0_hRHO194-hCNGB1a-SV40pA_modified	AAV5
hCNGA1 (NM_000087.5)	pGL2.1_hRHO-hCNGA1-mWPRE-BGHpA	AAV2\GL (Pavlou et al., 2021)

Production of rAAV2\GL.hCNGA1 was performed at LMU by the lab technicians Kerstin Skokann (Pharmacology for Natural Sciences, Department of Chemistry and Pharmacy, Ludwig-Maximilians-Universität München) and Tamara Gehringer (now ViGeneron GmbH). Production of rAAV5.hCNGB1\mod was performed at LMU with support of Kerstin Skokann.

3.5.1 Cell Cultivation

For in-house production of rAAVs, HEK293 derived Lenti-X 293T (HEK293T) cells (Clontech) were used. Cells were cultivated in T75 cell culture flasks (CELLSTAR®) and maintained in DMEM medium + GlutaMAX + 4.5 g/l glucose + 10% FBS + 1% penicillin/streptomycin in a CO_2 incubator (Heraeus, Thermo Fisher Scientific) at 37°C and 10% CO_2. Cells were passaged twice per week at a confluency of approximately 90%.

3.5.2 Triple Transfection and Harvest

For transfection, HEK293T cells were seeded onto 15 x 15 cm cell culture plates and incubated overnight at 37°C and 10% CO_2 until 60-80% confluency was reached. Prior to transfection, cell culture medium was replaced by FBS-free medium. Cells were transfected via polyethylenimine (PEI) transfection technique using a pAD Helper plasmid containing necessary adenoviral genes, a plasmid encoding AAV rep and cap genes (capsid plasmid), and a plasmid containing the inverted terminal repeats (ITR)-flanked gene of interest (GOI plasmid).

The following transfection mix was prepared:

Transfection Mix	Volume
GOI Plasmid	90 µg
pAD Helper Plasmid	X µg
Capsid Plasmid	Y µg
PEI	Z µg
FBS-free medium	ad 15 mL

The required amounts of pAD Helper plasmid and capsid plasmid were calculated via the following formulas:

$$X\ \mu g = \frac{90\ \mu g \times MM \text{ of pAD Helper}}{MM \text{ of GOI Plasmid}} \qquad Y\ \mu g = \frac{90\ \mu g \times MM \text{ of Capsid Plasmid}}{MM \text{ of GOI Plasmid}}$$

MM = molar mass of the double stranded plasmid

The required amount of PEI was calculated using the following formula:

$$Z\ \mu g = (90\ \mu g + X\ \mu g + Y\ \mu g) \times 4$$

The transfection mix was incubated for 15 min at RT before adding 1 mL dropwise to each plate. The plates were shaken gently and incubated for 72 h at 37°C and 10% CO_2.
Cells were harvested 72 h post-transfection by detaching them with a cell scraper and unifying cells from all 15 cell culture plates. Harvested cells were centrifuged for 15 min at 4.500 rpm and 4°C (JA-10 rotor, J2-MC high speed centrifuge, Beckmann Coulter). Supernatant and pellet were collected and further processed separately.

Pellet cells were lysed by adding 7.5 mL lysis buffer, followed by three freeze and thaw cycles. Freezing was carried out in liquid nitrogen (-196°C), thawing in a heated water bath (Haake) at 37°C. The lysed cell pellet was stored at -80°C until further use. The supernatant was sterile filtrated using a 0.45 µm filter unit (Nalgene, Thermo Fisher Scientific), a 40% polyethylene glycol (PEG) solution was added to a final concentration of 8% and incubated overnight at 4°C. The next day, the PEG-containing supernatant was centrifuged for 15 min at 4.000 rpm and 4°C (JA-10 rotor, J2-MC high speed centrifuge, Beckmann Coulter). The supernatant was discarded and the virus-containing PEG-pellet was kept at -20°C until further use.

Lysis Buffer*	**Volume**
NaCl	150 mM
Tris/HCl pH 8.5	59 mM
H_2O	ad 50 mL

* Sterile filtrated

3.5.3 Iodixanol Density Gradient Ultracentrifugation

Lysed cell pellet and PEG-pellet were thawed, unified, and incubated with Benzonase® (VWR) at a final concentration of 50 U/mL in a water bath at 37°C for 30 min to remove residual non-packaged DNA. Afterwards, the unified pellets were centrifuged for 25 min at 4.000 rpm and 4°C. The virus-containing supernatant was transferred into a Quick-Seal polypropylene tube (39 mL, Beckmann Coulter) and a density gradient was established by undercoating the virus-containing layer with different iodixanol solutions in the following order: 7 mL of 15%, 5 mL of 25%, 5 mL of 40%, and 6 mL of 60%. For this purpose, a MINIPULS 3 peristaltic pump (Gilson) was used. Afterwards, the tube was centrifuged for 105 min at 70.000 rpm and 18°C using an ultracentrifuge (Optima L-80K with a 70 Ti rotor; Beckman Coulter). The virus-containing 40% iodixanol phase was extracted and kept on ice for max. 24 h until further use.

15% Iodixanol*	Volume
10x PBS	5 mL
$MgCl_2$ 1M	50 µL
KCl 2.5M	50 µL
NaCl 5M	10 mL
Optiprep™ (Progen)	12.5 mL
Phenol red 1%	37.5 µL
H_2O	ad 50 mL

25% Iodixanol*	Volume
10x PBS	5 mL
$MgCl_2$ 1M	50 µL
KCl 2.5M	50 µL
Optiprep™ (Progen)	20.9 mL
Phenol red 1%	50 µL
H_2O	ad 50 mL

40% Iodixanol*	Volume
10x PBS	5 mL
$MgCl_2$ 1M	50 µL
KCl 2.5M	50 µL
NaCl 5M	10 mL
Optiprep™ (Progen)	33.3 mL
H_2O	ad 50 mL

60% Iodixanol*	Volume
$MgCl_2$ 1M	50 µL
KCl 2.5M	50 µL
Optiprep™ (Progen)	33.3 mL
Phenol red 1%	37.5 µL
H_2O	ad 50 mL

* Sterile filtrated

3.5.4 Anion Exchange Chromatography

For further virus purification, anion exchange chromatography was performed using the ÄKTAprime plus chromatography system (GE Healthcare) with a 5 mL HiTrap™ Q FF anion exchange chromatography column (GE Healthcare) and the PrimeView 5.31 software (GE Healthcare). Prior to sample loading, the column was equilibrated with ÄKTA buffer, and the virus-containing sample was diluted 1:1 in ÄKTA buffer. The sample was loaded onto the column using a loop injector (Superloop, 50 mL, GE Healthcare). UV-light absorbance and conductance were observed, and virus-containing fractions were collected when conduction peaked. All fractions were pooled and used for further processing. Afterwards, the column was washed with NaCl 2.5M pH 8.5 to remove remaining bound molecules.

ÄKTA Buffer*	Volume
Tris	20 mM
NaCl	15 mM
H_2O	ad 1 L

* pH adjusted to 8.5 and sterile filtrated

3.5.5 Concentration and Salination of rAAVs

To further increase the virus concentration, the collected fractions were transferred to an Amicon column (Amicon® Ultra-4 Centrifugal Filter Units, 100 kDa, Merck). The Amicon tube was centrifuged at 4.000 rpm (A-10 rotor, J2-MC High speed centrifuge, Beckman Coulter) and 4°C in 15 min intervals until the volume was reduced to 500 µL. Subsequently, the virus residuum was washed with 1 mL 0.014% Tween/PBS-MK and centrifuged again under the same conditions until the volume was reduced to 100 µL. Finally, 10 µL aliquots were prepared and stored at -80°C.

0.014% Tween/PBS-MK*	Volume
10x PBS	50 mL
$MgCl_2$ 1M	500 µL
KCl 1.5M	500 µL
Tween-20	70 µL
H_2O	ad 500 mL

* Sterile filtrated

3.5.6 rAAV Titer Determination

Genomic titers of rAAVs were determined by quantitative real-time PCR (qRT-PCR) using a QuantStudio™ 5 Real-Time PCR System (Applied Biosystems) as described in chapter 3.10.3. A standard curve was established to serve as a reference by generating a dilution series of an ITR fragment. The ITR fragment was amplified by PCR using the following primers (D'Costa et al., 2016):

ITR2 forward: 5’ - GGA ACC CCT AGT GAT GGA GTT - 3’
ITR2 reverse: 5’ - CGG CCT CAG TGA GCG A - 3’

The amplified fragments were purified using agarose gel electrophoresis and fragment isolation as described in chapter 3.3.3. DNA concentration was determined with a Nanodrop™ 2000c spectrophotometer (Thermo Fisher Scientific). A standard series was established by

preparing a 10^{10} ITR copy standard and serially diluting it further by factor 10 to generate a range of 10^5 - 10^9 ITR copies. For that purpose, the following formula was used:

$$c\ (10^{10}\ \text{copies}) = \frac{10^{10} \text{x } 660 \text{ x } 10^{12}\ \text{pg mol}^{-1} \text{ x fragment size}}{6.022 \text{ x } 10^{23}\ \text{mol}^{-1} \text{ x } 5\ \mu\text{L}}$$

The standard curve was constructed by plotting the resulting cycle threshold (C_t) values against the logarithm of the dilution factors. The genomic titers (virus genomes (vg)/µl) of rAAVs could be derived from corresponding C_t values of the standard curve.

3.6 *in vivo* Animal Experiments

All *in vivo* mice experiments were performed under anesthesia consisting of a combination of ketamine (100 mg/kg body weight; Medistar GmbH) and xylazine (10 mg/kg body weight, Xylariem®; Ecuphar GmbH), diluted in 0.9 % sodium chloride (NaCl 0.9 %, B. Braun). Anesthesia was applied by intraperitoneal injection.

Dog housing and subretinal injections of rAAVs for gene therapeutic treatment were carried out at the College of Veterinary Medicine at the Michigan State University, MA, USA, by the work group of Prof. Simon Petersen-Jones as described (Petersen-Jones et al., 2009).

3.6.1 Intraocular Injections

For subretinal or intravitreal injections, mice were anaesthetized as described above and pupils were dilated using tropicamide eye drops (Mydriaticum Stulln, Pharma Stulln GmbH). A NanoFil syringe (World Precision Instruments) with a 34-gauge beveled needle was used for manual operation. The process was monitored under a surgical microscope (OPMI 1 FR Pro, Zeiss). The needle was inserted from the ora serrata into the subretinal space for subretinal injections or into the vitreous for intravitreal injections at an angle of approximately 60°. One microliter of diluted viral particles at the indicated dose was slowly injected into the subretinal space or into the vitreous. For subretinal injections, an injection was considered successful if the formation of a bleb was visible indicating a temporal subretinal detachment of the retina. After the procedure, all injected eyes were treated with dexamethasone and gentamicin ophthalmic ointment (Dexamytrex®; Bausch and Lomb) for prevention of infection and for eye moisturization.

Injected viral vectors and corresponding vector diluents can be found in Table 1.

Table 1. Viral Vectors used for intraocular Injections.

Animal Model	Viral Vector	Vector Diluent
Cngb1$^{-/-}$ mice	AAV5.hRHO194-hCNGB1a-SV40pA_modified	0.014% Tween/PBS-MK
Cnga1^{MUT} mice	AAV2\GL.hRHO-hCNGA1-mWPRE-BGHpA	0.014% Tween/PBS-MK

3.6.2 Electroretinography

For full-field electroretinography (ERG) measurements, a Celeris Fullfield ERG (Diagnosys LLC) was used. For that purpose, mice were anaesthetized, and pupils were delated as described before. Eyes were moisturized with one drop of methylcellulose (Methocel 2%, OmniVision), which also served to establish corneal contact to the electrodes of the device. White light (6.500k) stimuli of different luminance were directed to the eyes via the electrodes and the responses were recorded with the ERG device.

Table 2. Scotopic Single-Flash ERG Protocol used for Scotopic ERGs Measurements.

Step	Luminance [cd s m^{-2}]	Time between Results [s]	Sweep pre-trigger time [ms]	Sweep post-trigger time [ms]	Sweeps	1st Sweep Delay [ms]	Inter-Sweep Delay [ms]
1	0.01	10	50	300	5	6000	5000
2	0.03	10	50	300	5	6000	5000
3	0.1	17	50	300	5	6000	10.000
4	0.3	17	50	300	5	6000	10.000
5	1	22	50	300	5	6000	10.000
6	3	22	50	300	5	6000	10.000
7	10	22	50	300	5	6000	10.000

ERGs were measured under scotopic (dark-adapted) to assess rod-dominated activity or photopic (light-adapted) conditions to assess rod- and cone-dominated activity. For scotopic measurements, animals were dark-adapted overnight (>12 h) prior to the measurements. ERG measurement protocols (Table 2 and Table 3) were based on the International Society for

Clinical Electrophysiology of Vision (ISCEV) standardized protocol for clinical ERG recordings (Marmor and Fishman, 1989).

Table 3. Photopic Single-Flash ERG Protocol used for Photopic ERGs Measurements.

Step	Luminance [cd s m^{-2}]	Time between Results [s]	Sweep pre-trigger time [ms]	Sweep post-trigger time [ms]	Sweeps	1st Sweep Delay [ms]	Inter-Sweep Delay [ms]
1	0.01	0	50	300	10	6000	987
2	0.03	0	50	300	10	6000	987
3	0.1	0	50	300	10	6000	987
4	0.3	0	50	300	10	6000	987
5	1	0	50	300	10	6000	987
6	3	0	50	300	10	6000	987
7	10	0	50	300	10	6000	987

All eyes received dexpanthenol eye and nose ointment (Bepanthen®, Bayer) after measurements. Espion software V6.59.9 (Diagnosys LLC) was used for data analysis.

3.6.3 Spectral-Domain Optical Coherence Tomography (SD-OCT)

Spectral-Domain Optical Coherence Tomography (SD-OCT) was carried out using an adapted Spectralis™ HRA + OCT diagnostic imaging platform (Heidelberg Engineering) as described previously (Schön et al., 2012; Mühlfriedel et al., 2019). Mice were anaesthetized and pupils were diluted as described above and mice were placed on a platform afterwards. The eye to be measured was moisturized with one drop of methylcellulose (Methocel 2%, OmniVision) and a corneal contact lens was applied to adapt the refractive index. OCT scans were produced in a 12° circular scan mode. All eyes received dexpanthenol eye and nose ointment (Bepanthen®, Bayer) after measurements. Heidelberg Eye explorer software V1.10.4.0 (Heidelberg Engineering) was used for data analysis. For subretinal injected eyes, the area of each eye that was within the subretinal bleb was used for OCT analysis. Only OCT scans that had the same distance from the optical nerve were used for comparison of wild type and *Cnga1*^{MUT} mice as well as for comparison of treated and sham-injected eyes of all mouse lines.

3.7 Tissue Collection

3.7.1 Tissue Preparation for Retinal Cross Sections

For dissection of mouse retinal tissue, isoflurane anesthesia was induced and mice were immediately sacrificed by cervical dislocation. After confirmation of death, mouse eyes were enucleated and placed in 0.1 M phosphate buffer (PB). Next, the eyes were punctured at the ora serrata with a 21 G cannula and fixed in 4 % paraformaldehyde (PFA; PFA, Sigma Aldrich, pH adjusted to 7.4) for 5 min on ice. After fixation, the eyes were positioned below a stereomicroscope (Stemi 2000, Zeiss) on a filter paper drenched with 0.1 M PB. The eyes were cut along the ora serrata using micro scissors (Vannas Spring Scissors – 2.5 mm Cutting Edge, Fine Science Tools) and micro forceps (Dumont #55, Fine Science Tools) to remove cornea, vitreous, and lens. The remaining eyecups were fixed in 4 % PFA on ice for 45 min, washed three times for 10 min in 0.1 M PB afterwards, and incubated in 30 % sucrose overnight at 4°C for cryoprotection. Subsequently, the eyecups were embedded in tissue freezing medium (Tissue-Tek® O.C.T.™ Compound, Sakura Finetek™), frozen on dry ice, and stored at -80 °C until use.

Tissue collection and embedding of *Pde6a*^{MUT}*xCngb1*$^{-/-}$ mouse retinal tissue was carried out at the Division of Ocular Neurodegeneration, Centre for Ophthalmology, Institute for Ophthalmic Research, University of Tübingen by the group of Dr. Regine Mühlfriedel.

Eye removal, fixation, and embedding of dog retinal tissue was performed at the College of Veterinary Medicine at the Michigan State University, MA, USA, by the work group of Prof. Simon Petersen-Jones. Embedded tissue was shipped to the LMU for slicing.

0.1 M Phosphate Buffer (PB)*	**Volume**
Na_2HPO_4 x $2H_2O$	28.48 g
$NaHPO_4$ x $2H_2O$	5.52 g
H_2O	ad 2 L

* pH adjusted to 7.4 and sterile filtrated

4 % Paraformaldehyde (PFA)*	**Volume**
Paraformaldehyde	6 g
0.1 M PB	ad 150 mL

* Dissolved at 60°C and sterile filtrated

3.7.2 Tissue Preparation for RNA/Protein Extraction

For RNA or protein extraction from mouse retinas, mice were sacrificed by cervical dislocation. A blunt forceps was positioned below the eye, the eye was incised using a sterile scalpel

(Swann-Morton) and the forceps was gradually moved upward to collect the retina. Retinal tissue was washed in 0.1 M PB, snap-frozen in liquid nitrogen, and stored at -80°C until use. Dog retinal and vitreal tissue was collected at the College of Veterinary Medicine at the Michigan State University, MA, USA, by the work group of Prof. Simon Petersen-Jones. Snap-frozen tissue was shipped to the LMU for RNA or protein extraction.

3.8 Immunohistochemistry

Table 4. Primary Antibodies used for Immunohistochemistry

Primary Antibody	No.	Producer	Dilution
α-5hmC	39769	Active Motif	1 : 1.000
α-Calbindin	C9848	Sigma-Aldrich	1 : 500
α-cGMP	-	Kindly provided by Dr. HWM Steinbusch, Maastricht University Medical Center	1 : 3.000
α-CNGA1	Pmc2G11	Kindly provided by Prof. Robert Molday, University of British Columbia (Molday et al., 1991)	1 : 30
α-CNGA1	-	Custom-made against the 19-mer C-RLTKVEKFLKPLIDTEFS-NH_2 (Wagner et al., 2021)	1 : 2.000
α-CNGB1	-	Custom-made against the 95-mer C-LRSNNKPKEEKSVLI LPPRAGTPKLFNAALAMTGKMGGKGAKGGKLAHLRARLKE LAALEAAAKQQ ELVEQAKSSQDVKGEEGSAAPDQHTHPKE-NH_2	1 : 5.000
α-Cone Arrestin	-	Kindly provided by Prof. Wolfgang Baehr, University of Utah (Zhang et al., 2012)	1 : 300
α-GFAP-Cy3	#C9205	Sigma-Aldrich	1 : 1.000
α-Iba1	234013	Synaptic Systems	1 : 500
α-PDE6A	NBP1-87312	Novus Biologicals	1 : 500
α-PCP2	sc-137064	Santa Cruz Biotechnology	1 : 500
α-PKC-Biotin	P108	Leinco Technologies	1 : 200
α-PNA-FITC	#L7381	Sigma-Aldrich	1 : 100
α-Rhodopsin	MAB5356	Merck	1 : 1.000

Embedded eyecups were prepared as described in chapter 3.7.1. Cryosections were obtained using a cryostat (Leica CM3050 S, Leica and Epredia™ CryoStar™ NX70, Thermo Fisher Scientific). Slices of 10 µm for mouse samples were collected on coated glass object slides (Super Frost Plus, Menzel, Thermo Fisher Scientific). Cryosections were stored at -20 °C.

For immunostainings, cryosections were thawed at RT and encircled using a Super PAP Pen Liquid Blocker (Science Services). Next, the sections were rehydrated with 0.1 M PB for 5 min and fixed with 4 % PFA for 10 min, followed by three washing steps with 0.1 M PB for 5 min each. Afterwards, the sections were incubated overnight at 4°C with a solution containing the primary antibodies (Table 4), 5 % ChemiBLOCKER (CB; Merck), and 0.3 % Triton X-100 in 0.1 M PB. The next day, the sections were washed three times with 0.1 M PB for 5 min each. Afterwards, the sections were incubated without light for 1.5 h at RT with a solution containing the secondary antibodies (Table 5) and 3 % CB in 0.1 M PB. After three subsequent washing steps with 0.1 M PB for 5 min each, cell nuclei were stained with 1 µg/mL DAPI solution (Thermo Fisher Scientific) or 5 µg/mL Hoechst 33342 solution (Invitrogen, Thermo Fisher Scientific) for 10 min at RT. After a final washing step with 0.1 M PB for 5 min, the sections were embedded in Fluoromount-G Mounting Medium (Thermo Fisher Scientific), covered by a cover slip (#1.5; Menzel, Thermo Fisher Scientific) and stored at 4°C.

Table 5. Secondary Antibodies used for Immunohistochemistry

Secondary Antibody	No.	Producer	Dilution
Alexa488 Anti-Rabbit IgG (H+L) $F(ab')_2$	4412	Cell Signaling	1 : 500
Alexa488 Donkey Anti-Rat IgG (H+L)	A-21208	Thermo Fisher	1 : 500
Alexa488 Donkey Anti-Sheep IgG (H+L)	A-11015	Thermo Fisher	1 : 500
Alexa488 Goat Anti-Mouse IgG (H+L)	A-11001	Invitrogen	1 : 500
Alexa488 Goat Anti-Mouse IgG1	A-21121	Thermo Fisher	1 : 500
Alexa488 Goat Anti-Mouse IgG2a	A-21131	Thermo Fisher	1 : 500
Alexa555 Goat Anti-Mouse IgG2b	A-21147	Thermo Fisher	1 : 500
Alexa594 Goat Anti-Mouse IgG2a	A-21135	Thermo Fisher	1 : 500
Alexa594 Donkey Anti-Sheep IgG (H+L)	A-11016	Thermo Fisher	1 : 500
Cy3 AffiniPure Donkey Anti-Rat IgG (H+L)	712-165-153	Jackson ImmunoResearch	1 : 400
Cy3 AffiniPure Donkey Anti-Mouse IgG (H+L)	715-165-150	Jackson ImmunoResearch	1 : 400
Cy3 AffiniPure Donkey Anti-Rabbit IgG (H+L)	711-165-152	Jackson ImmunoResearch	1 : 400
Cy2 AffiniPure Donkey Anti-Sheep IgG (H+L)	713-225-147	Jackson ImmunoResearch	1 : 200

3.9 Laser Scanning Confocal Microscopy

Laser scanning confocal microscopy images of immunostained retinal cross-sections were obtained using a Leica TCS SP8 inverted confocal laser scanning microscope (Leica Microsystems) equipped with the following lasers: 405, 448, 514, and 552 nm. The filter settings were chosen according to the emission spectrum of the respective dye. Images were acquired as confocal z stacks using LAS X software V3.5.1.18803 (Leica). Maximum projection (merging of all z stacks) and image processing was performed using Fiji ImageJ V2.1.0/1.53c software.

3.10 Quantitative Real-Time Polymerase Chain Reaction

3.10.1 RNA Extraction

Retinal tissue for RNA extraction was collected as described in chapter 0 and thawed at RT. RNA extraction was performed using the RNeasy Plus Mini Kit (Qiagen) according to the manufacturer's instructions. The tissue was lysed by adding 700 µL RNeasy lysis (RLT) buffer containing 1% β-mercaptoethanol (Sigma-Aldrich) and homogenized by using steel balls and a mixer mill (MM400, Retsch; 1 min, 30 Hz). The remaining steps were executed according to protocol. The RNA was eluted in 30 µL RNase-free water. RNA concentration was determined with a Nanodrop™ 2000c spectrophotometer (Thermo Fisher Scientific).

3.10.2 cDNA Synthesis

Reverse transcription of RNA to cDNA was performed using the RevertAid First Strand cDNA Synthesis Kit (Thermo Scientific) according to the manufacturer's instructions. Equal amounts of RNA were used per experiment.

The following reaction mix was prepared:

Substance	Volume
RNA	100 - 800 ng
Oligo $(dT)_{18}$ Primer	1 µL
Random Hexamer Primer	1 µL
Nuclease-free H_2O	ad 12 µL

The reaction mix was incubated for 5 min at 65°C to remove secondary structures of the RNA and subsequently chilled to 10°C.

Afterwards, the following components were added:

Substance	Volume
5x Reaction Buffer	4 µL
RiboLock RNase Inhibitor (20 U/µL)	1 µL
dNTP Mix (10 mM)	2 µL
RevertAid M-MuLV RT (200 U/µL)	1 µL

The following PCR cycle protocol was used for cDNA synthesis:

Temperature	Duration
25°C	5 min
42°C	60 min
70°C	5 min
10°C	hold

The cDNA was kept on ice until further use or stored at -80°C.

3.10.3 Quantitative Real-Time Polymerase Chain Reaction (qRT-PCR)

A QuantStudio™ 5 Real-Time PCR System (Applied Biosystems) was used for qRT-PCR. Primers were purchased from Eurofins Genomics (Table 6). qRT-PCR was performed using the PowerUp™ SYBR® Green Master Mix (Thermo Fisher).

The following reaction mix was prepared in technical triplicates per sample:

Substance	Volume
cDNA	5 µL
PowerUp™ SYBR® Green Master Mix	10 µL
Primer forward (10 µM)	0.6 µL
Primer reverse (10 µM)	0.6 µL
Nuclease-free H_2O	ad 20 µL

The following PCR cycle protocol was used for qRT-PCR:

Step	Temperature	Duration	Cycles
UDG Activation	50°C	2 min	1
Dual-Lock DNA polymerase	95°C	2 min	1
Denaturation	95°C	15 s	
Annealing	55-60°C*	15 s	40
Elongation	72°C	1 min	

* Annealing temperature was set to the melting point of the respective primers

The $\Delta\Delta C_T$-method was used to quantify changes in RNA levels and mALAS was used as housekeeping gene. Baseline settings and cycling threshold position were adjusted manually if necessary.

Table 6. Primers used for qRT-PCR

Target	Primer forward (5'-3')	Primer reverse (5'-3')
Cnga1	CTG TGA AGC TGG TCT GTT GG	TAA CTG CCG TCA CTC AAC AC
Cngb1	TCT GAA CAG GTG TCA GGA TGT T	CTG TTT CTG GCT GTG GTC CT
mAlas	TCG CCG ATG CCC ATT CTT ATC	GGC CCC AAC TTC CAT CAT CT

3.11 Western Blot

3.11.1 Protein Extraction

Retinal tissue for protein extraction was collected as described in chapter 0 and thawed at RT. The tissue was lysed by adding 70 µL RIPA lysis mix containing RIPA lysis buffer (Merck), glycerol and protease inhibitor (cOmplete™ ULTRA Tablets, Mini, EASYpacks Protease Inhibitor Cocktail, Roche). The tissue was homogenized by using steel balls and a mixer mill (MM400, Retsch; 30 s, 15 Hz). Afterwards, the tissue was rotated end-over-end (VWR™ tube rotator) for 40 min at 4°C. Subsequently, the lysates were centrifuged at 5.000xg for 10 min at 4°C. Protein concentration of the protein-containing supernatant was determined with a Qubit™ 4 Fluorometer (Invitrogen, Thermo Fisher Scientific) according to the Qubit™ Protein Assay Kit protocol and samples were stored at -20°C.

RIPA Lysis Mix*	Volume
10x RIPA Lysis Buffer	1 mL
100% Glycerol	1 mL
H_2O	8 mL

* 1 pill protease inhibitor added

3.11.2 Sodium Dodecyl Sulphate Polyacrylamide Gel Electrophoresis (SDS-PAGE)

35 µg protein were mixed with 6x Laemmli + DTT buffer and incubated at 72°C for 10 min. Proteins were separated by SDS-PAGE at RT and 140 V for 70 min in 1x electrophoresis buffer using 6-12% gradient separation polyacrylamide gels. PageRuler™ Plus Prestained Protein Ladder (Thermo Fisher Scientific) was used for protein size control.

6x Laemmli + DTT Buffer	Volume
4x Tris/HCl pH 6.8 buffer	7 mL
Glycerol	3 mL
SDS	1 g
Bromophenol blue	1.2 mg
DTT	0.93 g

4x Tris/HCl Buffer*	pH 8.8	pH 6.8
Tris/HCl	1.5 M	0.5 M
SDS	0.4 %	0.4 %

* pH adjusted

Gradient Separation Gel	6 %	12 %
30 % acrylamide/bis-acrylamide	2.3 mL	4.5 mL
4x Tris/HCl pH 8.8 buffer	2.8 mL	2.8 mL
APS	22.5 µL	22.5 µL
TEMED*	7.5 µL	7.5 µL
H_2O	6.2 mL	3.9 mL

* Added right before pouring of the gel

Stacking Gel	
30 % acrylamide/bis-acrylamide	1.0 mL
4x Tris/HCl pH 6.8 buffer	1.9 mL
APS	37.5 µL
TEMED*	7.5 µL
H_2O	4.6 mL

10x Electrophoresis Buffer	Volume
Tris	30 g
Glycine	144 g
SDS	10 g
H_2O	ad 1 L

3.11.3 Blotting and Immunostaining

The separated proteins were transferred to a PVDF membrane (PEQLAB, VWR) at RT and 100 V for 90 min in 1x blotting buffer by using a Mini Trans-Blot cell (Bio-Rad).

Afterwards, unspecific binding sites were blocked by incubating the membrane in a blocking solution containing 5% non-fat dried milk powder (AppliChem) in Tris buffered saline with Tween-20 (TBS-T) buffer for 1 h at RT. The blocked membrane was incubated in a solution containing the primary antibody (Table 7) in 1% TBS-T buffer overnight at 4°C. The next day, the membrane was washed three times in TBS-T for 5 min at RT each before incubation in a solution containing the secondary antibody (Table 7) in 1% TBS-T buffer for 1.5 h at RT. After another three washing steps in TBS-T for 5 min at RT and one washing step in H_2O for 5 min at RT, proteins were visualized using Western Blotting Luminol Reagent (Santa Cruz) according to the manufacturer's instructions. Chemiluminescence was detected with a ChemiDoc™ MP Imaging System (Bio-Rad) and analysis was performed with Image Lab™ Software (Bio-Rad).

TBS-T Buffer	Volume
Tris	1.21 g
NaCl	8.02 g
Tween-20	1 mL
H_2O	ad 1 L

10x Blotting Buffer	Volume
Tris	30 g
Glycine	144 g
H_2O	ad 1 L

Table 7. Primary and Secondary Antibodies used for Western Blotting

Antibody	No.	Producer	Dilution
α-β-Actin-Peroxidase	A3854	Sigma-Aldrich	1 : 25.000
α-CNGA1	-	Custom-made against the 19-mer C-RLTKVEKFLKPLIDTEFS-NH_2 (Wagner et al., 2021)	1 µg/mL
α-CNGB1	-	Custom-made against the 95-mer C-LRSNNKPKEEKSVLILPPRAGTPKLFNAALAMTGKMG GKGAKGGKLAHLRARLKE LAALEAAAKQQLVEQAKS SQDVKGEEGSAAPDQHTHPKE-NH_2	1 µg/mL
α-CNGB1	-	Custom-made against the mouse S-Link (Hüttl et al., 2005)	1 µg/mL
Mouse anti-rabbit IgG-HRP	sc-2357	Santa Cruz	1 : 2.000

3.12 Proteomics

3.12.1 Protein Extraction

Retinal tissue for protein extraction was collected as described in chapter 0 and thawed at RT. The tissue was lysed by adding 70 µL RIPA lysis mix without EDTA/EGTA containing RIPA lysis buffer -EDTA/EGTA, glycerol and protease inhibitor (cOmplete™ ULTRA Tablets, Mini, EASYpacks Protease Inhibitor Cocktail, Roche). The tissue was homogenized by using steel balls and a mixer mill (MM400, Retsch; 30 s, 15 Hz). Afterwards, the tissue was rotated end-over-end (VWR™ tube rotator) for 40 min at 4°C. Subsequently, the lysates were centrifuged at 5.000xg for 10 min at 4°C. Protein concentration of the protein-containing supernatant was determined with a Qubit™ 4 Fluorometer (Invitrogen, Thermo Fisher Scientific) according to the Qubit™ Protein Assay Kit protocol and samples were stored at -20°C.

10x RIPA Lysis Buffer -EDTA/EGTA	Volume
NaCl 5M	150 mM
Tris/HCl 1M pH 8.0	50 mM
Nonidet P-40	1 %
Sodium Deoxycholate	0.05 %
SDS	0.01 %
H_2O	ad 100 mL

RIPA Lysis Mix -EDTA/EGTA*	Volume
10x RIPA Lysis Buffer -EDTA/EGTA	1 mL
100% Glycerol	1 mL
H_2O	8 mL

* 1 pill protease inhibitor added

Further sample preparation, mass spectrometry and data analysis were carried out by Dr. Pavel Kielkowski (Institute for Chemical Epigenetics (ICEM), Ludwig-Maximilians-Universität München).

3.12.2 Sample Preparation

Samples were further prepared using the cells whole proteome analysis with a modified filter-aided sample preparation (FASP) protocol (Wisniewski et al., 2009) or the single-pot solid-phase-enhanced sample preparation protocol (Hughes et al., 2019).

3.12.3 Liquid Chromatography-Mass Spectrometry/Mass Spectrometry

Liquid Chromatography-Mass Spectrometry/Mass Spectrometry (LC-MS/MS) measurements were performed on a Orbitrap Eclipse™ Tribrid™ Mass Spectrometer (Thermo Fisher

Scientific) coupled to an UltiMate™ 3000 Nano-HPLC (Thermo Fisher Scientific) via an EASY-Spray™ source (Thermo Fisher Scientific) and FAIMS interface (Thermo Fisher Scientific). First, peptides were loaded on an Acclaim PepMap 100 µ-precolumn cartridge (5 µm, 100 °, 300 µm ID × 5 mm, Thermo Fisher Scientific). Peptides were separated at 40°C on a PicoTip emitter (noncoated, 15 cm, 75 µm ID, 8 µm tip, New Objective) that was in-house packed with Reprosil-Pur 120 C18-AQ material (1. µm, 150 A°, Dr. A. Maisch GmbH). The gradient was run from 4-35.2 % acetonitrile supplemented with 0.1 % formic acid during a 150 min method (0-5 min 4 %, 5-6 min to 7 %, 7-105 min to 24.8 %, 105-126 min to 35.2 %, 126-140 min to 80 %, 140-150 min to 4 %) at a flow rate of 300 nL/min. High-field asymmetric-waveform ion-mobility spectrometry (FAIMS) was performed with two alternating compensation voltages (CVs) including -50 V and -70 V. The spectrometer was operated in dd-MS2 mode with the following settings: Polarity: positive; MS1 resolution: 240k; MS1 AGC target: standard; MS1 maximum injection time: 50 ms, MS1 scan range: m/z 375-1500; MS2 ion trap scan rate: rapid; MS2 AGC target: standard; MS2 maximum injection time: 35 ms; MS2 cycle time: 1.7 s; MS2 isolation window: m/z 1.2; HCD stepped normalized collision energy: 30 %; intensity threshold: 1.0e4 counts; included charge states: 2-6; dynamic exclusion: 60 s.

3.12.4 Data analysis

For calculation, first, MS raw files were split by FAIMS-MzXML-generator and subsequently analysed with MaxQuant software 1.6.12.0. Peptides were searched against the in silico digested Uniprot database for Homo sapiens (taxon identifier: 9606), where two unique peptides were required for protein identification. False discovery rate (FDR) was determined by using a decoy database with a threshold of 1 % for both peptide-spectrum match and protein levels. LFQ intensities were calculated for each sample. For statistical analysis, the MaxQuant result table proteinGroups.txt was analyzed with Perseus software version 1.6.10.43. LFQ intensities were log2 transformed. Subsequently, sample rows were assigned into two groups including either control or mutant/knockout. Next, the annotated rows were filtered for at least 2 valid values out of 3 replicates in at least one group. Missing values were replaced from normal distribution and differences between control and mutant/knockout were calculated. $-\log_{10}$(p-values) were obtained by a two-sided one sample Student's t-test over replicates with the initial significance level of $\alpha = 0.05$ adjustment by the multiple testing

correction method of Benjamini and Hochberg (FDR = 0.05). Finally, Ingenuity Pathway Analysis (QIAGEN IPA) was performed with significantly altered proteins.

3.13 *In silico* Protein Structure Prediction Analysis

In silico protein structure prediction analysis was performed by Jacqueline Bogedein (Department of Ophthalmology, University Hospital, Ludwig-Maximilians-Universität München).

Models were generated using the RoseTTAfold deep learning algorithm (Baek et al., 2021) available at https://robetta.bakerlab.org/. For structure modeling of human and murine CNGA1, the protein data bank (PDB) file 7RHH (Xue et al., 2021a) was used as template structure. Sequences of human CNGA1 wild type and respective mutant were based on protein isoform 2 (NP_000078.3). Sequences of mouse CNGA1 wild type and respective mutant were based on NP_031749.2. Sequences were obtained from NCBI.

The generated 3D models were visualized using the UCSF Chimera software (https://www.cgl.ucsf.edu/chimera/).

3.14 Statistical Analysis

All experiments were performed in triplicates if not stated differently. Data analysis was performed using GraphPad Prism software version 8 and 9. Data is presented as mean $\pm$ standard error of the mean (SEM) if not stated differently. Statistical differences between two groups were assessed with student's t-test. Statistical differences between three or more groups were assessed with ordinary one-way ANOVA, followed by Tukey's multiple comparisons test. Statistical differences between groups with two different variables were assessed with ordinary two-way ANOVA, followed by Šídák's post-hoc test for multiple comparisons. For all statistical tests, $p \leq 0.05$ was considered significant (*$p \leq 0.05$, **$p \leq 0.01$, ***$p \leq 0.001$, ns = not statistically significant).

4 Results

4.1 *Cnga1* Mutation in Mice: Characterization of a Novel Mouse Model of RP

Reliable animal models of retinal degeneration are of great importance for a better understanding of the mechanisms leading to photoreceptor loss as well as for the preclinical development of therapies. In order to study the role of the CNGA1 subunit in a physiological context, a novel ENU-induced mutant mouse model was generated which carries a missense mutation in the *Cnga1* gene leading to lack of the CNGA1 subunit. In the present study, the retinal phenotype of *Cnga1*-deficient (*Cnga1*^{MUT}) mice was characterized.

4.1.1 Structural Analysis of the Murine and Corresponding Human *CNGA1* Mutation

For the generation of a novel *Cnga1*-deficient mouse line, the DNA archive of ENU-induced mutant mice of the Helmholtz Center (Sabrautzki et al., 2017) was screened for mutations affecting the *Cnga1* gene. The missense mutation c.1526A>G in the *Cnga1* gene was identified, which leads to the substitution of Tyr509 by Cys (p.Tyr509Cys). This Tyr is located in the CNBD of the CNGA1 subunit and is highly conserved in a variety of species (Figure 9), including humans (Figure 10A, B). Murine Tyr509 corresponds to human Tyr513 and is thus in close proximity to the mutant residue p.Gly509Arg, that was recently found to be disease-causing in human RP patients (Kandaswamy et al., unpublished).

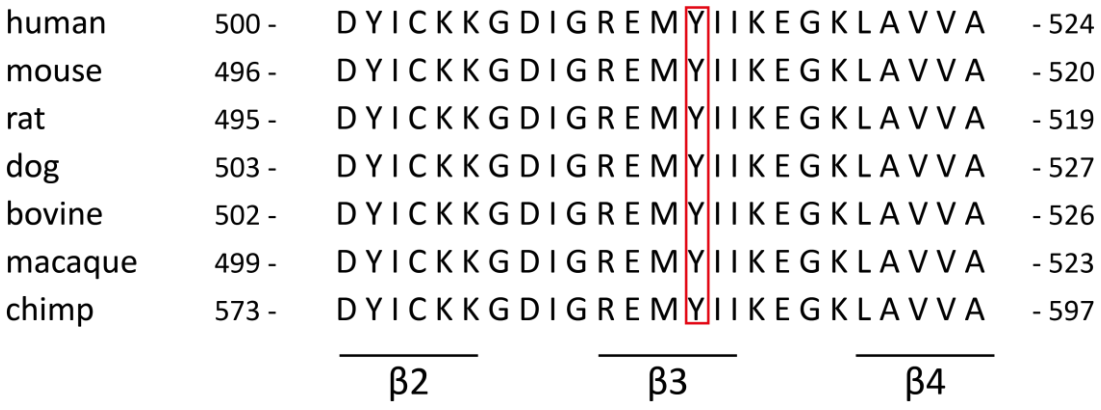

Figure 9. The affected Tyr of the CNGA1 protein is highly conserved in a variety of species. Partial sequence alignment of human, murine, rat, canine, bovine, macaque and chimpanzee CNGA1. The sequence section contains three β-strands (β2-β4), which are part of the β-roll of the CNBD. The β3-strand includes the conserved Tyr residue (red box).

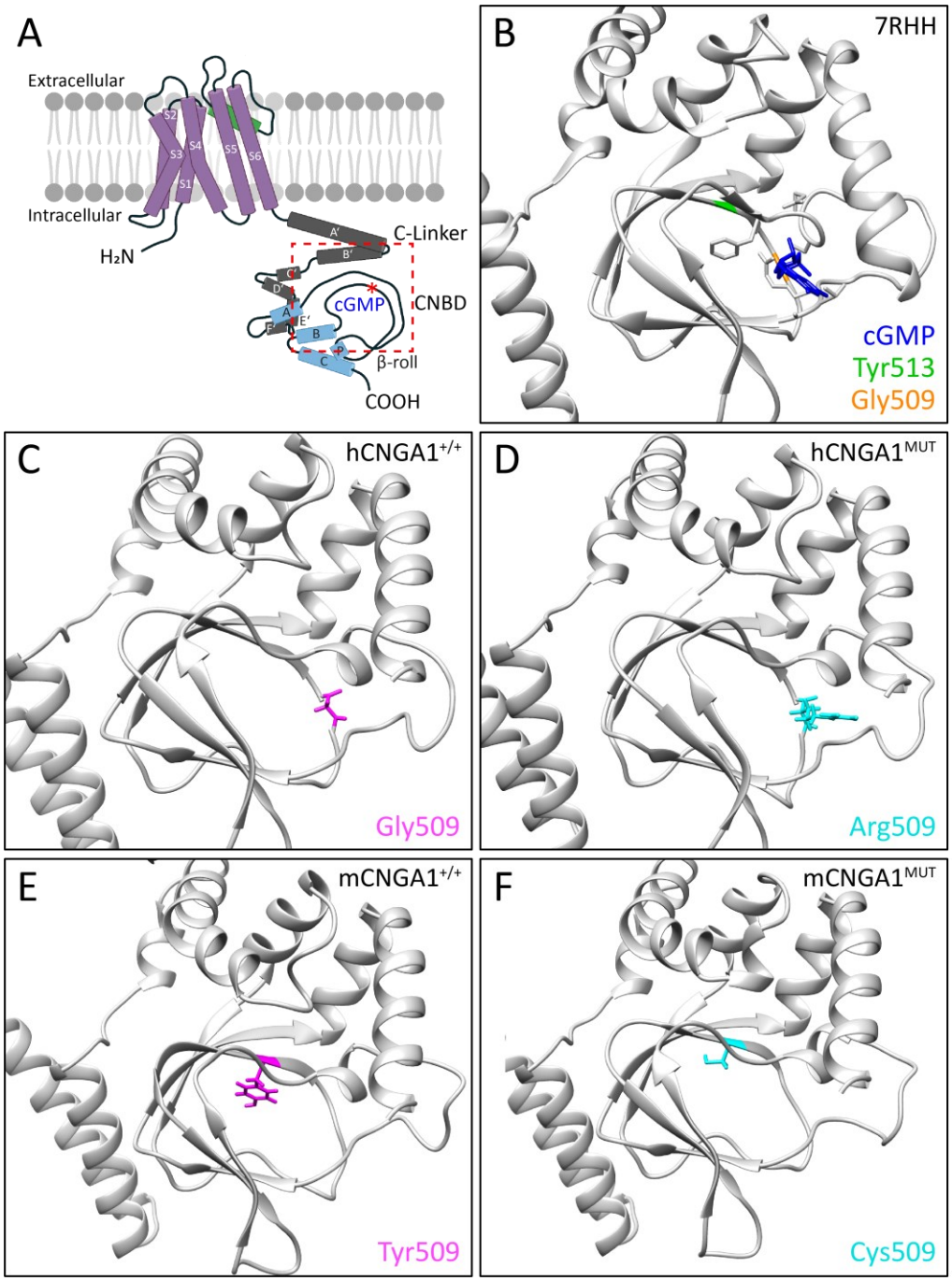

Figure 10. *In silico* prediction of the structure of wild type and mutant mouse CNGA1 proteins. (A) Schematic of the rod CNGA1 channel subunit showing the membrane topology and the position of the mutation (red asterisk). The red box marks the area shown in structural zoom-ins in (B-F). (B) RoseTTAfold model of protein data bank (PDB) file 7RHH (Xue et al., 2021a). The CNGA1 subunit is shown in grey. The amino acids of interest are highlighted in green (Tyr513) and orange (Gly509). The structure is shown in the cGMP bound form with cGMP highlighted in blue. The amino acid residues R561, T562, A563, F544, E546, I547, and S548 being responsible for cGMP binding are shown as atoms. (C-F) RoseTTAfold models of wild type ($CNGA1^{+/+}$; C, E) and mutant ($CNGA1^{MUT}$; D, F) of the human (C-D) and murine (E-F) CNGA1 subunit. The mutated amino acid is highlighted in magenta (wild type) or cyan (mutated), respectively, and shown as atoms.

For a better understanding of the protein structure of wild type and mutated CNGA1, RoseTTAfold-based *in silico* modelling was performed. Modelling of wild type and mutant CNGA1 proteins showed that respective mutations in both human and murine protein caused similar structural changes of the CNBD and the cGMP binding pocket structure (Figure 10C-F). It is well likely that the murine p.Tyr509Cys substitution and the human p.Gly509Arg mutation have similar detrimental effects on the protein structure.

4.1.2 Loss of CNG Channels by Disruption of the *Cnga1* Gene

In order to verify the disruption of the *Cnga1* gene and the expected resulting expression of non-functional CNGA1 protein, immunohistochemistry, western blot, and qRT-PCR analyses were performed.

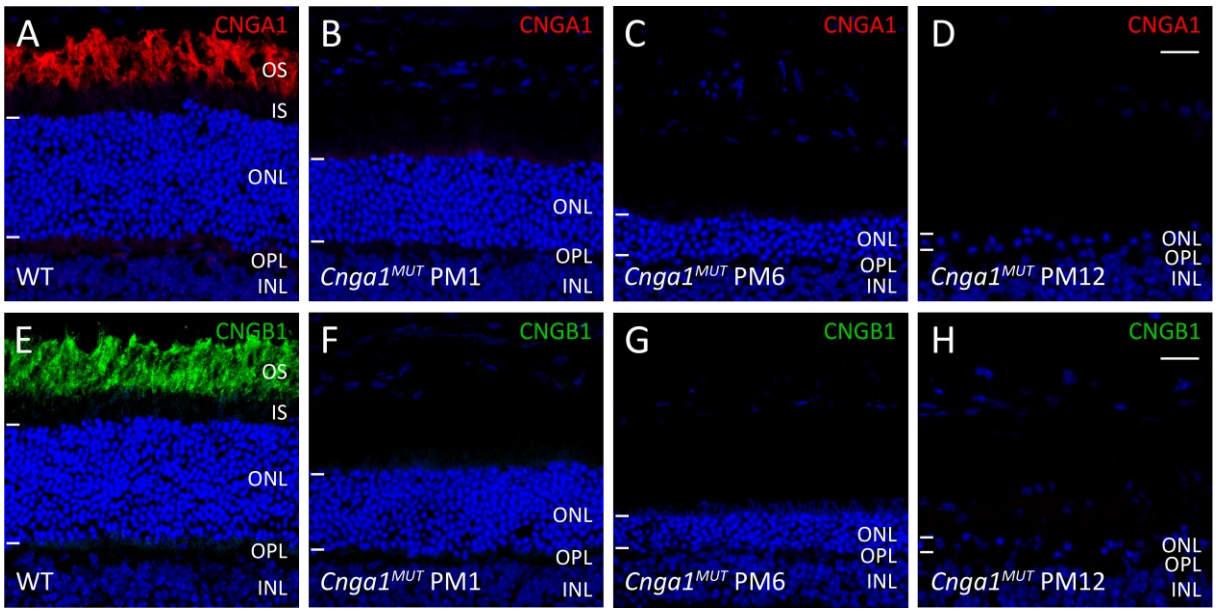

Figure 11. *Cnga1*^{MUT} mice are lacking CNGA1 and CNGB1 protein. Representative confocal images showing expression of CNGA1 (red; A-D) and CNGB1 protein (green; E-H) in retinal cross-sections of wild type (WT; PM1), and *Cnga1*^{MUT} mouse retinas at PM1, PM6 and PM12. The edges of the ONL are marked with horizontal bars. Cell nuclei were stained with DAPI (blue). OS, outer segments; IS, inner segments; ONL, outer nuclear layer; OPL, outer plexiform layer; INL, inner nuclear layer. Scale bars mark 20 µm.

CNGA1 protein is found in the photoreceptor outer segments (OS) of *Cnga1* wild type (WT) mice but could not be detected in retinal cross-sections of *Cnga1*^{MUT} mice (Figure 11A, B). This was evident at the age of 1 month (*postnatal* month 1, PM1) and at later time points (PM6

and PM12; Figure 11C, D). Moreover, *Cnga1*^{MUT} mice had a decreased thickness of the outer nuclear layer (ONL) compared to wild type mice, indicating photoreceptor degeneration.

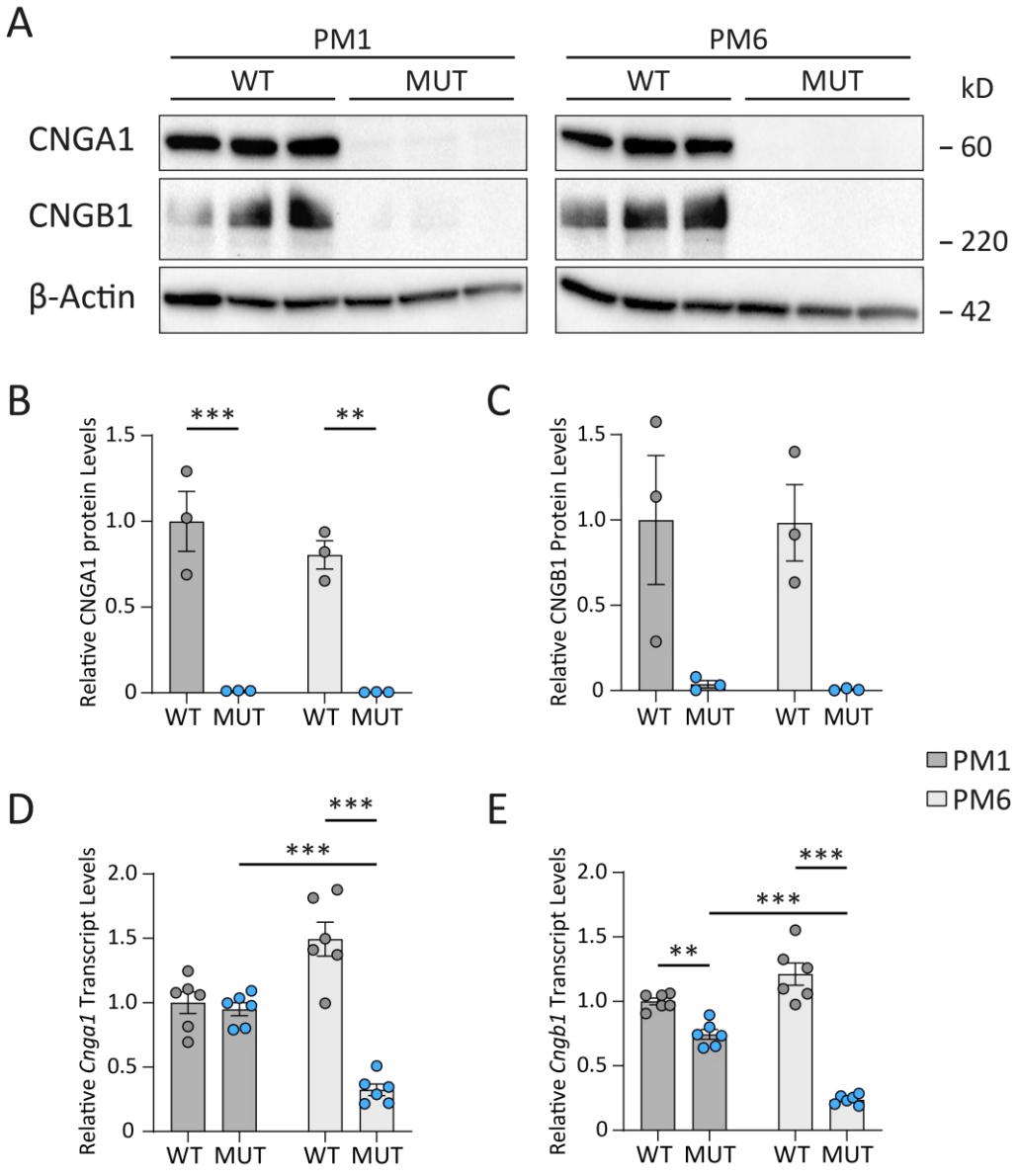

Figure 12. Disruption of the *Cnga1* gene causes altered expression of CNGA1 and CNGB1 subunits. (A-C) Western blot analysis of wild type (WT) and mutant (MUT) *Cnga1* mouse retinas at *postnatal* month 1 (PM1) and PM6 using CNGA1- and CNGB1-antibodies. β-Actin was used as loading control. Western blot stainings (A) and quantification of CNGA1 (B) and CNGB1 (C) expression. (D-E) qRT-PCR of *Cnga1* mouse retinas at PM1 and PM6 with murine *Cnga1*- (D) and *Cngb1*-specific primers (E). N = 3. Values are given as mean ±SEM (Ordinary one-way ANOVA paired with Tukey's post-hoc test; **p≤0.01, ***p≤0.001).

At PM1, the ONL was already degenerated to about 70 % of its original thickness (approximately 11 rows of cell nuclei instead of normal 16 rows), at PM6 to about 30 % (approximately 5 rows of cell nuclei), and at PM12 to about 10 % with only 1-2 discontinuous rows of cell nuclei remaining. Additionally, although the CNGB1 subunit itself is not affected, there was no CNGB1 protein expression in *Cnga1*^{MUT} mice at any age, showing that CNGB1 was intensively downregulated in the photoreceptor OS.

Western blot analysis of retinal lysates detected CNGA1 and CNGB1 protein in wild type mice at the expected size of ~60 kD and ~240 kD, respectively, and confirmed downregulation of CNG channel subunits in *Cnga1*^{MUT} mice at PM1 and PM6 (Figure 12A-C). Strikingly, although nearly no CNGA1 protein could be found at PM1, *Cnga1*^{MUT} transcript was expressed in similar levels as in the wild type control. (Figure 12D). Despite transcript levels of *Cngb1* were significantly reduced to about 70 % at PM1 in *Cnga1*^{MUT} mice compared to wild type (Figure 12E), this reduction cannot explain the complete loss of the protein signal (Figure 11F, G). At PM6, however, substantial ONL loss was also manifested in significantly decreased transcript levels of both *Cnga1* and *Cngb1*. These findings indicate that the reduction of CNGA1 and CNGB1 protein was not caused by a shutdown of gene expression but rather by translation repression or protein degradation.

While at PM1 the photoreceptor OS of *Cnga1*^{MUT} mice already lack CNGA1 protein, it is unclear whether the mutant protein is expressed at an earlier age before photoreceptor degeneration begins. Therefore, cross-sections of wild type and *Cnga1*^{MUT} mice retinas collected at postnatal day 11 (P11), P14, P17, and P21 were immunostained for CNGA1 and CNGB1 expression (Figure 13). In wild type mice, both subunits were already expressed at P11, when eyes begin to open (Figure 13A, I). As rod OS are short at this age, CNG channel expression is very low and strongly increases until P21 as OS expand (Figure 13B-D, J-L). In contrast, no expression of CNGA1 or CNGB1 could be detected in *Cnga1*^{MUT} mice at any age tested (Figure 13E-H, M-P). Moreover, the ONL thickness was comparable between wild type and *Cnga1*^{MUT} mice until P17 and first evidence of thinning only became obvious at P21, indicating ongoing photoreceptor degeneration at this stage.

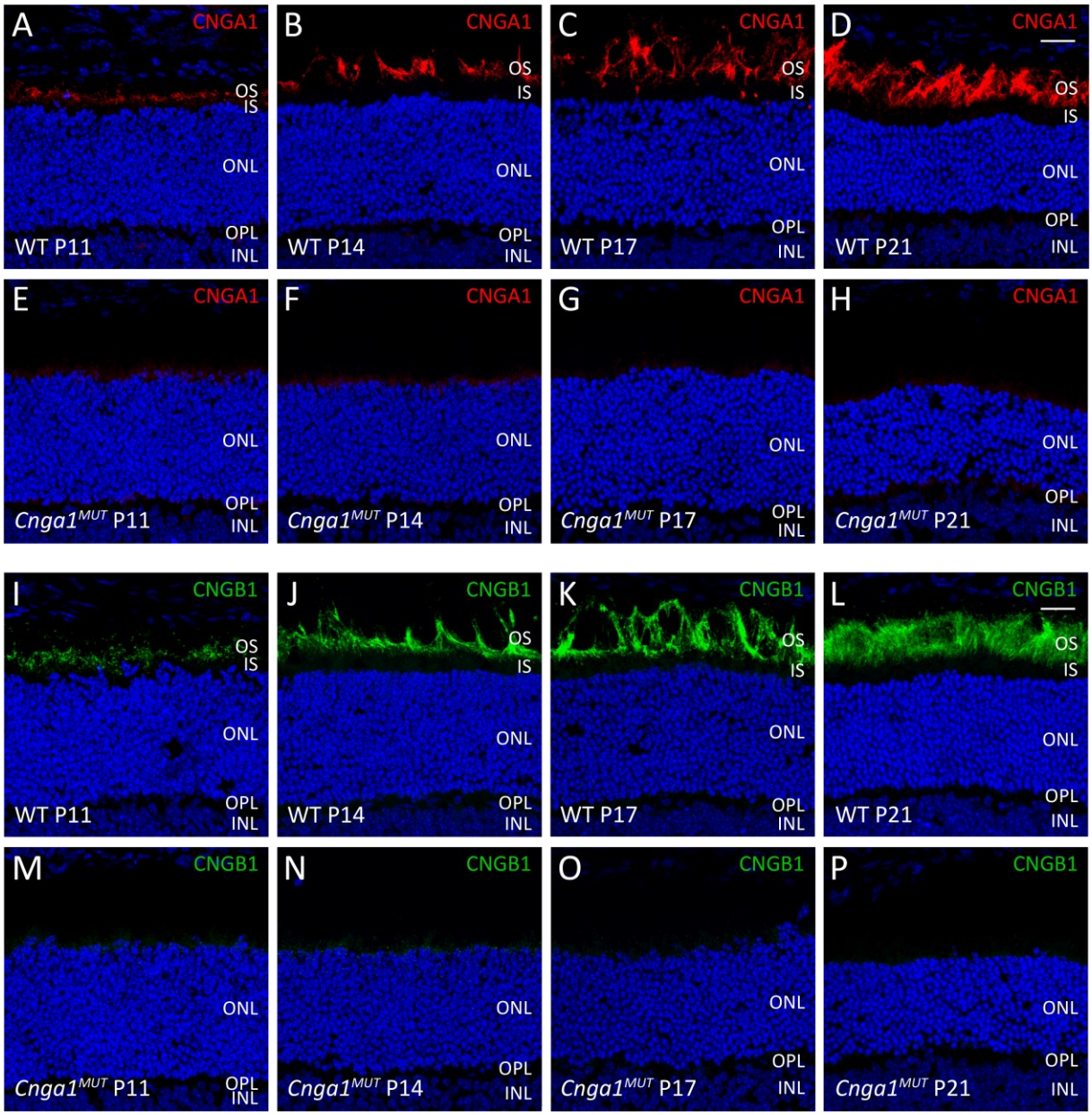

Figure 13. *Cnga1*^{MUT} mice do not express CNG channel subunits at any age. Representative confocal images showing expression of CNGA1 (red; A-H) and CNGB1 protein (green; I-P) in retinal cross-sections of wild type (WT) and *Cnga1*^{MUT} mouse retinas at P11, P14, P17, and P21. Cell nuclei were stained with DAPI (blue). OS, outer segments; IS, inner segments; ONL, outer nuclear layer; OPL, outer plexiform layer; INL, inner nuclear layer. Scale bars mark 20 µm.

Pathologically high levels of the intracellular second messenger cyclic guanosine monophosphate (cGMP), caused by a missing Ca^{2+}-mediated negative feedback on the cGMP-producing rod guanylate cyclases (GCs) were previously shown in multiple mouse models of retinal degeneration (Farber and Lolley, 1974; Tanaka et al., 1997; Paquet-Durand et al., 2009; Michalakis et al., 2010; Trifunovic et al., 2010; Paquet-Durand et al., 2011; Xu et al., 2013;

Schön et al., 2017). Furthermore, it is known that also knockout of the *Cngb1* gene goes along with profound accumulation of cGMP (Koch et al., 2012). Consistently, immunolabeling of paraformaldehyde-fixed cGMP revealed cGMP accumulation in *Cnga1*^{MUT} mice at PM1, which peaked at PM3 (Figure 14A-C). At later time points, cGMP accumulation decreased again due to progressing photoreceptor cell death (Figure 14D-F).

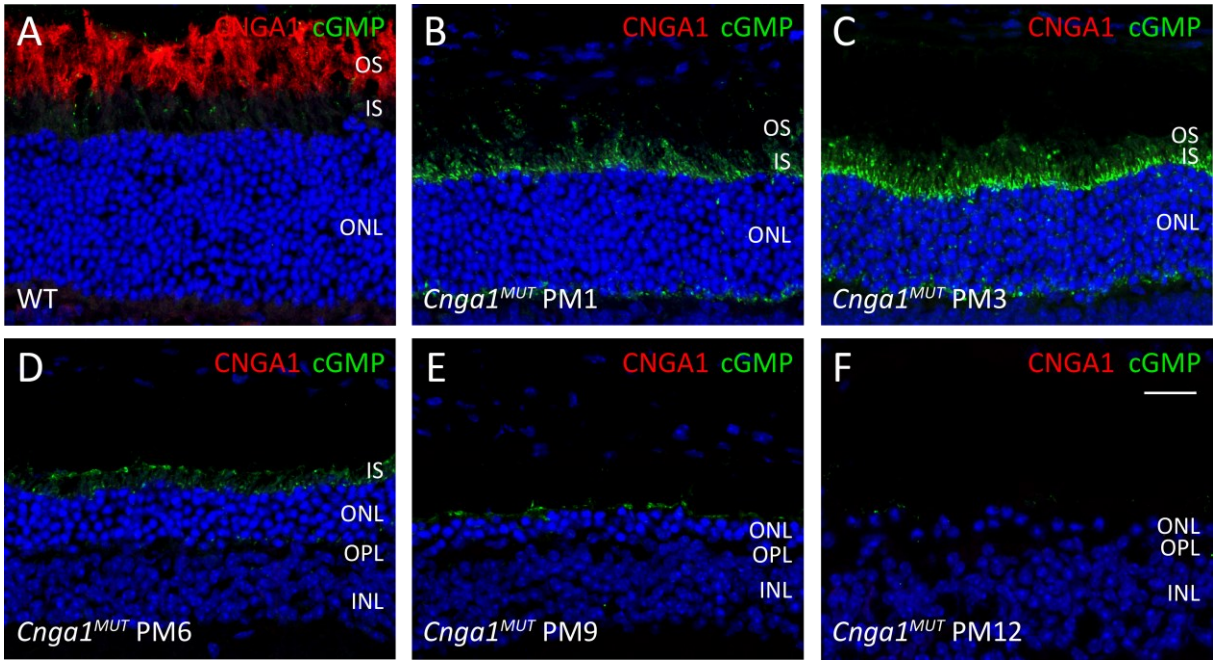

Figure 14. Non-functional CNGA1 leads to profound cGMP accumulation in *Cnga1*^{MUT} mice. Representative confocal images showing paraformaldehyde-fixed second messenger cGMP (green) and expression of CNGA1 protein (red) in retinal cross-sections of wild type (WT; PM1; A), and *Cnga1*^{MUT} mouse retinas at PM1 (B), PM3 (C), PM6 (D), PM9 (E), and PM12 (F). Cell nuclei were stained with DAPI (blue). OS, outer segments; IS, inner segments; ONL, outer nuclear layer; OPL, outer plexiform layer; INL, inner nuclear layer. Scale bar marks 20 µm.

4.1.3 Rod and Cone Photoreceptor Degeneration in *Cnga1*^{MUT} Mice

The degeneration and loss of photoreceptors in RP patients, but also in animal models of RP, can be monitored by spectral-domain optical coherence tomography (SD-OCT). To investigate the effect of CNGA1 loss on the retinal structure and morphology of photoreceptors in living *Cnga1*^{MUT} mice, SD-OCT was carried out over 12 months (Figure 15) and the total photoreceptor length, measured as combined thickness of photoreceptor OS and ONL (hereafter referred to as photoreceptor plus, or PR+) was analyzed. In wild type mice, the PR+ layer had reached its final thickness of approximately 100 µm at PM1 (Figure 15A, C, E). Until at least PM12, this thickness remained. In *Cnga1*^{MUT} mice, a slowly progressing thinning of the

PR+ layer was evident. From the beginning of measurements at P21, the PR+ layer was decreased to about 80 µm and continued to decrease with disease progression, resulting in an almost absent ONL at PM12 (Figure 15B, D, E). However, retinal structures other than photoreceptors, such as the retinal pigment epithelium (RPE), the inner nuclear layer (INL), or the ganglion cell layer (GCL), were not visibly affected by the deletion of CNGA1.

As cones make up only approximately 3% of all photoreceptors in the mouse retina (Jeon et al., 1998; Ortin-Martinez et al., 2014), these cells cannot be distinguished in SD-OCT but also do not substantially contribute to the PR+ thickness. Thus, the decrease of PR+ thickness especially reflects the degeneration of rod photoreceptors.

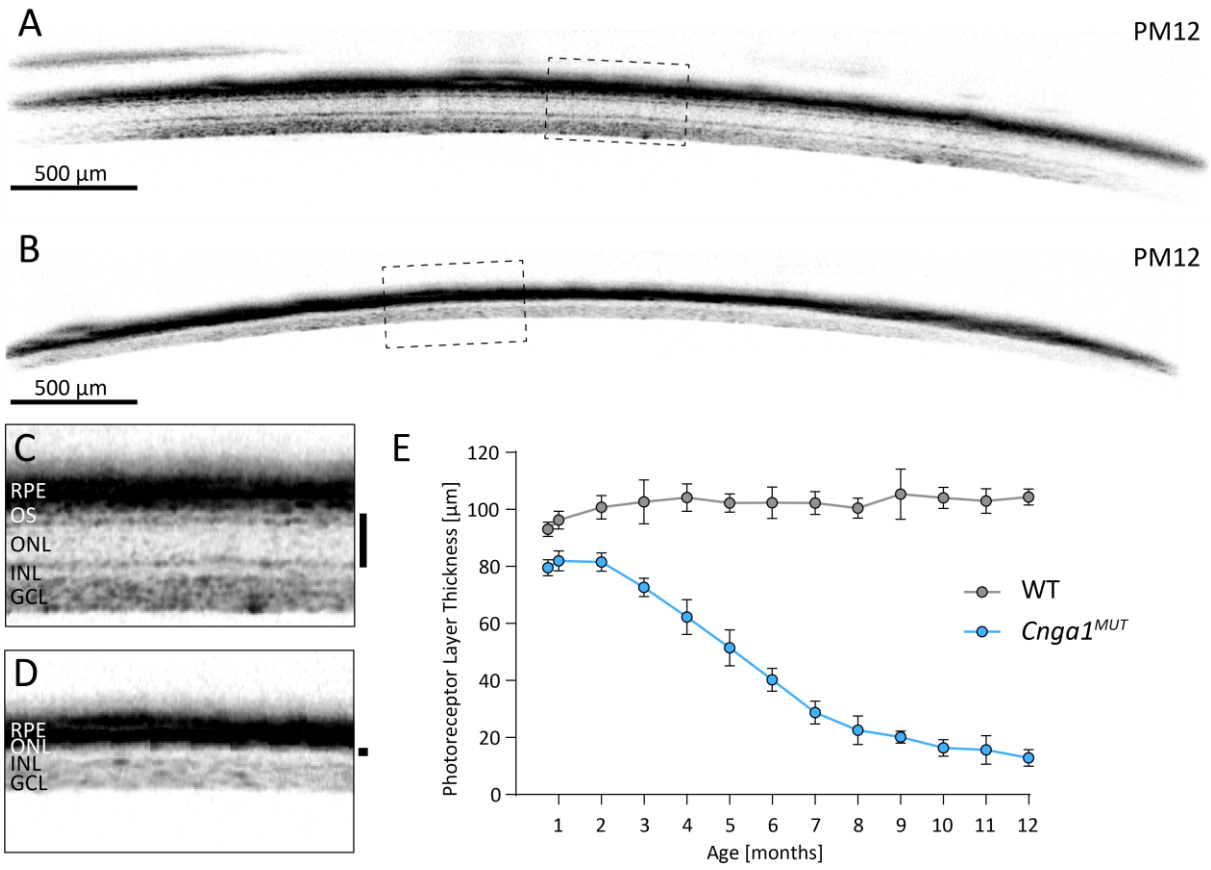

Figure 15. *Cnga1*^{MUT} mice show a reduced photoreceptor layer thickness. (A-D) Representative SD-OCT images of wild type (WT; A, C) and *Cnga1*^{MUT} mice (B, D) at the age of 12 months (PM12). Black bars in C and D mark the thickness of the photoreceptor layer. RPE, retinal pigment epithelium; OS, outer segments; ONL, outer nuclear layer; INL, inner nuclear layer; GCL, ganglion cell layer. (E) Degeneration progress of photoreceptor layer thickness (PR+) in *Cnga1*^{MUT} mice (blue) compared to WT mice (grey) from P21 until PM12. WT: N = 10; *Cnga1*^{MUT} mice: N = 12. Values are given as mean ± SD.

To further evaluate the morphology of rod photoreceptors, retinal cross-sections of *Cnga1*^{MUT} and wild type mice were immunostained with an antibody detecting the rod-specific photosensitive pigment rhodopsin (Figure 16). In *Cnga1*^{MUT} mice, rod OS were shortened already at PM1 compared to wild type (Figure 16A, B). While in wild type mice rhodopsin was strictly located in rod OS, it was also found in rod inner segments (IS) in *Cnga1*^{MUT} mice, indicating a destruction of rod OS and thus incomplete trafficking of rhodopsin to its actual location. Moreover, along with the progression of photoreceptor dell death, rod OS shortening proceeded with strongly destructed rods at PM6 (Figure 16D), until at PM9 rod OS and IS were completely lost (Figure 16E). At PM12, no more rhodopsin expression could be detected (Figure 16F).

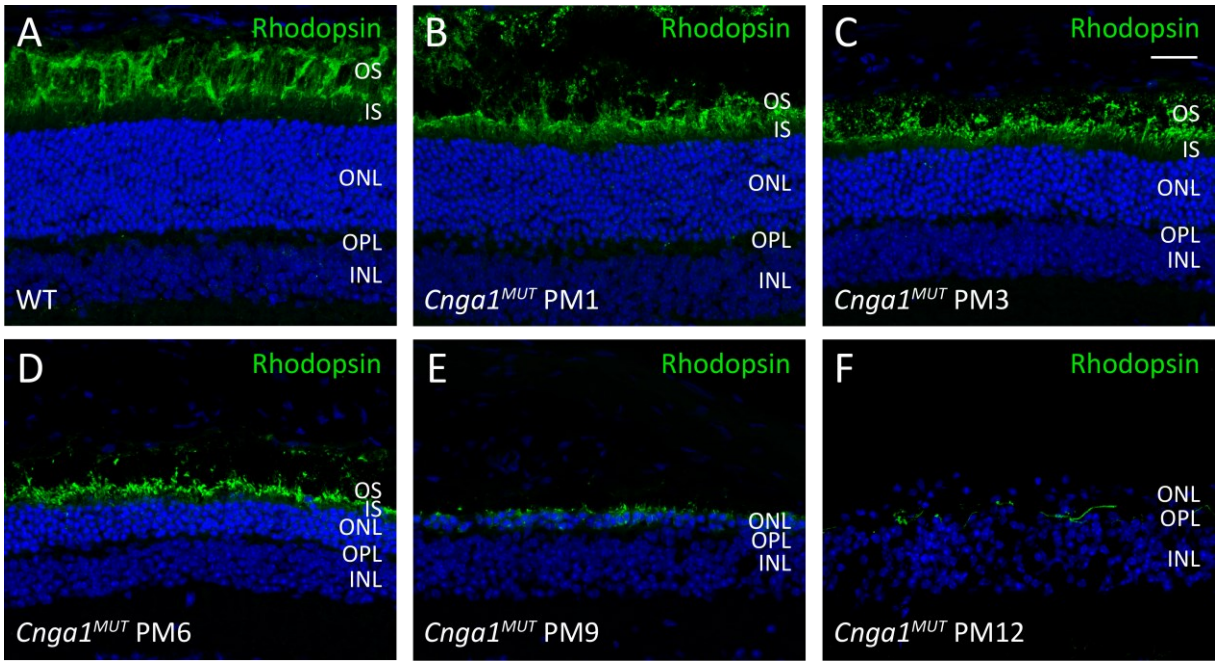

Figure 16. *Cnga1* deletion leads to shortened rod outer segments and rod degeneration in *Cnga1*^{MUT} mice. Representative confocal images showing expression of rhodopsin (green) in retinal cross-sections of wild type (WT; PM1; A), and *Cnga1*^{MUT} mouse retinas at PM1 (B), PM3 (C), PM6 (D), PM9 (E), and PM12 (F). Cell nuclei were stained with DAPI (blue). OS, outer segments; IS, inner segments; ONL, outer nuclear layer; OPL, outer plexiform layer; INL, inner nuclear layer. Scale bar marks 20 µm.

Interestingly, in contrast to an early impairment of rod morphology after *Cngb1* deletion (Hüttl et al., 2005), shortening of rod OS due to *Cnga1* deletion did not start before loss of cell nuclei (Figure 17). Immunostaining of rhodopsin in wild type and *Cnga1*^{MUT} mice at P11 revealed that rod OS formation was less impaired in *Cnga1*^{MUT} mice (Figure 17A, E). Additionally, rods were

natively shaped at P14 and P17 with OS comparable to wild type mice (Figure 17B-C, F-G). Although decrease of the ONL thickness had now started, rod OS of *Cnga1*^{MUT} mice still showed normal morphology at P21 (Figure 17D, H). Together with the findings of an unaltered ONL thickness until P17 and a clear decline starting from P21, these results further strengthen the assumption that primary degeneration of rod photoreceptor cell nuclei starts around P21, while rod OS shortening begins after loss of cell nuclei.

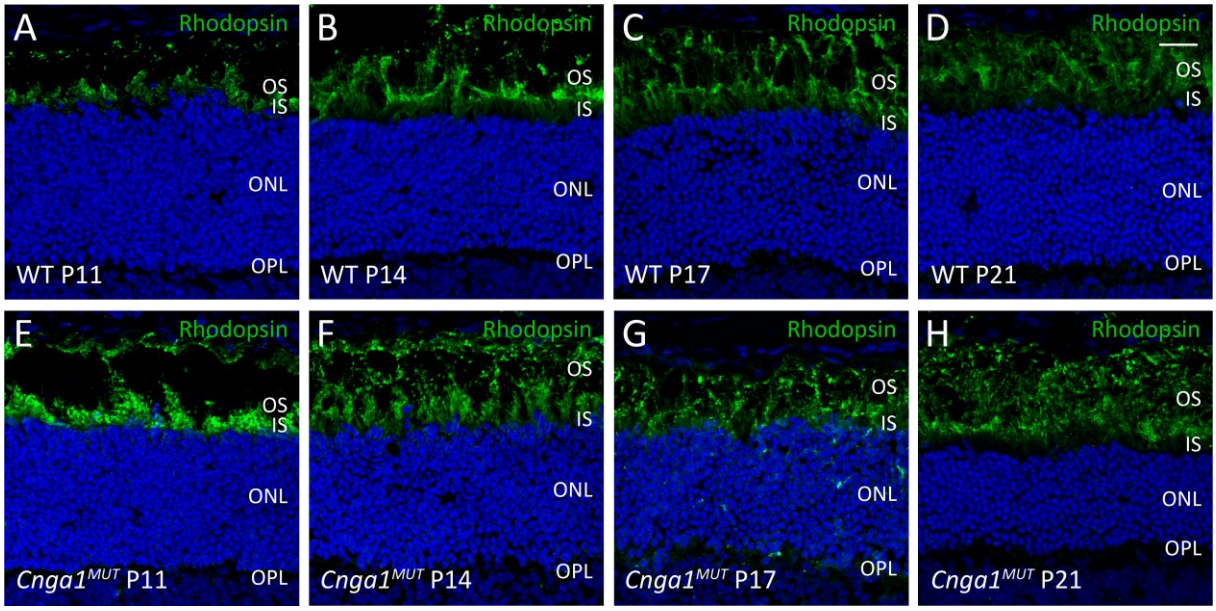

Figure 17. Primary degeneration of rod photoreceptors starts around P21. Representative confocal images showing expression of rhodopsin (green) in retinal cross-sections of wild type (WT) and *Cnga1*^{MUT} mouse retinas at P11, P14, P17, and P21. Cell nuclei were stained with DAPI (blue). OS, outer segments; IS, inner segments; ONL, outer nuclear layer; OPL, outer plexiform layer. Scale bar marks 20 µm.

Unlike rods, cones were initially unaffected by the mutation, since CNGA1 protein is not expressed in this type of photoreceptors. This became evident from immunolabeling of retinal cross-sections of wild type and *Cnga1*^{MUT} mice with an antibody against cone arrestin, a protein specifically expressed in cones (Figure 18A-F), and with peanut agglutinin (PNA; Figure 18G-L) that labels the extracellular matrix of cones (Ishikawa et al., 1997). In the wild type, cones were entirely stained by cone arrestin, including synapse, axon, cell body, IS, and OS (Figure 18A), while PNA only labels synaptic end feet, IS, and OS (Figure 18G). In *Cnga1*^{MUT} mice, the staining revealed a wild type-like shape of cones until the age of 3 months (Figure 18A-C, G-I). Although at PM6 cone OS started to collapse along with progressing demise of surrounding rod OS, cones were found at normal numbers (Figure 18D, J). Secondary

degeneration of cones eventually started after PM6, until at PM9 only so-called “dormant cones”, the non-functional cell body residues (Busskamp et al., 2010; Sahel et al., 2013), remained (Figure 18E-F). Finally, most cones were lost at PM12 and remaining cone arrestin-positive cones appeared rounded and degenerated (Figure 18K-L).

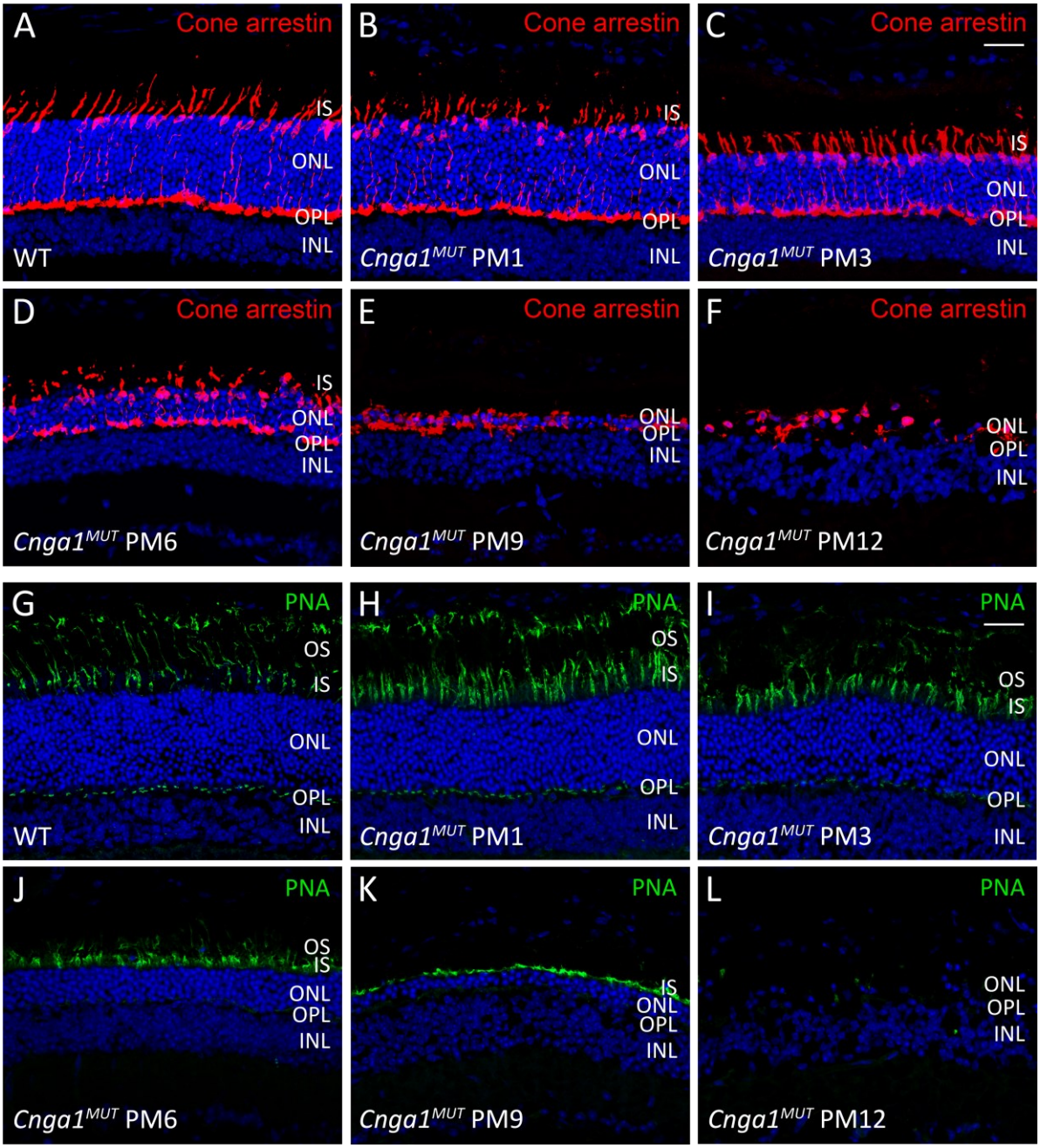

Figure 18. *Cnga1* deletion causes secondary degeneration of cone photoreceptors in *Cnga1*^{MUT} mice. Representative confocal images showing expression of cone arrestin (red; A-F) and peanut agglutinin (PNA; green; G-L) in retinal cross-sections of wild type (PM1; A, G), and *Cnga1*^{MUT} mouse retinas PM1 (B, H), PM3 (C, I), PM6 (D, J), PM9 (E, K), and PM12 (F, L). Cell nuclei were stained with DAPI (blue). OS, outer segments; IS, inner segments; ONL, outer nuclear layer; OPL, outer plexiform layer; INL, inner nuclear layer. Scale bars mark 20 µm.

4.1.4 Impaired Photoreceptor Function in *Cnga1*^{MUT} Mice

In the next step, changes in retinal rod function were evaluated over time by recording ERGs under dark-adapted (scotopic) conditions at different ages starting from P21 (Figure 19 and Figure 20).

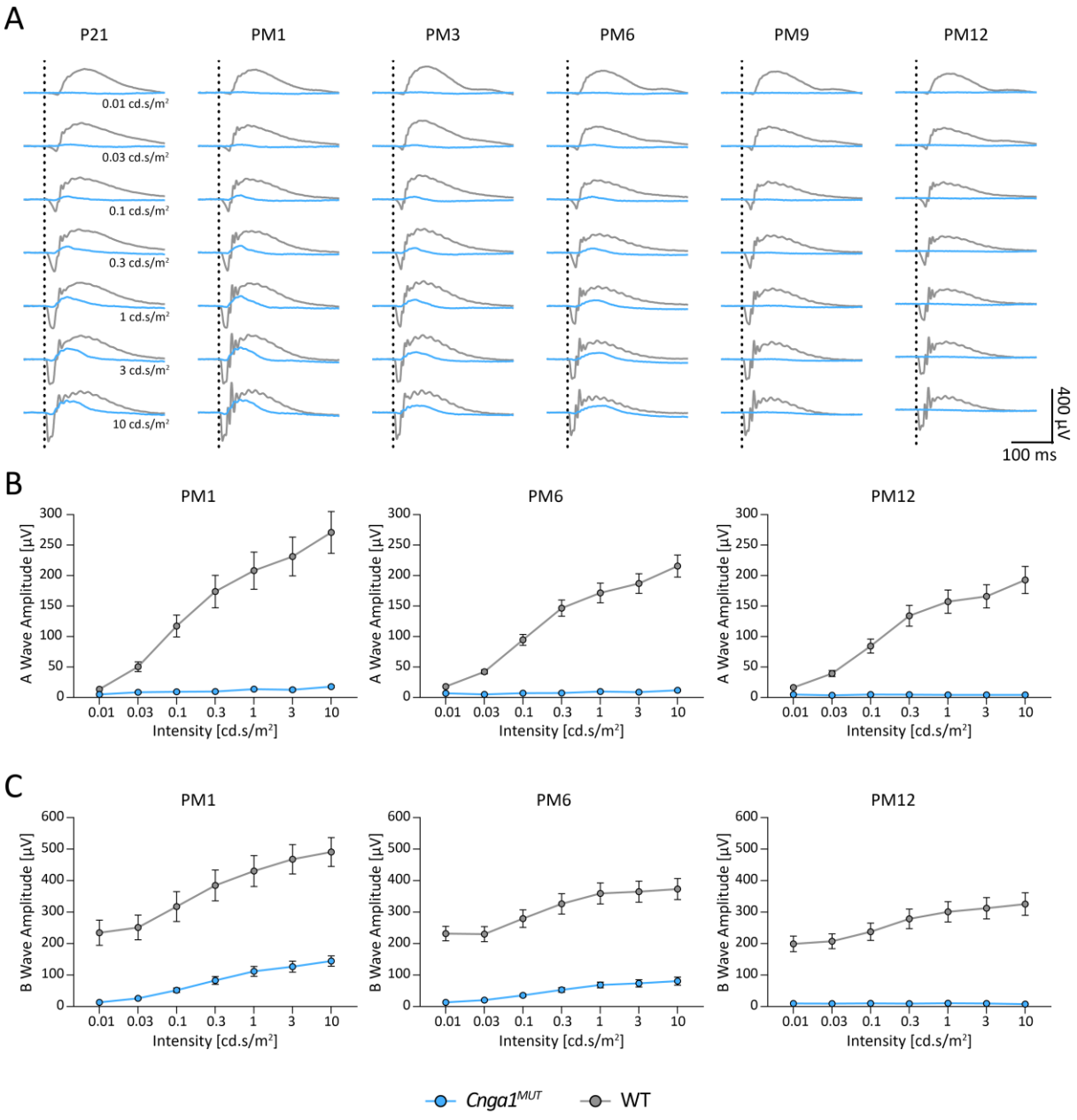

Figure 19. *Cnga1* deletion accompanies with loss of rod-driven retinal function in *Cnga1*^{MUT} mice. (A) Overlays of averaged scotopic electroretinography (ERG) signals of *Cnga1*^{MUT} (blue) compared to wild type mice (WT; grey) at P21, PM1, PM3, PM6, PM9 and PM12 at different light intensities. Vertical dotted lines mark the timepoint of light stimulation. (B-C) Quantification of a-wave (B) and b-wave (C) amplitudes of *Cnga1*^{MUT} mice (blue) compared to WT mice (grey) at different ages. WT: N = 10; *Cnga1*^{MUT}: N = 12. Values are given as mean ±SEM.

In dark-adapted conditions, wild type mice showed a response to light starting from the lowest light intensity of 0.01 cd.s/m^2 at all ages investigated (Figure 19A), which, as expected, decreased slightly depending on age. In contrast, in *Cnga1*^{MUT} mice, first responses to light were not observed before 0.1 cd.s/m^2, even at early ages, when photoreceptor degeneration just started (Figure 19A). Consistent with the total loss of photoreceptors at PM9 seen by immunolabeling of rods and cones (Figure 16 and Figure 18), no response to any light intensity could be observed after PM9 (Figure 19A) and *Cnga1*^{MUT} mice can be considered completely blind at this stage.

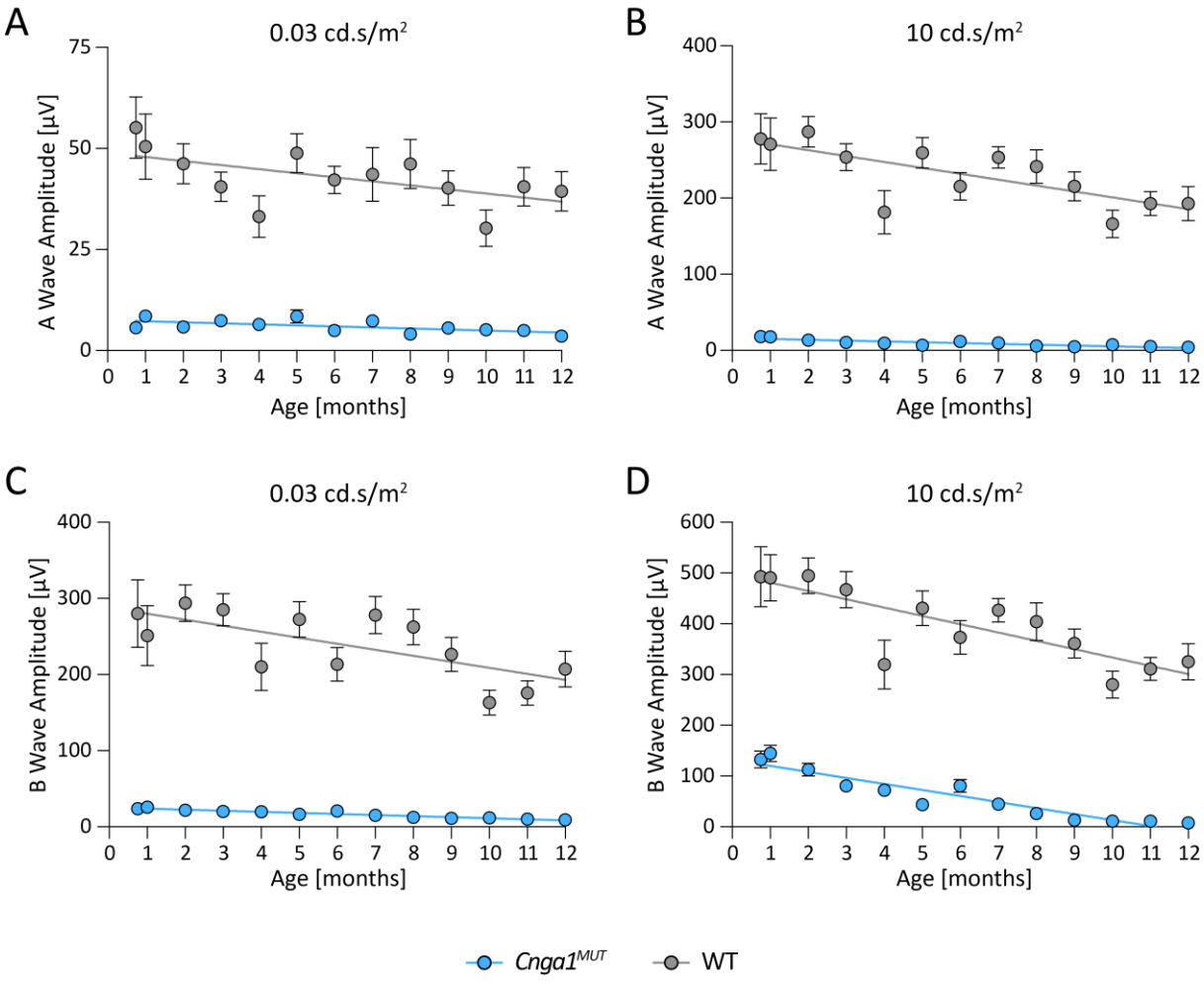

Figure 20. *Cnga1* deletion accompanies with loss of rod-driven retinal function in *Cnga1*^{MUT} mice. Quantification of a-wave (A, B) and b-wave (C, D) amplitudes of *Cnga1*^{MUT} mice (blue) compared to WT mice (grey) at the rod-specific light intensity of 0.03 cd.s/m^2 (A, C) and the rod- and cone-reflecting light intensity of 10 cd.s/m^2 (C, D). WT: N = 10; *Cnga1*^{MUT}: N = 12. Values are given as mean ± SEM.

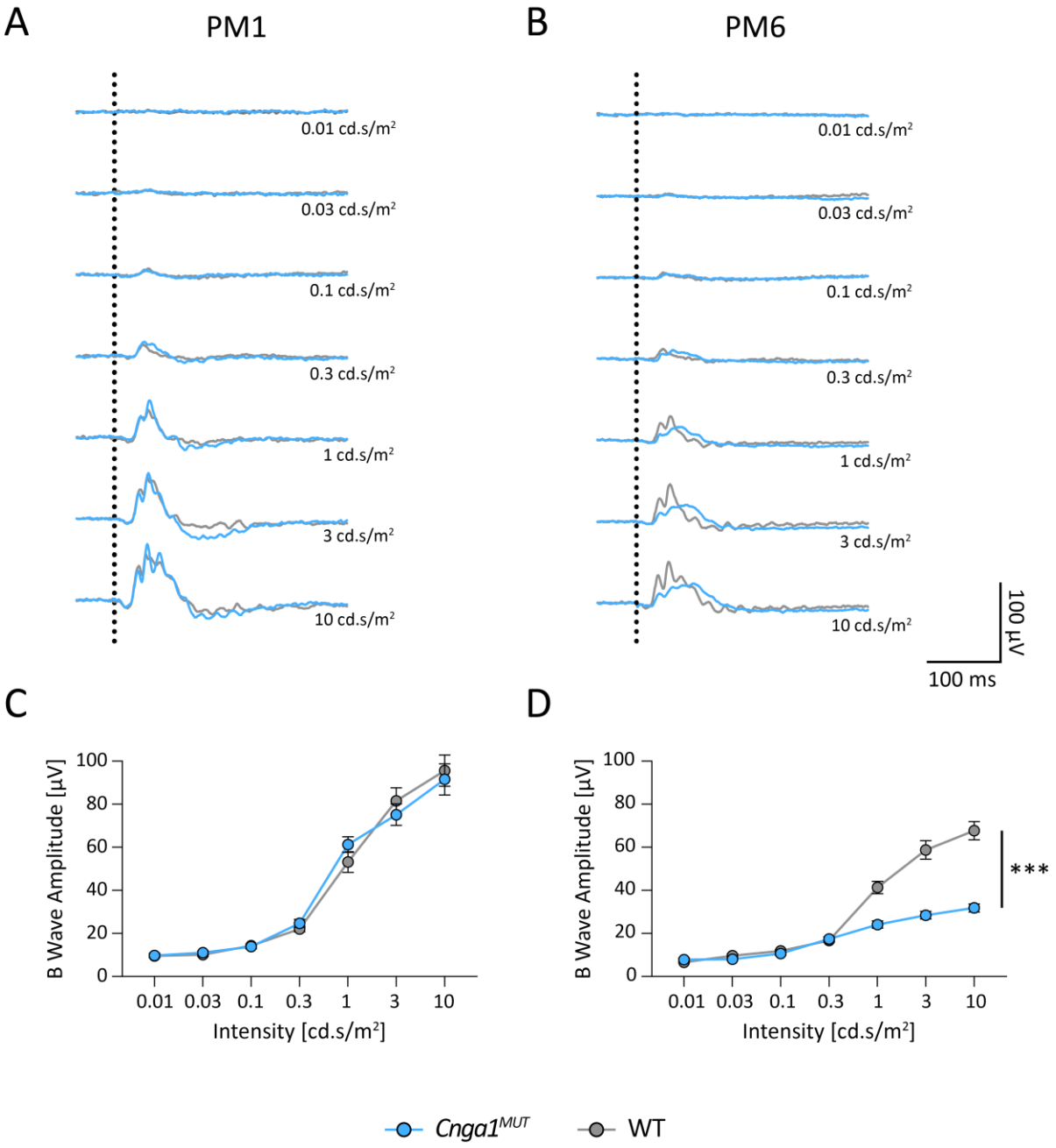

Figure 21. *Cnga1* mutation leads to secondary impairment of cone photoreceptor function in *Cnga1*^{MUT} mice. (A-B) Overlays of averaged photopic electroretinography (ERG) signals of *Cnga1*^{MUT} and WT mice at PM1 (A) and PM6 (B) at different light intensities. Vertical dotted lines mark the timepoint of light stimulation. (B-C) Quantification of light-adapted ERG a-wave (B) and b-wave (C) amplitudes of *Cnga1*^{MUT} mice at PM1 and PM6. N = 12. Values are given as mean ± SEM (Ordinary two-way ANOVA with Šídák's post-hoc test; ***p≤0.001).

In a rhodopsin knockout mouse model, a threshold of 0.01-0.03 cd.s/m^2 was found to mark rod-specific light responses (Jaissle et al., 2001). At 0.03 cd.s/m^2, *Cnga1*^{MUT} mice neither showed a- nor b-waves at any age (Figure 20A, C). Both a-wave, the initial negative deflection, and the positive-going b-wave are typical indicators of rod system activity (Biel et al., 1999a;

Tanimoto et al., 2013). Indeed, *Cnga1*^{MUT} mice completely missed an a-wave at all ages, even at the highest light intensity of 10 cd.s/m^2, which represents both rod and cone responses (Figure 19A, B, Figure 20B). In addition, also b-wave amplitudes of *Cnga1*^{MUT} mice were strongly reduced compared to those of wild type mice, again even at the highest light intensity of 10 cd.s/m^2 (Figure 19A, C, Figure 20D). Moreover, *Cnga1*^{MUT} mice also lacked the major oscillatory potentials (OPs) at the beginning of a b-wave signal. Thus, these findings indicate an impaired rod system already at P21.

Nevertheless, although b-wave signals were reduced in *Cnga1*^{MUT} mice compared to wild type, clear signals could be detected at least until PM6 for light intensities which in wild type elicit mixed rod and cone responses (10 cd.s/m^2; Figure 19A, C, Figure 20D). These findings from the scotopic ERG measurements suggest that the cone system is still intact in *Cnga1*^{MUT} mice, at least up to PM6.

To further investigate this assumption, light-adapted (photopic) ERGs were recorded (Figure 21). No response differences between *Cnga1*^{MUT} and wild type mice were observed at PM1 (Figure 21A, C), confirming intact functionality of the cone system. At PM6, however, when substantial loss of cones has occurred (Figure 18), light-adapted ERG signals vanished (Figure 21B, D). These data imply that secondary loss of cone function starts at PM6 and is complete after PM9.

4.1.5 Cellular Stress Response in the *Cnga1*^{MUT} Retina

Müller glia cells are known to respond early to retinal degeneration by morphological and physiological changes in order to maintain retinal survival (Bringmann et al., 2009; Bringmann and Wiedemann, 2012). The process, termed “Müller cell gliosis”, is characterized by the induction of intermediate fibers that are positive for proteins such as glial fibrillary acidic protein (GFAP) and extend along almost the entire length of these radial glia (de Raad et al., 1996; Bringmann and Reichenbach, 2001). Indeed, upregulation of GFAP was also detected in *Cnga1*^{MUT} mice (Figure 22A-F). Whereas GFAP expression in wild type mice was found only in astrocytes and Müller cell end feet at the inner limiting membrane underneath the GCL (Figure 22A), *Cnga1*^{MUT} mice showed the appearance of first GFAP-positive intermediate fibers already at PM1 (Figure 22B, arrowheads). GFAP upregulation became very pronounced at later timepoints Figure 22C-E) and suddenly declined as retinal degeneration progressed at PM12 (Figure 22F).

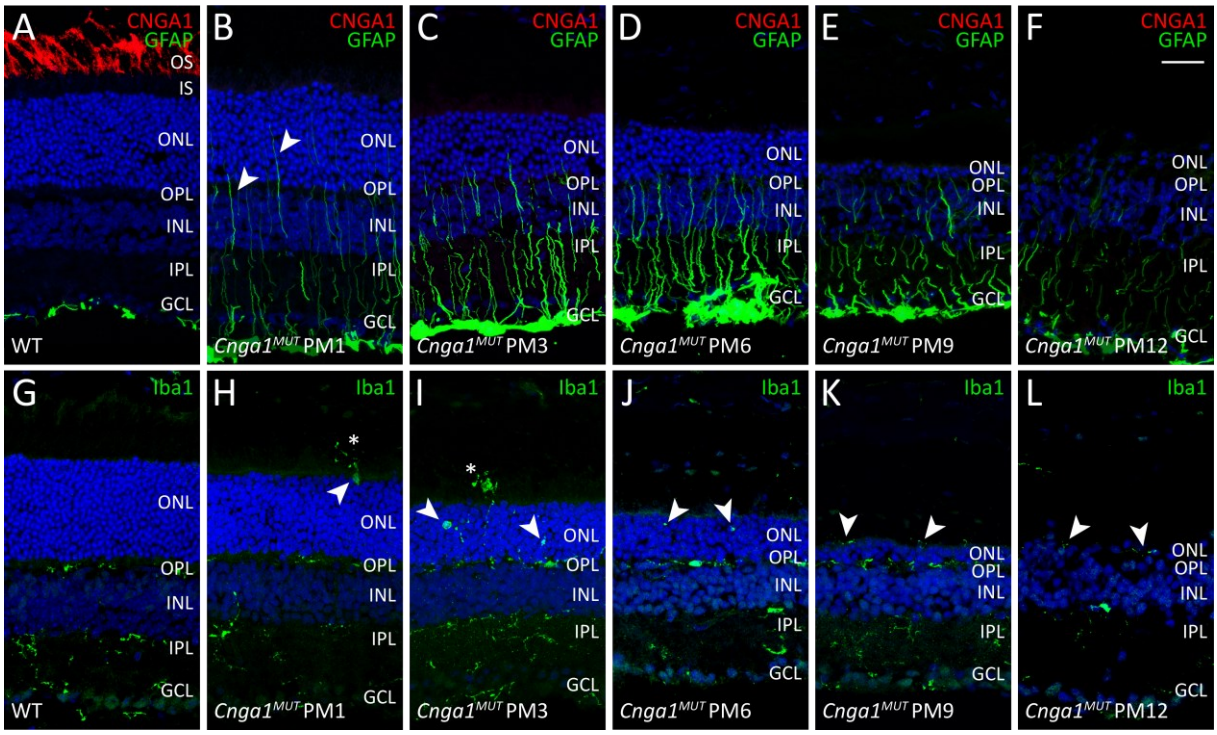

Figure 22. Retinal stress activates immunoreaction of retinal residential cells in *Cnga1*^{MUT} mice. Representative confocal images showing co-expression of CNGA1 (red) and glial fibrillar acidic protein (GFAP; green; A-F) or expression of ionized calcium-binding adapter molecule 1 (Iba1; green; G-L) in retinal cross-sections of wild type (PM1; A, G), and *Cnga1*^{MUT} mouse retinas at PM1 (B, H), PM3 (C, I), PM6 (D, J), PM9 (E, K), and PM12 (F, L). Cell nuclei were stained with DAPI (blue). Arrowheads indicate first intermediate fibers (A-F) or microglia migrated into the ONL (G-L). Asterisks indicate microglia migrated into the photoreceptor layer (G-L). OS, outer segments; IS, inner segments; ONL, outer nuclear layer; OPL, outer plexiform layer; INL, inner nuclear layer; IPL, inner plexiform layer; GCL, ganglion cell layer. Scale bars mark 20 µm.

In addition, activation of microglia in response to retinal degeneration was observed in several retinal degenerative mouse models (Karlstetter et al., 2015; Reyes et al., 2017). Although inflammatory processes generally protect the retina, pathological activation of microglia may contribute to neurodegenerative diseases including RP (Karlstetter et al., 2010; Prinz and Priller, 2014; Zhao et al., 2015; Gupta et al., 2018). Immunolabeling of retinal cross-sections of wild type and *Cnga1*^{MUT} mice with an antibody against ionized calcium-binding adapter molecule 1 (Iba1), a protein expressed in macrophages and microglia that is upregulated during the activation of these cells, revealed slight microglia activation in *Cnga1*^{MUT} mice Figure 22G-L). In wild type mice, microglia were found in their ramified inactive morphology and at their colonized sites in the outer and inner plexiform layers (OPL, IPL; Figure 22G). In

contrast, in *Cnga1*^{MUT} mice Iba1-positive cells migrated into the ONL and INL starting from PM1 (Figure 22H-L, arrowheads) and some had even infiltrated the photoreceptor layer (Figure 22H, I, asterisks). Additionally, microglia in *Cnga1*^{MUT} mice changed their inactive morphology to the motile amoeboid shape. This type of microglia produces inflammatory cytokines and randomly phagocytizes living photoreceptors, contributing to the phenotype of RP (Zhao et al., 2015; Okajima and Tsuruta, 2018). In summary, *Cnga1* deletion causes retinal stress that leads to early immunoreaction of retinal residential cells, such as Müller glia cells and microglia.

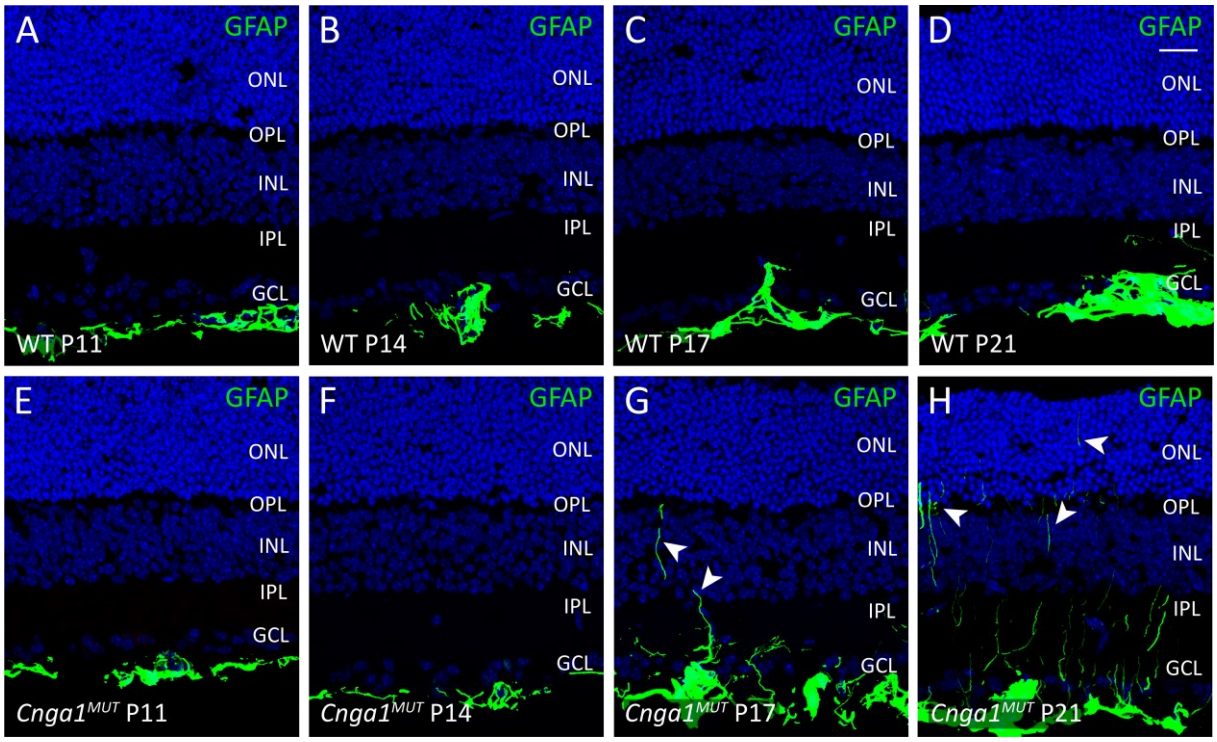

Figure 23. Early Müller cell gliosis attempts to maintain photoreceptor survival in young *Cnga1*^{MUT} mice. Representative confocal images showing expression of glial fibrillar acidic protein (GFAP; green) in retinal cross-sections of wild type (WT) and *Cnga1*^{MUT} mouse retinas at P11, P14, P17, and P21. Cell nuclei were stained with DAPI (blue). Arrowheads indicate first intermediate fibers. ONL, outer nuclear layer; OPL, outer plexiform layer; INL, inner nuclear layer; IPL, inner plexiform layer; GCL, ganglion cell layer. Scale bar marks 20 µm.

Because the first timepoint analyzed (PM1) already showed induction of both markers, retinal cross-sections of wild type and *Cnga1*^{MUT} mice were examined at the early ages P11, P14, P17 and P21 to determine the starting point for GFAP upregulation (Figure 23) and microglia activation. First intermediate fibers were found at P17 in *Cnga1*^{MUT} mice (Figure 23G), and their number continued to increase until P21 (Figure 23H). While thus Müller cell gliosis seems

to start already before photoreceptor degeneration in order to maintain photoreceptor survival, microglia activation and infiltration was not observed at these early stages (data not shown).

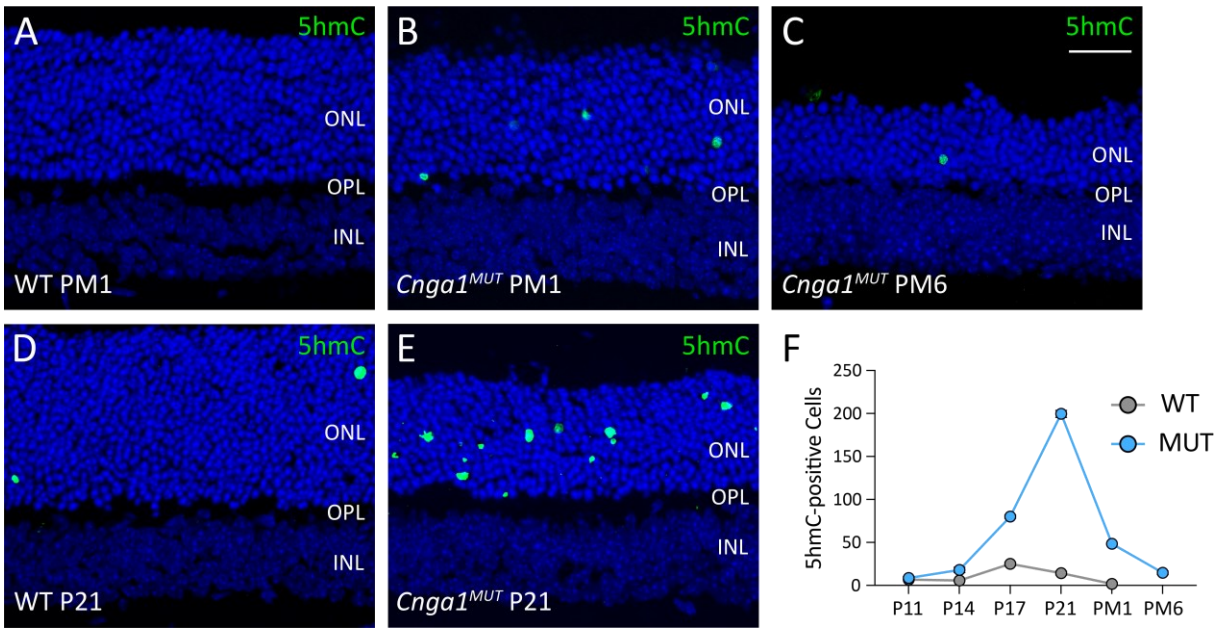

Figure 24. Photoreceptor cell death peaks in the early development period of *Cnga1*^{MUT} mice. (A-E) Representative confocal images showing 5-hydroxymethylcytosine (5hmC)-accessible cells (green) in retinal cross-sections of wild type (WT) and *Cnga1*^{MUT} mouse retinas at PM1, PM6, and P21. Cell nuclei were stained with DAPI (blue). ONL, outer nuclear layer; OPL, outer plexiform layer; INL, inner nuclear layer. Scale bar marks 20 µm. (F) Quantification of 5hmC-positive cells in WT (grey) and *Cnga1*^{MUT} mouse retinas (blue) at different timepoints. N = 3. Values are given as mean ± SEM.

5-Hydroxymethylcytosine (5hmC), a methylated version of the DNA base cytosine, is an important epigenetic marker in neurogenesis as well as in neurodegeneration (Wahlin et al., 2013; Perera et al., 2015). It has been shown that the immunosignal from antibodies that specifically bind genomic 5hmC increases in degenerating photoreceptors (Wahlin et al., 2013). Genomic 5hmC marks in normal cells are inaccessible to antibodies unless the integrity of the cell nucleus and chromatin structure has been changed and 5hmC becomes accessible during induction of cell death. Thus, 5hmC can serve as marker for photoreceptor degeneration. Immunolabeling of 5hmC in retinal cross sections of wild type and *Cnga1*^{MUT} mice revealed slightly increased photoreceptor cell death at PM1 and PM6 compared to wild type (Figure 24A-C). However, this moderate upregulation of cell death does not cover the total photoreceptor degeneration during disease onset and progression. Indeed, examination

of earlier timepoints showed that photoreceptor cell death started after P14, reaching peak at P21 and declining afterwards (Figure 24D-F). These results are in line with previous findings of primary rod photoreceptor degeneration starting around P21 in *Cnga1*^{MUT} mice.

In summary, the present study provides a comprehensive characterization of the novel *Cnga1*^{MUT} mouse model, which revealed that loss of CNGA1 leads to early impairment of rod photoreceptor morphology and function starting around P21, while cone photoreceptors remain unaffected until PM6.

4.2 Retinal Response to RP at the Molecular Level

Until now, the mechanisms that contribute to the phenotype of RP still remain unclear. In order to elucidate potential mechanisms underlying photoreceptor cell death, different animal models of RP, whose mutations affect several distinct steps during phototransduction, were investigated.

4.2.1 Altered Signaling Pathways Induced by Mutations linked to RP

To gain insight into the underlying mechanisms of photoreceptor cell death, proteomics analysis of retinal protein lysates of *Cnga1*^{MUT} mice at PM1 and PM6, and *Pde6a*$^{-/-}$ dogs at the age of 3 years (PM39) was performed.

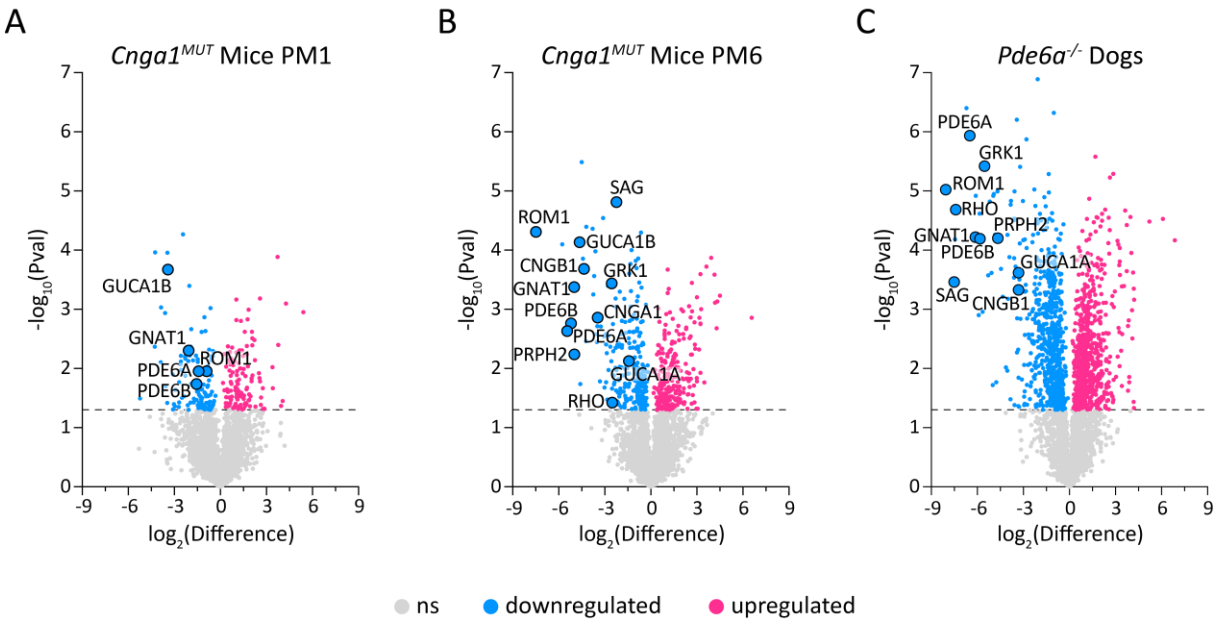

Figure 25. A huge number of proteins is altered in animal models of RP. Volcano plots of proteomics analysis of *Cnga1*^{MUT} mice at PM1 (A) and PM6 (B), and *Pde6a*$^{-/-}$ dogs (PM39; C) over age-matched wild type control animals. Differentially expressed proteins (DEPs) are shown in blue (downregulated) or pink (upregulated), while non-DEPs are shown in grey. Important proteins are highlighted. N = 3.

In *Cnga1*^{MUT} mice, a total of 2.976 proteins was detected, of which 248 were categorized as differentially expressed proteins (DEPs) with $p \leq 0.05$ at PM1. 132 of these were upregulated and 116 were downregulated in *Cnga1*^{MUT} mice compared to wild type mice (Figure 25A). At PM6, 520 proteins were categorized as DEPs, of which 264 were upregulated and 256 were downregulated (Figure 25B). In *Pde6a*$^{-/-}$ dogs, a total of 3.424 proteins was detected, of which

1.425 were categorized as DEPs with 746 proteins being upregulated and 679 proteins being downregulated compared to wild type dogs (Figure 25C).

In both animal models, a huge number of proteins involved in vision cycle and phototransduction pathways were found to be significantly downregulated compared to respective wild type control animals (Figure 25, highlighted proteins, Figure 26). Interestingly, at PM1 a less intense difference between *Cnga1*^{MUT} and wild type mice was observed compared to PM6, confirming an exacerbation of the retinal phenotype with age.

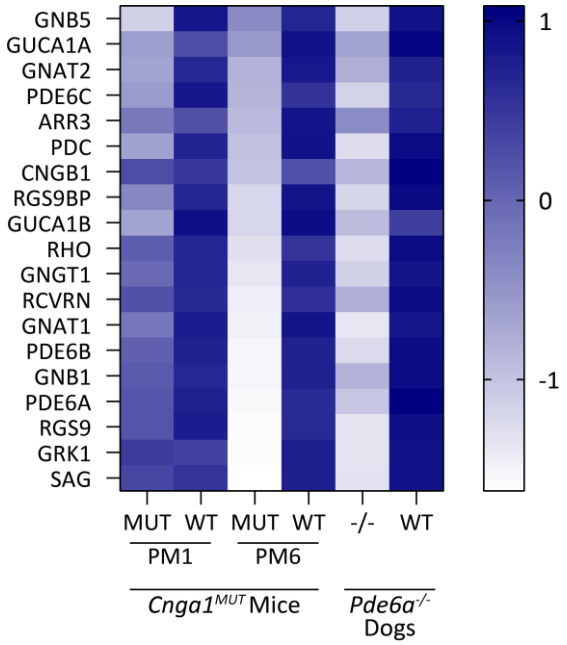

Figure 26. Phototransduction proteins are significantly altered in animal models of RP. Heat map of z-scores of altered proteins involved in phototransduction of *Cnga1*^{MUT} mice at PM1 and PM6, and *Pde6a*$^{-/-}$ dogs (PM39) over age-matched wild type control animals. N = 3.

In the next step, protein expression data were further analyzed by Ingenuity Pathway Analysis (IPA) of DEPs to identify potential shifts in specific signaling pathways in animal models of RP. Confirming previous results on the retinal phenotype of both animal models, "phototransduction pathway" was among the top deregulated IPA canonical pathways (*Cnga1*^{MUT} PM1: p = 1,91E-06; *Cnga1*^{MUT} PM6: p = 3,98E-22, *Pde6a*$^{-/-}$: p = 3,16E-11).

4.2.1.1 Cell Death Mechanisms and Pathways in Animal Models of RP

Different pathways contributing to photoreceptor cell death were previously reported in animal models of RP, including ER stress, oxidative stress, and metabolic stress (Newton and

Megaw, 2020). Thus, IPA results were analyzed for alterations in processes contributing to these pathways (Figure 27). Interestingly, ER stress activation was observed in *Cnga1*^{MUT} mice already at the early stage of degeneration (PM1) and persisted at the later time point (PM6), noticed by the activation of eukaryotic initiation factor 2 (EIF2) signaling, a downstream effector of the ER stress-sensor R-like endoplasmic reticulum kinase (PERK) (Figure 27A-B). Moreover, it has been hypothesized that also high intracellular Ca^{2+} levels may induce ER stress (van Vliet et al., 2017) and trigger programmed cell death mechanisms by activation of the proteolytic enzymes calpains (Cheng et al., 2018). Indeed, IPA detected activation of Ca^{2+} signaling and transport as well as alterations of calpain protease regulations in *Cnga1*^{MUT} mice and *Pde6a*$^{-/-}$ dogs (Figure 27A-C). Additionally, upregulation of the unfolded protein response (UPR), a compensatory mechanism to reduce ER stress by decreasing the load of unfolded protein in the ER (Hetz and Papa, 2018), was observed in *Pde6a*$^{-/-}$ dogs (Figure 27C). These results lead to the assumption that ER stress might contribute to photoreceptor cell death by ER stress-associated programmed cell death mechanisms across different animal models of RP.

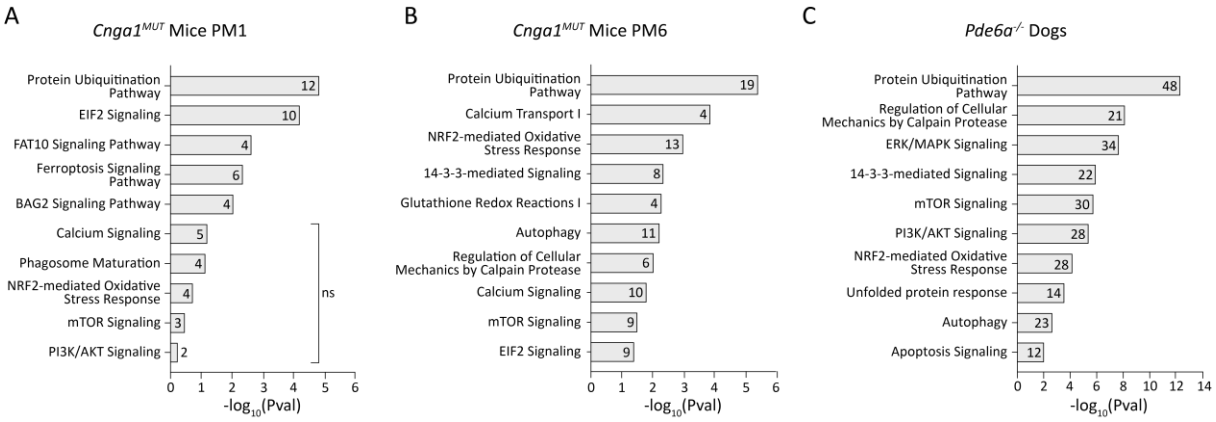

Figure 27. Animal models of RP show alterations in ER stress, autophagy and oxidative stress pathways. Altered cell death pathways in *Cnga1*^{MUT} mice at PM1 (A) and PM6 (B), and *Pde6a*$^{-/-}$ dogs (PM39; C) over age-matched wild type control animals revealed by ingenuity canonical pathway analysis of DEPs. The number in the bar indicates the number of altered proteins in the pathway. ns = not significant. N = 3.

In addition to enhanced ER stress, IPA also detected alterations in processes involved in macroautophagy (hereafter only referred to as autophagy) and proteasome regulation by the ubiquitin-proteasome system (UPS). While autophagy, a lysosome-mediated degradation process to maintain cell function and survival, can degrade long-lived proteins and whole cell

organelles, UPS is responsible for short-lived and misfolded proteins (Newton and Megaw, 2020). In both animal models, not only direct changes in autophagy processes were found but also alterations in negative regulating pathways, such as mammalian target of rapamycin (mTOR) signaling, phosphatidylinositol-3 kinase (PI3K) / protein kinase B (AKT) signaling or 14-3-3-mediated signaling (Figure 27A-C). Upstream regulator analysis suggested a deactivation of mTOR in both animal models (Table 8). Unexpectedly, phosphatase and tensin homologue (PTEN), which is a negative regulator of mTOR and thus an activator of autophagy was also predicted to be decreased (Table 8). In line with this, *Cnga1*^{MUT} mice at PM6 and *Pde6a*$^{-/-}$ dogs showed an activation of the mTOR upstream regulator AKT (Table 8). These data indicate dysregulation of autophagic processes in these RP models.

Moreover, differences in human leukocyte antigen-F adjacent transcript 10 (FAT10) signaling and protein ubiquitination pathway demonstrate impairment of the UPS. Altogether, these results are in line with previous findings that an imbalance between autophagy and UPS promotes photoreceptor cell death (Newton and Megaw, 2020).

Table 8. Upstream regulators related to the PI3K/AKT/mTOR pathway in animal models of RP. Predicted activation state identified by z-scores, p values of overlap, and counts of altered proteins involved in the respective pathway, of upstream regulators in *Cnga1*^{MUT} mice at PM1 and PM6, and *Pde6a*$^{-/-}$ dogs (PM39) over age-matched wild type control animals. Data was assessed via proteomics analysis and IPA. N = 3.

Upstream Regulator	Predicted Activation State	Pval of Overlap	Count
***Cnga1*^{MUT} PM1**			
mTOR	Deactivated	1,25E-03	11
PTEN	Deactivated	3,31E-03	16
***Cnga1*^{MUT} PM6**			
mTOR	Deactivated	1,39E-06	24
PTEN	Deactivated	1,34E-04	32
AKT	Activated	2,98E-02	15
***Pde6a*$^{-/-}$**			
mTOR	Deactivated	3,69E-10	53
PTEN	Deactivated	4,41E-09	82
AKT	Activated	1,63E-02	34

Photoreceptors are known to be vulnerable to oxidative stress due to their high metabolism and oxygen demand. Accordingly, hyperoxia was shown to cause photoreceptor death in several studies (Wellard et al., 2005; Natoli et al., 2011; Zeviani and Carelli, 2021). Indeed, IPA of both animal models showed indications of increased oxidative stress by changes in

pathways such as NRF2-mediated oxidative stress response or glutathione redox reactions, which neutralize reactive oxygen species (ROS) (Figure 27A-C).

4.2.1.2 Metabolic Shift Causes Mitochondrial Dysfunction in Animal Models of RP

Given that IPA revealed increased oxidative stress in *Cnga1*^{MUT} mouse and *Pde6a*$^{-/-}$ dog models of RP, which is known to be linked to mitochondrial dysfunction and subsequent photoreceptor degeneration (Murphy, 2009; Leveillard and Sahel, 2017; Petit et al., 2018; Rajala, 2020). IPA results were further examined for changes in mitochondrial pathways (Figure 28).

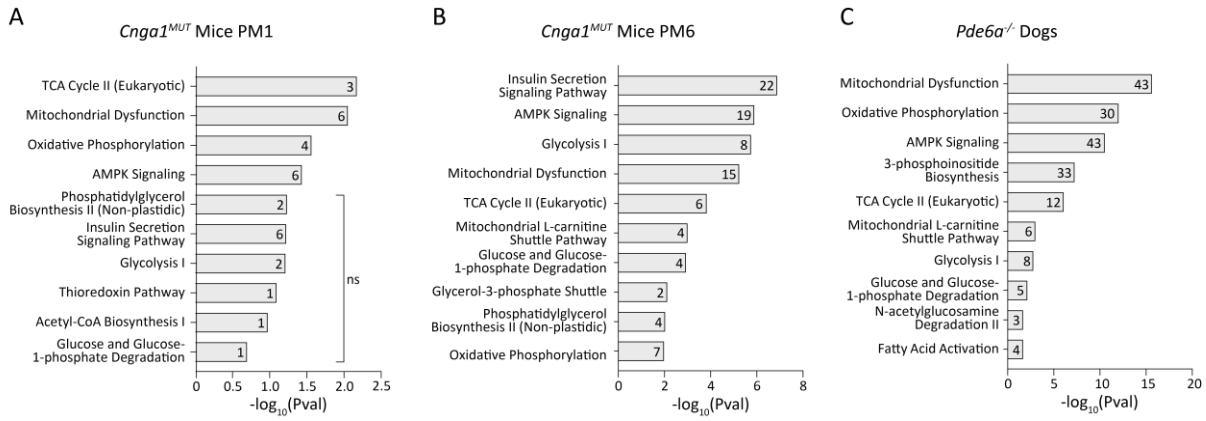

Figure 28. RP leads to altered metabolic pathways and mitochondrial dysfunction in different animal models. Altered metabolism pathways in *Cnga1*^{MUT} mice at PM1 (A) and PM6 (B), and *Pde6a*$^{-/-}$ dogs (PM39; C) over age-matched wild type control animals revealed by ingenuity canonical pathway analysis of DEPs. The number in the bar indicates the number of altered proteins in the pathway. ns = not significant. N = 3.

In both animal models, several relevant canonical pathways, such as oxidative phosphorylation, adenosine monophosphate-activated protein kinase (AMPK) signaling, and tricarboxylic acid (TCA) cycle II were found to be dysregulated (Figure 28). To gain more detailed insight into metabolic changes, proteomics data were screened for specific proteins involved in metabolic pathways (Table 9). Interestingly, a downregulation of hexokinase 2 (HK2), an enzyme necessary for aerobic glycolysis, was observed. Despite photoreceptors are generally able to produce energy by oxidative phosphorylation (OXPHOS), they preferentially metabolize glucose by aerobic glycolysis, an effect known as the “Warburg effect” (Warburg, 1956; Ng et al., 2015). Previous studies have shown that loss of HK2 and thus impairment of aerobic glycolysis led to photoreceptor death (Petit et al., 2018). In addition to HK2, *Cnga1*^{MUT}

mice also showed decreased expression of pyruvate kinase isoform M2 (PKM2, Table 9), another glycolytic enzyme whose knockout leads to a profound retinal phenotype (Chinchore et al., 2017). Furthermore, a slight upregulation of hexokinase 1 (HK1) was detected in the *Cnga1*^{MUT} mouse model, which is consistent with previous findings that loss of HK2 is often followed by a compensatory upregulation of HK1 (Weh et al., 2020; Zhang et al., 2020). Additional hints for retinal metabolic remodeling were found by the upregulation of oxoglutarate dehydrogenase (OGDH; Table 9), a mitochondrial enzyme involved in the TCA cycle. Moreover, decreased levels of mitochondrial glutathione reductase (GSR; Table 9) indicate limited antioxidant activity and thus mitochondrial dysfunction (Figure 28).
In summary, these data suggest a metabolic shift from aerobic glycolysis to mitochondrial OXPHOS in animal models of RP, thereby leading to mitochondrial dysfunction.

Table 9. Proteins being involved in mitochondrial metabolism and function are altered in animal models of RP. P values and differences of specific proteins altered in *Cnga1*^{MUT} mice at PM1 and PM6, and *Pde6a*$^{-/-}$ dogs (PM39) over age-matched wild type control animals. Data was assessed via proteomics analysis. n/d = not detected; n/a = not altered. N = 3.

Protein	*Cnga1*^{MUT} Mice PM1		*Cnga1*^{MUT} Mice PM6		*Pde6a*$^{-/-}$ Dogs	
	Pval	Difference	Pval	Difference	Pval	Difference
HK1	4,45E-02	0,355	4,04E-02	0,396	n/d	n/d
HK2	7,85E-02	-2,352	5,89E-02	-2,436	2,67E-04	-5,286
PMK2	7,38E-02	-0,584	4,91E-04	-1,288	n/d	n/d
OGDH	n/d	n/d	7,36E-04	4,337	n/d	n/d
GSR	n/a	n/a	1,65E-02	-0,377	2,23E-03	-1,396

4.2.1.3 Recruitment and Activation of Immune Cells Contributes to Photoreceptor Death in Animal Models of RP

As already mentioned above, RP is often accompanied by retinal infiltration of activated microglia and blood-derived macrophages, as well as Müller cell gliosis before and during early stages of rod photoreceptor degeneration (Newton and Megaw, 2020). Such phenomena were also observed in *Cnga1*^{MUT} mice (Figure 22). This was corroborated by the IPA results from the proteomic analysis of retinal protein lysates of *Cnga1*^{MUT} mice and *Pde6a*$^{-/-}$ dogs (Figure 29).

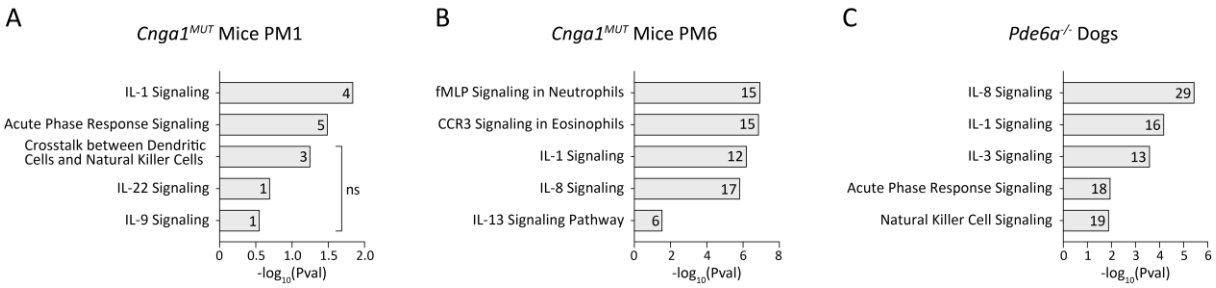

Figure 29. RP activates immunological pathways in different animal models. Altered immunological pathways in *Cnga1*^{MUT} mice at PM1 (A) and PM6 (B), and *Pde6a*$^{-/-}$ dogs (PM39; C) over age-matched wild type control animals revealed by ingenuity canonical pathway analysis of DEPs. The number in the bar indicates the number of altered proteins in the pathway. ns = not significant. N = 3.

Activation of the immune system was apparent in *Cnga1*^{MUT} mice already at PM1 (Figure 29A-B), as well as in the *Pde6a*$^{-/-}$ dog model (Figure 29C). This was indicated by upregulation of proteins involved in pathways like acute phase response signaling, interleukin (IL)-1 signaling or natural killer cell signaling. Pathological activation of microglia was shown to contribute to photoreceptor death in other degeneration models (Zhao et al., 2015; Gupta et al., 2018), and these results suggest that this is also the case in the animal models of RP analyzed in this study.

4.2.2 Synaptic Changes in Response to RP

Synaptogenesis demonstrated by neurite outgrowth into the outer retina as a response to photoreceptor impairment was previously shown in several studies (Claes et al., 2004; Hüttl et al., 2005; Michalakis et al., 2013). In order to investigate neuronal sprouting processes as a reaction of secondary neurons in response to RP, immunohistochemistry and proteomics analysis were performed with retinal samples from *Cnga1*^{MUT} mice.

First, retinal cross sections were labeled with antibodies against calbindin, protein kinase C alpha (PKCα), and Purkinje cell protein 2 (PCP2) (Figure 30). Calbindin is normally localized in horizontal cells and amacrine cells in the OPL and IPL as detected in wild type mice (Figure 30A). While these structures also appeared normal in *Cnga1*^{MUT} mice at PM1 (Figure 30B), some sporadic outgrowth of horizontal cells was observed at PM6 (Figure 30C, arrowheads), i.e., just at the point of beginning cone degeneration. However, cell numbers in the OPL seemed to be decreased at PM6 resulting in a reduced thickness of the OPL. Thus, the observed outgrowth-like processes could also arise from horizontal cells trying to fit into a thinner OPL. Similar sprouting-like processes were detected by labeling of PKCα (Figure 30F),

that is abundant in rod bipolar cells, and PCP2 (Figure 30I), which is expressed in ON-bipolar cells. Remarkably, despite showing roughly wild type-like morphology at PM1 (Figure 30E, H), numbers of bipolar synaptic end feet were apparently reduced compared to wild type mice (Figure 30D, G). Moreover, this reduction of synaptic end feet increased until PM6 (Figure 30F, I), indicating synaptic degeneration.

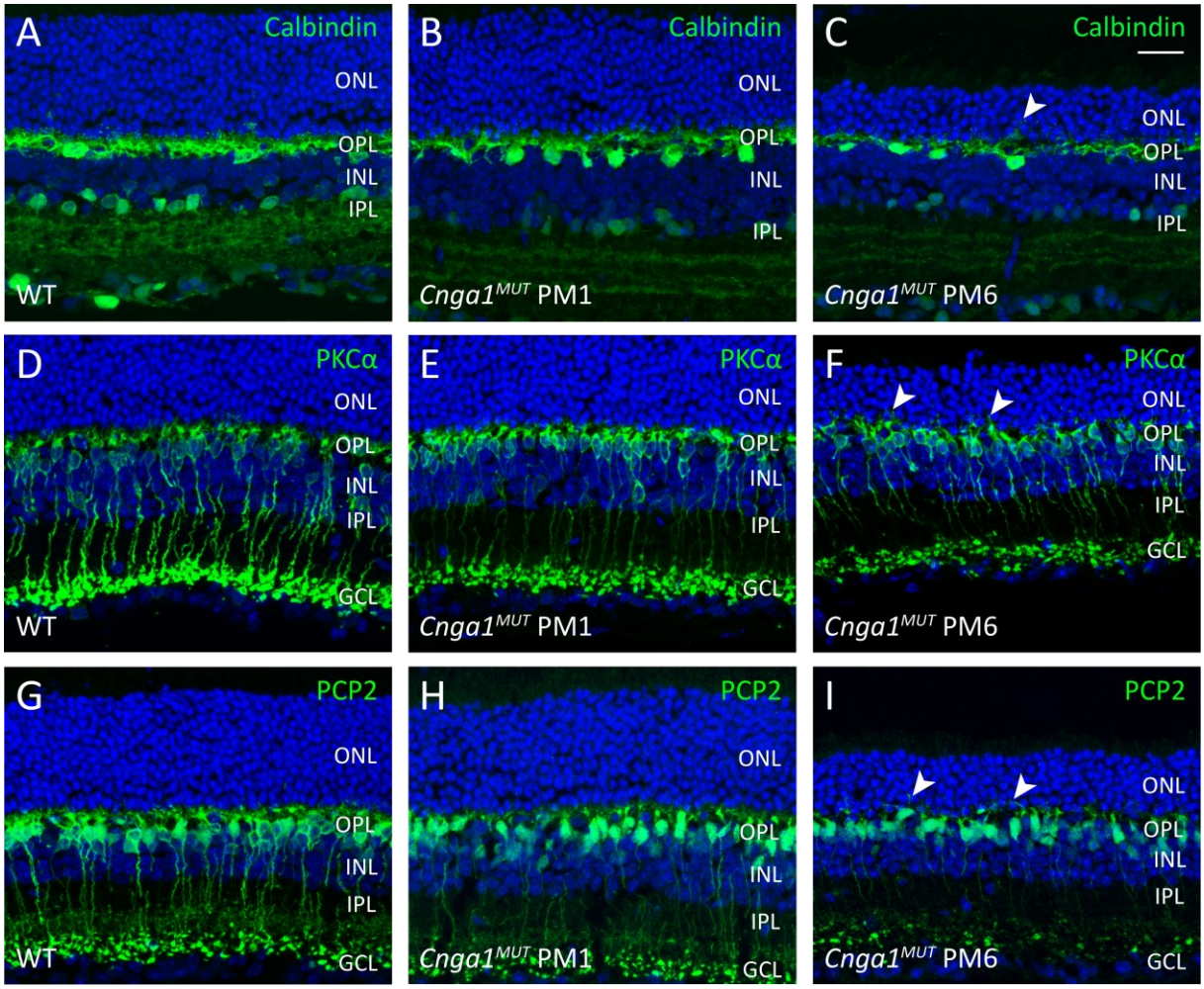

Figure 30. Mutation in *Cnga1* accompanies with degeneration of synaptic end feet. Representative confocal images showing expression of calbindin (green; A-C), PKCα (green; D-F) or PCP2 (green; G-I) in retinal cross-sections of wild type (WT; A, D, G) and *Cnga1*^{MUT} mouse retinas at PM1 (B, E, H) and PM6 (C, F, I). Cell nuclei were stained with DAPI (blue). Arrowheads indicate signs of neuronal outgrowth into the ONL. ONL, outer nuclear layer; OPL, outer plexiform layer; INL, inner nuclear layer; IPL, inner plexiform layer; GCL, ganglion cell layer. Scale bar marks 20 µm.

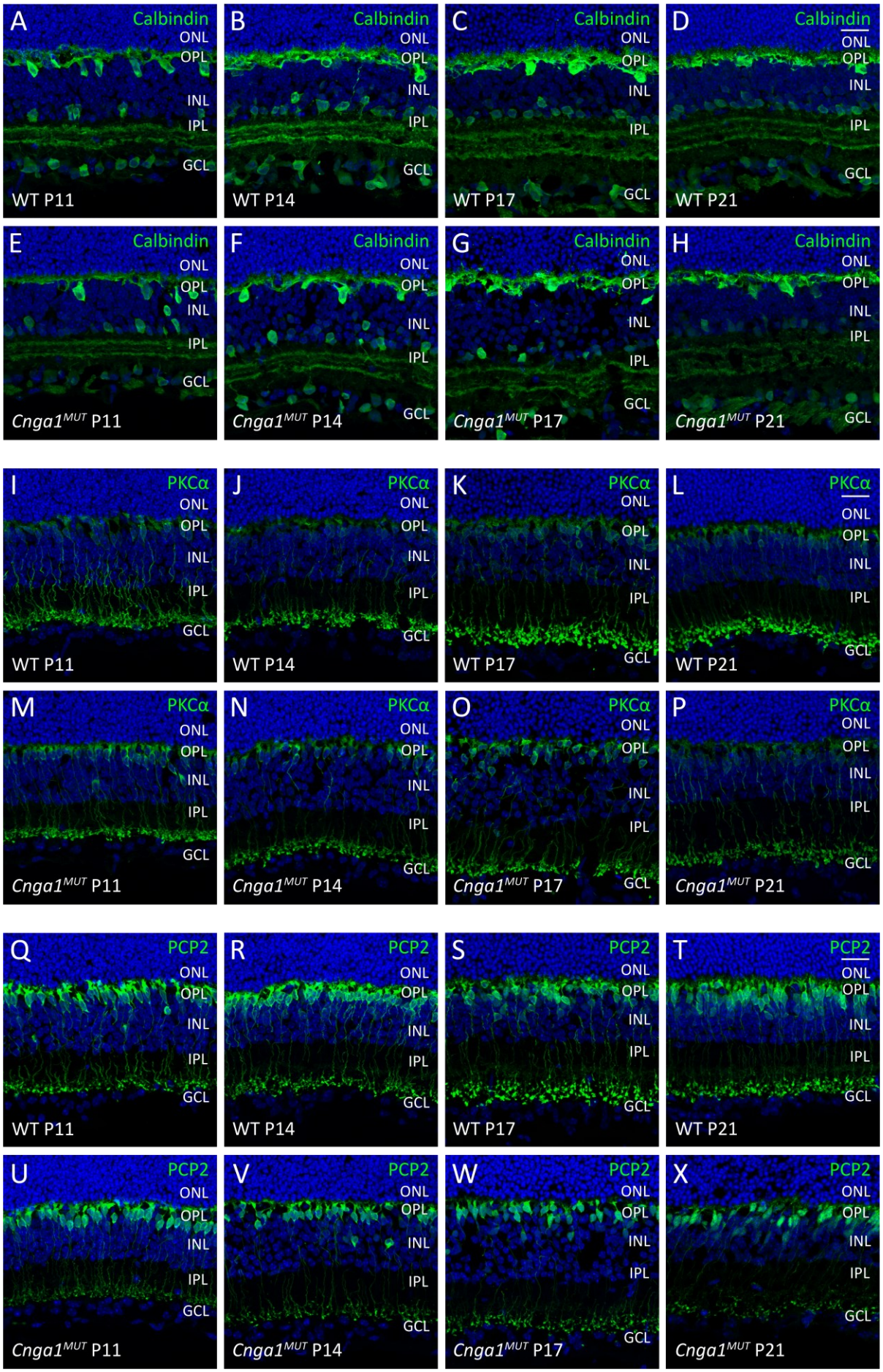
A
Calbindin
ONL
OPL
INL
IPL
GCL
WT P11
B
Calbindin
ONL
OPL
INL
IPL
GCL
WT P14
C
Calbindin
ONL
OPL
INL
IPL
GCL
WT P17
D
Calbindin
ONL
OPL
INL
IPL
GCL
WT P21
E
Calbindin
ONL
OPL
INL
IPL
GCL
Cnga1MUT P11
F
Calbindin
ONL
OPL
INL
IPL
GCL
Cnga1MUT P14
G
Calbindin
ONL
OPL
INL
IPL
GCL
Cnga1MUT P17
H
Calbindin
ONL
OPL
INL
IPL
GCL
Cnga1MUT P21
I
PKCα
ONL
OPL
INL
IPL
GCL
WT P11
J
PKCα
ONL
OPL
INL
IPL
GCL
WT P14
K
PKCα
ONL
OPL
INL
IPL
GCL
WT P17
L
PKCα
ONL
OPL
INL
IPL
GCL
WT P21
M
PKCα
ONL
OPL
INL
IPL
GCL
Cnga1MUT P11
N
PKCα
ONL
OPL
INL
IPL
GCL
Cnga1MUT P14
O
PKCα
ONL
OPL
INL
IPL
GCL
Cnga1MUT P17
P
PKCα
ONL
OPL
INL
IPL
GCL
Cnga1MUT P21
Q
PCP2
ONL
OPL
INL
IPL
GCL
WT P11
R
PCP2
ONL
OPL
INL
IPL
GCL
WT P14
S
PCP2
ONL
OPL
INL
IPL
GCL
WT P17
T
PCP2
ONL
OPL
INL
IPL
GCL
WT P21
U
PCP2
ONL
OPL
INL
IPL
GCL
Cnga1MUT P11
V
PCP2
ONL
OPL
INL
IPL
GCL
Cnga1MUT P14
W
PCP2
ONL
OPL
INL
IPL
GCL
Cnga1MUT P17
X
PCP2
ONL
OPL
INL
IPL
GCL
Cnga1MUT P21

Figure 31. Neurites do not outgrow in young *Cnga1*^{MUT} mice. Representative confocal images showing expression of calbindin (green; A-H), PKCα (green; I-P) or PCP2 (green; Q-X) in retinal cross-sections of wild type (WT) and *Cnga1*^{MUT} mouse retinas at P11, P14, P17, and P21. Cell nuclei were stained with DAPI (blue). ONL, outer nuclear layer; OPL, outer plexiform layer; INL, inner nuclear layer; IPL, inner plexiform layer; GCL, ganglion cell layer. Scale bars mark 20 µm.

To further investigate whether neuronal sprouting processes may occur even earlier as a response to primary rod photoreceptor degeneration, *Cnga1*^{MUT} and wild type control retinas at the early ages of P11, P14, P17, and P21 were also immunolabeled for calbindin, PKCα, and PCP2 (Figure 31). Interestingly, no neurite outgrowth was observed in young *Cnga1*^{MUT} mice. Moreover, reduction of synaptic end feet was detected already starting from P17 (Figure 31O, W).

In the next step, retinal protein lysates from *Cnga1*^{MUT} and corresponding wild type mice at PM1 and PM6 were used for proteomics analysis. DEPs were determined and IPA was carried out in order to investigate the proteomic changes underlying synapse formation and degeneration. IPA identified 17 dysregulated biological functions at PM1 and 16 at PM6, that are related to axon or neurite growth and development (Table 10). Strikingly, at PM1 biological functions related to neurite sprouting, such as “outgrowth of neurites” and “branching of neurons”, were decreased in *Cnga1*^{MUT} mice compared to respective wild type control animals. Moreover, biological functions related to neuronal cell death were increased, indicating retraction and degeneration of neurites in response to CNGA1 ablation. Interestingly, these processes seemed to be reversed at PM6, when cone degeneration starts: Biological functions related to neurite sprouting were increased, while cell death functions were decreased (Table 10). These findings are in consistence with slight neuronal sprouting, as observed by immunohistochemistry in *Cnga1*^{MUT} mice at PM6.

In summary, these data indicate an early retraction of rod neurites followed by neuronal degeneration, but also neurite sprouting as a response to beginning cone degeneration at later time points.

Table 10. Biological functions related to neurite outgrowth and synapse formation in *Cnga1*^{MUT} mice. Predicted activation state identified by z-scores, counts of altered proteins involved in the respective function, and p values of specific proteins altered in *Cnga1*^{MUT} mice at PM1 and PM6 over age-matched wild type control animals. Data was assessed via proteomics analysis and IPA. N = 3.

Biological Function	Predicted Activation State	Count	Pval
PM1			
Growth of neurites	Decreased	21	6,13E-06
Outgrowth of neurites	Decreased	18	1,12E-05
Growth of axons	Decreased	10	1,56E-04
Outgrowth of axons	Decreased	7	2,36E-04
Dendritic growth/branching	Decreased	12	4,37E-04
Branching of neurons	Decreased	14	4,42E-04
Morphogenesis of neurons	Decreased	21	6,12E-04
Development of neurons	Decreased	25	8,19E-04
Sprouting	Decreased	16	8,59E-04
Branching of neurites	Decreased	13	1,06E-03
Synaptic transmission	Decreased	13	1,57E-03
Neurotransmission	Decreased	14	4,03E-03
Density of neurons	Decreased	7	4,36E-03
Neuronal cell death	Increased	27	9,02E-05
Apoptosis of neurons	Increased	14	5,56E-03
Degeneration of neurons	Increased	9	9,10E-03
Degeneration of neurons	Increased	9	9,10E-03
PM6			
Quantity of neurons	Increased	39	1,15E-08
Growth of neurites	Increased	38	8,05E-08
Development of neurons	Increased	56	1,15E-07
Proliferation of neuronal cells	Increased	42	1,20E-07
Neuritogenesis	Increased	46	1,29E-07
Outgrowth of neurons	Increased	33	1,44E-07
Outgrowth of neurites	Increased	32	2,71E-07
Growth of axons	Increased	18	3,84E-06
Branching of neurons	Increased	27	6,73E-06
Developmental process of synapse	Increased	19	1,39E-05
Density of neurons	Increased	15	2,92E-05
Neurotransmission	Decreased	47	4,59E-14
Synaptic transmission	Decreased	39	2,49E-12
Neuronal cell death	Decreased	63	4,93E-11
Synaptic transmission of cells	Decreased	12	4,65E-07
Degeneration of neurons	Decreased	22	6,74E-06

4.2.3 Rescue of the *PDE6A*-linked Retinal Phenotype of RP by Ablation of CNG Channels

Recent studies, in which the additional ablation of CNG channels in *Pde6b*- and *Pde6g*-deficient mice resulted in morphological rescue of rod photoreceptors, attributed a key role in photoreceptor degeneration to CNG channels (Paquet-Durand et al., 2011; Wang et al., 2017). In order to further investigate the role of CNG channels in RP, the following two double-mutant (DBM) *Pde6a*^{MUT}*xCngb1*$^{-/-}$ mouse models (hereafter referred to as DBM *Pde6a*^{MUT} mice) were analyzed by immunohistochemical methods: *Pde6a*^{V685M}*xCngb1*$^{-/-}$ (V685M DBM) and *Pde6a*^{R562W}*xCngb1*$^{-/-}$ (R562W DBM), whose corresponding single-mutant (SM) animal models are both characterized by a fast-progressing RP phenotype.

4.2.3.1 Ablation of CNG Channels Preserves Retinal Morphology in DBM *Pde6a*^{MUT} Mice

To confirm additional CNGB1 deletion in *Pde6a*^{MUT} DBMs, immunolabeling of CNGB1 protein was carried out (Figure 32). Wild type rod OS showed strong expression of CNGB1 protein (Figure 32A), whereas no CNGB1 was found in SM *Cngb1*$^{-/-}$ mice at PM1 (Figure 32D). Due to progressed photoreceptor degeneration and consequent loss of photoreceptor OS, also no CNGB1 was detected in both SM *Pde6a*^{MUT} mouse models (Figure 32B-C). Moreover, despite a clearly visible rescue of photoreceptor cells, no CNGB1 protein was expressed in *Pde6a*^{MUT} DBMs (Figure 32E-F), confirming the additional knockout of the *Cngb1* gene.

To assess PDE6A expression in the DBM *Pde6a*^{MUT} mouse models, immunolabeling with an antibody against PDE6A was performed (Figure 33). While there was robust PDE6A expression in rod OS of wild type retinas (PM1; Figure 33A), no PDE6a was detected in both SM *Pde6a*^{MUT} mouse retinas (Figure 33B-C). In contrast, SM *Cngb1*$^{-/-}$ mice at PM1 showed clear PDE6A expression (Figure 33D), although less than in wild type mice owing to shortened rod OS. Consistent with the SM *Pde6a*^{MUT} mouse retinas, no PDE6A protein was found in the V685M DBM at PM1, PM3 and PM6 (Figure 33E-G), while faint expression was detected in rod OS and IS of the R562W DMB at PM1 (Figure 33H) that decreased over time (Figure 33I-J). This spare expression can be attributed to a residual PDE6 activity of 10% in the R562W mutant (Sothilingam et al., 2015). However, remarkably, DBMs of both *Pde6a*^{MUT} showed pronounced rescue of the ONL compared to their respective SMs. While in R562W SM at PM1, only ~15 % of the ONL were left compared to wild type (Figure 33C), additional ablation of *Cngb1* in R562W DBMs caused a 6-fold rescue to about 85 % of wild type ONL (Figure 33H).

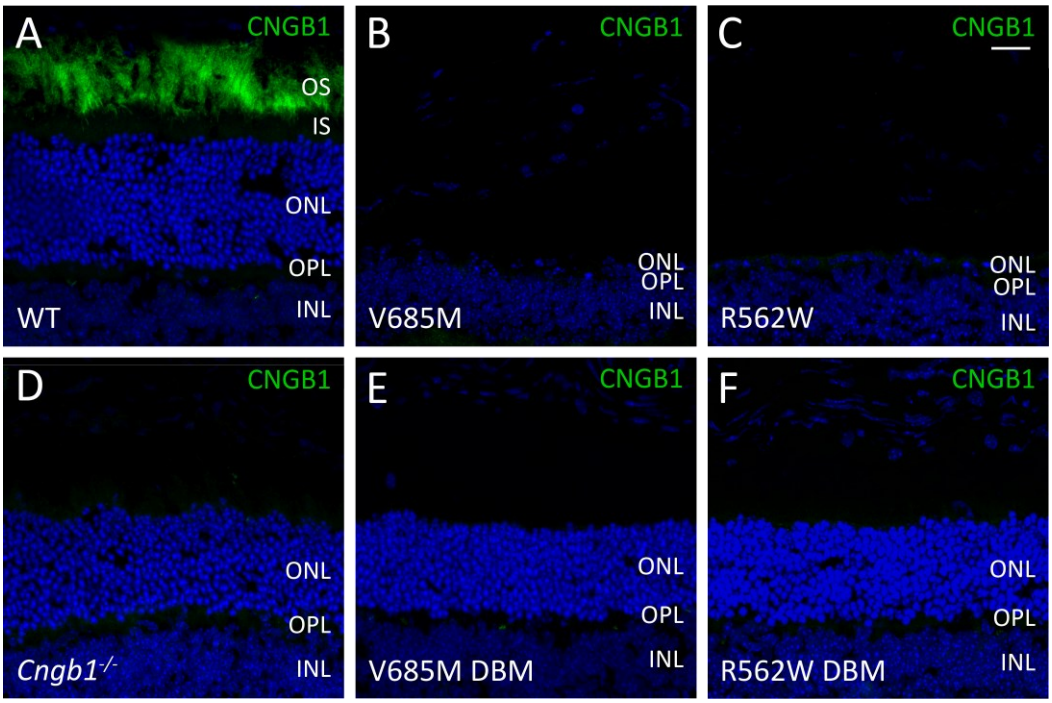

Figure 32. Double-mutant *Pde6a*^{MUT} mice do not express CNGB1. Representative confocal images showing expression of CNGB1 (green) in retinal cross-sections of wild type (WT; A), single-mutant *Pde6a*^{V685M} (V685M; B), single-mutant *Pde6a*^{R562W} (R562W; C), and single-mutant *Cngb1*$^{-/-}$ (D) mouse retinas, as well as in double-mutant *Pde6a*^{V685M}*xCngb1*$^{-/-}$ (V685M DBM; E) and *Pde6a*^{R562W}*xCngb1*$^{-/-}$ (R562W DBM; F) mouse retinas at PM1. Cell nuclei were stained with DAPI (blue). OS, outer segments; IS, inner segments; ONL, outer nuclear layer; OPL, outer plexiform layer; INL, inner plexiform layer. Scale bar marks 20 µm.

Although ongoing degeneration led to further reduction of the ONL, a 5-fold rescue was still observed at PM3 (Figure 33I). At PM6, a similar thickness to that of the corresponding SM at PM1 was reached (Figure 33J), demonstrating a 6-months deceleration of degeneration in R562W DBM compared to SM. An even higher rescue was observed in the V685M DBM. While the ONL of V685M SM was reduced to ~2 % compared to wild type (Figure 33B), almost 90 % were still present in V685M DBM at PM1 (Figure 33E), corresponding to a 40-fold rescue. At PM3, still a 25-fold rescue was observed (Figure 33F), which continued to decrease until PM6 but still resulted in an ONL thickness of 30 % of the wild type (15-fold rescue compared to V685M SM; Figure 33G). These data demonstrate a striking deceleration of degeneration by additional *Cngb1* deletion in both DBM *Pde6a*^{MUT} mouse models.

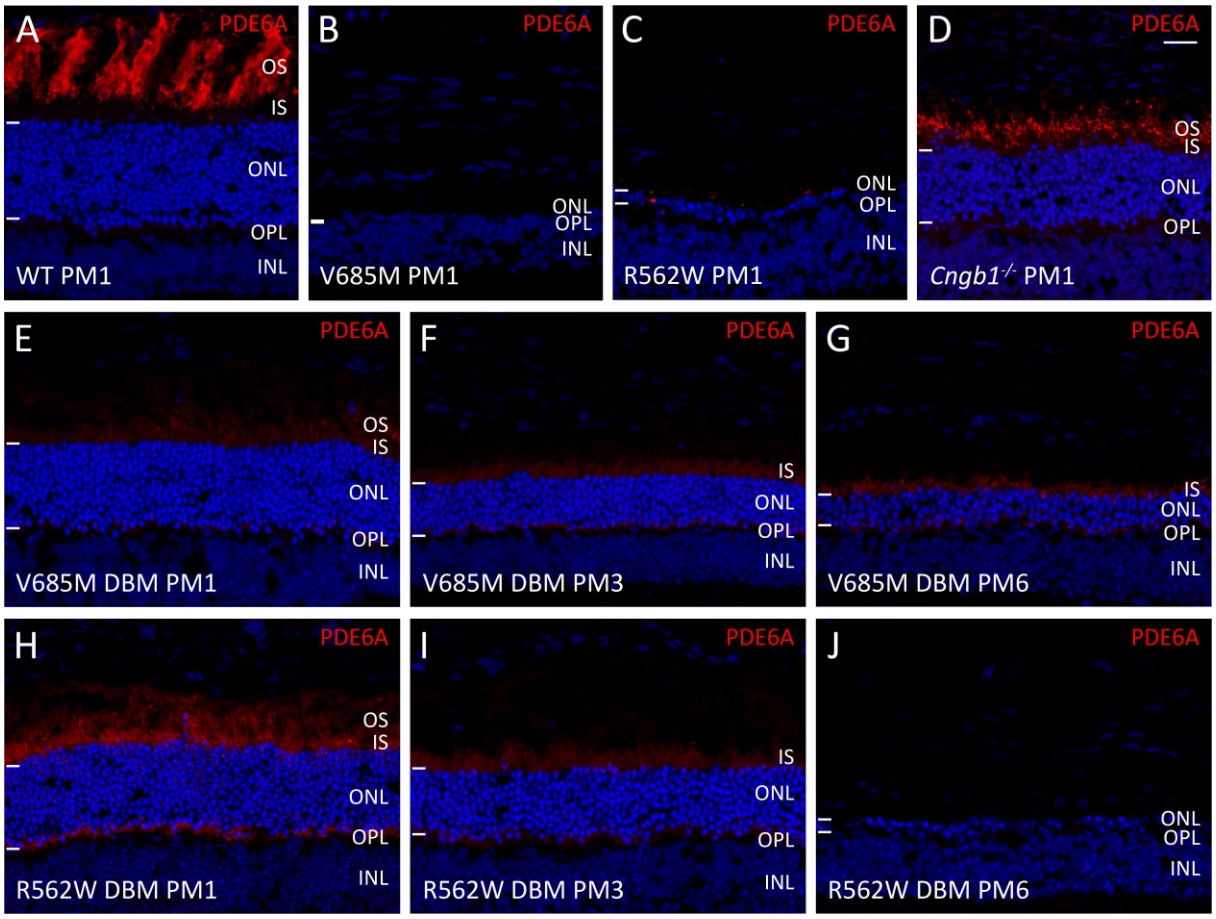

Figure 33. CNG channel ablation leads to photoreceptor rescue in double-mutant *Pde6a^{MUT}* mice. Representative confocal images showing expression of PDE6A (red) in retinal cross-sections of wild type (WT; A), single-mutant *Pde6a^{V685M}* (V685M; B), single-mutant *Pde6a^{R562W}* (R562W; C), and single-mutant *Cngb1$^{-/-}$* (D) mouse retinas at PM1, as well as in double-mutant *Pde6a^{V685M}xCngb1$^{-/-}$* (V685M DBM; E-G) and *Pde6a^{R562W}xCngb1$^{-/-}$* (R562W DBM; H-J) mouse retinas at PM1, PM3 and PM6. The edges of the ONL are marked with horizontal bars. Cell nuclei were stained with DAPI (blue). OS, outer segments; IS, inner segments; ONL, outer nuclear layer; OPL, outer plexiform layer; INL, inner plexiform layer. Scale bar marks 20 µm.

In the next step, rod (Figure 34) and cone (Figure 35) photoreceptor morphology was analyzed to further assess preservation of photoreceptor cells in DBM *Pde6a^{MUT}* mice. Wild type mice correctly formed rod OS, which were labeled by an antibody against the rod-specific photosensitive pigment rhodopsin (Figure 34A). No rod OS were found in SM *Pde6a^{MUT}* mouse retinas (Figure 34B-C), while they were clearly shortened but still present in SM *Cngb1$^{-/-}$* mice (Figure 34D). Notably, in both DBM *Pde6a^{MUT}* mouse models, wild type-like rhodopsin expression was detected at PM1 (Figure 34E, H), confirming proper formation of rod OS. Moreover, rod morphology was still preserved at PM3 although rod OS shortening had already

started in V685M DBM mice (Figure 34F, I). Consistent with the reduction of the ONL, rod OS were lost at PM6 in both DBM *Pde6a*^{MUT} mouse models (Figure 34G, J).

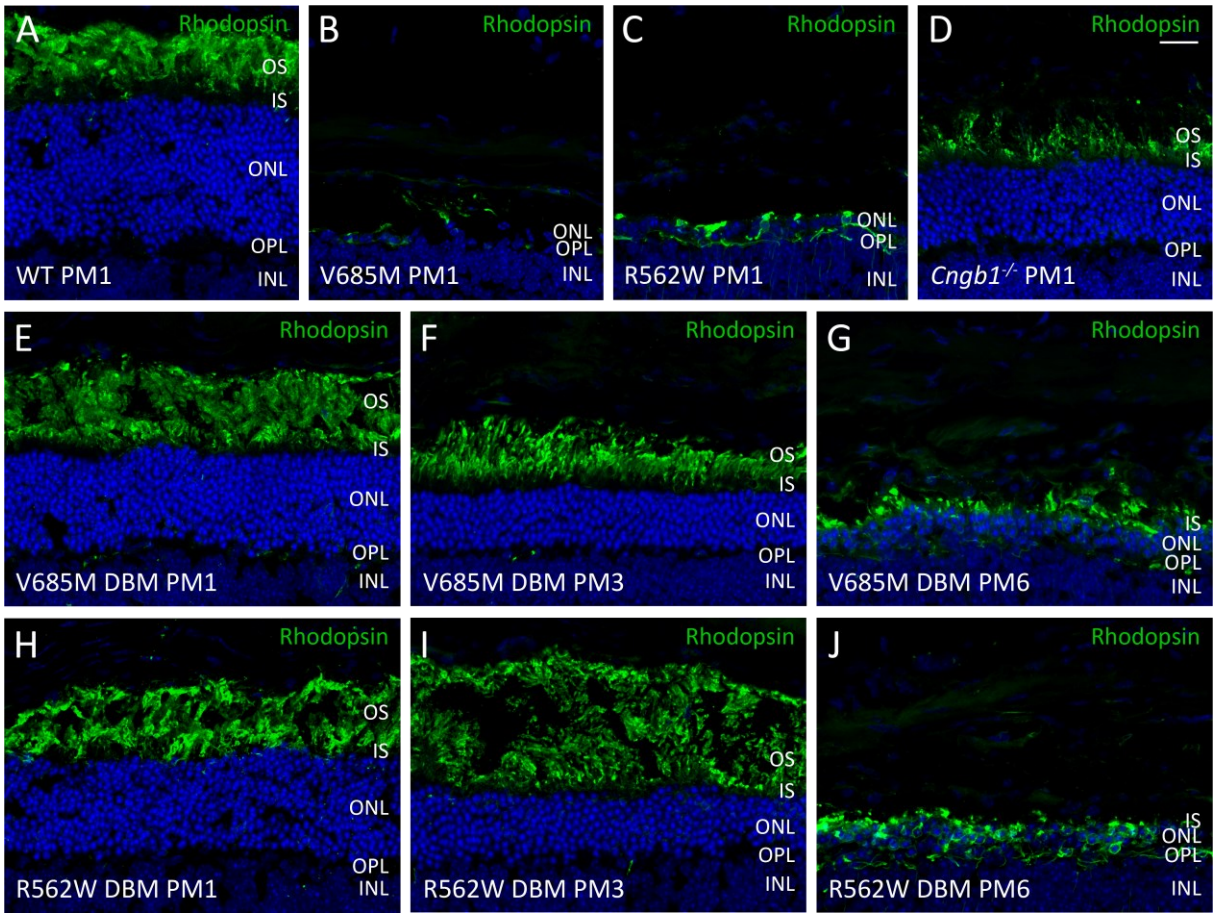

Figure 34. Rod photoreceptor morphology is preserved in double-mutant *Pde6a*^{MUT} mice. Representative confocal images showing expression of rhodopsin (green) in retinal cross-sections of wild type (WT; A), single-mutant *Pde6a*^{V685M} (V685M; B), single-mutant *Pde6a*^{R562W} (R562W; C), and single-mutant *Cngb1*$^{-/-}$ (D) mouse retinas at PM1, as well as in double-mutant *Pde6a*^{V685M}*xCngb1*$^{-/-}$ (V685M DBM; E-G) and *Pde6a*^{R562W}*xCngb1*$^{-/-}$ (R562W DBM; H-J) mouse retinas at PM1, PM3 and PM6. Cell nuclei were stained with DAPI (blue). OS, outer segments; IS, inner segments; ONL, outer nuclear layer; OPL, outer plexiform layer; INL, inner plexiform layer. Scale bar marks 20 µm.

Furthermore, also a rescue of cone photoreceptors was observed in DBM *Pde6a*^{MUT} mice (Figure 35). Additional knockout of *Cngb1* in V685M mice resulted in wild type-like cone morphology with properly positioned cell bodies and synapses at PM1 and PM3, although at the latter, cone axons seemed to have adjusted their length to fit in the thinner ONL (Figure 35E-F). Additionally, a rescue of cones was still visible at PM6 (Figure 35G) compared to its corresponding single-mutant, in which cones were completely lost already at PM1 (Figure

35B). Despite cones had already started to collapse at this time point, they still might be functional as previously seen in *Cngb1*- (Hüttl et al., 2005) and *Cnga1*-deficient mouse models. Apart from this, also R562W DBM mice benefitted from additional *Cngb1* deletion. Similar to V685M DBM mice, wild type-like morphology was also observed in this mutant at PM1 and PM3 (Figure 35H-I). At PM6, cones showed similar morphology to the corresponding PM1 single-mutant (Figure 35C, J), indicating less rescue in R562W DBM mice than in V685M DBM mice derived from the more severe SM phenotype.

In summary, additional ablation of *Cngb1* in *Pde6a*^{MUT} DBM mice caused deceleration of photoreceptor degeneration, as well as preservation of rod and cone morphology.

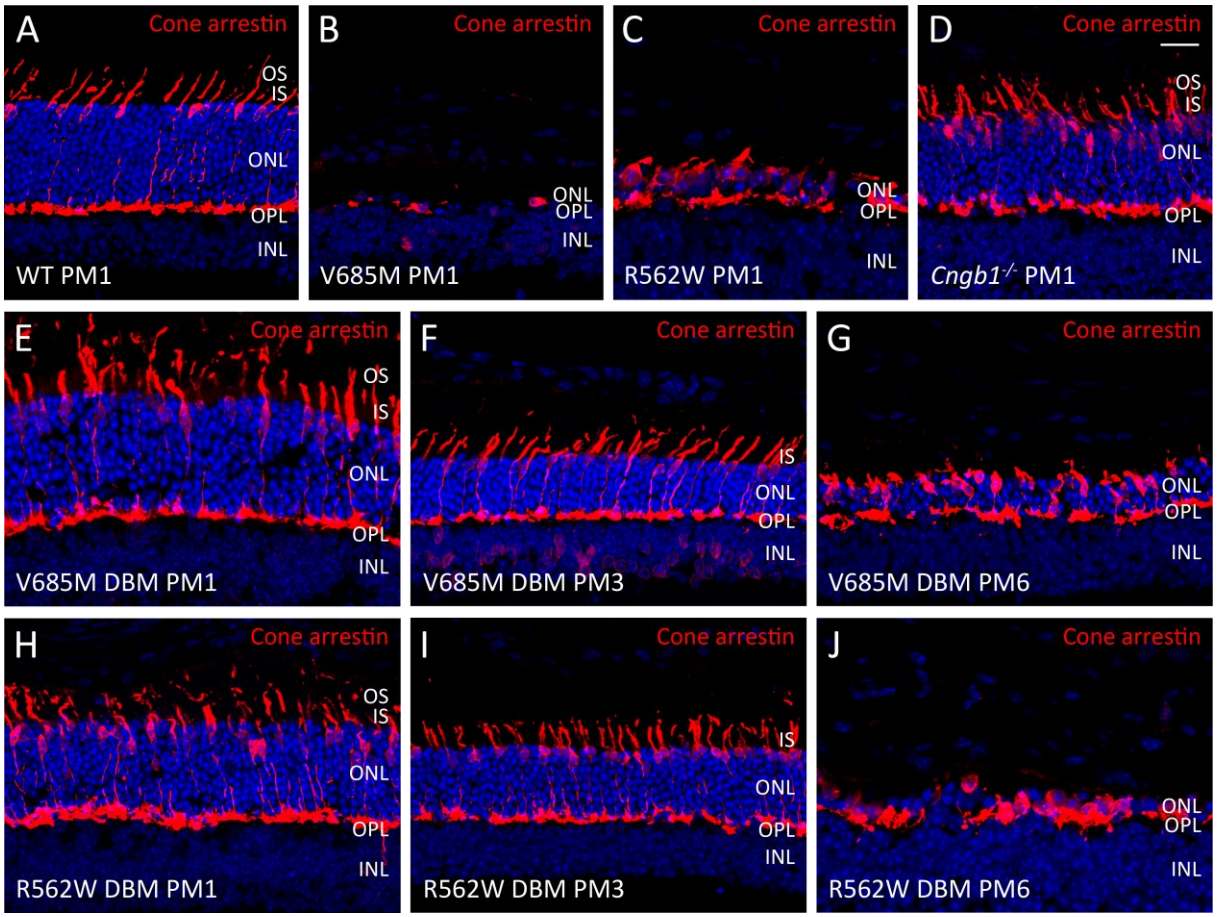

Figure 35. *Cngb1* deletion rescues cone photoreceptor morphology in double-mutant *Pde6a*^{MUT} mice. Representative confocal images showing expression of cone arrestin (red) in retinal cross-sections of wild type (WT; A), single-mutant *Pde6a*^{V685M} (V685M; B), single-mutant *Pde6a*^{R562W} (R562W; C), and single-mutant *Cngb1*$^{-/-}$ (D) mouse retinas at PM1, as well as in double-mutant *Pde6a*^{V685M}*xCngb1*$^{-/-}$ (V685M DBM; E-G) and *Pde6a*^{R562W}*xCngb1*$^{-/-}$ (R562W DBM; H-J) mouse retinas at PM1, PM3 and PM6. Cell nuclei were stained with DAPI (blue). OS, outer segments; IS, inner segments; ONL, outer nuclear layer; OPL, outer plexiform layer; INL, inner plexiform layer. Scale bar marks 20 µm.

4.2.3.2 CNG Channel Ablation Normalizes Extensive cGMP Levels in DBM *Pde6a*^{MUT} Mice

In both *Pde6a*^{MUT} SM mouse models, it was shown that absence of PDE6A correlated with strong accumulation of the second messenger cGMP (Sothilingam et al., 2015). Additional ablation of CNG channels has already been demonstrated to reduce cGMP accumulation in the *rd1* mouse model (Paquet-Durand et al., 2011).

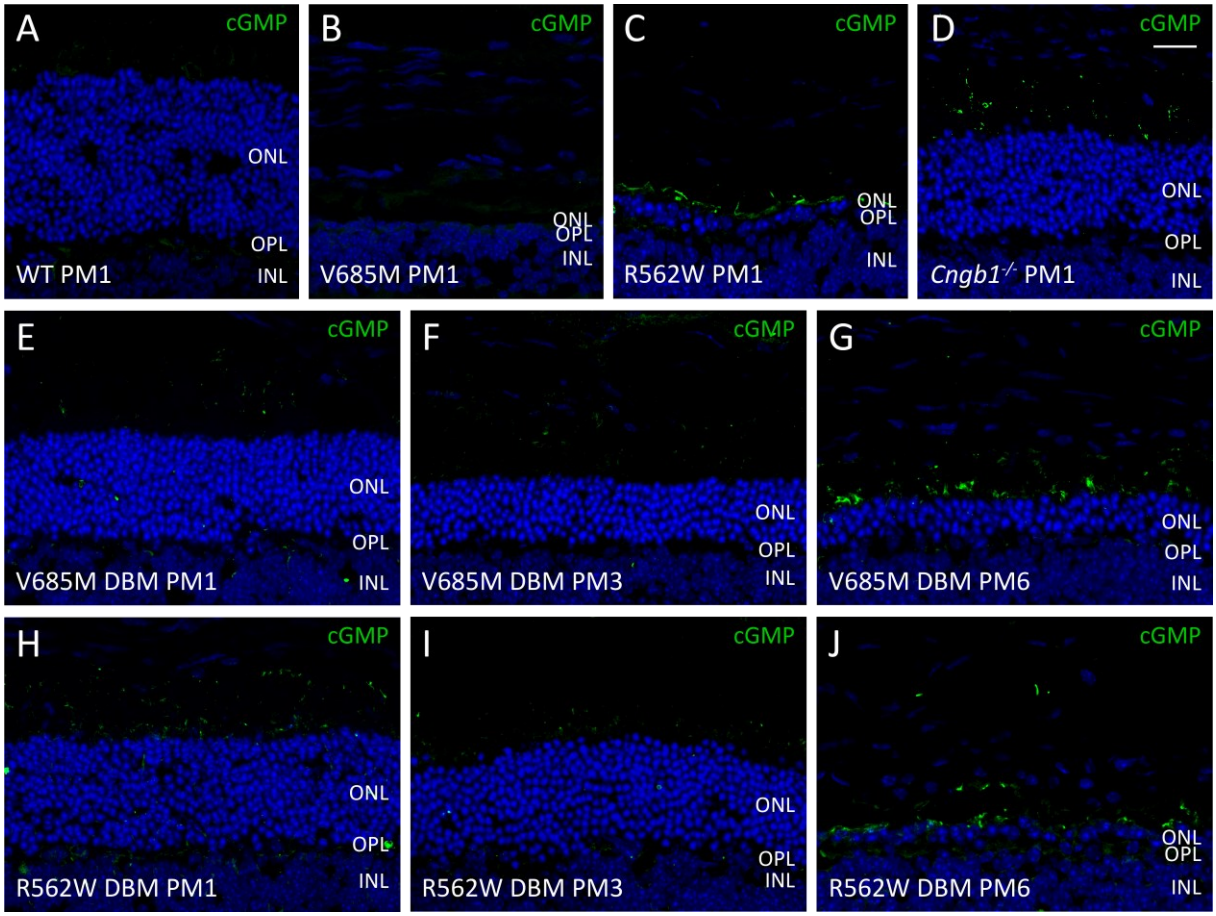

Figure 36. cGMP accumulation is reduced in double-mutant *Pde6a*^{MUT} mice. Representative confocal images showing paraformaldehyde-fixed cGMP (green) in retinal cross-sections of wild type (WT; A), single-mutant *Pde6a*^{V685M} (V685M; B), single-mutant *Pde6a*^{R562W} (R562W; C), and single-mutant *Cngb1*$^{-/-}$ (D) mouse retinas at PM1, as well as in double-mutant *Pde6a*^{V685M}*xCngb1*$^{-/-}$ (V685M DBM; E-G) and *Pde6a*^{R562W}*xCngb1*$^{-/-}$ (R562W DBM; H-J) mouse retinas at PM1, PM3 and PM6. Cell nuclei were stained with DAPI (blue). ONL, outer nuclear layer; OPL, outer plexiform layer; INL, inner plexiform layer. Scale bar marks 20 µm.

In order to investigate whether an additional knockout of *Cngb1* can also achieve reduction of cGMP in the DBM *Pde6a*^{MUT} mouse models, paraformaldehyde-fixed cGMP was immunolabeled in corresponding retinal cross-sections (Figure 36). Although high levels of cGMP accumulation were observed in V685M SM at P11 (Sothilingam et al., 2015), no cGMP

was detected at PM1 (Figure 36B), probably owing to the progressed retinal degeneration and no photoreceptor cells being left at this time point. R562W SM mice, however, still showed intense cGMP accumulation at PM1 (Figure 36C). Notably, despite an accumulation of cGMP was also observed in SM *Cngb1*$^{-/-}$ mice (Figure 36D), both V685M DBM and R562W DBM were characterized by a dominant reduction of cGMP levels at PM1 (Figure 36E, H) and PM3 (Figure 36F, I), comparable to that of wild type mice (Figure 36A). Consistent with the previous findings that photoreceptor degeneration is slowed down until PM6, increased cGMP accumulation was detected first at PM6 (Figure 36G, J), when degeneration reached an extent that was still lower (V685M) or comparable (R562W) to their respective single-mutants at PM1.

4.2.3.3 Additional *Cngb1* Deletion Decelerates Müller Cell Gliosis and Increases Photoreceptor Survival in DBM *Pde6a*^{MUT} Mice

Response to retinal stress can be noticed by upregulation of GFAP and development of intermediate fibers by Müller cells, as shown in several animal models suffering from RP (Ekstrom et al., 1988; Hüttl et al., 2005). To assess the effect of additional removal of CNG channels in DBM *Pde6a*^{MUT} mice on retinal stress responses, immunolabeling of GFAP was performed (Figure 37). Since both *Pde6a*^{MUT} SM mice and *Cngb1*$^{-/-}$ SM mice developed Müller cell gliosis (Figure 37B-C), thus it is not surprising that also *Pde6a*^{MUT} DBM mice showed intermediate fibers at all time points investigated (Figure 37E-J). However, despite prominent GFAP expression, Müller cell gliosis was reduced in both V685M DBM and R562W DBM mice compared to their respective single-mutant controls (Figure 37E-J). These results indicate deceleration of Müller cell gliosis in both *Pde6a*^{MUT} DBM mouse models.

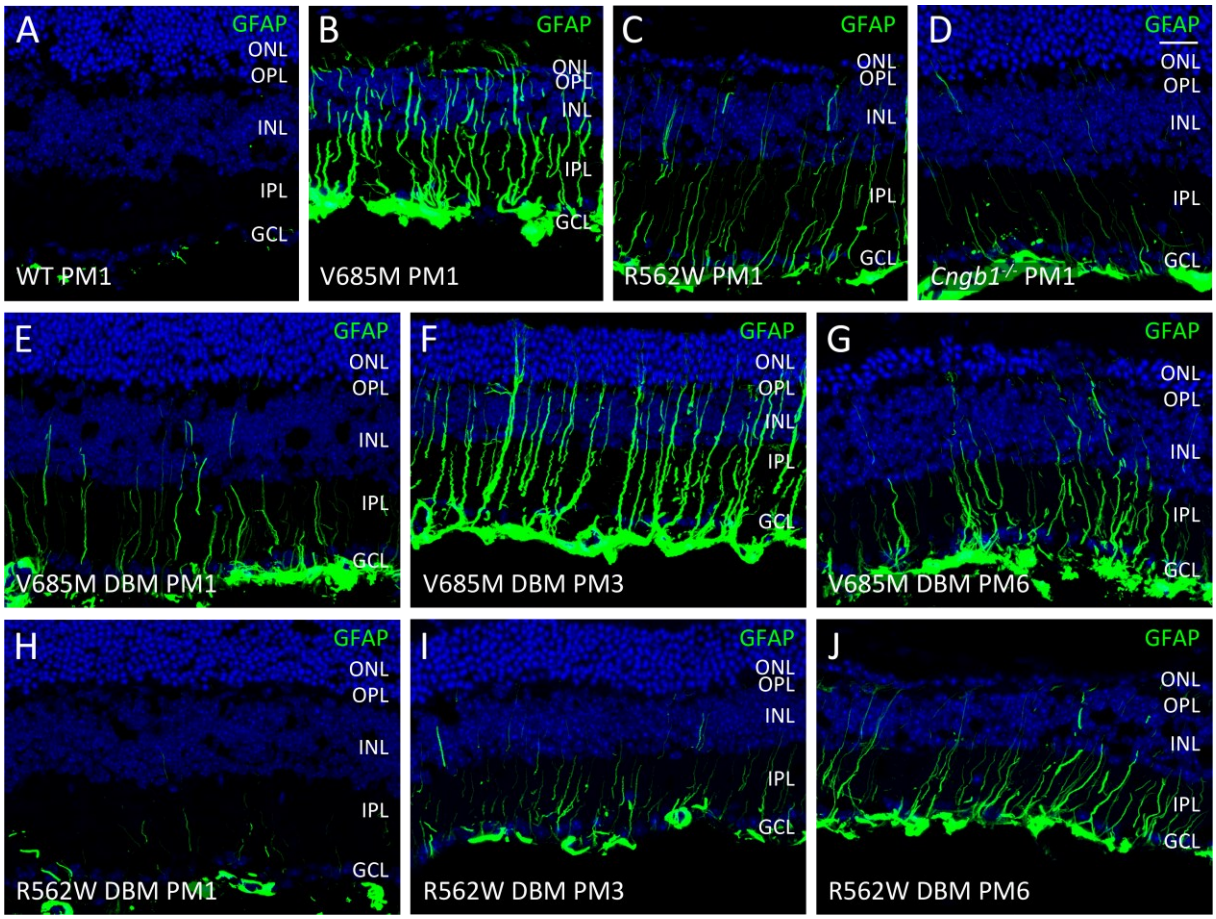

Figure 37. Double-mutant *Pde6a*^{MUT} mice show decelerated Müller cell gliosis. Representative confocal images showing expression of GFAP (green) in retinal cross-sections of wild type (WT; A), single-mutant *Pde6a*^{V685M} (V685M; B), single-mutant *Pde6a*^{R562W} (R562W; C), and single-mutant *Cngb1*$^{-/-}$ (D) mouse retinas at PM1, as well as in double-mutant *Pde6a*^{V685M}*xCngb1*$^{-/-}$ (V685M DBM; E-G) and *Pde6a*^{R562W}*xCngb1*$^{-/-}$ (R562W DBM; H-J) mouse retinas at PM1, PM3 and PM6. Cell nuclei were stained with DAPI (blue). OS, outer segments; IS, inner segments; ONL, outer nuclear layer; OPL, outer plexiform layer; INL, inner plexiform layer; IPL, inner plexiform layer; GCL, ganglion cell layer. Scale bar marks 20 µm.

To further assess photoreceptor cell death in the DBM *Pde6a*^{MUT} mice, immunolabeling of 5hmC was performed (Figure 38). At PM1, V685M and R562W DMB mice showed counts of 5hmC-positive cells that are similar to *Cngb1*$^{-/-}$ control mice (Figure 38D, E, H, K) but increased compared to their respective SM controls (Figure 38B-C, K). Characterization of single-mutant V685M and R562W mice revealed cell death peaking at P12 in V685M mice and at P15 in R562W mice, and declining afterwards (Sothilingam et al., 2015). Such a decrease was also observed in DBM *Pde6a*^{MUT} mice, with lower numbers of 5hmC-positive cells after PM1 (Figure 38F-G, I-J, L).

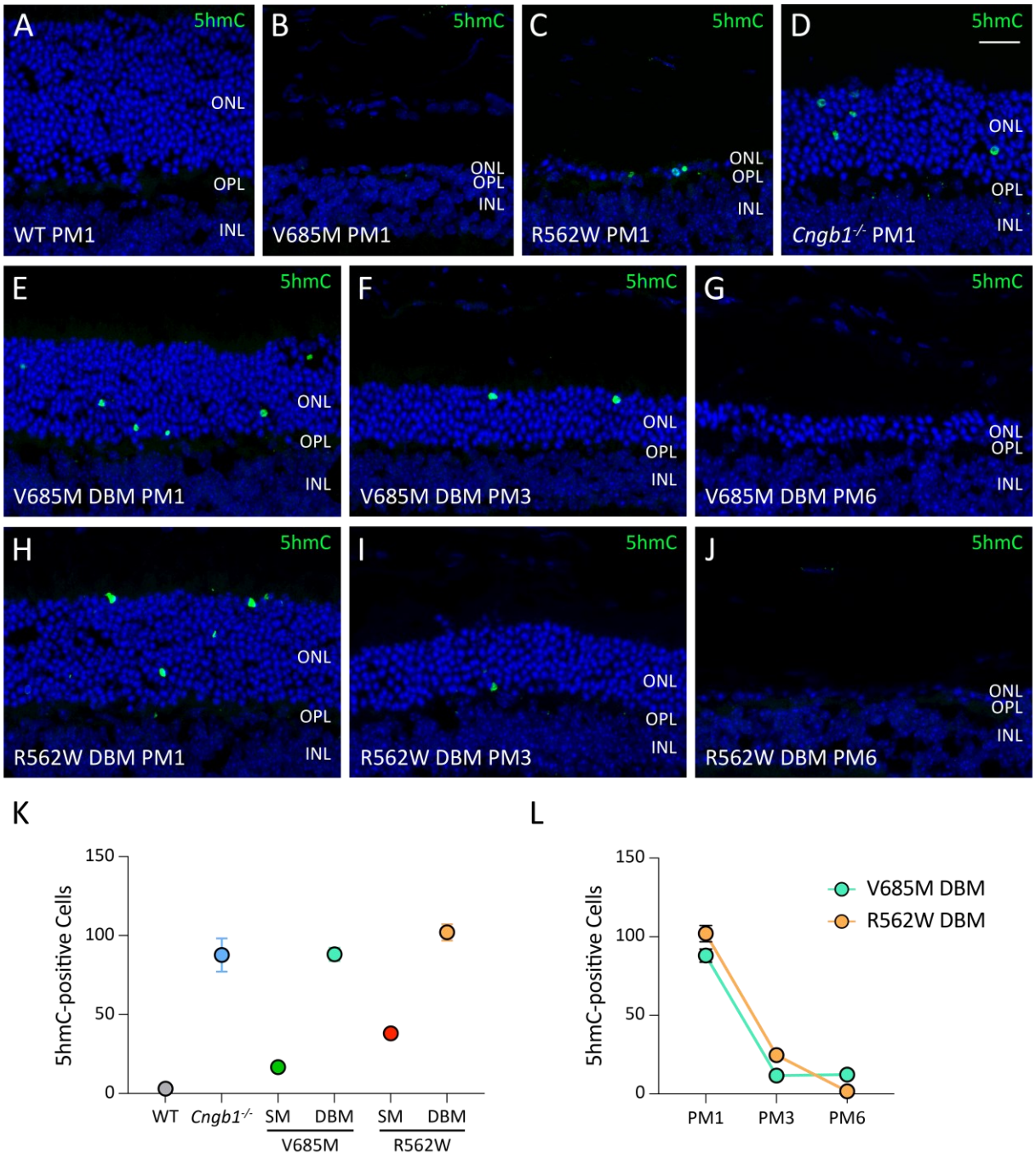

Figure 38. Photoreceptor cell death is delayed in double-mutant *Pde6a^{MUT}* mice. Representative confocal images showing 5hmC-accessible cells (green) in retinal cross-sections of wild type (WT; A), single-mutant *Pde6a^{V685M}* (V685M; B), single-mutant *Pde6a^{R562W}* (R562W; C), and single-mutant *Cngb1$^{-/-}$* (D) mouse retinas at PM1, as well as in double-mutant *Pde6a^{V685M}xCngb1$^{-/-}$* (V685M DBM; E-G) and *Pde6a^{R562W}xCngb1$^{-/-}$* (R562W DBM; H-J) mouse retinas at PM1, PM3 and PM6. Cell nuclei were stained with DAPI (blue). OS, outer segments; IS, inner segments; ONL, outer nuclear layer; OPL, outer plexiform layer; INL, inner plexiform layer; IPL, inner plexiform layer; GCL, ganglion cell layer. Scale bar marks 20 µm. (K-L) Quantification of 5hmC-positive cells in (K) WT, *Cngb1$^{-/-}$* SM, V685M SM and DBM, and R562W SM and DBM at PM1 and (L) in V685M and R562W DBM mouse retinas at different ages. N = 3. Values are given as mean ± SEM.

This suggests that cell death has just or not yet peaked at PM1 in DBM V685M and R562W mice, indicating delayed onset of degeneration compared to their corresponding SM mouse models.

In summary, additional ablation of CNG channels in two different *Pde6a*^{MUT} mouse models resulted in a magnificent 6-month rescue of the *PDE6A*-linked RP phenotype, confirming a key role of CNG channels in photoreceptor degeneration during progression of RP.

4.3 Gene Augmentation Therapy Approaches for RP

To date, there is no curative treatment option for RP. To overcome this problem, new potential gene augmentation therapy approaches for autosomal-recessive RP were developed in this study. To this end, rAAV vectors expressing the respective therapeutic transgenes were administered to *Cngb1*- and *Cnga1*-deficient mouse models in preclinical studies.

4.3.1 hCNGB1 Gene Augmentation Therapy

A recent study has shown that treatment of *Cngb1*$^{-/-}$ mice with an AAV5 serotype vector comprising human *CNGB1* (rAAV5.hCNGB1) under control of a short human rhodopsin promoter (*hRHO194*) resulted in deceleration of retinal degeneration and prevention of secondary cone photoreceptor degeneration (Wagner et al., 2021). In the present study, a further developed, modified version of rAAV5.hCNGB1 (rAAV5.hCNGB1/mod) was tested for its potency in treating the RP phenotype in the *Cngb1*$^{-/-}$ mouse model.

4.3.1.1 rAAV5.hCNGB1/mod Achieves Efficient and Specific Transgene Expression in Rod Photoreceptors

The cDNA sequence of full-length human *CNGB1* used in rAAV5.hCNGB1 (Wagner et al., 2021) was based on transcript variant 1 (NCBI Reference Sequence NM_001297.4). However, two sequence modifications leading to amino acid changes were found: K404del and K1091Q. In the present study, these modifications were corrected (Q403_L404insK and Q1091K). A gene expression cassette including the modified *hCNGB1* cDNA together with a short SV40 polyA sequence and AAV2-ITRs was generated (Figure 39A). Due to the size of full-length *hCNGB1* (~3.7 kb), that, together with a full-length *hRHO* promoter (Allocca et al., 2007), would exceed the packaging capacity of an AAV (~4.7 kb), the short *hRHO194* promoter (Wagner et al., 2021) was used to control gene expression. Finally, the AAV5 serotype vector rAAV5.hCNGB1/mod was produced and administered into the subretinal space of 4-week-old *Cngb1*$^{-/-}$ mice (10^{10} total vg in 1 µL volume). The contralateral (sham-injected) control eye received 1 µL of vector diluent (0.014% Tween/PBS-MK).

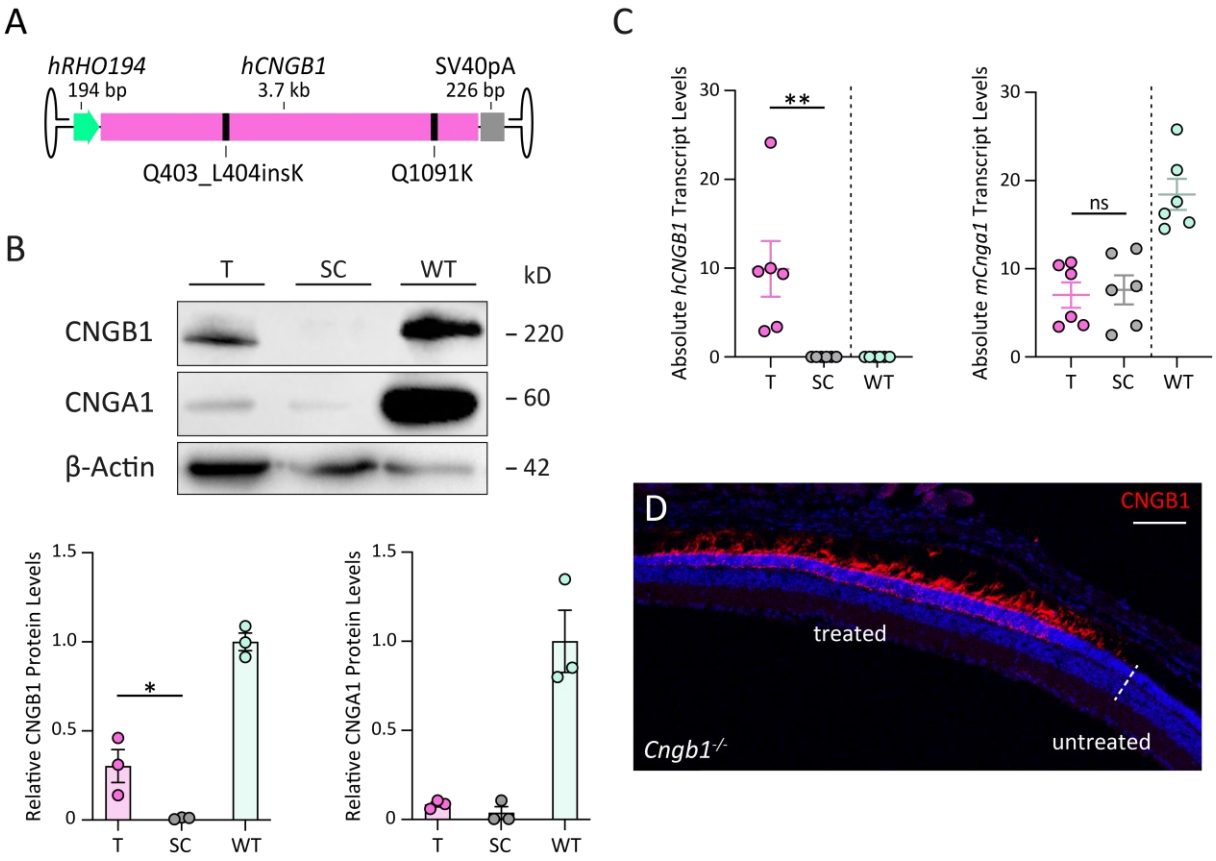

Figure 39. Subretinal delivery of rAAV5.hCNGB1/mod results in the expression of full-length CNGB1. (A) Schematic of the gene expression cassette of rAAV5.hCNGB1/mod including the two modification sites Q403_L404insK and Q1091K. (B) Western blot analysis of treated (T; 10^{10} vg, rAAV5.hCNGB1/mod) and sham-injected control (SC) *Cngb1*$^{-/-}$ mice, as well as of wild type mice (WT) at *postnatal* month 3 (2 months *post-injection*, PI2) using CNGA1- and CNGB1-antibodies. β-Actin was used as loading control. (C) qRT-PCR of treated (T) and sham-injected control (SC) *Cngb1*$^{-/-}$ mice, as well as of wild type mice (WT) at PM3 (2 months *post-injection*, PI2) using human *Cngb1*- and murine *Cnga1*-specific primers. WB: N = 3; qRT-PCR: N = 6. Values are given as mean ±SEM (Ordinary one-way ANOVA paired with Tukey's post-hoc test; *p≤0.05, **p≤0.01, ns = not significant). (D) Representative confocal overview image showing the treated (within the subretinal bleb) and untreated (outside the subretinal bleb) parts of the retina. The treatment border is marked with a dashed line. Cell nuclei were stained with DAPI (blue). OS, outer segments; IS, inner segments; ONL, outer nuclear layer; OPL, outer plexiform layer. Scale bar marks 100 µm.

In order to first evaluate vector-derived transgene expression, injected mice were sacrificed 2 months *post-injection* (PI2) and Western blot analysis as well as qRT-PCR were performed (Figure 39B-C). As the antibody against hCNGB1 also detects endogenous CNGB1 protein, profound expression of native CNGB1 was found in wild type mice at the expected size of ~250 kDa (Figure 39B). While sham control eyes of *Cngb1*$^{-/-}$ mice did not show any CNGB1 expression, subretinal delivery of rAAV5.hCNGB1/mod resulted in the expression of full-length

hCNGB1. Moreover, also expression of the 63 kDa endogenous mouse CNGA1 subunit could be rescued by treatment with rAAV5.hCNGB1/mod, which is otherwise degraded in the absence of mouse CNGB1 protein (Hüttl et al., 2005; Koch et al., 2012). Additionally, qRT-PCR with *hCNGB1*-specific primers showed significantly enriched *hCNGB1* transcript levels in treated *Cngb1*$^{-/-}$ mice compared to sham control and wild type (Figure 39C, left panel). Interestingly, transcript levels of endogenous *mCnga1* were reduced to about 50 % in treated *Cngb1*$^{-/-}$ mice compared to wild type but unaltered compared to sham control (Figure 39C, right panel). As the reduction of transcript levels can be explained by the fact that in *Cngb1*$^{-/-}$ mice only ~50-60 % of rod photoreceptors are left at this age (Petersen-Jones et al., 2018), these findings indicate that in *Cngb1*$^{-/-}$ mice endogenous *Cnga1* transcripts are completely translated into protein, which is, however, degraded when CNGB1 protein is absent. Nevertheless, emerging expression of hCNGB1 protein by gene augmentation therapy with rAAV5.hCNGB1/mod rescues endogenous CNGA1 from degradation.

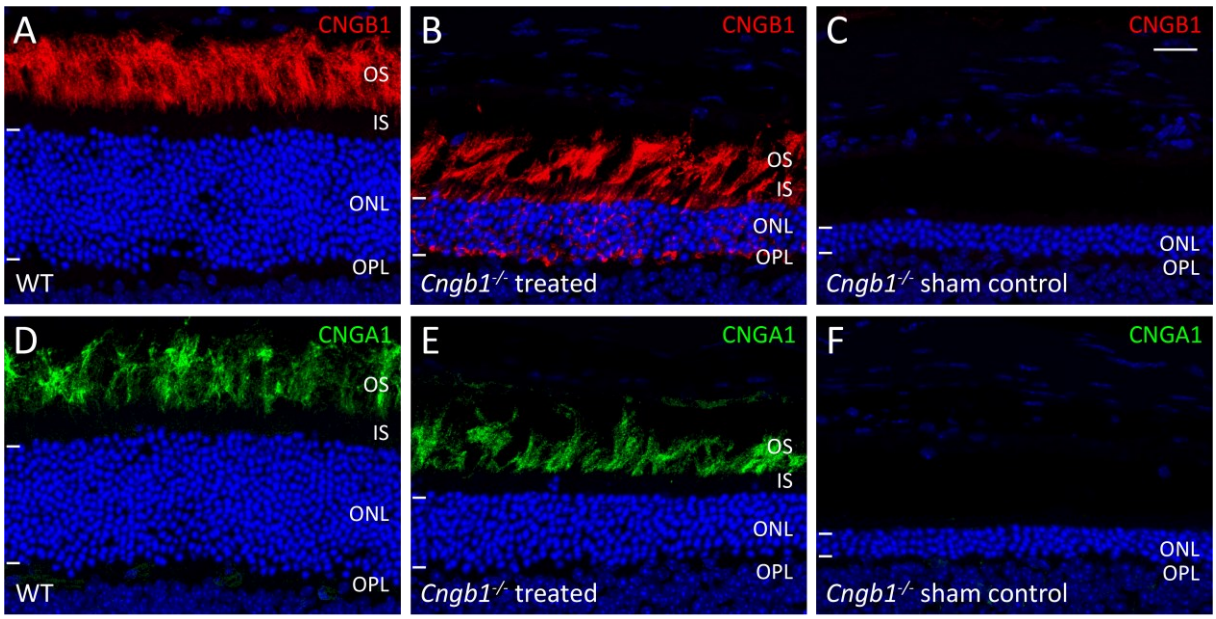

Figure 40. rAAV5.hCNGB1/mod obtains efficient and rod-specific hCNGB1 and endogenous CNGA1 expression in *Cngb1*$^{-/-}$ mice. Representative confocal images showing expression of hCNGB1 (red, the antibody detects mouse and human CNGB1; A-C) and endogenous mCNGA1 protein (green; D-F) in retinal cross-sections of wild type (WT; A, D), treated (10^{10} vg, rAAV5.hCNGB1/mod; B, E), and sham-injected control *Cngb1*$^{-/-}$ mouse retinas (C, F) at 7 months of age (6 months *post-injection*). The edges of the ONL are marked with horizontal bars. Cell nuclei were stained with DAPI (blue). OS, outer segments; IS, inner segments; ONL, outer nuclear layer; OPL, outer plexiform layer. Scale bar marks 20 µm.

In the next step, immunohistochemical analysis was performed in order to evaluate correct localization of vector-derived hCNGB1. A representative overview image of a treated *Cngb1*$^{-/-}$ mouse retina 6 months *post-injection* (PI6; Figure 39D) shows that hCNGB1 protein is expressed in the treated area (within the subretinal bleb), but not in the untreated area (outside the subretinal bleb). Higher magnification confocal images (Figure 40) revealed prominent expression of native CNGB1 limited to rod OS in wild type mice (Figure 40A). In contrast, no CNGB1 expression was found in the sham control *Cngb1*$^{-/-}$ retina and, moreover, the ONL was decreased to about 20 % compared to wild type (Figure 40C). Although the ONL was also reduced in treated *Cngb1*$^{-/-}$ mice to about 50 %, efficient expression of hCNGB1 could be detected (Figure 40B). Importantly, as already shown by Western blot analysis, expression of hCNGB1 also rescued the expression of the endogenous mCNGA1 protein (Figure 40D-F).

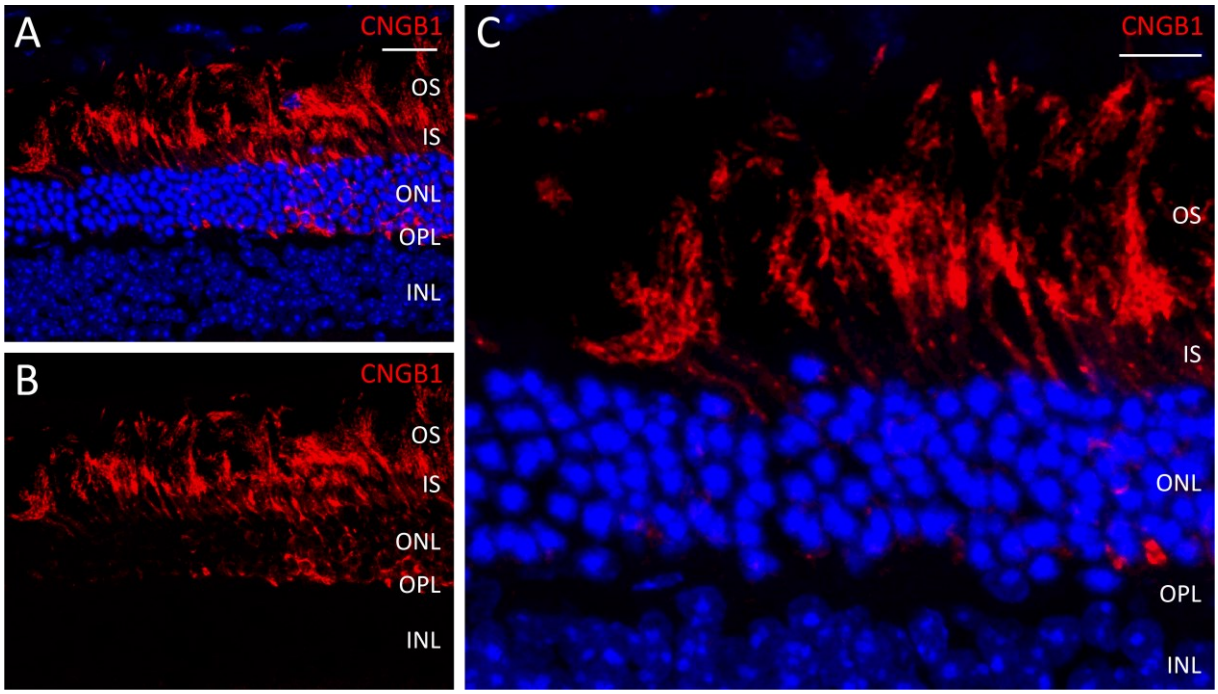

Figure 41. hCNGB1 is exclusively localized to rod OS in the transition region between treated and untreated area of a *Cngb1*$^{-/-}$ mouse retina. (A-B) Representative merged (A) and single (B) confocal images showing hCNGB1 expression (red, the antibody detects mouse and human CNGB1) in the transition area in retinal cross-sections of a treated *Cngb1*$^{-/-}$ mouse retina (10^{10} vg, rAAV5.hCNGB1/mod) at 7 months of age (6 months *post-injection*). (C) Zoom-in of (A). Cell nuclei were stained with DAPI (blue). OS, outer segments; IS, inner segments; ONL, outer nuclear layer; OPL, outer plexiform layer; INL, inner nuclear layer. Scale bars mark 20 µm (A) and 10 µm (C).

Consistent with the previous study using rAAV5.hCNGB1 (Wagner et al., 2021), vector-derived hCNGB1 localized not only to its natural expression site in rod OS, although expression of

rescued endogenous mCNGA1 was found exclusively there (Figure 40B, C). Instead, a substantial amount of CNGB1 was also found in rod IS and the ONL. These results might indicate a mismatch of vector-derived hCNGB1 and endogenous CNGA1 and thus an accumulation of hCNGB1 in rod IS and ONL, as only properly formed CNG channels are transported to rod OS. However, studying the transition region between the treated and untreated area uncovered a small part where hCNGB1 was strictly localized to rod OS with consistent ONL thickness (Figure 41). As in the transition region the effective therapeutic vector dose is lower than in the fully treated region, these findings indicate that a lower optimal vector dose should be achievable without loss of therapeutic effect.

4.3.1.2 rAAV5.hCNGB1/mod Results in Reactivation of Rod CNG Channels

The second messenger cGMP, the natural ligand of CNG channels, is known to accumulate in rod photoreceptors of *Cngb1*$^{-/-}$ mice due to a missing Ca^{2+}-mediated negative feedback on the cGMP-producing rod guanylate cyclase (Tanaka et al., 1997; Koch et al., 2012). In the dark, cGMP activates CNG channels in healthy rod photoreceptors leading to a cationic inward current (known as the “dark current”). While influx of Ca^{2+} would then inhibit cGMP production, this deactivation is absent in rods of *Cngb1*$^{-/-}$ mice causing cGMP accumulation inside the cell.

However, normalization of cGMP levels was previously shown as a result of successful CNGB1 gene therapy and confirmed formation of functional rod CNG channels (Koch et al., 2012; Wagner et al., 2021). To investigate whether rAAV5.hCNGB1/mod treatment also leads to functional CNG channel formation, immunohistochemistry of paraformaldehyde-fixed cGMP was performed in *Cngb1*$^{-/-}$ and wild type mice (Figure 42). While in the wild type retina cGMP is efficiently degraded (Figure 42A, A’), the sham control *Cngb1*$^{-/-}$ mouse retina clearly showed cGMP accumulation in the remaining rod IS (Figure 42C, C’). In the treated *Cngb1*$^{-/-}$ mouse retina, however, there was decreased, wild type-like cGMP signal (Figure 42B, B’), illustrating cGMP normalization and thus functional CNG channel formation after treatment with rAAV5.hCNGB1/mod.

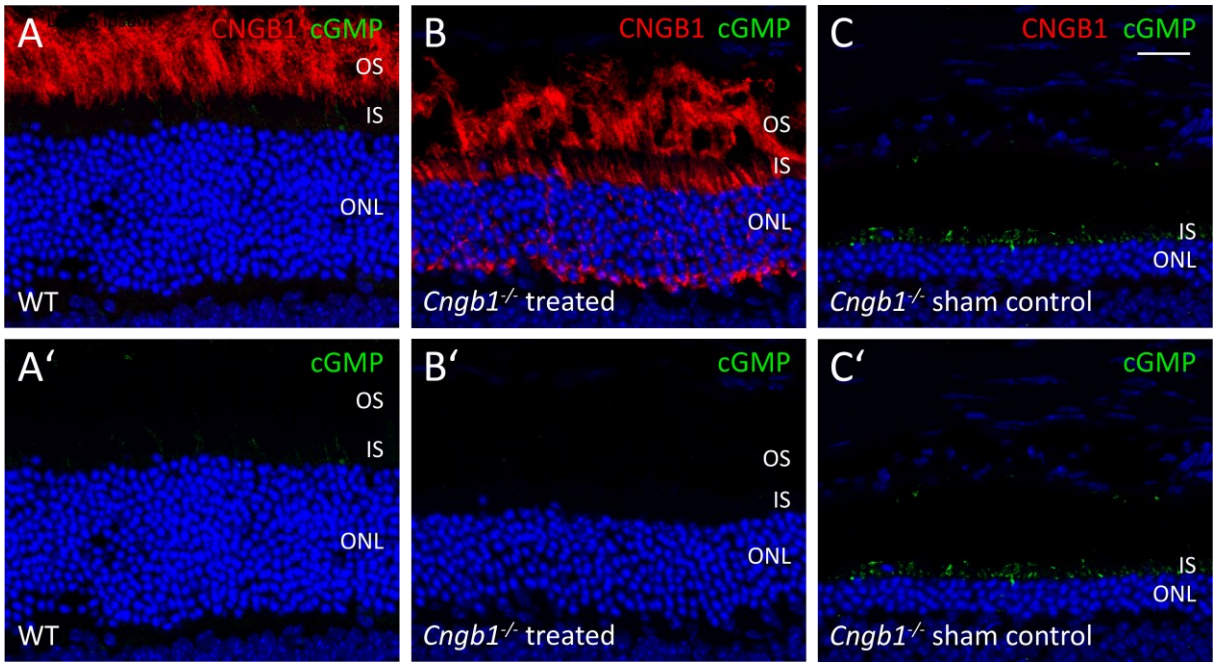

Figure 42. rAAV5.hCNGB1/mod normalizes cGMP levels in *Cngb1*$^{-/-}$ mice. Representative confocal images showing paraformaldehyde-fixed cGMP (green) and CNGB1 (red, the antibody detects mouse and human CNGB1; A-C) in retinal cross-sections of wild type (WT; A, A'), treated (10^{10} vg, rAAV5.hCNGB1/mod; B, B'), and sham-injected control *Cngb1*$^{-/-}$ mouse retinas (C, C') at 7 months of age (6 months *post-injection*). Cell nuclei were stained with DAPI (blue). OS, outer segments; IS, inner segments; ONL, outer nuclear layer. Scale bar marks 20 µm.

4.3.1.3 rAAV5.hCNGB1/mod Causes Gain of Rod Function

In the next step, the effect of rAAV5.hCNGB1/mod on the function of rod photoreceptors was investigated by recording ERG signals under scotopic (dark-adapted) conditions (Figure 43). Mice were examined during an in-life period of 6 months at PI1, PI3 and PI5. As expected, ERG signals at PI1 did not differ between treated and sham control *Cngb1*$^{-/-}$ mice (Figure 43A, B, left panels), since degeneration had not progressed so far. However, the treated eye already showed a rescue of the major oscillatory potentials (OPs) at the beginning of the b-wave signals. At 3 months *pi*, when degeneration had progressed, positive deflections of b-waves were reduced in sham-injected *Cngb1*$^{-/-}$ control mice (Figure 43A, B, middle panels). In contrast, increased b-wave amplitudes could be detected after rAAV5.hCNGB1/mod treatment. Moreover, although a general decline of b-wave amplitudes was present, rAAV5.hCNGB1/mod treatment resulted in a maintained functional benefit of photoreceptors at PI5 (Figure 43A, B, right panels). Remarkably, a gain of b-wave amplitudes was also observed at the rod-specific luminances (0.01-0.03 cd.s/m^2). At PI3 a small but nevertheless clear

increase in b-wave amplitudes of 6-16 % for rod-specific luminances could be detected, while at PI5 even a gain of up to 50 % was recorded.

In summary, subretinal gene therapy of *Cngb1*$^{-/-}$ mice with rAAV5.hCNGB1/mod was confirmed to rescue rod-function over a medium-term period of at least 6 months.

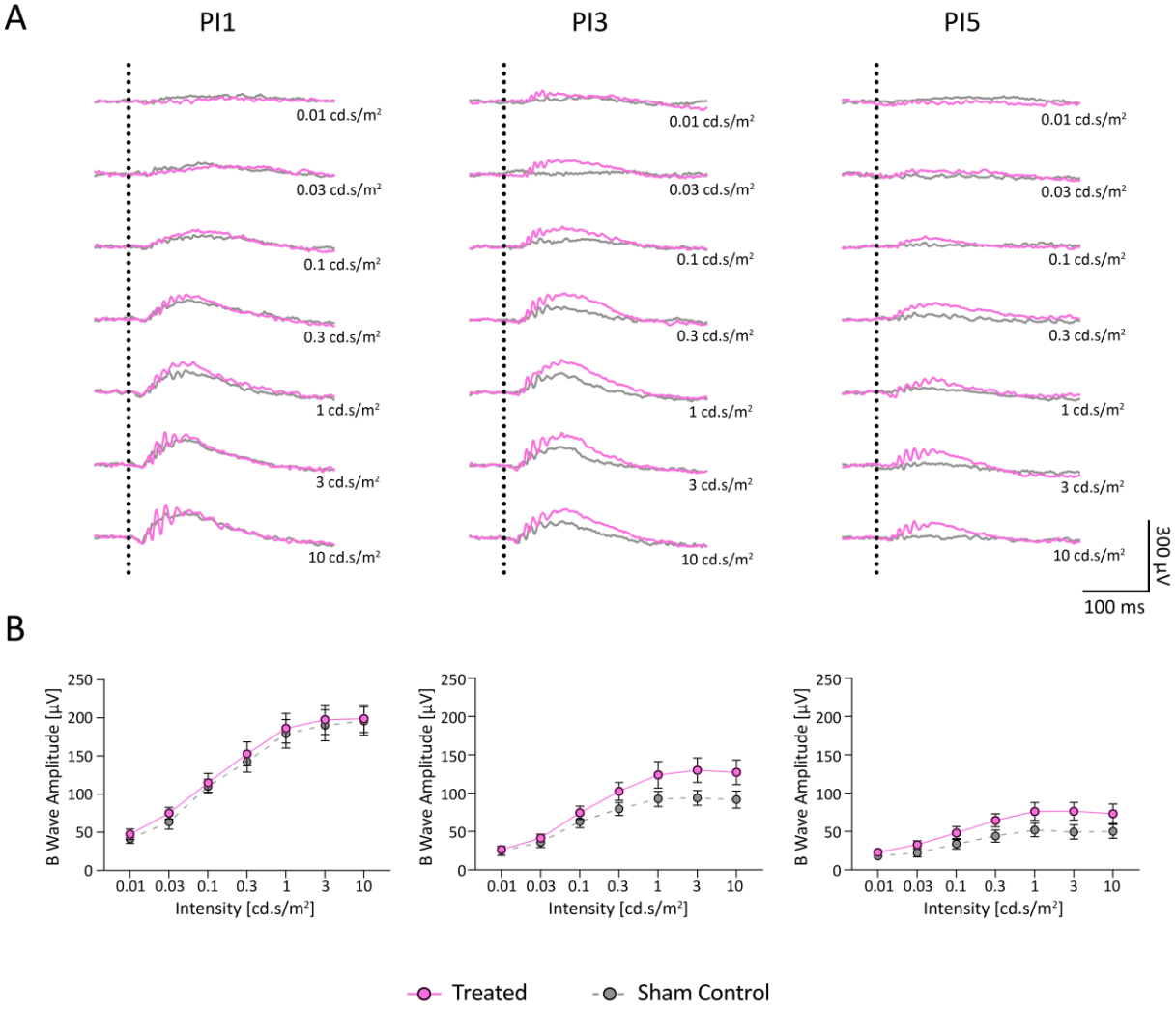

Figure 43. rAAV5.hCNGB1/mod rescues rod function in treated *Cngb1*$^{-/-}$ mice. (A) Overlays of representative scotopic electroretinography (ERG) signals of a treated *Cngb1*$^{-/-}$ eye (10^{10} vg, rAAV5.hCNGB1/mod; magenta) compared to the respective sham-injected control eye (grey) at 1, 3 and 5 months *post-injection* (PI) at different light intensities. Vertical dotted lines mark the timepoint of light stimulation. (B) Quantification of b-wave amplitudes of treated and sham-injected *Cngb1*$^{-/-}$ mice at PI1, PI3, and PI5. N = 9. Values are given as mean ±SEM.

4.3.1.4 rAAV5.hCNGB1/mod Preserves Photoreceptor Layer Thickness and Prolongs Cone Survival

In order to further assess and confirm the deceleration of retinal degeneration in *Cngb1*$^{-/-}$ mice after subretinal treatment with rAAV5.hCNGB1/mod, *in vivo* SD-OCT measurements were

performed (Figure 44). Gene supplementation of hCNGB1 resulted in preservation of the ONL as well as the photoreceptor OS layer (PR+ layer; Figure 44A, B). In contrast, the PR+ layer was severely decreased in the untreated area of the same retina (Figure 44A, C). While quantification of the PR+ layer demonstrated a continuous decrease over time in sham-injected control eyes, a significant overall rescue could be detected in the contralateral treated eyes (Figure 44D). Moreover, at PI3 a rescue of already ~10 % was observed, which was even increased to about 30 % at PI5. Additionally, consistent with the previous study using rAAV5.hCNGB1 (Wagner et al., 2021), rAAV5.hCNGB1/mod did not affect other retinal structures, such as the retinal pigment epithelium (RPE), the inner nuclear layer (INL), or the ganglion cell layer (GCL).

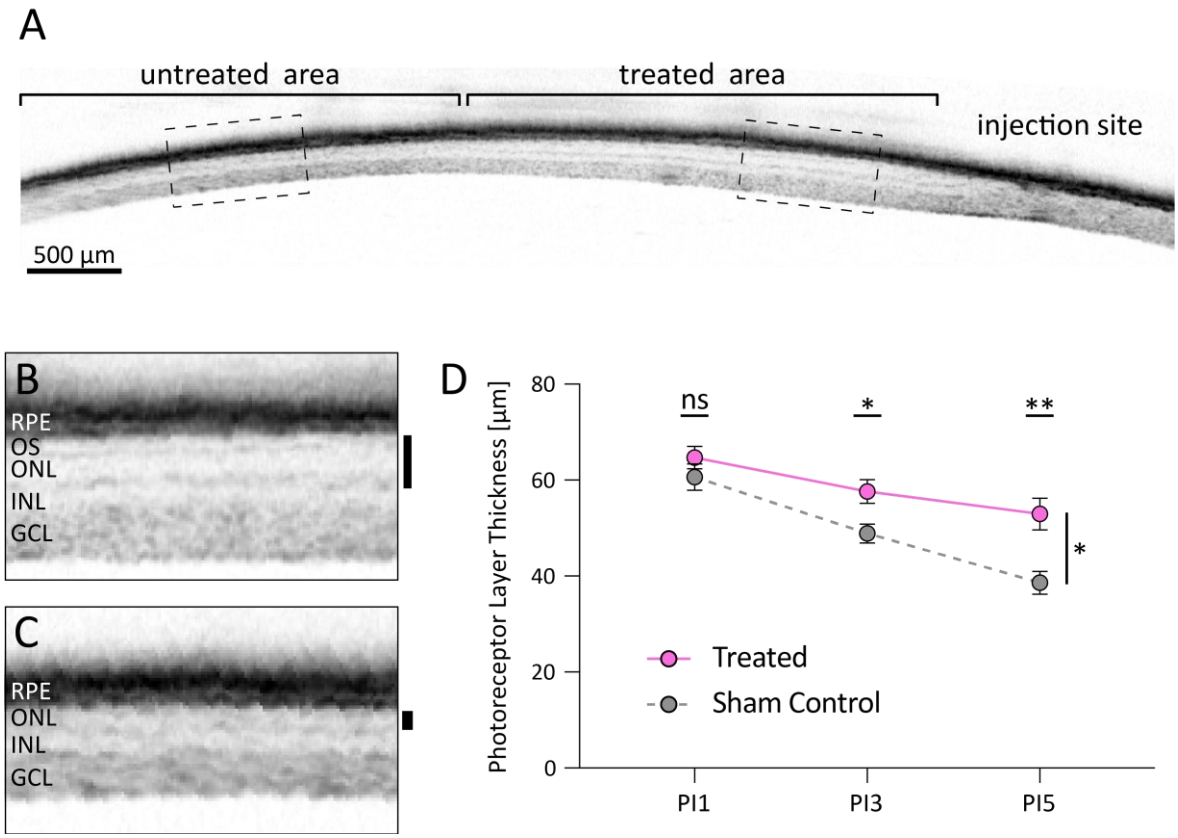

Figure 44. rAAV5.hCNGB1/mod gene therapy preserves photoreceptor layer thickness. (A) Representative SD-OCT image of a treated *Cngb1*$^{-/-}$ mice (10^{10} vg, rAAV5.hCNGB1/mod) at 6 months of age. (B-C) Zoom-ins of (A) showing the treated area (B) and the untreated area (C). Black bars mark the photoreceptor plus (PR+) layer. (D) Quantification of photoreceptor layer thickness (µm) in *Cngb1*$^{-/-}$ mice eyes after treatment at 1, 3, and 5 months *post-injection* (PI) compared with their respective sham-injected contralateral eyes. N = 9. Values are given as mean ±SEM (Ordinary two-way ANOVA and paired Student's t-test; *p≤0.05; **p≤0.01; ns = not significant).

Secondary degeneration of cone photoreceptors is a well-known phenomenon in RP and also occurs in *Cngb1*-deficent animal models (Hüttl et al., 2005; Petersen-Jones et al., 2018). As daylight vision mostly relies on cone photoreceptors, prevention of secondary cone degeneration is of great importance for RP therapies. Thus, immunohistochemistry was performed to evaluate the ability of rAAV5.hCNGB1/mod to prevent secondary loss of cones (Figure 45).

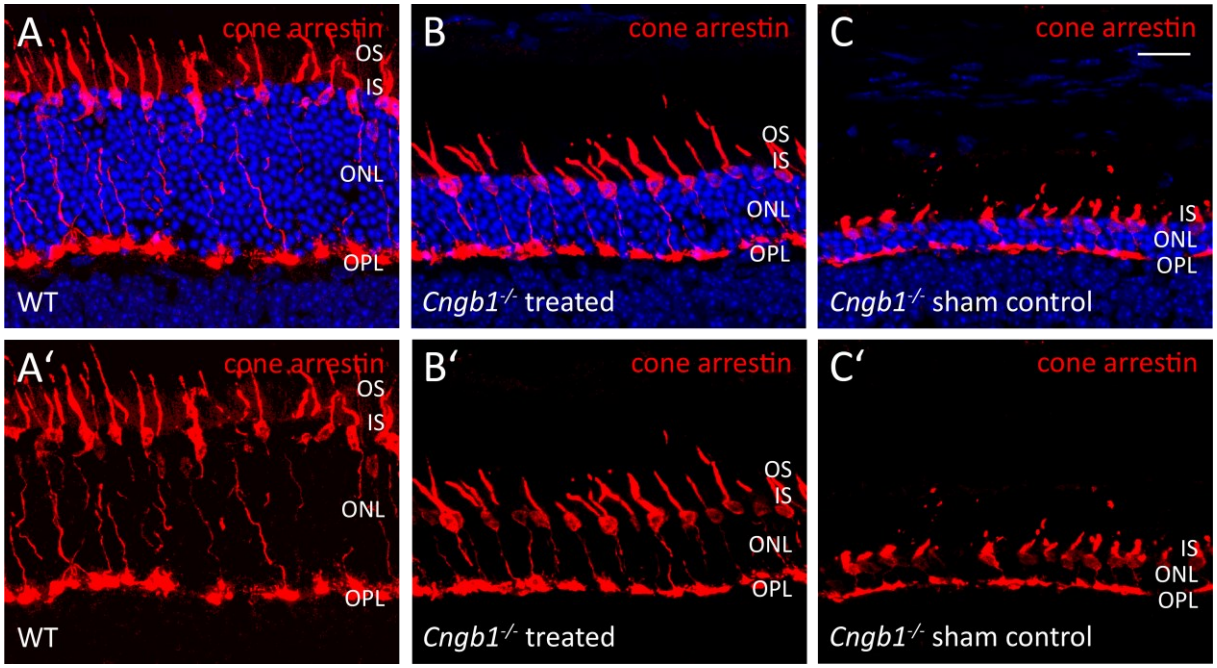

Figure 45. rAAV5.hCNGB1/mod gene therapy prolongs cone photoreceptor survival in *Cngb1*$^{-/-}$ mice. Representative confocal images showing expression of cone arrestin (red) in retinal cross-sections of wild type (WT; A, A'), treated (10^{10} vg, rAAV5.hCNGB1/mod; B, B'), and sham-injected control (C, C') *Cngb1*$^{-/-}$ mouse retinas at the age of 7 months (PI6). Cell nuclei were stained with DAPI (blue). OS, outer segments; IS, inner segments; ONL, outer nuclear layer; OPL, outer plexiform layer. Scale bar marks 20 µm.

Immunolabeling of cone arrestin confirmed the previously investigated secondary cone degeneration in untreated (sham control) *Cngb1*$^{-/-}$ mice at the age of 7 months (PI6; Figure 45C, C'). At this age, cone OS start to collapse due to progressing demise of cone-stabilizing rod OS. In contrast, rAAV5.hCNGB1/mod treatment resulted in abundant rescue of cones with wild type-like morphology and accurate position (Figure 45A-B, A'-B'), together suggesting maintained daylight vision after *hCNGB1* gene augmentation therapy.

4.3.1.5 rAAV5.hCNGB1/mod Reduces Müller Cell Gliosis

Profound upregulation of GFAP and development of intermediate fibers, a typical reaction of Müller cells in response to retinal stress, was found in the novel *Cnga1*^{MUT} mouse model, and it is known that this phenomenon also occurs in *Cngb1*-deficient mice (Hüttl et al., 2005).
A murine gene augmentation therapy approach has already been demonstrated to result in reduction of Müller cell gliosis (Koch et al., 2012). Additionally, also the previous study using rAAV5.hCNGB1 (Wagner et al., 2021) confirmed a positive effect of the treatment on retinal stress by reduction of GFAP expression. Indeed, also the new therapeutic vector rAAV5.hCNGB1/mod successfully decreased intermediate fibers (Figure 46). While extensive GFAP upregulation was shown in sham control *Cngb1*$^{-/-}$ mouse retinas compared to age-matched wild type control (Figure 46A, C), almost no intermediate fibers were recognizable in treated *Cngb1*$^{-/-}$ mouse retinas (Figure 46B). These results revealed reduced Müller cell gliosis after treatment with rAAV5.hCNGB1/mod, suggesting decline of degeneration-induced retinal stress.

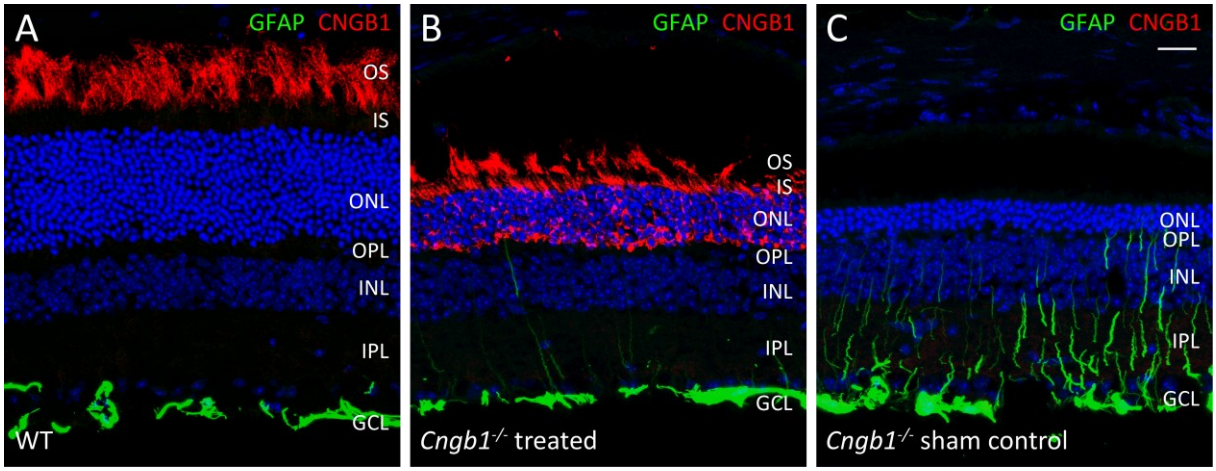

Figure 46. rAAV5.hCNGB1/mod treatment reduces Müller cell gliosis in *Cngb1*$^{-/-}$ mice. Representative confocal images showing co-expression of GFAP (green) and CNGB1 (red, the antibody detects mouse and human CNGB1) in retinal cross-sections of wild type (WT; A), treated (10^{10} vg, rAAV5.hCNGB1/mod; B), and sham-injected control (C) *Cngb1*$^{-/-}$ mouse retinas at the age of 7 months (PI6). Cell nuclei were stained with DAPI (blue). OS, outer segments; IS, inner segments; ONL, outer nuclear layer; OPL, outer plexiform layer; INL, inner nuclear layer; IPL, inner plexiform layer; GCL, ganglion cell layer. Scale bar marks 20 µm.

In summary, gene augmentation therapy with a single subretinal injection of rAAV5.hCNGB1/mod led to efficient hCNGB1 transgene expression and deceleration of retinal

degeneration. Altogether, this study resulted in substantial improvements in rod function as well as preservation of cone photoreceptors.

4.3.2 Proof-of-Concept: hCNGA1 Gene Augmentation Therapy

In the past, the lack of a suitable *Cnga1*-deficient mouse model for RP has (drastically) challenged the development of an appropriate therapy. In the present study, a first proof-of-concept approach using an rAAV-based vector for gene augmentation of human *CNGA1* was tested in the novel *Cnga1*^{MUT} mouse model. A gene expression cassette including full-length human *CNGA1* cDNA based on transcript variant 2 (NCBI Reference Sequence NM_000087.5) under the control of full-length *hRHO*, together with a mouse WPRE and a BGH polyA sequence, and AAV2-ITRs was generated (Figure 47A). The AAV2\GL serotype (Pavlou et al., 2021), a novel AAV2-based capsid variant with characteristics superior to those of the AAV2 wild type capsid, was used to produce rAAV2\GL.hCNGA1.

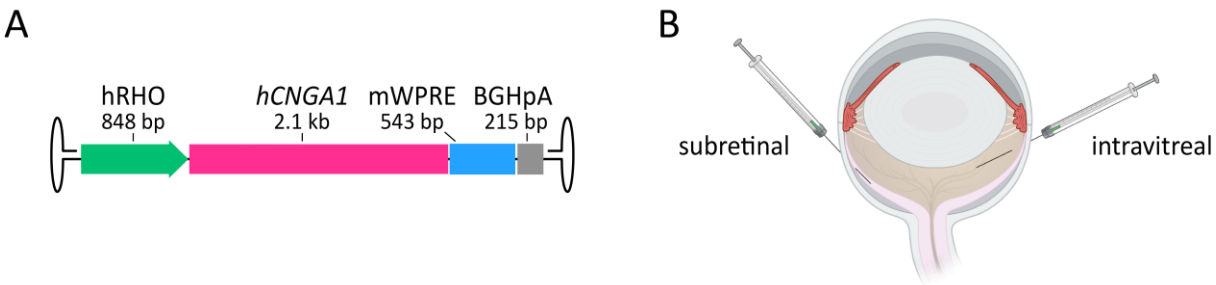

Figure 47. Proof-of-concept study design for treatment of *Cnga1*^{MUT} mice with rAAV2\GL.hCNGA1. (A) Schematic of the gene expression cassette of rAAV2\GL.hCNGA1. (B) Schematic of routes of administration: the conventional subretinal route (left) and the less invasive intravitreal route (right).

4.3.2.1 Subretinal Administration of rAAV2\GL.hCNGA1

In a preliminary proof-of-concept trial, the novel rAAV2\GL.hCNGA1 was tested via subretinal injection, the conventional route of administration. Thus, a single *Cnga1*^{MUT} mouse was injected subretinally at the age of 3 weeks with 6 x 10^9 total vg in 1 µL volume (Figure 47B). The contralateral (sham-injected) control eye received 1 µL of vector diluent (0.014% Tween/PBS-MK). After a short in-life observation period of 8 weeks, the mouse was sacrificed for immunohistochemical analysis at the age of 3 months (PI2).

First, immunolabeling with an antibody against murine and human CNGA1 was perfomed in order to investigate whether the novel rAAV2\GL.hCNGA1 was able to cause expression of

hCNGA1 protein (Figure 48). As expected, endogenous CNGA1 was detected in rod OS of the age-matched wild type control (Figure 48A), while no protein expression was found in the sham control eye (Figure 48C). Remarkably, robust expression of hCNGA1 was observed after treatment with rAAV2\GL.hCNGA1 (Figure 48B), confirming successful delivery and transcription/translation of *hCNGA1* in photoreceptors of a *Cnga1*^{MUT} mouse. However, hCNGA1 was found not only in rod OS but also in IS and, to a lesser extent, in the ONL, which was observed in previous studies using trans-species gene supplementation therapies as well (Wagner et al., 2021). Nevertheless, rAAV2\GL.hCNGA1 additionally achieved rescue of endogenous mCNGB1 protein (Figure 48D-F). Analysis of the ONL thickness revealed a ~16 % rescue after subretinal treatment with rAAV2\GL.hCNGA1 compared to sham control, indicating a great therapeutic potential of rAAV2\GL.hCNGA1.

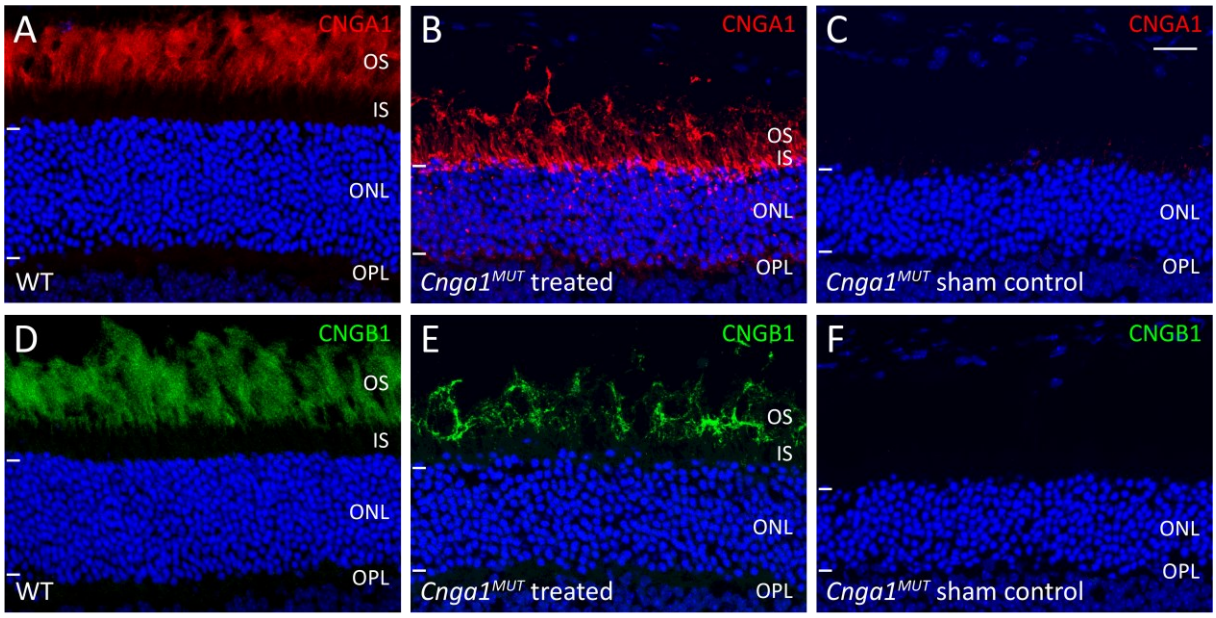

Figure 48. Subretinal injection of rAAV2\GL.hCNGA1 leads to robust hCNGA1 expression and rescues endogenous CNGB1 expression in a *Cnga1*^{MUT} mouse. Representative confocal images showing expression of hCNGA1 (red the antibody detects mouse and human CNGA1; A-C) and endogenous mCNGB1 protein (green; D-F) in retinal cross-sections of wild type (WT; A, D), treated (6 x 10^9 vg, rAAV2\GL.hCNGA1; B, E), and sham-injected control *Cnga1*^{MUT} mouse retinas (C, F) at 3 months of age (PI2). The edges of the ONL are marked with horizontal bars. Cell nuclei were stained with DAPI (blue). OS, outer segments; IS, inner segments; ONL, outer nuclear layer; OPL, outer plexiform layer. Scale bar marks 20 µm.

To analyze the rod-dependent retinal function, dark-adapted (scotopic) ERGs were recorded during the in-life phase at 8 weeks *pi* (Figure 49). Consistent with the previous data (Figure

19), the sham-injected control eye first responded to light at the luminance of 0.1 cd.s/m^2 (Figure 49A). Due to a still intact cone-system, clear positive b-wave deflections were recorded at higher luminances. However, distinct increases in b-wave amplitudes were observed in the treated eye and additionally, also a slight recovery of a-wave amplitudes could be seen from 0.1 cd.s/m^2 upwards. Importantly, especially positive deflections at rod-specific luminances (0.01-0.03 cd.s/m^2) were recovered after treatment with rAAV2\GL.hCNGA1. B-wave amplitudes of the treated eye were 3-fold higher than those of the sham control eye (Figure 49B), indicating a pronounced regain of rod-function after subretinal injection of rAAV2\GL.hCNGA1.

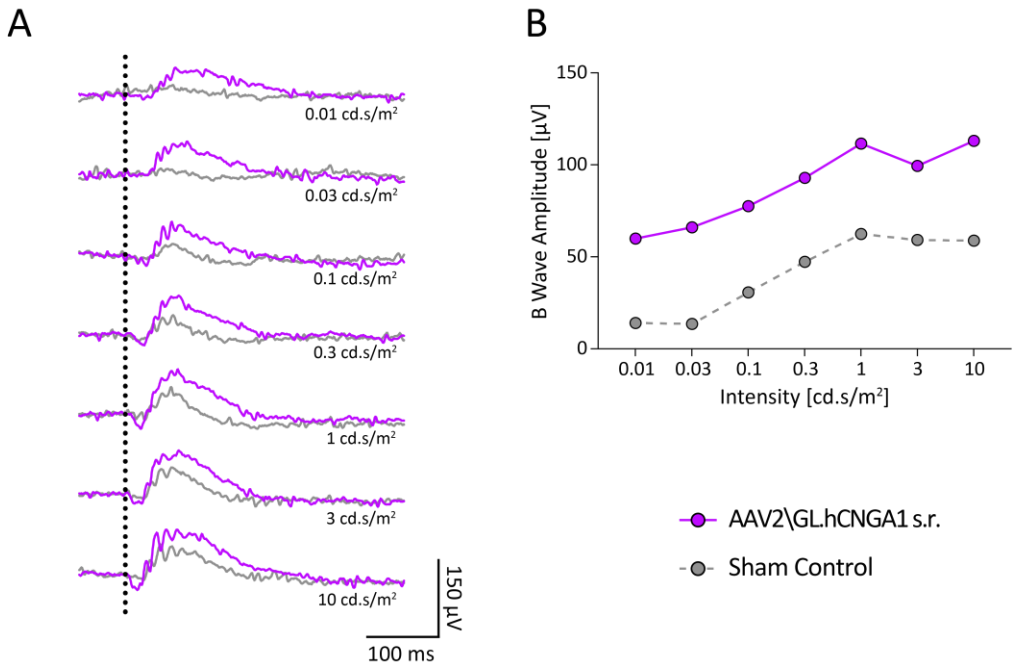

Figure 49. rAAV2\GL.hCNGA1 rescues rod function in a treated *Cnga1^{MUT}* mouse after subretinal injection. (A) Overlays of scotopic electroretinography (ERG) signals of a treated *Cnga1^{MUT}* eye (6 x 10^9 vg, rAAV2\GL.hCNGA1; purple) compared to the respective sham-injected control eye (grey) 8 weeks *post-injection* at different light intensities. Vertical dotted lines mark the timepoint of light stimulation. (B) Quantification of b-wave amplitudes of treated and sham-injected *Cnga1^{MUT}* eyes. N = 1.

4.3.2.2 Intravitreal Administration of rAAV2\GL.hCNGA1

Based on the promising results of subretinal delivery of rAAV2\GL.hCNGA1, a second study was performed in *Cnga1^{MUT}* mice. This time, an intravitreal administration of the therapeutic vector was chosen (Figure 47B), since this less-invasive injection route would be superior to the conventional. For that purpose, *Cnga1^{MUT}* mice at the age of 3 weeks received a single

intravitreal injection (6 x 10^9 total vg in 1 µL volume) of rAAV2\GL.hCNGA1. The contralateral (sham-injected) control eye received 1 µL of vector diluent (0.014% Tween/PBS-MK). Again, after a short in-life observation period of 8 weeks, mice were sacrificed for immunohistochemical analysis at the age of 3 months (PI2).

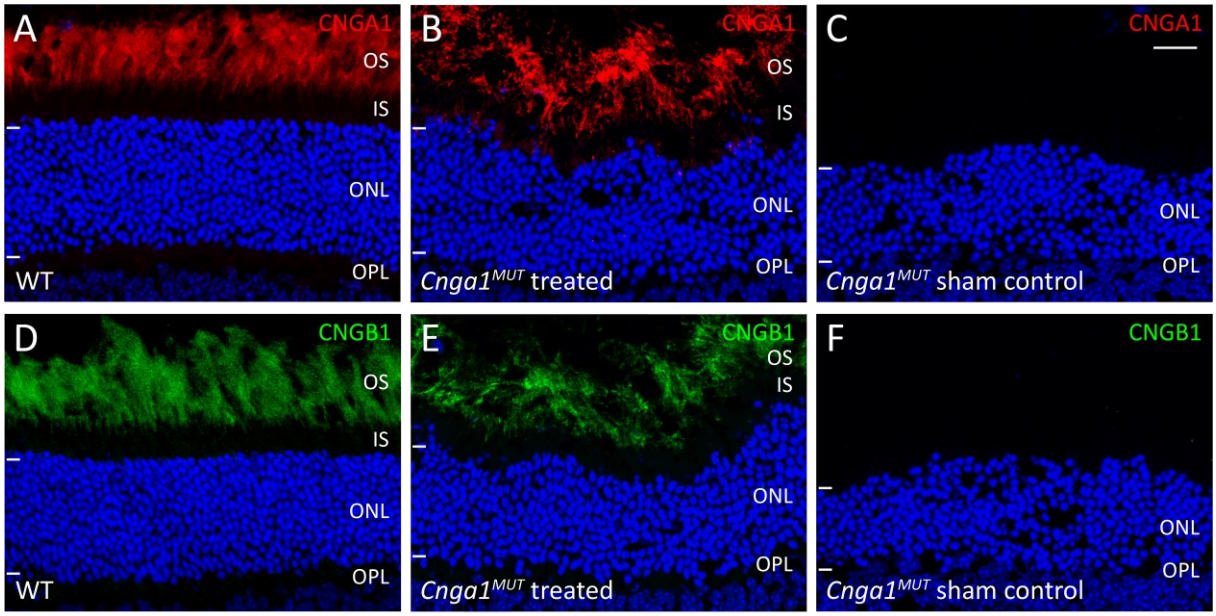

Figure 50. Intravitreal injection of rAAV2\GL.hCNGA1 leads to pronounced rod OS-specific hCNGA1 expression and rescues endogenous CNGB1 expression in *Cnga1*^{MUT} mice. Representative confocal images showing expression of hCNGA1 (red, the antibody detects mouse and human CNGA1; A-C) and endogenous CNGB1 protein (green; D-F) in retinal cross-sections of wild type (WT; A, D), treated (6 x 10^9 vg, rAAV2\GL.hCNGA1; B, E), and sham-injected control *Cnga1*^{MUT} mouse retinas (C, F) at 3 months of age (PI2). The edges of the ONL are marked with horizontal bars. Cell nuclei were stained with DAPI (blue). OS, outer segments; IS, inner segments; ONL, outer nuclear layer; OPL, outer plexiform layer. Scale bar marks 20 µm.

Like subretinal injection, also intravitreal injection of rAAV2\GL.hCNGA1 was able to successfully elicit pronounced hCNGA1 expression in treated *Cnga1*^{MUT} mice (Figure 50A-C). However, hCNGA1 protein was strictly found in rod OS after intravitreal injection (Figure 50B). As vector doses for subretinal and intravitreal injection were similar, these findings suggest a less efficient transduction efficiency following intravitreal injection, causing a lower (more optimal) viral concentration and thus rod OS-specific transgene expression. Nevertheless, endogenous mCNGB1 could still be rescued by intravitreal injection (Figure 50D-F). Moreover, rAAV2\GL.hCNGA1 treatment led to preservation of the overall thickness of the ONL to about

95 % compared to wild type (Figure 50D, E), while only ~70 % were left in sham control treated animals (Figure 50F).

Accumulation of cGMP as a result of non-functional CNG channels was observed in *Cnga1*^{MUT} mice (Figure 14). However, gene therapeutic approaches have demonstrated cGMP normalization after treatment (Koch et al., 2012; Wagner et al., 2021). In order to investigate whether rAAV2\GL.hCNGA1 treatment can also achieve normalization of accumulated cGMP levels and thus functional CNG channel formation, immunohistochemistry of paraformaldehyde-fixed cGMP was performed in retinal cross-sections of treated and sham control eyes of intravitreally injected *Cnga1*^{MUT} mice (Figure 51). While prominent cGMP accumulation was found in the sham control eye (Figure 51C, C'), an imposing reduction of cGMP to wild type-like levels was detected in treated *Cnga1*^{MUT} mice (Figure 51A-B, A'-B'). These findings confirm formation of functional chimeric CNG channels consisting of human CNGA1 and mouse CNGB1 after a single intravitreal injection of rAAV2\GL.hCNGA1.

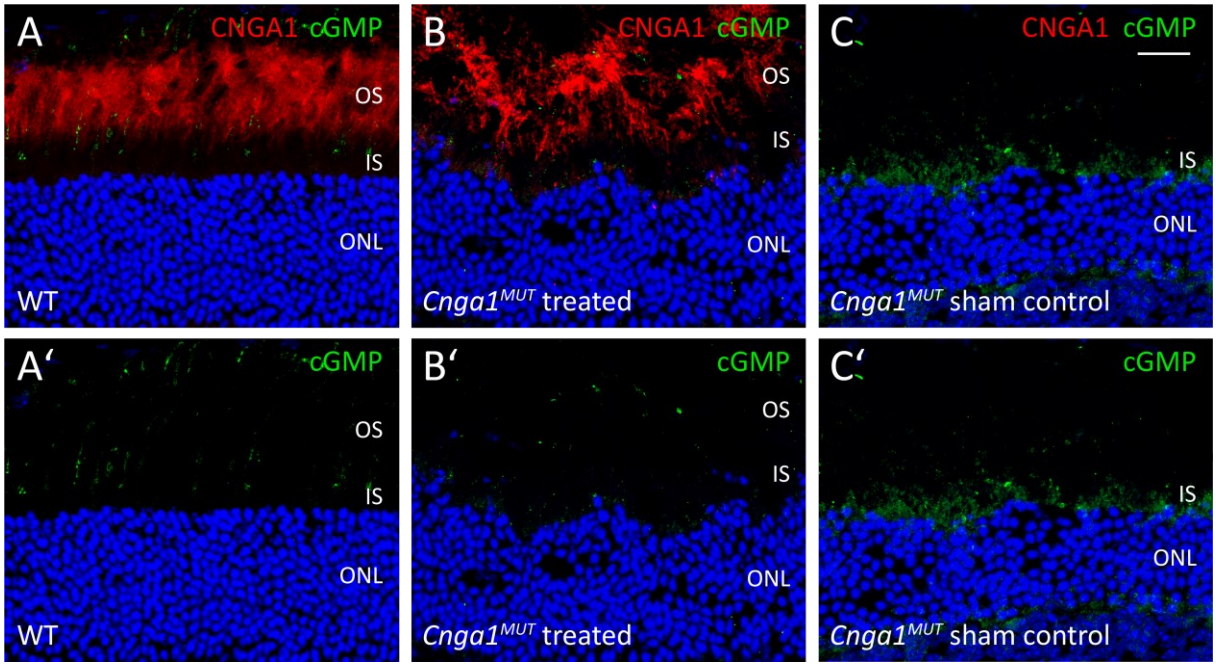

Figure 51. Single intravitreal injection of rAAV2\GL.hCNGA1 normalizes cGMP levels in *Cnga1*^{MUT} mice. Representative confocal images showing paraformaldehyde-fixed cGMP (green) and CNGA1 (red, the antibody detects mouse and human CNGA1; A-C) in retinal cross-sections of wild type (WT; A, A'), treated (6 x 10^9 vg, rAAV2\GL.hCNGA1; B, B'), and sham-injected control *Cnga1*^{MUT} mouse retinas (C, C') at 3 months of age (PI2). Cell nuclei were stained with DAPI (blue). OS, outer segments; IS, inner segments; ONL, outer nuclear layer. Scale bar marks 20 µm.

Since subretinal injection of rAAV2\GL.hCNGA1 achieved a pronounced regain of rod function, a possible effect on rod function was expected also after intravitreal injection. To assess rod-driven ERG signals, dark-adapted (scotopic) ERGs were recorded in intravitreally injected *Cnga1*^{MUT} mice during the in-life phase at 8 weeks *pi* (Figure 52). Indeed, rAAV2\GL.hCNGA1 also achieved a gain in rod function following intravitreal injection. Again, the sham-injected control eye first responded to light at the luminance of 0.1 cd.s/m^2, but there were clear positive deflections at higher light intensities representing both rod and cone responses (Figure 52A). In contrast, ERG signals from treated *Cnga1*^{MUT} mouse eyes showed highly increased b-waves, especially at the rod-specific luminances of 0.01-0.03 cd.s/m^2 (Figure 52A). B-wave amplitudes were ~1.5- to 2-fold higher in intravitreally treated *Cnga1*^{MUT} than in sham control eyes, illustrating a significant overall increase in b-wave amplitudes (Figure 52B). The smaller differences at higher light intensities can be explained by a still well-functional cone system in untreated (sham control) eyes. In conclusion, these data demonstrate a beneficial gain of rod function also after intravitreal injection of rAAV2\GL.hCNGA1.

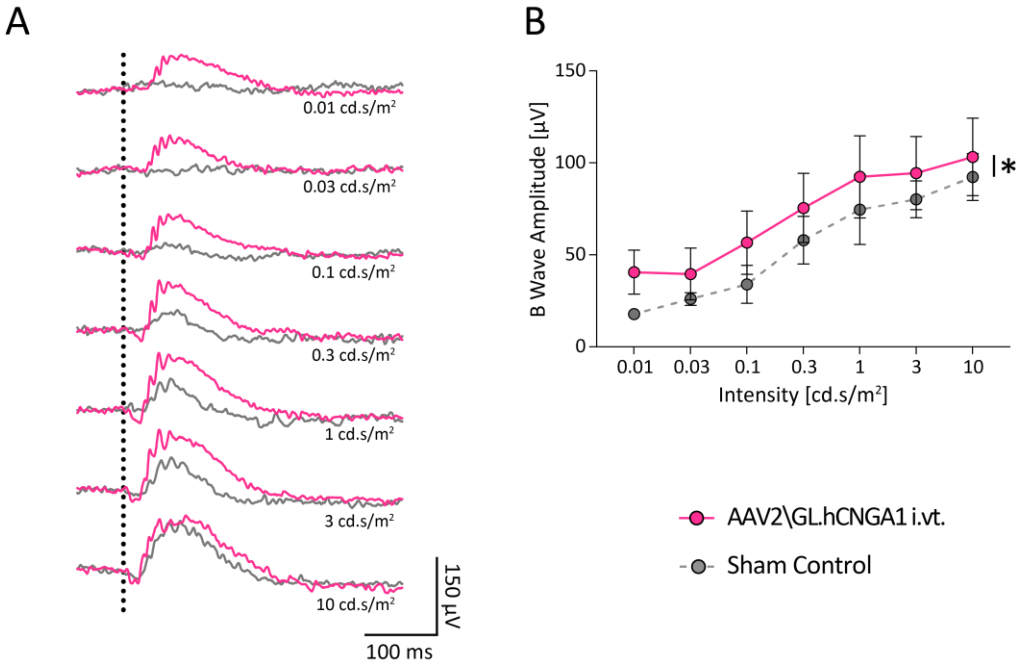

Figure 52. rAAV2\GL.hCNGA1 rescues rod function in treated *Cnga1*^{MUT} mice after intravitreal injection. (A) Overlays of scotopic electroretinography (ERG) signals of treated *Cnga1*^{MUT} eye (6 x 10^9 vg, rAAV2\GL.hCNGA1; pink) compared to the respective sham-injected control eye (grey) 8 weeks *post-injection* at different light intensities. Vertical dotted lines mark the timepoint of light stimulation. (B) Quantification of b-wave amplitudes of treated and sham-injected *Cnga1*^{MUT} eyes. N = 5. Values are given as mean ±SEM (Ordinary two-way ANOVA with Šídák's post-hoc test; *p≤0.05).

In the next step, it was investigated whether rAAV2\GL.hCNGA1 can reduce occurring Müller cell gliosis, as observed in several other gene supplementation therapy approaches (Koch et al., 2012; Wagner et al., 2021). To this end, immunolabeling of treated and sham control retinal cross-sections of intravitreally injected *Cnga1*^{MUT} mice was performed (Figure 53). Indeed, in treated eyes less GFAP-expressing intermediate fibers were detected in treated eyes (Figure 53B) than in sham control eyes (Figure 53C), although Müller cell gliosis was still clearly visible in comparison to wild type (Figure 53A). However, these findings indicate a positive effect of rAAV2\GL.hCNGA1 by reducing retinal stress, resulting in less severe Müller cell gliosis.

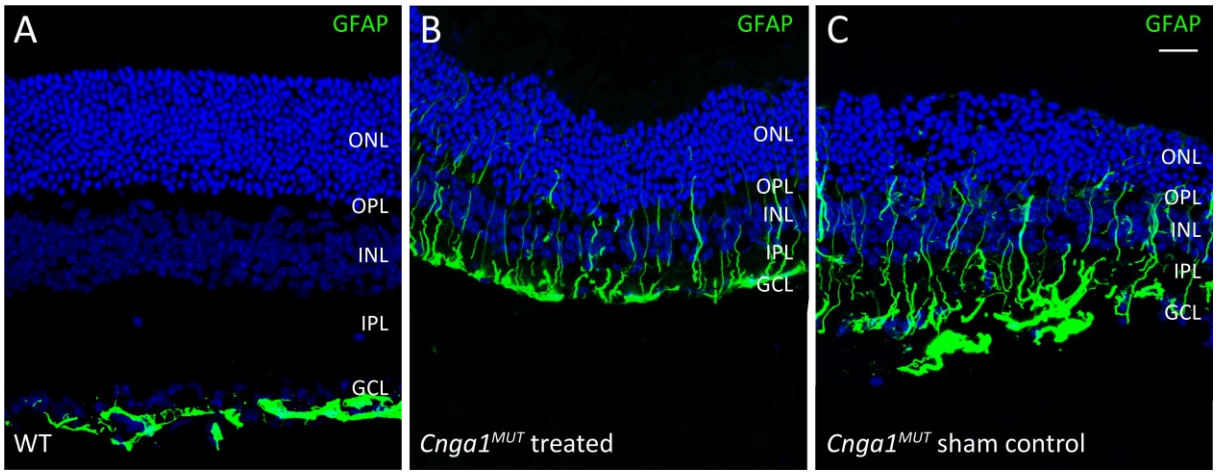

Figure 53. Intravitreal injection of rAAV2\GL.hCNGA1 reduces Müller cell gliosis in *Cnga1*^{MUT} mice. Representative confocal images showing expression of GFAP (green) in retinal cross-sections of wild type (WT; A), treated (6 x 10^9 vg, rAAV2\GL.hCNGA1; B) and sham-injected control (C) retinas of *Cnga1*^{MUT} mouse retinas at PI2. Cell nuclei were stained with DAPI (blue). ONL, outer nuclear layer; OPL, outer plexiform layer; INL, inner nuclear layer; IPL, inner plexiform layer; GCL, ganglion cell layer. Scale bar marks 20 µm.

In summary, rAAV2\GL.hCNGA1 was demonstrated to efficiently transduce photoreceptor cells of *Cnga1*^{MUT} mice, leading to expression of hCNGA1 and endogenous mCNGB1, and formation of functional CNG channels. Moreover, both the conventional subretinal route of administration as well as the less invasive intravitreal injection resulted in beneficial treatment effects of rAAV2\GL.hCNGA1.

5 Discussion

5.1 A Novel Mouse Model of *CNGA1*-linked RP

Establishing reliable and well-characterized animal models of retinal degeneration is important for a better understanding of retinal diseases associated with photoreceptor loss and for the development of therapies. Until recently, only one transgenic *Cnga1* mouse model was available. These animals are characterized by a 50 % reduction of *Cnga1* transcript levels due to overexpression of a *Cnga1* antisense mRNA (Leconte and Barnstable, 2000), leading to progressive retinal degeneration comparable to human RP patients. However, overexpression of antisense mRNA bears the risk to induce toxic effects that could possibly affect the phenotype. In 2021, a first KO mouse model was established using the CRISPR/Cas technique (Liu et al., 2021). In parallel to this, a novel mouse model of *CNGA1*-linked RP was characterized in the present study, which can be used for studying retinal degeneration and developing potential therapeutic approaches.

CNG channels are a specific class of ion channels that are critically important for retinal phototransduction. The main characteristic feature of CNG channels lies in activation by binding of the second messenger cGMP to the CNBD within the intracellular C-terminus of the channel. *Cnga1*^{MUT} mice carry a c.1526A>G mutation in the *Cnga1* gene leading to a Tyr509Cys exchange in CNGA1 protein. Murine Tyr509 corresponds to human Tyr513, which is known to participate in the formation of the CNBD. This highly conserved Tyr residue is also found in other cyclic nucleotide-binding proteins, such as hyperpolarization-activated cyclic nucleotide-gated (HCN) channels, cGMP-dependent protein kinase 1 (PRKG1), and cAMP-dependent protein kinase catalytic subunit alpha (PRKACA), highlighting its importance for proper channel function. Interestingly, the structurally related potassium voltage-gated channel subfamily H member 1 (KCNH1) protein with a presumably nonfunctional CNBD also carries a Cys instead of a Tyr at the corresponding position (aa 619) and cannot be modulated by cyclic nucleotides (Brelidze et al., 2009).

Recently, the very similar mutation Gly509Arg was found in human RP patients (Kandaswamy et al., unpublished), which is in very close proximity to the murine Tyr509Cys mutation. Indeed, morphological and functional analysis confirmed the novel *Cnga1*^{MUT} mouse model to reflect the human RP49 phenotype, which is characterized by progressive photoreceptor

degeneration and early loss of rod-mediated function. In consistence with *Cngb1*-deficient mouse (Hüttl et al., 2005) and dog models (Petersen-Jones et al., 2018), *Cnga1* deletion is accompanied by a lack of CNGB1. This further demonstrates a dependency between both proteins with the generally unaffected protein being degraded in the absence of the other. However, *Cnga1* transcript levels remained unaffected in *Cnga1*^{MUT} mice, thus suggesting the Tyr509Cys mutation to have major impact on protein structure and stability, resulting in CNGA1 degradation rather than non-expression.

In the present study, the progression rate of rod and cone degeneration was examined for a period of about one year, allowing for precise characterization of photoreceptor loss over time. Initial signs of rod degeneration including gliosis and cell death were observed starting from P17. At 5 months of age, the number of photoreceptors was reduced to about 50 %, and it took ~9 months for complete loss of rods. Although both the novel Tyr509Cys mutation and the previously described KO of *Cnga1* led to a relatively rapid rod degeneration (Liu et al., 2021), *Cnga1*^{MUT} mice still showed about 60 % photoreceptor layer thickness at PM4, while the thickness was already reduced to about 20 % in *Cnga1* KO mice. The reason for the different rate of degeneration in these two *Cnga1* mouse models is unknown. Unfortunately, Western blot and immunohistochemistry protein data are missing in the *Cnga1* KO study, meaning that the complete absence of rod CNG channel proteins can only be assumed. Moreover, both mouse models demonstrated reduced rod-mediated retinal response. However, *Cnga1*^{MUT} mice did not show any rod-driven ERG response from the earliest observation point at P21, while *Cnga1* KO mice took 10 weeks to develop complete loss of ERG scotopic response. Nevertheless, Liu et al. only used a 3 cd.s/m^2 ERG stimulus for scotopic ERG measurements, which elicits a mixed response of rods and cones, whereas in the present study rod-specific stimuli of 0.01-0.03 cd.s/m^2 were used. In contrast to primary rod degeneration, secondary degeneration of cone photoreceptors appears to proceed at similar rates in both mouse models, with slower kinetics than rod degeneration.

In conclusion, the missense mutation Tyr509Cys in the CNBD of the rod CNG channel subunit A leads to loss of both channel subunits at the protein level, resulting in profound photoreceptor degeneration and early loss of rod function. The novel *Cnga1*^{MUT} mouse model reflects the phenotype of RP49 very well and is thus excellently suited for future studies on *CNGA1*-linked RP.

5.2 Identification of Retinal Response Pathways to RP

Despite growing knowledge about RP-linked mutations, the precise mechanisms leading to the phenotype of RP are still not well understood. Given the highly heterogeneous nature of the different genetic subtypes of RP, identification and understanding of common retinal response mechanisms is critical for the development of appropriate treatments. To gain better insight into these mechanisms, the present study utilizes proteomic analysis of retinal protein lysates obtained from *Cnga1*^{MUT} mice and *Pde6a*$^{-/-}$ dogs.

5.2.1 Photoreceptor Cell Death by Activation of Stress Response Pathways

Several mechanisms, that may contribute to photoreceptor cell death, have been identified in the past, including ER stress, oxidative stress, and metabolic stress (Newton and Megaw, 2020).

ER stress is defined as an imbalance between the demand for protein synthesis and the capacity of the ER for protein folding. It is known that accumulation of mutant and/or misfolded proteins can cause ER stress, which might also arise in *Cnga1*^{MUT} mice. ER stress can be activated by three sensors (Hetz and Papa, 2018): R-like endoplasmic reticulum kinase (PERK), inositol-requiring enzyme 1 (IRE1) and activating transcription factor 6 (ATF6). In response to ER stress, UPR can be activated to reduce unfolded protein load in the ER (Hetz and Papa, 2018). However, ER stress can also be induced by extensive intracellular Ca^{2+} levels, like observed in *Pde6a*-deficient dogs. The present study provides evidence for the occurrence of ER stress by activation of the PERK pathway as well as increased Ca^{2+} signaling, and subsequent compensatory mechanisms like UPR in both animal models, *Cnga1*^{MUT} mice and *Pde6a*$^{-/-}$ dogs. While several studies suggested that photoreceptor cell death is caused by caspase-dependent apoptosis (Kunte et al., 2012; Choudhury et al., 2013), this was not confirmed in *Cnga1*^{MUT} mice and *Pde6a*$^{-/-}$ dogs. Instead, calpain activation might lead to caspase-independent mechanisms of cell death, which was also observed in different other mouse models (Rodriguez-Muela et al., 2015; Comitato et al., 2020).

Increased ER stress has been hypothesized to result in autophagic cell death (Yao et al., 2018). However, the role of autophagy, a lysosome-mediated degradation process to maintain cell function and survival, has been discussed controversially in the past. Inhibition of autophagy was shown to increase photoreceptor survival in some studies (Yao et al., 2018), whereas others suggested that autophagy has a protective function at least in the early stages of

degeneration (Li et al., 2019). As autophagy is interconnected to the proteasome regulation by the UPS (Kocaturk and Gozuacik, 2018), an imbalance of these systems may promote photoreceptor cell death. The present study demonstrates alterations of several pathways involved in autophagic processes and UPS in both *Cnga1*^{MUT} mice and *Pde6a*$^{-/-}$ dogs by proteomics analysis, thereby strengthening the assumption that dysregulation of both systems contributes to photoreceptor cell death in RP. However, with proteomics analysis showing controversial results, it is not clear whether autophagy is increased or decreased in these animal models. It could be speculated that deactivation of PTEN and activation of AKT occur in an attempt to downregulate autophagy in a compensatory manner. However, for unknown reasons, this is not successful and inactivation of the PI3K/AKT/mTOR pathway follows. To better understand the exact cellular mechanism, further studies are needed to investigate the autophagic and UPS flux through the entire process, including examination of specific markers, such as Atg5, LC3-II or LAMP-2.

The PI3K/AKT/mTOR pathway also plays a role in the regulation of metabolic stress. Several studies demonstrated the involvement of this pathway in reprogramming of the glycolytic machinery in photoreceptors (Punzo et al., 2009; Venkatesh et al., 2015; Zhang et al., 2016). It is well known that photoreceptors preferentially meet their extraordinarily high energy demand by aerobic glycolysis, an effect known as the “Warburg effect” (Warburg, 1956; Ng et al., 2015; Leveillard and Sahel, 2017; Petit et al., 2018; Zhang et al., 2020). However, they are also generally able to produce energy by OXPHOS. Consistently with previous studies (Wubben et al., 2017; Rajala, 2020; Weh et al., 2020), the present study provides evidence for a metabolic shift from aerobic glycolysis to OXPHOS in animal models of RP. Proteomics data revealed overall alteration of several canonical pathways involved in metabolism as well as expression changes of specific proteins within these pathways, such as HK2, PKM2 and HK1. It is known that photoreceptors are vulnerable to oxidative stress due to their high oxygen demand (Wellard et al., 2005; Zeviani and Carelli, 2021) and the high production of ROS during the phototransduction process (Pan et al., 2021). On the one hand OXPHOS activation serves to compensate for metabolic stress caused by loss of aerobic glycolysis and PR death. On the other hand, excessive OXPHOS further enhances the already high production of ROS (Petit et al., 2018; Zhang et al., 2020; Pan et al., 2021). Moreover, hyperoxia, as a consequence of primary photoreceptor cell death and resulting decreased oxygen consumption, additionally causes production of ROS. High levels of ROS induce oxidative stress, which was also observed

in *Cnga1*^{MUT} mice and *Pde6a*$^{-/-}$ dogs. Moreover, downregulation of antioxidant enzyme systems like GSR, which are critical for photoreceptor survival, confirmed the failure to limit oxidative damage in animal models of RP. Increased oxidative stress is known to cause mitochondrial dysfunction and consequently photoreceptor degeneration (Murphy, 2009; Leveillard and Sahel, 2017; Petit et al., 2018; Rajala, 2020). In line with this, this study presents data also suggestive of mitochondrial dysfunction.

Taken together, the results from proteomic analysis of *Cnga1*^{MUT} mice and *Pde6a*$^{-/-}$ dogs demonstrate several hints that initial degeneration of rod photoreceptors is induced by ER stress and by an imbalance between autophagy and the UPS. Secondary cone degeneration then might be a result of increased metabolic and oxidative stress following rod cell death. This is mostly in agreement with previous studies as well as with the morphological and functional data. However, the exact relationship between all these pathways is not yet clear and requires further investigation. More extensive and detailed analyses of the respective processes will be necessary to complement and confirm the exact cellular pathways and their interactions leading to photoreceptor cell death.

5.2.2 Contribution of CNG Channels to the Phenotype of RP

It has previously been postulated that high as well as low intracellular Ca^{2+} levels may have an important impact on photoreceptor degeneration in RP (Biel and Michalakis, 2007; Paquet-Durand et al., 2011; Das et al., 2021). In both cases, accumulation of cGMP is significantly involved. Mutations affecting PDE6 (as in *Pde6a*$^{-/-}$ dogs or *Pde6a*^{MUT} mice) directly result in cGMP accumulation and thus in CNG channel overactivation and extensive Ca^{2+} influx. CNG channelopathies caused by mutation in *Cnga1* or *Cngb1* (as in *Cnga1*^{MUT} or *Cngb1*$^{-/-}$ mice), however, lead to low intracellular Ca^{2+} followed by disinhibition of GCs and indirect cGMP accumulation. Both high intracellular Ca^{2+} levels as well as CNG channel depletion result in photoreceptor depolarization (Schön et al., 2016a; Das et al., 2021). This in turn activates L-type voltage-gated Ca^{2+} channels (VGCCs), which then promote even more Ca^{2+} influx resulting in calpain activation and cell death. CNG channels as well as VGCCs are suggested to have a major impact on calpain activation (Schön et al., 2016a; Schön et al., 2016b). Proteomics data presented in this study indicate both alterations in Ca^{2+} levels and in calpain activation in *Pde6a*$^{-/-}$ and *Cnga1*^{MUT} animal models, confirming their participation in photoreceptor cell death and pointing out a key role for CNG channels. Previous studies also showed

morphological rescue of rod photoreceptors by ablation of CNG channels in *Pde6b*- and *Pde6g*-deficient mice (Paquet-Durand et al., 2011; Wang et al., 2017). In the present study, two DBM *Pde6a*^{MUT}*xCngb1*$^{-/-}$ mouse models were investigated for similar effects. Indeed, additional CNG channel ablation in *Pde6a*-deficient mice also resulted in outstanding rescue of photoreceptor morphology. This suggests that extensive Ca^{2+} influx is prevented by depletion of CNG channels, resulting in less calpain activity and reduced photoreceptor cell death. Conversely, pharmacological blockade of CNG channels and thus Ca^{2+} influx by the Ca^{2+} channel blocker diltiazem was recently demonstrated to reduce photoreceptor viability, suggesting a protective role for low level Ca^{2+} influx (Das et al., 2022). Thus, it is not clear whether a reduction of Ca^{2+} influx is responsible for the retinal rescue in *Pde6a*^{MUT}*xCngb1*$^{-/-}$ DBM mice, despite a prevention of calpain activity can be assumed. Moreover, a recent study discovered that poly (ADP-ribose) polymerase (PARP), a DNA repair enzyme, is dependent on CNG channel and VGCC activity (Yan et al., 2022). PARP is suggested to be activated by cGMP accumulation (Power et al., 2020) and was reported to be involved in parthanatos, a specific form of cell death, thereby contributing to photoreceptor cell death in RP (David et al., 2009). Moreover, Yan et al. found PARP to be an upstream regulator of calpain. Thus, *Pde6a*^{MUT}*xCngb1*$^{-/-}$ mice might also benefit from decreased PARP activity as a consequence of CNG channel depletion, resulting in less calpain activation. However, Ca^{2+}, PARP and calpain levels were not directly examined in this study and further investigations are needed.

Synaptogenesis, as observed by neurite sprouting into the outer retina as a response to photoreceptor degeneration, has previously been reported in human patients and animal models of RP (Li et al., 1995; Claes et al., 2004; Hüttl et al., 2005; Michalakis et al., 2013). Since such processes were detected in mice lacking CNG channels by knockout of *Cngb1* (Hüttl et al., 2005), it was expected to find neurite sprouting in *Cnga1*^{MUT} mice as well. However, no evidence for synaptogenesis was found in mice lacking CNGA1 at early stages of degeneration, neither by immunohistochemistry nor proteomics analysis. On the contrary, in fact, rather a retraction and loss of retinal neurons was detected. The same phenomenon of neurite retraction was also observed in *rd10* mice (Barhoum et al., 2008; Phillips et al., 2010). These findings led to the hypothesis that rods lacking CNGB1 still have remaining electrical signal which triggers neurite sprouting towards rods, and that the CNGA1 subunit is responsible for generating this signal. In *Cnga1*^{MUT} mice, however, the deficiency of the electrical signal-generating subunit CNGA1 causes totally non-active rods, leading to retraction of neurons

owing to missing electrical stimuli. However, *Cnga1*^{MUT} mice at PM6 showed spontaneous late neurite growth. Additionally, and in contrast to PM1 data, proteomics analysis revealed, a downregulation of neuronal cell death and an upregulation of neurite outgrowth at PM6. As these events occur simultaneously to the onset of cone degeneration, late neurite sprouting may be an attempt to preserve and rescue declining neurotransmission in cones. However, another study showed cone neurite sprouting already starting with onset of rod degeneration in *rd1* mice (Fei, 2002), which could not be confirmed in *Cnga1*^{MUT} mice. Moreover, it is not clear whether only rods or cones or both participate in the occurring synapse degeneration and synaptogenesis in *Cnga1*^{MUT} mice. Further investigations are needed including the use of specific markers like mGluR6 as well as the analysis of the exact onset of late neurite sprouting. Taken together, it is clear that loss of CNG channels causes the typical phenotype of RP. However, is has also been shown that additional CNG channel ablation in different *Pde6*-deficient animal models results in outstanding rescue of photoreceptor morphology and function. As there are several possible mechanisms by which dysfunctional or absent CNG channels could contribute to the phenotype of RP at the cellular level, future studies will need to directly examine these potential cellular pathways. Moreover, the reason for the differential occurrence of neurite sprouting in different animal models of RP is not yet fully understood and requires further investigation.

5.3 Novel Gene Augmentation Therapies for RP

Currently, there is no curative treatment for RP available. However, several preclinical studies using gene therapeutic approaches demonstrated encouraging results (Petersen-Jones et al., 2009; Beltran et al., 2015; Mowat et al., 2017; Occelli et al., 2017; Schön et al., 2017; Cideciyan et al., 2018; Cehajic-Kapetanovic et al., 2020; Wagner et al., 2021). In the present study, rAAV vectors expressing the respective therapeutic transgenes were administered to *Cngb1*- and, for the first time, to *Cnga1*-deficient mouse models.

5.3.1 Improvement of Gene Augmentation Therapy for *CNGB1*-linked RP

In the past, preclinical proof-of-concept studies using rAAV-mediated, species-matched gene supplementation in mice and dogs have already shown great success (Koch et al., 2012; Petersen-Jones et al., 2018). In this study, rAAV5.hCNGB1/mod, a novel modified rAAV for gene augmentation of human CNGB1, was developed. One-time subretinal treatment of *Cngb1*$^{-/-}$ mice resulted in morphological rescue of rods and cones as well as functional benefit. Although being only a modulatory subunit, CNGB1 is essential for formation, intracellular transport, and functionality of the rod CNG channel. Comparable to its predecessor (Wagner et al., 2021), rAAV5.hCNGB1/mod achieved robust expression of hCNGB1 as well as rescue of endogenous murine CNGA1 protein, resulting in formation of functional CNG channels in *Cngb1*$^{-/-}$ mice. Notably, comparing both therapeutic vectors revealed optimal expression results of hCNGB1 at different doses. While rAAV5.hCNGB1 only needed a total vector dose of 10^9 vg, a higher dose of 10^{10} vg was necessary using rAAV5.hCNGB1/mod. However, this is most likely due to the different production methods of the two therapeutic vectors: rAAV5.hCNGB1 was produced in a HeLa producer cell line, whereas rAAV5.hCNGB1/mod was obtained by triple-transfection of HEK293T cells. While mCNGA1, rescued by treatment with rAAV5.hCNGB1/mod, localized exclusively to rod OS, vector-derived hCNGB1 expression was also found in rod IS and cell bodies. This was not observed in species-matched approaches (Koch et al., 2012; Petersen-Jones et al., 2018). However, proper hCNGB1 localization was detected in the transition region between treated and untreated part in the same retina, suggesting an oversupply of vector-derived hCNGB1. CNG channels are built of three CNGA1 and one CNGB1 subunit. Thus, CNGA1 might represent the limiting factor for assembly of CNG channels, preventing treated rods from exceeding the number of wild type levels CNG channels. Nevertheless, a dose reduction in order to cause hCNGB1 localization in rod OS only,

might not achieve sufficient functional rescue of rod photoreceptors. In the previous study, treatment with a lower dose of rAAV5.hCNGB1 showed morphologic rescue but less improvement in functionality. Moreover, also this lower dose resulted in improperly localized hCNGB1 (Wagner et al., 2021). An explanation for this difference to species-matched approaches includes that oversupplied mCNGB1 is degraded immediately after species-matched gene therapy, while elimination of hCNGB1 takes longer and thus degradation products were detected in rod IS and ONL. In addition, species-matched CNGB1 and CNGA1 protein are expected to fuse with 100 % fidelity, whereas hCNGB1 and mCNGA1 fuse with only ~70 % cross-species fidelity (Wagner et al., 2021), possibly also contributing to improper localization of hCNGB1.

Overall, comparison of rAAV5.hCNGB1/mod with its template rAAV5.hCNGB1 revealed similar results regarding expression levels, rescue of rod-mediated function, and photoreceptor layer thickness with both therapeutic vectors. Remarkably, treatment with rAAV5.hCNGB1/mod resulted in even less Müller cell gliosis than treatment with rAAV5.hCNGB1, possibly indicating its potential for greater reduction of retinal stress. However, the mechanisms contributing to retinal stress are not well understood, and further investigation is needed to determine the potential of therapeutic vectors to reduce retinal stress.

In summary, the present study showed efficient beneficial effects on retinal morphology and rescue of retinal function by treatment with rAAV5.hCNGB1/mod, which was comparable to treatment with rAAV5.hCNGB1.

5.3.2 Heading Towards Minimally Invasive Technique: Intravitreal Gene Augmentation Therapy for *CNGA1*-linked RP

Until recently, no suitable *Cnga1*-deficient mouse model was available, making the development of an appropriate therapy for *CNGA1*-linked RP almost impossible. However, the generation and characterization of the *Cnga1*^{MUT} mouse model now offers new possibilities. In a first proof-of-concept study, *Cnga1*^{MUT} mice were treated with a one-time subretinal administration of rAAV2\GL.hCNGA1. Conventional subretinal treatment resulted in robust expression of vector-derived hCNGA1, together with rescue of endogenous mCNGB1. Notably, considerably less improper localization of vector-derived human transgene product, as observed in *Cngb1*$^{-/-}$ mice, was detected after treatment with rAAV2\GL.hCNGA1. Instead, hCNGA1 localized mostly in rod OS and IS. Moreover, rAAV2\GL.hCNGA1 achieved

improvement of rod-mediated function as detected by profound increases in ERG b-wave amplitudes. However, subretinal injections are invasive and require iatrogenic retinal detachment, potentially leading to photoreceptor damage and vision impairment (Jacobson et al., 2006; Peng et al., 2017). In addition, only small parts of the retina can be treated by single injections, which either requires multiple injections and thus carries a higher risk or leads to a lower therapeutic effect. Therefore, intravitreal injections have recently received more and more attention. These are easier to perform and less invasive, reach a wide retinal area, and cause less damage to the retina. However, delivery to the outer retinal cells seems to be less efficient (Harvey et al., 2002; Dalkara et al., 2009). Hence, AAV capsid engineering to overcome these limitations has become of great interest in recent years (Petrs-Silva et al., 2009; Dalkara et al., 2013; Kay et al., 2013; Zinn et al., 2015; Grimm and Buning, 2017; Barnes et al., 2019; Katada et al., 2019; Pavlou et al., 2021; Ross and Ofri, 2021). The novel engineered AAV2\GL capsid was recently shown to efficiently transduce photoreceptors after a single intravitreal injection in mice, dogs and non-human primates (NHP) (Pavlou et al., 2021). In the present study, it was demonstrated that rAAV2\GL.hCNGA1 can achieve beneficial effects on retinal function by conventional subretinal injection, as well as by intravitreal injection. Interestingly, after intravitreal injection, vector-derived hCNGA1 was expressed exclusively in rod OS. Considering that transduction of outer retinal cells is less efficient after intravitreal injections, it is tempting to speculate that the apparent disadvantage of this method in this case led to the delivery of a more optimal viral dose. Indeed, not only proper protein localization, but also intact functionality of chimeric CNG channels consisting of hCNGA1 and endogenous mCNGB1 was demonstrated. On the one hand, this is supported by normalization of the aberrantly high levels of cGMP in *Cnga1*^{MUT} rods arising from missing negative feedback on cGMP-producing GCs. On the other hand, intravitreal administration of rAAV2\GL.hCNGA1 led to improvements in retinal function as detected by ERG, further confirming functional CNG channel formation. Moreover, treatment with rAAV2\GL.hCNGA1 also reduced Müller cell gliosis, a commonly observed phenomenon in retinal degeneration.

In conclusion, the present study is the first to demonstrate successful therapy of *CNGA1*-linked RP using a potent therapeutic vector that shows significant treatment effects not only by subretinal but also by intravitreal injection.

5.4 Summary

RP, a group of hereditary blinding diseases that affect more than 1.5 million patients worldwide, is characterized by progressive retinal degeneration beginning with primary degeneration of rod photoreceptors, followed by the secondary loss of cone photoreceptors. RP is usually caused by mutations in genes that are necessary for the phototransduction process. Despite great scientific efforts, the underlying mechanisms are still unclear. However, understanding the common mechanisms that lead to photoreceptor death in RP is important for developing therapies, as currently no curative treatment options exist.

In the present study, the novel *Cnga1*^{MUT} mouse line was characterized. It was shown that the missense mutation Tyr509Cys in the A subunit of the major rod CNG channel leads to loss of both channel subunits, resulting in profound photoreceptor degeneration and early loss of rod function. This is accompanied by progressive retinal degeneration and by secondary loss of cone photoreceptors at later stages. Thus, the new *Cnga1*^{MUT} mouse model closely reflects the phenotype of human RP49 and provides new opportunities for future studies on *CNGA1*-linked RP as well as for the development of potential therapeutic approaches.

Moreover, by taking different animal models into account, proteomic analysis revealed several signaling pathways to be altered in RP. These suggest the involvement of ER stress, autophagy, metabolic and oxidative stress in photoreceptor cell death. Further in-depth investigation of such common retinal response mechanisms among the different genetic subtypes of RP will be critical for the development of appropriate treatments.

Finally, two novel therapeutic vectors aiming to treat *CNGB1*- and *CNGA1*-linked RP were developed. Both vectors showed beneficial effect on retinal morphology and rescue of retinal function by either one-time subretinal or even less invasive intravitreal injection, together demonstrating gene augmentation therapy as a promising approach to treat RP.

Overall, this study contributes to a broader knowledge of the pathogenesis of RP and offers new directions for expand treatment options for human patients.

6 References

Ahonen, S.J., Arumilli, M. and Lohi, H. (2013). "A CNGB1 frameshift mutation in Papillon and Phalene dogs with progressive retinal atrophy." PLoS One **8**(8): e72122.

Allocca, M., Mussolino, C., Garcia-Hoyos, M., Sanges, D., Iodice, C., Petrillo, M., Vandenberghe, L.H., Wilson, J.M., Marigo, V., Surace, E.M. and Auricchio, A. (2007). "Novel adeno-associated virus serotypes efficiently transduce murine photoreceptors." J Virol **81**(20): 11372-11380.

Ardell, M.D., Aragon, I., Oliveira, L., Porche, G.E., Burke, E. and Pittler, S.J. (1996). "The beta subunit of human rod photoreceptor cGMP-gated cation channel is generated from a complex transcription unit." FEBS Lett **389**(2): 213-218.

Ardell, M.D., Bedsole, D.L., Schoborg, R.V. and Pittler, S.J. (2000). "Genomic organization of the human rod photoreceptor cGMP-gated cation channel beta-subunit gene." Gene **245**(2): 311-318.

Arshavsky, V.Y. and Burns, M.E. (2012). "Photoreceptor signaling: supporting vision across a wide range of light intensities." J Biol Chem **287**(3): 1620-1626.

Auricchio, A. (2003). "Pseudotyped AAV vectors for constitutive and regulated gene expression in the eye." Vision Res **43**(8): 913-918.

Azam, M., Collin, R.W., Malik, A., Khan, M.I., Shah, S.T., Shah, A.A., Hussain, A., Sadeque, A., Arimadyo, K., Ajmal, M., Azam, A., Qureshi, N., Bokhari, H., Strom, T.M., Cremers, F.P., Qamar, R. and den Hollander, A.I. (2011). "Identification of novel mutations in Pakistani families with autosomal recessive retinitis pigmentosa." Arch Ophthalmol **129**(10): 1377-1378.

Ba-Abbad, R., Holder, G.E., Robson, A.G., Neveu, M.M., Waseem, N., Arno, G. and Webster, A.R. (2019). "Isolated rod dysfunction associated with a novel genotype of CNGB1." Am J Ophthalmol Case Rep **14**: 83-86.

Baccus, S.A., Olveczky, B.P., Manu, M. and Meister, M. (2008). "A retinal circuit that computes object motion." J Neurosci **28**(27): 6807-6817.

Baek, M., DiMaio, F., Anishchenko, I., Dauparas, J., Ovchinnikov, S., Lee, G.R., Wang, J., Cong, Q., Kinch, L.N., Schaeffer, R.D., Millan, C., Park, H., Adams, C., Glassman, C.R., DeGiovanni, A., Pereira, J.H., Rodrigues, A.V., van Dijk, A.A., Ebrecht, A.C., Opperman, D.J., Sagmeister, T., Buhlheller, C., Pavkov-Keller, T., Rathinaswamy, M.K., Dalwadi, U., Yip, C.K., Burke, J.E., Garcia, K.C., Grishin, N.V., Adams, P.D., Read, R.J. and Baker, D. (2021). "Accurate prediction of protein structures and interactions using a three-track neural network." Science **373**(6557): 871-876.

Bainbridge, J.W., Smith, A.J., Barker, S.S., Robbie, S., Henderson, R., Balaggan, K., Viswanathan, A., Holder, G.E., Stockman, A., Tyler, N., Petersen-Jones, S., Bhattacharya, S.S., Thrasher, A.J., Fitzke, F.W., Carter, B.J., Rubin, G.S., Moore, A.T. and Ali, R.R. (2008). "Effect of gene therapy on visual function in Leber's congenital amaurosis." N Engl J Med **358**(21): 2231-2239.

Bareil, C., Hamel, C.P., Delague, V., Arnaud, B., Demaille, J. and Claustres, M. (2001). "Segregation of a mutation in CNGB1 encoding the beta-subunit of the rod cGMP-gated channel in a family with autosomal recessive retinitis pigmentosa." Hum Genet **108**(4): 328-334.

Barhoum, R., Martinez-Navarrete, G., Corrochano, S., Germain, F., Fernandez-Sanchez, L., de la Rosa, E.J., de la Villa, P. and Cuenca, N. (2008). "Functional and structural modifications during retinal degeneration in the rd10 mouse." Neuroscience **155**(3): 698-713.

Barnes, C., Scheideler, O. and Schaffer, D. (2019). "Engineering the AAV capsid to evade immune responses." Curr Opin Biotechnol **60**: 99-103.

Beltran, W.A., Cideciyan, A.V., Iwabe, S., Swider, M., Kosyk, M.S., McDaid, K., Martynyuk, I., Ying, G.S., Shaffer, J., Deng, W.T., Boye, S.L., Lewin, A.S., Hauswirth, W.W., Jacobson, S.G. and Aguirre, G.D. (2015). "Successful arrest of photoreceptor and vision loss expands the therapeutic window of retinal gene therapy to later stages of disease." Proc Natl Acad Sci U S A **112**(43): E5844-5853.

Biel, M. and Michalakis, S. (2007). "Function and dysfunction of CNG channels: insights from channelopathies and mouse models." Mol Neurobiol **35**(3): 266-277.

Biel, M. and Michalakis, S. (2009). "Cyclic nucleotide-gated channels." Handb Exp Pharmacol(191): 111-136.

Biel, M., Seeliger, M., Pfeifer, A., Kohler, K., Gerstner, A., Ludwig, A., Jaissle, G., Fauser, S., Zrenner, E. and Hofmann, F. (1999a). "Selective loss of cone function in mice lacking the cyclic nucleotide-gated channel CNG3." Proc Natl Acad Sci U S A **96**(13): 7553-7557.

Biel, M., Zong, X., Ludwig, A., Sautter, A. and Hofmann, F. (1999b). "Structure and function of cyclic nucleotide-gated channels." Rev Physiol Biochem Pharmacol **135**: 151-171.

Black, A., Vasireddy, V., Chung, D.C., Maguire, A.M., Gaddameedi, R., Tolmachova, T., Seabra, M. and Bennett, J. (2014). "Adeno-associated virus 8-mediated gene therapy for choroideremia: preclinical studies in in vitro and in vivo models." J Gene Med **16**(5-6): 122-130.

Bocquet, B., Marzouka, N.A., Hebrard, M., Manes, G., Senechal, A., Meunier, I. and Hamel, C.P. (2013). "Homozygosity mapping in autosomal recessive retinitis pigmentosa families detects novel mutations." Mol Vis **19**: 2487-2500.

Bönigk, W., Bradley, J., Muller, F., Sesti, F., Boekhoff, I., Ronnett, G.V., Kaupp, U.B. and Frings, S. (1999). "The native rat olfactory cyclic nucleotide-gated channel is composed of three distinct subunits." J Neurosci **19**(13): 5332-5347.

Botto, C., Rucli, M., Tekinsoy, M.D., Pulman, J., Sahel, J.A. and Dalkara, D. (2021). "Early and late stage gene therapy interventions for inherited retinal degenerations." Prog Retin Eye Res: 100975.

Brelidze, T.I., Carlson, A.E. and Zagotta, W.N. (2009). "Absence of direct cyclic nucleotide modulation of mEAG1 and hERG1 channels revealed with fluorescence and electrophysiological methods." J Biol Chem **284**(41): 27989-27997.

Bringmann, A., Iandiev, I., Pannicke, T., Wurm, A., Hollborn, M., Wiedemann, P., Osborne, N.N. and Reichenbach, A. (2009). "Cellular signaling and factors involved in Muller cell gliosis: neuroprotective and detrimental effects." Prog Retin Eye Res **28**(6): 423-451.

Bringmann, A. and Reichenbach, A. (2001). "Role of Muller cells in retinal degenerations." Front Biosci **6**: E72-92.

Bringmann, A. and Wiedemann, P. (2012). "Muller glial cells in retinal disease." Ophthalmologica **227**(1): 1-19.

Buch, P.K., MacLaren, R.E. and Ali, R.R. (2007). "Neuroprotective gene therapy for the treatment of inherited retinal degeneration." Curr Gene Ther **7**(6): 434-445.

Burnight, E.R., Gupta, M., Wiley, L.A., Anfinson, K.R., Tran, A., Triboulet, R., Hoffmann, J.M., Klaahsen, D.L., Andorf, J.L., Jiao, C., Sohn, E.H., Adur, M.K., Ross, J.W., Mullins, R.F., Daley, G.Q., Schlaeger, T.M., Stone, E.M. and Tucker, B.A. (2017). "Using CRISPR-Cas9 to Generate Gene-Corrected Autologous iPSCs for the Treatment of Inherited Retinal Degeneration." Mol Ther **25**(9): 1999-2013.

Busskamp, V., Duebel, J., Balya, D., Fradot, M., Viney, T.J., Siegert, S., Groner, A.C., Cabuy, E., Forster, V., Seeliger, M., Biel, M., Humphries, P., Paques, M., Mohand-Said, S., Trono, D., Deisseroth, K., Sahel, J.A., Picaud, S. and Roska, B. (2010). "Genetic reactivation of cone photoreceptors restores visual responses in retinitis pigmentosa." Science **329**(5990): 413-417.

Carter-Dawson, L.D. and LaVail, M.M. (1979). "Rods and cones in the mouse retina. I. Structural analysis using light and electron microscopy." J Comp Neurol **188**(2): 245-262.

Carvalho, L.S., Xu, J., Pearson, R.A., Smith, A.J., Bainbridge, J.W., Morris, L.M., Fliesler, S.J., Ding, X.Q. and Ali, R.R. (2011). "Long-term and age-dependent restoration of visual function in a mouse model of CNGB3-associated achromatopsia following gene therapy." Hum Mol Genet **20**(16): 3161-3175.

Cehajic-Kapetanovic, J., Xue, K., Martinez-Fernandez de la Camara, C., Nanda, A., Davies, A., Wood, L.J., Salvetti, A.P., Fischer, M.D., Aylward, J.W., Barnard, A.R., Jolly, J.K., Luo, E., Lujan, B.J., Ong, T., Girach, A., Black, G.C.M., Gregori, N.Z., Davis, J.L., Rosa, P.R., Lotery, A.J., Lam, B.L., Stanga, P.E. and MacLaren, R.E. (2020). "Initial results from a first-in-human gene therapy trial on X-linked retinitis pigmentosa caused by mutations in RPGR." Nat Med **26**(3): 354-359.

Chen, T.Y., Peng, Y.W., Dhallan, R.S., Ahamed, B., Reed, R.R. and Yau, K.W. (1993). "A new subunit of the cyclic nucleotide-gated cation channel in retinal rods." Nature **362**(6422): 764-767.

Chen, X., Zhao, K., Sheng, X., Li, Y., Gao, X., Zhang, X., Kang, X., Pan, X., Liu, Y., Jiang, C., Shi, H., Chen, X., Rong, W., Chen, L.J., Lai, T.Y., Liu, Y., Wang, X., Yuan, S., Liu, Q., Vollrath, D., Pang, C.P. and Zhao, C. (2013). "Targeted sequencing of 179 genes associated with hereditary retinal dystrophies and 10 candidate genes identifies novel and known mutations in patients with various retinal diseases." Invest Ophthalmol Vis Sci **54**(3): 2186-2197.

Cheng, S.Y., Wang, S.C., Lei, M., Wang, Z. and Xiong, K. (2018). "Regulatory role of calpain in neuronal death." Neural Regen Res **13**(3): 556-562.

Chinchore, Y., Begaj, T., Wu, D., Drokhlyansky, E. and Cepko, C.L. (2017). "Glycolytic reliance promotes anabolism in photoreceptors." Elife **6**.

Choudhury, S., Bhootada, Y., Gorbatyuk, O. and Gorbatyuk, M. (2013). "Caspase-7 ablation modulates UPR, reprograms TRAF2-JNK apoptosis and protects T17M rhodopsin mice from severe retinal degeneration." Cell Death Dis **4**: e528.

Chow, A.Y., Chow, V.Y., Packo, K.H., Pollack, J.S., Peyman, G.A. and Schuchard, R. (2004). "The artificial silicon retina microchip for the treatment of vision loss from retinitis pigmentosa." Arch Ophthalmol **122**(4): 460-469.

Cideciyan, A.V., Sudharsan, R., Dufour, V.L., Massengill, M.T., Iwabe, S., Swider, M., Lisi, B., Sumaroka, A., Marinho, L.F., Appelbaum, T., Rossmiller, B., Hauswirth, W.W., Jacobson, S.G., Lewin, A.S., Aguirre, G.D. and Beltran, W.A. (2018). "Mutation-independent rhodopsin gene therapy by knockdown and replacement with a single AAV vector." Proc Natl Acad Sci U S A **115**(36): E8547-E8556.

Claes, E., Seeliger, M., Michalakis, S., Biel, M., Humphries, P. and Haverkamp, S. (2004). "Morphological characterization of the retina of the CNGA3(-/-)Rho(-/-) mutant mouse lacking functional cones and rods." Invest Ophthalmol Vis Sci **45**(6): 2039-2048.

Comitato, A., Schiroli, D., Montanari, M. and Marigo, V. (2020). "Calpain Activation Is the Major Cause of Cell Death in Photoreceptors Expressing a Rhodopsin Misfolding Mutation." Mol Neurobiol **57**(2): 589-599.

Corton, M., Blanco, M.J., Torres, M., Sanchez-Salorio, M., Carracedo, A. and Brion, M. (2010). "Identification of a novel mutation in the human PDE6A gene in autosomal recessive retinitis pigmentosa: homology with the nmf28/nmf28 mice model." Clin Genet **78**(5): 495-498.

Cote, R.H. (2021). "Photoreceptor phosphodiesterase (PDE6): activation and inactivation mechanisms during visual transduction in rods and cones." Pflugers Arch **473**(9): 1377-1391.

Craven, K.B. and Zagotta, W.N. (2006). "CNG and HCN channels: two peas, one pod." Annu Rev Physiol **68**: 375-401.

Curcio, C.A., Sloan, K.R., Kalina, R.E. and Hendrickson, A.E. (1990). "Human photoreceptor topography." J Comp Neurol **292**(4): 497-523.

D'Costa, S., Blouin, V., Broucque, F., Penaud-Budloo, M., Francois, A., Perez, I.C., Le Bec, C., Moullier, P., Snyder, R.O. and Ayuso, E. (2016). "Practical utilization of recombinant AAV vector reference standards: focus on vector genomes titration by free ITR qPCR." Mol Ther Methods Clin Dev **5**: 16019.

Dalkara, D., Byrne, L.C., Klimczak, R.R., Visel, M., Yin, L., Merigan, W.H., Flannery, J.G. and Schaffer, D.V. (2013). "In vivo-directed evolution of a new adeno-associated virus for therapeutic outer retinal gene delivery from the vitreous." Sci Transl Med **5**(189): 189ra176.

Dalkara, D., Goureau, O., Marazova, K. and Sahel, J.A. (2016). "Let There Be Light: Gene and Cell Therapy for Blindness." Hum Gene Ther **27**(2): 134-147.

Dalkara, D., Kolstad, K.D., Caporale, N., Visel, M., Klimczak, R.R., Schaffer, D.V. and Flannery, J.G. (2009). "Inner limiting membrane barriers to AAV-mediated retinal transduction from the vitreous." Mol Ther **17**(12): 2096-2102.

Dalkara, D. and Sahel, J.A. (2014). "Gene therapy for inherited retinal degenerations." C R Biol **337**(3): 185-192.

Das, S., Chen, Y., Yan, J., Christensen, G., Belhadj, S., Tolone, A. and Paquet-Durand, F. (2021). "The role of cGMP-signalling and calcium-signalling in photoreceptor cell death: perspectives for therapy development." Pflugers Arch **473**(9): 1411-1421.

Das, S., Popp, V., Power, M., Groeneveld, K., Yan, J., Melle, C., Rogerson, L., Achury, M., Schwede, F., Strasser, T., Euler, T., Paquet-Durand, F. and Nache, V. (2022). "Redefining the role of Ca(2+)-permeable channels in photoreceptor degeneration using diltiazem." Cell Death Dis **13**(1): 47.

David, K.K., Andrabi, S.A., Dawson, T.M. and Dawson, V.L. (2009). "Parthanatos, a messenger of death." Front Biosci (Landmark Ed) **14**(3): 1116-1128.

Dawood, M., Lin, S., Din, T.U., Shah, I.U., Khan, N., Jan, A., Marwan, M., Sultan, K., Nowshid, M., Tahir, R., Ahmed, A.N., Yasin, M., Baple, E.L., Crosby, A.H. and Saleha, S. (2021). "Novel mutations in PDE6A and CDHR1 cause retinitis pigmentosa in Pakistani families." Int J Ophthalmol **14**(12): 1843-1851.

de Raad, S., Szczesny, P.J., Munz, K. and Reme, C.E. (1996). "Light damage in the rat retina: glial fibrillary acidic protein accumulates in Muller cells in correlation with photoreceptor damage." Ophthalmic Res **28**(2): 99-107.

Dhallan, R.S., Macke, J.P., Eddy, R.L., Shows, T.B., Reed, R.R., Yau, K.W. and Nathans, J. (1992). "Human rod photoreceptor cGMP-gated channel: amino acid sequence, gene structure, and functional expression." J Neurosci **12**(8): 3248-3256.

Diamond, J.S. (2017). "Inhibitory Interneurons in the Retina: Types, Circuitry, and Function." Annu Rev Vis Sci **3**: 1-24.

Dias, M.F., Joo, K., Kemp, J.A., Fialho, S.L., da Silva Cunha, A., Jr., Woo, S.J. and Kwon, Y.J. (2018). "Molecular genetics and emerging therapies for retinitis pigmentosa: Basic research and clinical perspectives." Prog Retin Eye Res **63**: 107-131.

Ding, X.Q., Matveev, A., Singh, A., Komori, N. and Matsumoto, H. (2012). "Biochemical characterization of cone cyclic nucleotide-gated (CNG) channel using the infrared fluorescence detection system." Adv Exp Med Biol **723**: 769-775.

Drack, A.V., Dumitrescu, A.V., Bhattarai, S., Gratie, D., Stone, E.M., Mullins, R. and Sheffield, V.C. (2012). "TUDCA slows retinal degeneration in two different mouse models of retinitis pigmentosa and prevents obesity in Bardet-Biedl syndrome type 1 mice." Invest Ophthalmol Vis Sci **53**(1): 100-106.

Dryja, T.P., Finn, J.T., Peng, Y.W., McGee, T.L., Berson, E.L. and Yau, K.W. (1995). "Mutations in the gene encoding the alpha subunit of the rod cGMP-gated channel in autosomal recessive retinitis pigmentosa." Proc Natl Acad Sci U S A **92**(22): 10177-10181.

Dryja, T.P., Rucinski, D.E., Chen, S.H. and Berson, E.L. (1999). "Frequency of mutations in the gene encoding the alpha subunit of rod cGMP-phosphodiesterase in autosomal recessive retinitis pigmentosa." Invest Ophthalmol Vis Sci **40**(8): 1859-1865.

Ekstrom, P., Sanyal, S., Narfstrom, K., Chader, G.J. and van Veen, T. (1988). "Accumulation of glial fibrillary acidic protein in Muller radial glia during retinal degeneration." Invest Ophthalmol Vis Sci **29**(9): 1363-1371.

Euler, T., Haverkamp, S., Schubert, T. and Baden, T. (2014). "Retinal bipolar cells: elementary building blocks of vision." Nat Rev Neurosci **15**(8): 507-519.

Fahim, A.T., Daiger, S.P. and Weleber, R.G. (1993). Nonsyndromic Retinitis Pigmentosa Overview. GeneReviews((R)). M. P. Adam, H. H. Ardinger, R. A. Pagon et al. Seattle (WA).

Fain, G.L. (2006). "Why photoreceptors die (and why they don't)." Bioessays **28**(4): 344-354.

Farber, D.B. and Lolley, R.N. (1974). "Cyclic guanosine monophosphate: elevation in degenerating photoreceptor cells of the C3H mouse retina." Science **186**(4162): 449-451.

Fei, Y. (2002). "Cone neurite sprouting: an early onset abnormality of the cone photoreceptors in the retinal degeneration mouse." Mol Vis **8**: 306-314.

Finn, J.T., Grunwald, M.E. and Yau, K.W. (1996). "Cyclic nucleotide-gated ion channels: an extended family with diverse functions." Annu Rev Physiol **58**: 395-426.

Fiscus, R.R. (2002). "Involvement of cyclic GMP and protein kinase G in the regulation of apoptosis and survival in neural cells." Neurosignals **11**(4): 175-190.

Flynn, G.E. and Zagotta, W.N. (2001). "Conformational changes in S6 coupled to the opening of cyclic nucleotide-gated channels." Neuron **30**(3): 689-698.

Fox, D.A., Poblenz, A.T. and He, L. (1999). "Calcium overload triggers rod photoreceptor apoptotic cell death in chemical-induced and inherited retinal degenerations." Ann N Y Acad Sci **893**: 282-285.

Fradin, M., Colin, E., Hannouche-Bared, D., Audo, I., Sahel, J.A., Biskup, S., Carre, W., Ziegler, A., Wilhelm, C., Guichet, A., Odent, S. and Bonneau, D. (2016). "Run of homozygosity analysis reveals a novel nonsense variant of the CNGB1 gene involved in retinitis pigmentosa 45." Ophthalmic Genet **37**(3): 357-359.

Frasson, M., Sahel, J.A., Fabre, M., Simonutti, M., Dreyfus, H. and Picaud, S. (1999). "Retinitis pigmentosa: rod photoreceptor rescue by a calcium-channel blocker in the rd mouse." Nat Med **5**(10): 1183-1187.

Fu, Q., Wang, F., Wang, H., Xu, F., Zaneveld, J.E., Ren, H., Keser, V., Lopez, I., Tuan, H.F., Salvo, J.S., Wang, X., Zhao, L., Wang, K., Li, Y., Koenekoop, R.K., Chen, R. and Sui, R. (2013). "Next-generation sequencing-based molecular diagnosis of a Chinese patient cohort with autosomal recessive retinitis pigmentosa." Invest Ophthalmol Vis Sci **54**(6): 4158-4166.

Fu, Y. (1995). Phototransduction in Rods and Cones. Webvision: The Organization of the Retina and Visual System. H. Kolb, E. Fernandez and R. Nelson. Salt Lake City (UT).

Gao, G., Vandenberghe, L.H., Alvira, M.R., Lu, Y., Calcedo, R., Zhou, X. and Wilson, J.M. (2004). "Clades of Adeno-associated viruses are widely disseminated in human tissues." J Virol **78**(12): 6381-6388.

Gao, G.P., Alvira, M.R., Wang, L., Calcedo, R., Johnston, J. and Wilson, J.M. (2002). "Novel adeno-associated viruses from rhesus monkeys as vectors for human gene therapy." Proc Natl Acad Sci U S A **99**(18): 11854-11859.

Gao, Q., Liu, Y., Lei, X., Deng, Q., Tong, Y., Du, L. and Shen, Y. (2019). "A Novel CNGA1 Gene Mutation (c.G622A) of Autosomal Recessive Retinitis Pigmentosa Leads to the CNGA1 Protein Reduction on Membrane." Biochem Genet **57**(4): 540-554.

Garafalo, A.V., Cideciyan, A.V., Heon, E., Sheplock, R., Pearson, A., WeiYang Yu, C., Sumaroka, A., Aguirre, G.D. and Jacobson, S.G. (2020). "Progress in treating inherited retinal diseases: Early subretinal gene therapy clinical trials and candidates for future initiatives." Prog Retin Eye Res **77**: 100827.

Goulding, E.H., Tibbs, G.R., Liu, D. and Siegelbaum, S.A. (1993). "Role of H5 domain in determining pore diameter and ion permeation through cyclic nucleotide-gated channels." Nature **364**(6432): 61-64.

Griffin, C.A., Ding, C.L., Jabs, E.W., Hawkins, A.L., Li, X. and Levine, M.A. (1993). "Human rod cGMP-gated cation channel gene maps to 4p12-->centromere by chromosomal in situ hybridization." Genomics **16**(1): 302-303.

Grimes, W.N., Zhang, J., Graydon, C.W., Kachar, B. and Diamond, J.S. (2010). "Retinal parallel processors: more than 100 independent microcircuits operate within a single interneuron." Neuron **65**(6): 873-885.

Grimm, D. and Buning, H. (2017). "Small But Increasingly Mighty: Latest Advances in AAV Vector Research, Design, and Evolution." Hum Gene Ther **28**(11): 1075-1086.

Grimm, D. and Kay, M.A. (2003). "From virus evolution to vector revolution: use of naturally occurring serotypes of adeno-associated virus (AAV) as novel vectors for human gene therapy." Curr Gene Ther **3**(4): 281-304.

Guadagni, V., Novelli, E., Piano, I., Gargini, C. and Strettoi, E. (2015). "Pharmacological approaches to retinitis pigmentosa: A laboratory perspective." Prog Retin Eye Res **48**: 62-81.

Gupta, N., Shyamasundar, S., Patnala, R., Karthikeyan, A., Arumugam, T.V., Ling, E.A. and Dheen, S.T. (2018). "Recent progress in therapeutic strategies for microglia-mediated neuroinflammation in neuropathologies." Expert Opin Ther Targets **22**(9): 765-781.

Habibi, I., Chebil, A., Kort, F., Schorderet, D.F. and El Matri, L. (2017). "Exome sequencing confirms ZNF408 mutations as a cause of familial retinitis pigmentosa." Ophthalmic Genet **38**(5): 494-497.

Hafler, B.P. (2017). "Clinical Progress in Inherited Retinal Degenerations: Gene Therapy Clinical Trials and Advances in Genetic Sequencing." Retina **37**(3): 417-423.

Hagins, W.A., Penn, R.D. and Yoshikami, S. (1970). "Dark current and photocurrent in retinal rods." Biophys J **10**(5): 380-412.

Hamel, C. (2006). "Retinitis pigmentosa." Orphanet J Rare Dis **1**: 40.

Hanany, M., Rivolta, C. and Sharon, D. (2020). "Worldwide carrier frequency and genetic prevalence of autosomal recessive inherited retinal diseases." Proc Natl Acad Sci U S A **117**(5): 2710-2716.

Hao, W., Wenzel, A., Obin, M.S., Chen, C.K., Brill, E., Krasnoperova, N.V., Eversole-Cire, P., Kleyner, Y., Taylor, A., Simon, M.I., Grimm, C., Reme, C.E. and Lem, J. (2002). "Evidence for two apoptotic pathways in light-induced retinal degeneration." Nat Genet **32**(2): 254-260.

Hartong, D.T., Berson, E.L. and Dryja, T.P. (2006). "Retinitis pigmentosa." Lancet **368**(9549): 1795-1809.

Harvey, A.R., Kamphuis, W., Eggers, R., Symons, N.A., Blits, B., Niclou, S., Boer, G.J. and Verhaagen, J. (2002). "Intravitreal injection of adeno-associated viral vectors results in the transduction of different types of retinal neurons in neonatal and adult rats: a comparison with lentiviral vectors." Mol Cell Neurosci **21**(1): 141-157.

Hastie, E. and Samulski, R.J. (2015). "Adeno-associated virus at 50: a golden anniversary of discovery, research, and gene therapy success--a personal perspective." Hum Gene Ther **26**(5): 257-265.

Henn, D.K., Baumann, A. and Kaupp, U.B. (1995). "Probing the transmembrane topology of cyclic nucleotide-gated ion channels with a gene fusion approach." Proc Natl Acad Sci U S A **92**(16): 7425-7429.

Herrmann, R., Heflin, S.J., Hammond, T., Lee, B., Wang, J., Gainetdinov, R.R., Caron, M.G., Eggers, E.D., Frishman, L.J., McCall, M.A. and Arshavsky, V.Y. (2011). "Rod vision is controlled by dopamine-dependent sensitization of rod bipolar cells by GABA." Neuron **72**(1): 101-110.

Hetz, C. and Papa, F.R. (2018). "The Unfolded Protein Response and Cell Fate Control." Mol Cell **69**(2): 169-181.

Hoon, M., Okawa, H., Della Santina, L. and Wong, R.O. (2014). "Functional architecture of the retina: development and disease." Prog Retin Eye Res **42**: 44-84.

Hrabe de Angelis, M.H., Flaswinkel, H., Fuchs, H., Rathkolb, B., Soewarto, D., Marschall, S., Heffner, S., Pargent, W., Wuensch, K., Jung, M., Reis, A., Richter, T., Alessandrini, F., Jakob, T., Fuchs, E., Kolb, H., Kremmer, E., Schaeble, K., Rollinski, B., Roscher, A., Peters, C., Meitinger, T., Strom, T., Steckler, T., Holsboer, F., Klopstock, T., Gekeler, F., Schindewolf, C., Jung, T., Avraham, K., Behrendt, H., Ring, J., Zimmer, A., Schughart, K., Pfeffer, K., Wolf, E. and Balling, R. (2000). "Genome-wide, large-scale production of mutant mice by ENU mutagenesis." Nat Genet **25**(4): 444-447.

Huang, S.H., Pittler, S.J., Huang, X., Oliveira, L., Berson, E.L. and Dryja, T.P. (1995). "Autosomal recessive retinitis pigmentosa caused by mutations in the alpha subunit of rod cGMP phosphodiesterase." Nat Genet **11**(4): 468-471.

Hughes, C.S., Moggridge, S., Muller, T., Sorensen, P.H., Morin, G.B. and Krijgsveld, J. (2019). "Single-pot, solid-phase-enhanced sample preparation for proteomics experiments." Nat Protoc **14**(1): 68-85.

Hull, S., Attanasio, M., Arno, G., Carss, K., Robson, A.G., Thompson, D.A., Plagnol, V., Michaelides, M., Holder, G.E., Henderson, R.H., Raymond, F.L., Moore, A.T. and Webster, A.R. (2017). "Clinical Characterization of CNGB1-Related Autosomal Recessive Retinitis Pigmentosa." JAMA Ophthalmol **135**(2): 137-144.

Hüttl, S., Michalakis, S., Seeliger, M., Luo, D.G., Acar, N., Geiger, H., Hudl, K., Mader, R., Haverkamp, S., Moser, M., Pfeifer, A., Gerstner, A., Yau, K.W. and Biel, M. (2005). "Impaired

channel targeting and retinal degeneration in mice lacking the cyclic nucleotide-gated channel subunit CNGB1." J Neurosci **25**(1): 130-138.

Ishikawa, M., Hashimoto, Y., Tonosaki, A. and Sakuragi, S. (1997). "Preference of peanut agglutinin labeling for long-wavelength-sensitive cone photoreceptors in the dace retina." Vision Res **37**(4): 383-387.

Jacobson, S.G., Acland, G.M., Aguirre, G.D., Aleman, T.S., Schwartz, S.B., Cideciyan, A.V., Zeiss, C.J., Komaromy, A.M., Kaushal, S., Roman, A.J., Windsor, E.A., Sumaroka, A., Pearce-Kelling, S.E., Conlon, T.J., Chiodo, V.A., Boye, S.L., Flotte, T.R., Maguire, A.M., Bennett, J. and Hauswirth, W.W. (2006). "Safety of recombinant adeno-associated virus type 2-RPE65 vector delivered by ocular subretinal injection." Mol Ther **13**(6): 1074-1084.

Jacobson, S.G., Cideciyan, A.V., Ratnakaram, R., Heon, E., Schwartz, S.B., Roman, A.J., Peden, M.C., Aleman, T.S., Boye, S.L., Sumaroka, A., Conlon, T.J., Calcedo, R., Pang, J.J., Erger, K.E., Olivares, M.B., Mullins, C.L., Swider, M., Kaushal, S., Feuer, W.J., Iannaccone, A., Fishman, G.A., Stone, E.M., Byrne, B.J. and Hauswirth, W.W. (2012). "Gene therapy for leber congenital amaurosis caused by RPE65 mutations: safety and efficacy in 15 children and adults followed up to 3 years." Arch Ophthalmol **130**(1): 9-24.

Jaissle, G.B., May, C.A., Reinhard, J., Kohler, K., Fauser, S., Lutjen-Drecoll, E., Zrenner, E. and Seeliger, M.W. (2001). "Evaluation of the rhodopsin knockout mouse as a model of pure cone function." Invest Ophthalmol Vis Sci **42**(2): 506-513.

Jayakody, S.A., Gonzalez-Cordero, A., Ali, R.R. and Pearson, R.A. (2015). "Cellular strategies for retinal repair by photoreceptor replacement." Prog Retin Eye Res **46**: 31-66.

Jeon, C.J., Strettoi, E. and Masland, R.H. (1998). "The major cell populations of the mouse retina." J Neurosci **18**(21): 8936-8946.

Jin, X., Qu, L.H., Hou, B.K., Xu, H.W., Meng, X.H., Pang, C.P. and Yin, Z.Q. (2016). "Novel compound heterozygous mutation in the CNGA1 gene underlie autosomal recessive retinitis pigmentosa in a Chinese family." Biosci Rep **36**(1): e00289.

Jones, M.K., Lu, B., Girman, S. and Wang, S. (2017). "Cell-based therapeutic strategies for replacement and preservation in retinal degenerative diseases." Prog Retin Eye Res **58**: 1-27.

Kandaswamy, S., Zobel, L., John, B., Santhiya, S.T., Bogedein, J., Przemeck, G.K.H., Gailus-Durner, V., Fuchs, H., Biel, M., Hrabě de Angelis, M., Graw, J., Michalakis, S. and Amarie, O.V. (unpublished). "Mutations within the cGMP-binding domain of CNGA1 causing autosomal recessive retinitis pigmentosa in human and animal model."

Karlstetter, M., Ebert, S. and Langmann, T. (2010). "Microglia in the healthy and degenerating retina: insights from novel mouse models." Immunobiology **215**(9-10): 685-691.

Karlstetter, M., Scholz, R., Rutar, M., Wong, W.T., Provis, J.M. and Langmann, T. (2015). "Retinal microglia: just bystander or target for therapy?" Prog Retin Eye Res **45**: 30-57.

Katada, Y., Kobayashi, K., Tsubota, K. and Kurihara, T. (2019). "Evaluation of AAV-DJ vector for retinal gene therapy." PeerJ **7**: e6317.

Katagiri, S., Akahori, M., Sergeev, Y., Yoshitake, K., Ikeo, K., Furuno, M., Hayashi, T., Kondo, M., Ueno, S., Tsunoda, K., Shinoda, K., Kuniyoshi, K., Tsurusaki, Y., Matsumoto, N., Tsuneoka, H. and Iwata, T. (2014). "Whole exome analysis identifies frequent CNGA1 mutations in Japanese population with autosomal recessive retinitis pigmentosa." PLoS One **9**(9): e108721.

Kaupp, U.B., Niidome, T., Tanabe, T., Terada, S., Bonigk, W., Stuhmer, W., Cook, N.J., Kangawa, K., Matsuo, H., Hirose, T. and et al. (1989). "Primary structure and functional expression from complementary DNA of the rod photoreceptor cyclic GMP-gated channel." Nature **342**(6251): 762-766.

Kaupp, U.B. and Seifert, R. (2002). "Cyclic nucleotide-gated ion channels." Physiol Rev **82**(3): 769-824.

Kay, C.N., Ryals, R.C., Aslanidi, G.V., Min, S.H., Ruan, Q., Sun, J., Dyka, F.M., Kasuga, D., Ayala, A.E., Van Vliet, K., Agbandje-McKenna, M., Hauswirth, W.W., Boye, S.L. and Boye, S.E. (2013). "Targeting photoreceptors via intravitreal delivery using novel, capsid-mutated AAV vectors." PLoS One **8**(4): e62097.

Kerr, J.F., Wyllie, A.H. and Currie, A.R. (1972). "Apoptosis: a basic biological phenomenon with wide-ranging implications in tissue kinetics." Br J Cancer **26**(4): 239-257.

Khan, S.Y., Ali, S., Naeem, M.A., Khan, S.N., Husnain, T., Butt, N.H., Qazi, Z.A., Akram, J., Riazuddin, S., Ayyagari, R., Hejtmancik, J.F. and Riazuddin, S.A. (2015). "Splice-site mutations identified in PDE6A responsible for retinitis pigmentosa in consanguineous Pakistani families." Mol Vis **21**: 871-882.

Kocaturk, N.M. and Gozuacik, D. (2018). "Crosstalk Between Mammalian Autophagy and the Ubiquitin-Proteasome System." Front Cell Dev Biol **6**: 128.

Koch, S., Sothilingam, V., Garcia Garrido, M., Tanimoto, N., Becirovic, E., Koch, F., Seide, C., Beck, S.C., Seeliger, M.W., Biel, M., Mühlfriedel, R. and Michalakis, S. (2012). "Gene therapy restores vision and delays degeneration in the CNGB1(-/-) mouse model of retinitis pigmentosa." Hum Mol Genet **21**(20): 4486-4496.

Kolb, H. (1995). Simple Anatomy of the Retina. Webvision: The Organization of the Retina and Visual System. H. Kolb, E. Fernandez and R. Nelson. Salt Lake City (UT).

Komaromy, A.M., Alexander, J.J., Rowlan, J.S., Garcia, M.M., Chiodo, V.A., Kaya, A., Tanaka, J.C., Acland, G.M., Hauswirth, W.W. and Aguirre, G.D. (2010). "Gene therapy rescues cone function in congenital achromatopsia." Hum Mol Genet **19**(13): 2581-2593.

Kondo, H., Qin, M., Mizota, A., Kondo, M., Hayashi, H., Hayashi, K., Oshima, K., Tahira, T. and Hayashi, K. (2004). "A homozygosity-based search for mutations in patients with autosomal

recessive retinitis pigmentosa, using microsatellite markers." Invest Ophthalmol Vis Sci **45**(12): 4433-4439.

Körschen, H.G., Illing, M., Seifert, R., Sesti, F., Williams, A., Gotzes, S., Colville, C., Muller, F., Dose, A., Godde, M. and et al. (1995). "A 240 kDa protein represents the complete beta subunit of the cyclic nucleotide-gated channel from rod photoreceptor." Neuron **15**(3): 627-636.

Kuehlewein, L., Zobor, D., Andreasson, S.O., Ayuso, C., Banfi, S., Bocquet, B., Bernd, A.S., Biskup, S., Boon, C.J.F., Downes, S.M., Fischer, M.D., Holz, F.G., Kellner, U., Leroy, B.P., Meunier, I., Nasser, F., Rosenberg, T., Rudolph, G., Stingl, K., Thiadens, A., Wilhelm, B., Wissinger, B., Zrenner, E., Kohl, S., Weisschuh, N. and Consortium, R.-C. (2020). "Clinical Phenotype and Course of PDE6A-Associated Retinitis Pigmentosa Disease, Characterized in Preparation for a Gene Supplementation Trial." JAMA Ophthalmol **138**(12): 1241-1250.

Kunte, M.M., Choudhury, S., Manheim, J.F., Shinde, V.M., Miura, M., Chiodo, V.A., Hauswirth, W.W., Gorbatyuk, O.S. and Gorbatyuk, M.S. (2012). "ER stress is involved in T17M rhodopsin-induced retinal degeneration." Invest Ophthalmol Vis Sci **53**(7): 3792-3800.

Lamb, T.D. and Pugh, E.N., Jr. (2006). "Phototransduction, dark adaptation, and rhodopsin regeneration the proctor lecture." Invest Ophthalmol Vis Sci **47**(12): 5137-5152.

Latella, M.C., Di Salvo, M.T., Cocchiarella, F., Benati, D., Grisendi, G., Comitato, A., Marigo, V. and Recchia, A. (2016). "In vivo Editing of the Human Mutant Rhodopsin Gene by Electroporation of Plasmid-based CRISPR/Cas9 in the Mouse Retina." Mol Ther Nucleic Acids **5**(11): e389.

Leconte, L. and Barnstable, C.J. (2000). "Impairment of rod cGMP-gated channel alpha-subunit expression leads to photoreceptor and bipolar cell degeneration." Invest Ophthalmol Vis Sci **41**(3): 917-926.

Leveillard, T. and Sahel, J.A. (2017). "Metabolic and redox signaling in the retina." Cell Mol Life Sci **74**(20): 3649-3665.

Li, M., Zhou, X., Wang, S., Michailidis, I., Gong, Y., Su, D., Li, H., Li, X. and Yang, J. (2017). "Structure of a eukaryotic cyclic-nucleotide-gated channel." Nature **542**(7639): 60-65.

Li, Y., Wang, C., Liu, Y., You, J. and Su, G. (2019). "Autophagy, lysosome dysfunction and mTOR inhibition in MNU-induced photoreceptor cell damage." Tissue Cell **61**: 98-108.

Li, Z.Y., Kljavin, I.J. and Milam, A.H. (1995). "Rod photoreceptor neurite sprouting in retinitis pigmentosa." J Neurosci **15**(8): 5429-5438.

Lipinski, D.M., Thake, M. and MacLaren, R.E. (2013). "Clinical applications of retinal gene therapy." Prog Retin Eye Res **32**: 22-47.

Lisman, J. and Fain, G. (1995). "Support for the equivalent light hypothesis for RP." Nat Med **1**(12): 1254-1255.

Liu, Y., Wang, Y., Xiao, Y., Li, X., Ruan, S., Luo, X., Wan, X., Wang, F. and Sun, X. (2021). "Retinal degeneration in mice lacking the cyclic nucleotide-gated channel subunit CNGA1." FASEB J **35**(9): e21859.

Lockshin, R.A. and Zakeri, Z. (2001). "Programmed cell death and apoptosis: origins of the theory." Nat Rev Mol Cell Biol **2**(7): 545-550.

Maeder, M.L., Stefanidakis, M., Wilson, C.J., Baral, R., Barrera, L.A., Bounoutas, G.S., Bumcrot, D., Chao, H., Ciulla, D.M., DaSilva, J.A., Dass, A., Dhanapal, V., Fennell, T.J., Friedland, A.E., Giannoukos, G., Gloskowski, S.W., Glucksmann, A., Gotta, G.M., Jayaram, H., Haskett, S.J., Hopkins, B., Horng, J.E., Joshi, S., Marco, E., Mepani, R., Reyon, D., Ta, T., Tabbaa, D.G., Samuelsson, S.J., Shen, S., Skor, M.N., Stetkiewicz, P., Wang, T., Yudkoff, C., Myer, V.E., Albright, C.F. and Jiang, H. (2019). "Development of a gene-editing approach to restore vision loss in Leber congenital amaurosis type 10." Nat Med **25**(2): 229-233.

Maguire, A.M., Russell, S., Wellman, J.A., Chung, D.C., Yu, Z.F., Tillman, A., Wittes, J., Pappas, J., Elci, O., Marshall, K.A., McCague, S., Reichert, H., Davis, M., Simonelli, F., Leroy, B.P., Wright, J.F., High, K.A. and Bennett, J. (2019). "Efficacy, Safety, and Durability of Voretigene Neparvovec-rzyl in RPE65 Mutation-Associated Inherited Retinal Dystrophy: Results of Phase 1 and 3 Trials." Ophthalmology **126**(9): 1273-1285.

Maranhao, B., Biswas, P., Gottsch, A.D., Navani, M., Naeem, M.A., Suk, J., Chu, J., Khan, S.N., Poleman, R., Akram, J., Riazuddin, S., Lee, P., Riazuddin, S.A., Hejtmancik, J.F. and Ayyagari, R. (2015). "Investigating the Molecular Basis of Retinal Degeneration in a Familial Cohort of Pakistani Decent by Exome Sequencing." PLoS One **10**(9): e0136561.

Maria, M., Ajmal, M., Azam, M., Waheed, N.K., Siddiqui, S.N., Mustafa, B., Ayub, H., Ali, L., Ahmad, S., Micheal, S., Hussain, A., Shah, S.T., Ali, S.H., Ahmed, W., Khan, Y.M., den Hollander, A.I., Haer-Wigman, L., Collin, R.W., Khan, M.I., Qamar, R. and Cremers, F.P. (2015). "Homozygosity mapping and targeted sanger sequencing reveal genetic defects underlying inherited retinal disease in families from pakistan." PLoS One **10**(3): e0119806.

Marmor, M.F. and Fishman, G.A. (1989). "At last. A standard electroretinography protocol." Arch Ophthalmol **107**(6): 813-814.

Masland, R.H. (1996). "Processing and encoding of visual information in the retina." Curr Opin Neurobiol **6**(4): 467-474.

Mattapallil, M.J., Wawrousek, E.F., Chan, C.C., Zhao, H., Roychoudhury, J., Ferguson, T.A. and Caspi, R.R. (2012). "The Rd8 mutation of the Crb1 gene is present in vendor lines of C57BL/6N mice and embryonic stem cells, and confounds ocular induced mutant phenotypes." Invest Ophthalmol Vis Sci **53**(6): 2921-2927.

McClements, M.E. and MacLaren, R.E. (2017). "Adeno-associated Virus (AAV) Dual Vector Strategies for Gene Therapy Encoding Large Transgenes." Yale J Biol Med **90**(4): 611-623.

McLaughlin, M.E., Sandberg, M.A., Berson, E.L. and Dryja, T.P. (1993). "Recessive mutations in the gene encoding the beta-subunit of rod phosphodiesterase in patients with retinitis pigmentosa." Nat Genet **4**(2): 130-134.

Michalakis, S., Becirovic, E. and Biel, M. (2018). "Retinal Cyclic Nucleotide-Gated Channels: From Pathophysiology to Therapy." Int J Mol Sci **19**(3).

Michalakis, S., Mühlfriedel, R., Tanimoto, N., Krishnamoorthy, V., Koch, S., Fischer, M.D., Becirovic, E., Bai, L., Huber, G., Beck, S.C., Fahl, E., Buning, H., Paquet-Durand, F., Zong, X., Gollisch, T., Biel, M. and Seeliger, M.W. (2010). "Restoration of cone vision in the CNGA3-/- mouse model of congenital complete lack of cone photoreceptor function." Mol Ther **18**(12): 2057-2063.

Michalakis, S., Schaferhoff, K., Spiwoks-Becker, I., Zabouri, N., Koch, S., Koch, F., Bonin, M., Biel, M. and Haverkamp, S. (2013). "Characterization of neurite outgrowth and ectopic synaptogenesis in response to photoreceptor dysfunction." Cell Mol Life Sci **70**(10): 1831-1847.

Michalakis, S., Zong, X., Becirovic, E., Hammelmann, V., Wein, T., Wanner, K.T. and Biel, M. (2011). "The glutamic acid-rich protein is a gating inhibitor of cyclic nucleotide-gated channels." J Neurosci **31**(1): 133-141.

Mizobuchi, K., Katagiri, S., Hayashi, T., Yoshitake, K., Fujinami, K., Kuniyoshi, K., Mishima, R., Tsunoda, K., Iwata, T. and Nakano, T. (2019). "Clinical findings of end-stage retinitis pigmentosa with a homozygous PDE6A variant (p.R653X)." Am J Ophthalmol Case Rep **13**: 110-115.

Molday, R.S. and Molday, L.L. (1998). "Molecular properties of the cGMP-gated channel of rod photoreceptors." Vision Res **38**(10): 1315-1323.

Molday, R.S., Molday, L.L., Dose, A., Clark-Lewis, I., Illing, M., Cook, N.J., Eismann, E. and Kaupp, U.B. (1991). "The cGMP-gated channel of the rod photoreceptor cell characterization and orientation of the amino terminus." J Biol Chem **266**(32): 21917-21922.

Molday, R.S. and Moritz, O.L. (2015). "Photoreceptors at a glance." J Cell Sci **128**(22): 4039-4045.

Mori, S., Wang, L., Takeuchi, T. and Kanda, T. (2004). "Two novel adeno-associated viruses from cynomolgus monkey: pseudotyping characterization of capsid protein." Virology **330**(2): 375-383.

Mowat, F.M., Occelli, L.M., Bartoe, J.T., Gervais, K.J., Bruewer, A.R., Querubin, J., Dinculescu, A., Boye, S.L., Hauswirth, W.W. and Petersen-Jones, S.M. (2017). "Gene Therapy in a Large Animal Model of PDE6A-Retinitis Pigmentosa." Front Neurosci **11**: 342.

Mühlfriedel, R., Michalakis, S., Garrido, M.G., Sothilingam, V., Schon, C., Biel, M. and Seeliger, M.W. (2019). "Optimized Subretinal Injection Technique for Gene Therapy Approaches." Methods Mol Biol **1834**: 405-412.

Murphy, M.P. (2009). "How mitochondria produce reactive oxygen species." Biochem J **417**(1): 1-13.

Nair, P., Hamzeh, A.R., Malik, E.M., Oberoi, D., Al-Ali, M.T. and Bastaki, F. (2017). "Novel PDE6A mutation in an Emirati patient with retinitis pigmentosa." Oman J Ophthalmol **10**(3): 228-231.

Natoli, R., Valter, K., Chrysostomou, V., Stone, J. and Provis, J. (2011). "Morphological, functional and gene expression analysis of the hyperoxic mouse retina." Exp Eye Res **92**(4): 306-314.

Newton, F. and Megaw, R. (2020). "Mechanisms of Photoreceptor Death in Retinitis Pigmentosa." Genes (Basel) **11**(10).

Ng, S.K., Wood, J.P., Chidlow, G., Han, G., Kittipassorn, T., Peet, D.J. and Casson, R.J. (2015). "Cancer-like metabolism of the mammalian retina." Clin Exp Ophthalmol **43**(4): 367-376.

Nikonov, S.S., Kholodenko, R., Lem, J. and Pugh, E.N., Jr. (2006). "Physiological features of the S- and M-cone photoreceptors of wild-type mice from single-cell recordings." J Gen Physiol **127**(4): 359-374.

Nishiguchi, K.M., Tearle, R.G., Liu, Y.P., Oh, E.C., Miyake, N., Benaglio, P., Harper, S., Koskiniemi-Kuendig, H., Venturini, G., Sharon, D., Koenekoop, R.K., Nakamura, M., Kondo, M., Ueno, S., Yasuma, T.R., Beckmann, J.S., Ikegawa, S., Matsumoto, N., Terasaki, H., Berson, E.L., Katsanis, N. and Rivolta, C. (2013). "Whole genome sequencing in patients with retinitis pigmentosa reveals pathogenic DNA structural changes and NEK2 as a new disease gene." Proc Natl Acad Sci U S A **110**(40): 16139-16144.

Occelli, L.M., Schon, C., Seeliger, M.W., Biel, M., Michalakis, S. and Petersen-Jones, S.M. (2017). "Gene Supplementation Rescues Rod Function and Preserves Photoreceptor and Retinal Morphology in Dogs, Leading the Way Toward Treating Human PDE6A-Retinitis Pigmentosa." Hum Gene Ther **28**(12): 1189-1201.

Ofri, R., Averbukh, E., Ezra-Elia, R., Ross, M., Honig, H., Obolensky, A., Rosov, A., Hauswirth, W.W., Gootwine, E. and Banin, E. (2018). "Six Years and Counting: Restoration of Photopic Retinal Function and Visual Behavior Following Gene Augmentation Therapy in a Sheep Model of CNGA3 Achromatopsia." Hum Gene Ther **29**(12): 1376-1386.

Okajima, T. and Tsuruta, F. (2018). "Microglial dynamics during brain development." Neural Regen Res **13**(2): 222-223.

Ortin-Martinez, A., Nadal-Nicolas, F.M., Jimenez-Lopez, M., Alburquerque-Bejar, J.J., Nieto-Lopez, L., Garcia-Ayuso, D., Villegas-Perez, M.P., Vidal-Sanz, M. and Agudo-Barriuso, M.

(2014). "Number and distribution of mouse retinal cone photoreceptors: differences between an albino (Swiss) and a pigmented (C57/BL6) strain." PLoS One **9**(7): e102392.

Palczewski, K. (2014). "Chemistry and biology of the initial steps in vision: the Friedenwald lecture." Invest Ophthalmol Vis Sci **55**(10): 6651-6672.

Paloma, E., Martinez-Mir, A., Garcia-Sandoval, B., Ayuso, C., Vilageliu, L., Gonzalez-Duarte, R. and Balcells, S. (2002). "Novel homozygous mutation in the alpha subunit of the rod cGMP gated channel (CNGA1) in two Spanish sibs affected with autosomal recessive retinitis pigmentosa." J Med Genet **39**(10): E66.

Pan, W.W., Wubben, T.J. and Besirli, C.G. (2021). "Photoreceptor metabolic reprogramming: current understanding and therapeutic implications." Commun Biol **4**(1): 245.

Paquet-Durand, F., Beck, S., Michalakis, S., Goldmann, T., Huber, G., Mühlfriedel, R., Trifunovic, D., Fischer, M.D., Fahl, E., Duetsch, G., Becirovic, E., Wolfrum, U., van Veen, T., Biel, M., Tanimoto, N. and Seeliger, M.W. (2011). "A key role for cyclic nucleotide gated (CNG) channels in cGMP-related retinitis pigmentosa." Hum Mol Genet **20**(5): 941-947.

Paquet-Durand, F., Hauck, S.M., van Veen, T., Ueffing, M. and Ekstrom, P. (2009). "PKG activity causes photoreceptor cell death in two retinitis pigmentosa models." J Neurochem **108**(3): 796-810.

Pavlou, M., Schön, C., Occelli, L.M., Rossi, A., Meumann, N., Boyd, R.F., Bartoe, J.T., Siedlecki, J., Gerhardt, M.J., Babutzka, S., Bogedein, J., Wagner, J.E., Priglinger, S.G., Biel, M., Petersen-Jones, S.M., Buning, H. and Michalakis, S. (2021). "Novel AAV capsids for intravitreal gene therapy of photoreceptor disorders." EMBO Mol Med **13**(4): e13392.

Pearring, J.N., Martinez-Marquez, J., Willer, J.R., Lieu, E.C., Salinas, R.Y. and Arshavsky, V.Y. (2021). "The GARP Domain of the Rod CNG Channel's beta1-Subunit Contains Distinct Sites for Outer Segment Targeting and Connecting to the Photoreceptor Disk Rim." J Neurosci **41**(14): 3094-3104.

Pearring, J.N., Salinas, R.Y., Baker, S.A. and Arshavsky, V.Y. (2013). "Protein sorting, targeting and trafficking in photoreceptor cells." Prog Retin Eye Res **36**: 24-51.

Peng, C., Rich, E.D. and Varnum, M.D. (2004). "Subunit configuration of heteromeric cone cyclic nucleotide-gated channels." Neuron **42**(3): 401-410.

Peng, Y., Tang, L. and Zhou, Y. (2017). "Subretinal Injection: A Review on the Novel Route of Therapeutic Delivery for Vitreoretinal Diseases." Ophthalmic Res **58**(4): 217-226.

Perera, A., Eisen, D., Wagner, M., Laube, S.K., Kunzel, A.F., Koch, S., Steinbacher, J., Schulze, E., Splith, V., Mittermeier, N., Muller, M., Biel, M., Carell, T. and Michalakis, S. (2015). "TET3 is recruited by REST for context-specific hydroxymethylation and induction of gene expression." Cell Rep **11**(2): 283-294.

Perez-Carro, R., Corton, M., Sanchez-Navarro, I., Zurita, O., Sanchez-Bolivar, N., Sanchez-Alcudia, R., Lelieveld, S.H., Aller, E., Lopez-Martinez, M.A., Lopez-Molina, M.I., Fernandez-San Jose, P., Blanco-Kelly, F., Riveiro-Alvarez, R., Gilissen, C., Millan, J.M., Avila-Fernandez, A. and Ayuso, C. (2016). "Panel-based NGS Reveals Novel Pathogenic Mutations in Autosomal Recessive Retinitis Pigmentosa." Sci Rep **6**: 19531.

Petersen-Jones, S.M., Bartoe, J.T., Fischer, A.J., Scott, M., Boye, S.L., Chiodo, V. and Hauswirth, W.W. (2009). "AAV retinal transduction in a large animal model species: comparison of a self-complementary AAV2/5 with a single-stranded AAV2/5 vector." Mol Vis **15**: 1835-1842.

Petersen-Jones, S.M., Entz, D.D. and Sargan, D.R. (1999). "cGMP phosphodiesterase-alpha mutation causes progressive retinal atrophy in the Cardigan Welsh corgi dog." Invest Ophthalmol Vis Sci **40**(8): 1637-1644.

Petersen-Jones, S.M., Occelli, L.M., Winkler, P.A., Lee, W., Sparrow, J.R., Tsukikawa, M., Boye, S.L., Chiodo, V., Capasso, J.E., Becirovic, E., Schon, C., Seeliger, M.W., Levin, A.V., Michalakis, S., Hauswirth, W.W. and Tsang, S.H. (2018). "Patients and animal models of CNGbeta1-deficient retinitis pigmentosa support gene augmentation approach." J Clin Invest **128**(1): 190-206.

Petit, L., Ma, S., Cipi, J., Cheng, S.Y., Zieger, M., Hay, N. and Punzo, C. (2018). "Aerobic Glycolysis Is Essential for Normal Rod Function and Controls Secondary Cone Death in Retinitis Pigmentosa." Cell Rep **23**(9): 2629-2642.

Petrs-Silva, H., Dinculescu, A., Li, Q., Min, S.H., Chiodo, V., Pang, J.J., Zhong, L., Zolotukhin, S., Srivastava, A., Lewin, A.S. and Hauswirth, W.W. (2009). "High-efficiency transduction of the mouse retina by tyrosine-mutant AAV serotype vectors." Mol Ther **17**(3): 463-471.

Phillips, M.J., Otteson, D.C. and Sherry, D.M. (2010). "Progression of neuronal and synaptic remodeling in the rd10 mouse model of retinitis pigmentosa." J Comp Neurol **518**(11): 2071-2089.

Pierce, E.A. (2001). "Pathways to photoreceptor cell death in inherited retinal degenerations." Bioessays **23**(7): 605-618.

Pittler, S.J., Baehr, W., Wasmuth, J.J., McConnell, D.G., Champagne, M.S., vanTuinen, P., Ledbetter, D. and Davis, R.L. (1990). "Molecular characterization of human and bovine rod photoreceptor cGMP phosphodiesterase alpha-subunit and chromosomal localization of the human gene." Genomics **6**(2): 272-283.

Poetsch, A., Molday, L.L. and Molday, R.S. (2001). "The cGMP-gated channel and related glutamic acid-rich proteins interact with peripherin-2 at the rim region of rod photoreceptor disc membranes." J Biol Chem **276**(51): 48009-48016.

Power, M., Das, S., Schutze, K., Marigo, V., Ekstrom, P. and Paquet-Durand, F. (2020). "Cellular mechanisms of hereditary photoreceptor degeneration - Focus on cGMP." Prog Retin Eye Res **74**: 100772.

Prinz, M. and Priller, J. (2014). "Microglia and brain macrophages in the molecular age: from origin to neuropsychiatric disease." Nat Rev Neurosci **15**(5): 300-312.

Ptito, M., Bleau, M. and Bouskila, J. (2021). "The Retina: A Window into the Brain." Cells **10**(12).

Pugh, E.N., Jr., Duda, T., Sitaramayya, A. and Sharma, R.K. (1997). "Photoreceptor guanylate cyclases: a review." Biosci Rep **17**(5): 429-473.

Punzo, C., Kornacker, K. and Cepko, C.L. (2009). "Stimulation of the insulin/mTOR pathway delays cone death in a mouse model of retinitis pigmentosa." Nat Neurosci **12**(1): 44-52.

Rajala, R.V.S. (2020). "Aerobic Glycolysis in the Retina: Functional Roles of Pyruvate Kinase Isoforms." Front Cell Dev Biol **8**: 266.

Reichenbach, A. and Bringmann, A. (2020). "Glia of the human retina." Glia **68**(4): 768-796.

Reyes, N.J., O'Koren, E.G. and Saban, D.R. (2017). "New insights into mononuclear phagocyte biology from the visual system." Nat Rev Immunol **17**(5): 322-332.

Riazuddin, S.A., Zulfiqar, F., Zhang, Q., Yao, W., Li, S., Jiao, X., Shahzadi, A., Amer, M., Iqbal, M., Hussnain, T., Sieving, P.A., Riazuddin, S. and Hejtmancik, J.F. (2006). "Mutations in the gene encoding the alpha-subunit of rod phosphodiesterase in consanguineous Pakistani families." Mol Vis **12**: 1283-1291.

Rieke, F. (2000). "Mechanisms of single-photon detection in rod photoreceptors." Methods Enzymol **316**: 186-202.

Rieke, F. and Baylor, D.A. (2000). "Origin and functional impact of dark noise in retinal cones." Neuron **26**(1): 181-186.

Rodriguez-Muela, N., Hernandez-Pinto, A.M., Serrano-Puebla, A., Garcia-Ledo, L., Latorre, S.H., de la Rosa, E.J. and Boya, P. (2015). "Lysosomal membrane permeabilization and autophagy blockade contribute to photoreceptor cell death in a mouse model of retinitis pigmentosa." Cell Death Differ **22**(3): 476-487.

Rodriguez-Munoz, A., Aller, E., Jaijo, T., Gonzalez-Garcia, E., Cabrera-Peset, A., Gallego-Pinazo, R., Udaondo, P., Salom, D., Garcia-Garcia, G. and Millan, J.M. (2020). "Expanding the Clinical and Molecular Heterogeneity of Nonsyndromic Inherited Retinal Dystrophies." J Mol Diagn **22**(4): 532-543.

Ross, M. and Ofri, R. (2021). "The future of retinal gene therapy: evolving from subretinal to intravitreal vector delivery." Neural Regen Res **16**(9): 1751-1759.

Sabrautzki, S., Kaiser, G., Przemeck, G.K.H., Gerst, F., Lorza-Gil, E., Panse, M., Sartorius, T., Hoene, M., Marschall, S., Haring, H.U., Hrabe de Angelis, M. and Ullrich, S. (2017). "Point

mutation of Ffar1 abrogates fatty acid-dependent insulin secretion, but protects against HFD-induced glucose intolerance." Mol Metab **6**(10): 1304-1312.

Sahel, J., Bonnel, S., Mrejen, S. and Paques, M. (2010). "Retinitis pigmentosa and other dystrophies." Dev Ophthalmol **47**: 160-167.

Sahel, J.A., Leveillard, T., Picaud, S., Dalkara, D., Marazova, K., Safran, A., Paques, M., Duebel, J., Roska, B. and Mohand-Said, S. (2013). "Functional rescue of cone photoreceptors in retinitis pigmentosa." Graefes Arch Clin Exp Ophthalmol **251**(7): 1669-1677.

Sakamoto, K., McCluskey, M., Wensel, T.G., Naggert, J.K. and Nishina, P.M. (2009). "New mouse models for recessive retinitis pigmentosa caused by mutations in the Pde6a gene." Hum Mol Genet **18**(1): 178-192.

Sampath, A.P. and Rieke, F. (2004). "Selective transmission of single photon responses by saturation at the rod-to-rod bipolar synapse." Neuron **41**(3): 431-443.

Sancho-Pelluz, J., Arango-Gonzalez, B., Kustermann, S., Romero, F.J., van Veen, T., Zrenner, E., Ekstrom, P. and Paquet-Durand, F. (2008). "Photoreceptor cell death mechanisms in inherited retinal degeneration." Mol Neurobiol **38**(3): 253-269.

Sandell, J.H., Masland, R.H., Raviola, E. and Dacheux, R.F. (1989). "Connections of indoleamine-accumulating cells in the rabbit retina." J Comp Neurol **283**(2): 303-313.

Saqib, M.A., Nikopoulos, K., Ullah, E., Sher Khan, F., Iqbal, J., Bibi, R., Jarral, A., Sajid, S., Nishiguchi, K.M., Venturini, G., Ansar, M. and Rivolta, C. (2015). "Homozygosity mapping reveals novel and known mutations in Pakistani families with inherited retinal dystrophies." Sci Rep **5**: 9965.

Sautter, A., Zong, X., Hofmann, F. and Biel, M. (1998). "An isoform of the rod photoreceptor cyclic nucleotide-gated channel beta subunit expressed in olfactory neurons." Proc Natl Acad Sci U S A **95**(8): 4696-4701.

Schmidt, M., Grot, E., Cervenka, P., Wainer, S., Buck, C. and Chiorini, J.A. (2006). "Identification and characterization of novel adeno-associated virus isolates in ATCC virus stocks." J Virol **80**(10): 5082-5085.

Schön, C., Asteriti, S., Koch, S., Sothilingam, V., Garcia Garrido, M., Tanimoto, N., Herms, J., Seeliger, M.W., Cangiano, L., Biel, M. and Michalakis, S. (2016a). "Loss of HCN1 enhances disease progression in mouse models of CNG channel-linked retinitis pigmentosa and achromatopsia." Hum Mol Genet **25**(6): 1165-1175.

Schön, C., Hoffmann, N.A., Ochs, S.M., Burgold, S., Filser, S., Steinbach, S., Seeliger, M.W., Arzberger, T., Goedert, M., Kretzschmar, H.A., Schmidt, B. and Herms, J. (2012). "Long-term in vivo imaging of fibrillar tau in the retina of P301S transgenic mice." PLoS One **7**(12): e53547.

Schön, C., Paquet-Durand, F. and Michalakis, S. (2016b). "Cav1.4 L-Type Calcium Channels Contribute to Calpain Activation in Degenerating Photoreceptors of rd1 Mice." PLoS One **11**(6): e0156974.

Schön, C., Sothilingam, V., Mühlfriedel, R., Garcia Garrido, M., Beck, S.C., Tanimoto, N., Wissinger, B., Paquet-Durand, F., Biel, M., Michalakis, S. and Seeliger, M.W. (2017). "Gene Therapy Successfully Delays Degeneration in a Mouse Model of PDE6A-Linked Retinitis Pigmentosa (RP43)." Hum Gene Ther **28**(12): 1180-1188.

Schorderet, D.F., Iouranova, A., Favez, T., Tiab, L. and Escher, P. (2013). "IROme, a new high-throughput molecular tool for the diagnosis of inherited retinal dystrophies." Biomed Res Int **2013**: 198089.

Shintani, K., Shechtman, D.L. and Gurwood, A.S. (2009). "Review and update: current treatment trends for patients with retinitis pigmentosa." Optometry **80**(7): 384-401.

Shuart, N.G., Haitin, Y., Camp, S.S., Black, K.D. and Zagotta, W.N. (2011). "Molecular mechanism for 3:1 subunit stoichiometry of rod cyclic nucleotide-gated ion channels." Nat Commun **2**: 457.

Simpson, D.A., Clark, G.R., Alexander, S., Silvestri, G. and Willoughby, C.E. (2011). "Molecular diagnosis for heterogeneous genetic diseases with targeted high-throughput DNA sequencing applied to retinitis pigmentosa." J Med Genet **48**(3): 145-151.

Slijkerman, R.W., Song, F., Astuti, G.D., Huynen, M.A., van Wijk, E., Stieger, K. and Collin, R.W. (2015). "The pros and cons of vertebrate animal models for functional and therapeutic research on inherited retinal dystrophies." Prog Retin Eye Res **48**: 137-159.

Song, J., Smaoui, N., Ayyagari, R., Stiles, D., Benhamed, S., MacDonald, I.M., Daiger, S.P., Tumminia, S.J., Hejtmancik, F. and Wang, X. (2011). "High-throughput retina-array for screening 93 genes involved in inherited retinal dystrophy." Invest Ophthalmol Vis Sci **52**(12): 9053-9060.

Sothilingam, V., Garcia Garrido, M., Jiao, K., Buena-Atienza, E., Sahaboglu, A., Trifunovic, D., Balendran, S., Koepfli, T., Muhlfriedel, R., Schon, C., Biel, M., Heckmann, A., Beck, S.C., Michalakis, S., Wissinger, B., Seeliger, M.W. and Paquet-Durand, F. (2015). "Retinitis pigmentosa: impact of different Pde6a point mutations on the disease phenotype." Hum Mol Genet **24**(19): 5486-5499.

Srivastava, A. (2016). "In vivo tissue-tropism of adeno-associated viral vectors." Curr Opin Virol **21**: 75-80.

Stryer, L. (1986). "Cyclic GMP cascade of vision." Annu Rev Neurosci **9**: 87-119.

Takano, Y., Ohguro, H., Dezawa, M., Ishikawa, H., Yamazaki, H., Ohguro, I., Mamiya, K., Metoki, T., Ishikawa, F. and Nakazawa, M. (2004). "Study of drug effects of calcium channel blockers on retinal degeneration of rd mouse." Biochem Biophys Res Commun **313**(4): 1015-1022.

Tanaka, J., Markerink-van Ittersum, M., Steinbusch, H.W. and De Vente, J. (1997). "Nitric oxide-mediated cGMP synthesis in oligodendrocytes in the developing rat brain." Glia **19**(4): 286-297.

Tanimoto, N., Sothilingam, V. and Seeliger, M.W. (2013). "Functional phenotyping of mouse models with ERG." Methods Mol Biol **935**: 69-78.

Thoreson, W.B. and Dacey, D.M. (2019). "Diverse Cell Types, Circuits, and Mechanisms for Color Vision in the Vertebrate Retina." Physiol Rev **99**(3): 1527-1573.

Tiab, L., Largueche, L., Chouchane, I., Derouiche, K., Munier, F.L., El Matri, L. and Schorderet, D.F. (2013). "A novel homozygous R764H mutation in crumbs homolog 1 causes autosomal recessive retinitis pigmentosa." Mol Vis **19**: 829-834.

Trapani, I. (2019). "Adeno-Associated Viral Vectors as a Tool for Large Gene Delivery to the Retina." Genes (Basel) **10**(4).

Trifunovic, D., Dengler, K., Michalakis, S., Zrenner, E., Wissinger, B. and Paquet-Durand, F. (2010). "cGMP-dependent cone photoreceptor degeneration in the cpfl1 mouse retina." J Comp Neurol **518**(17): 3604-3617.

Trifunovic, D., Sahaboglu, A., Kaur, J., Mencl, S., Zrenner, E., Ueffing, M., Arango-Gonzalez, B. and Paquet-Durand, F. (2012). "Neuroprotective strategies for the treatment of inherited photoreceptor degeneration." Curr Mol Med **12**(5): 598-612.

Tucker, C.L., Woodcock, S.C., Kelsell, R.E., Ramamurthy, V., Hunt, D.M. and Hurley, J.B. (1999). "Biochemical analysis of a dimerization domain mutation in RetGC-1 associated with dominant cone-rod dystrophy." Proc Natl Acad Sci U S A **96**(16): 9039-9044.

Tuntivanich, N., Pittler, S.J., Fischer, A.J., Omar, G., Kiupel, M., Weber, A., Yao, S., Steibel, J.P., Khan, N.W. and Petersen-Jones, S.M. (2009). "Characterization of a canine model of autosomal recessive retinitis pigmentosa due to a PDE6A mutation." Invest Ophthalmol Vis Sci **50**(2): 801-813.

van Soest, S., Westerveld, A., de Jong, P.T., Bleeker-Wagemakers, E.M. and Bergen, A.A. (1999). "Retinitis pigmentosa: defined from a molecular point of view." Surv Ophthalmol **43**(4): 321-334.

van Vliet, A.R., Giordano, F., Gerlo, S., Segura, I., Van Eygen, S., Molenberghs, G., Rocha, S., Houcine, A., Derua, R., Verfaillie, T., Vangindertael, J., De Keersmaecker, H., Waelkens, E., Tavernier, J., Hofkens, J., Annaert, W., Carmeliet, P., Samali, A., Mizuno, H. and Agostinis, P. (2017). "The ER Stress Sensor PERK Coordinates ER-Plasma Membrane Contact Site Formation through Interaction with Filamin-A and F-Actin Remodeling." Mol Cell **65**(5): 885-899 e886.

Venkatesh, A., Ma, S., Le, Y.Z., Hall, M.N., Ruegg, M.A. and Punzo, C. (2015). "Activated mTORC1 promotes long-term cone survival in retinitis pigmentosa mice." J Clin Invest **125**(4): 1446-1458.

Verbakel, S.K., van Huet, R.A.C., Boon, C.J.F., den Hollander, A.I., Collin, R.W.J., Klaver, C.C.W., Hoyng, C.B., Roepman, R. and Klevering, B.J. (2018). "Non-syndromic retinitis pigmentosa." Prog Retin Eye Res **66**: 157-186.

Wagner, J.E., Zobel, L., Gerhardt, M.J., O'Riordan, C.R., Frederick, A., Petersen-Jones, S.M., Biel, M. and Michalakis, S. (2021). "In Vivo Potency Testing of Subretinal rAAV5.hCNGB1 Gene Therapy in the Cngb1 Knockout Mouse Model of Retinitis Pigmentosa." Hum Gene Ther **32**(19-20): 1158-1170.

Wahlin, K.J., Enke, R.A., Fuller, J.A., Kalesnykas, G., Zack, D.J. and Merbs, S.L. (2013). "Epigenetics and cell death: DNA hypermethylation in programmed retinal cell death." PLoS One **8**(11): e79140.

Wang, L., Zou, T., Lin, Y., Li, L., Zhang, P., Gong, B., Hao, J. and Zhang, H. (2020). "Identification of a novel homozygous variant in the CNGA1 gene in a Chinese family with autosomal recessive retinitis pigmentosa." Mol Med Rep **22**(3): 2516-2520.

Wang, M., Gan, D., Huang, X. and Xu, G. (2016). "Novel compound heterozygous mutations in CNGA1in a Chinese family affected with autosomal recessive retinitis pigmentosa by targeted sequencing." BMC Ophthalmol **16**: 101.

Wang, T., Tsang, S.H. and Chen, J. (2017). "Two pathways of rod photoreceptor cell death induced by elevated cGMP." Hum Mol Genet **26**(12): 2299-2306.

Warburg, O. (1956). "On the origin of cancer cells." Science **123**(3191): 309-314.

Wässle, H. and Boycott, B.B. (1991). "Functional architecture of the mammalian retina." Physiol Rev **71**(2): 447-480.

Weh, E., Lutrzykowska, Z., Smith, A., Hager, H., Pawar, M., Wubben, T.J. and Besirli, C.G. (2020). "Hexokinase 2 is dispensable for photoreceptor development but is required for survival during aging and outer retinal stress." Cell Death Dis **11**(6): 422.

Weitz, D., Ficek, N., Kremmer, E., Bauer, P.J. and Kaupp, U.B. (2002). "Subunit stoichiometry of the CNG channel of rod photoreceptors." Neuron **36**(5): 881-889.

Wellard, J., Lee, D., Valter, K. and Stone, J. (2005). "Photoreceptors in the rat retina are specifically vulnerable to both hypoxia and hyperoxia." Vis Neurosci **22**(4): 501-507.

Wenzel, A., Grimm, C., Samardzija, M. and Reme, C.E. (2005). "Molecular mechanisms of light-induced photoreceptor apoptosis and neuroprotection for retinal degeneration." Prog Retin Eye Res **24**(2): 275-306.

Winkler, P.A., Ekenstedt, K.J., Occelli, L.M., Frattaroli, A.V., Bartoe, J.T., Venta, P.J. and Petersen-Jones, S.M. (2013). "A large animal model for CNGB1 autosomal recessive retinitis pigmentosa." PLoS One **8**(8): e72229.

Wisniewski, J.R., Zougman, A., Nagaraj, N. and Mann, M. (2009). "Universal sample preparation method for proteome analysis." Nat Methods **6**(5): 359-362.

Wu, Z., Yang, H. and Colosi, P. (2010). "Effect of genome size on AAV vector packaging." Mol Ther **18**(1): 80-86.

Wubben, T.J., Pawar, M., Smith, A., Toolan, K., Hager, H. and Besirli, C.G. (2017). "Photoreceptor metabolic reprogramming provides survival advantage in acute stress while causing chronic degeneration." Sci Rep **7**(1): 17863.

Xiang, Q., Guo, Y., Cao, Y., Xiong, W., Deng, X., Xu, H., Li, Y., Du, D. and Deng, H. (2018). "Identification of a CNGB1 Frameshift Mutation in a Han Chinese Family with Retinitis Pigmentosa." Optom Vis Sci **95**(12): 1155-1161.

Xu, J., Morris, L., Thapa, A., Ma, H., Michalakis, S., Biel, M., Baehr, W., Peshenko, I.V., Dizhoor, A.M. and Ding, X.Q. (2013). "cGMP accumulation causes photoreceptor degeneration in CNG channel deficiency: evidence of cGMP cytotoxicity independently of enhanced CNG channel function." J Neurosci **33**(37): 14939-14948.

Xu, Y., Guan, L., Xiao, X., Zhang, J., Li, S., Jiang, H., Jia, X., Yang, J., Guo, X., Yin, Y., Wang, J. and Zhang, Q. (2015). "Mutation analysis in 129 genes associated with other forms of retinal dystrophy in 157 families with retinitis pigmentosa based on exome sequencing." Mol Vis **21**: 477-486.

Xue, J., Han, Y., Zeng, W. and Jiang, Y. (2021a). "Structural mechanisms of assembly, permeation, gating, and pharmacology of native human rod CNG channel." Neuron.

Xue, J., Han, Y., Zeng, W., Wang, Y. and Jiang, Y. (2021b). "Structural mechanisms of gating and selectivity of human rod CNGA1 channel." Neuron **109**(8): 1302-1313 e1304.

Yan, J., Gunter, A., Das, S., Muhlfriedel, R., Michalakis, S., Jiao, K., Seeliger, M.W. and Paquet-Durand, F. (2022). "Inherited Retinal Degeneration: PARP-Dependent Activation of Calpain Requires CNG Channel Activity." Biomolecules **12**(3).

Yan, W., Lewin, A. and Hauswirth, W. (1998). "Selective degradation of nonsense beta-phosphodiesterase mRNA in the heterozygous rd mouse." Invest Ophthalmol Vis Sci **39**(13): 2529-2536.

Yanai, D., Weiland, J.D., Mahadevappa, M., Greenberg, R.J., Fine, I. and Humayun, M.S. (2007). "Visual performance using a retinal prosthesis in three subjects with retinitis pigmentosa." Am J Ophthalmol **143**(5): 820-827.

Yang, R.B., Foster, D.C., Garbers, D.L. and Fulle, H.J. (1995). "Two membrane forms of guanylyl cyclase found in the eye." Proc Natl Acad Sci U S A **92**(2): 602-606.

Yao, J., Qiu, Y., Frontera, E., Jia, L., Khan, N.W., Klionsky, D.J., Ferguson, T.A., Thompson, D.A. and Zacks, D.N. (2018). "Inhibiting autophagy reduces retinal degeneration caused by protein misfolding." Autophagy **14**(7): 1226-1238.

Young, R.W. (1967). "The renewal of photoreceptor cell outer segments." J Cell Biol **33**(1): 61-72.

Young, R.W. and Bok, D. (1969). "Participation of the retinal pigment epithelium in the rod outer segment renewal process." J Cell Biol **42**(2): 392-403.

Yu, F.H., Yarov-Yarovoy, V., Gutman, G.A. and Catterall, W.A. (2005). "Overview of molecular relationships in the voltage-gated ion channel superfamily." Pharmacol Rev **57**(4): 387-395.

Zeviani, M. and Carelli, V. (2021). "Mitochondrial Retinopathies." Int J Mol Sci **23**(1).

Zhang, L., Du, J., Justus, S., Hsu, C.W., Bonet-Ponce, L., Wu, W.H., Tsai, Y.T., Wu, W.P., Jia, Y., Duong, J.K., Mahajan, V.B., Lin, C.S., Wang, S., Hurley, J.B. and Tsang, S.H. (2016). "Reprogramming metabolism by targeting sirtuin 6 attenuates retinal degeneration." J Clin Invest **126**(12): 4659-4673.

Zhang, Q., Zulfiqar, F., Riazuddin, S.A., Xiao, X., Ahmad, Z., Riazuddin, S. and Hejtmancik, J.F. (2004). "Autosomal recessive retinitis pigmentosa in a Pakistani family mapped to CNGA1 with identification of a novel mutation." Mol Vis **10**: 884-889.

Zhang, R., Shen, W., Du, J. and Gillies, M.C. (2020). "Selective knockdown of hexokinase 2 in rods leads to age-related photoreceptor degeneration and retinal metabolic remodeling." Cell Death Dis **11**(10): 885.

Zhang, T., Baehr, W. and Fu, Y. (2012). "Chemical chaperone TUDCA preserves cone photoreceptors in a mouse model of Leber congenital amaurosis." Invest Ophthalmol Vis Sci **53**(7): 3349-3356.

Zhang, Y., Molday, L.L., Molday, R.S., Sarfare, S.S., Woodruff, M.L., Fain, G.L., Kraft, T.W. and Pittler, S.J. (2009). "Knockout of GARPs and the beta-subunit of the rod cGMP-gated channel disrupts disk morphogenesis and rod outer segment structural integrity." J Cell Sci **122**(Pt 8): 1192-1200.

Zhao, L., Zabel, M.K., Wang, X., Ma, W., Shah, P., Fariss, R.N., Qian, H., Parkhurst, C.N., Gan, W.B. and Wong, W.T. (2015). "Microglial phagocytosis of living photoreceptors contributes to inherited retinal degeneration." EMBO Mol Med **7**(9): 1179-1197.

Zheng, J., Trudeau, M.C. and Zagotta, W.N. (2002). "Rod cyclic nucleotide-gated channels have a stoichiometry of three CNGA1 subunits and one CNGB1 subunit." Neuron **36**(5): 891-896.

Zheng, X., Fu, Z., Su, D., Zhang, Y., Li, M., Pan, Y., Li, H., Li, S., Grassucci, R.A., Ren, Z., Hu, Z., Li, X., Zhou, M., Li, G., Frank, J. and Yang, J. (2020). "Mechanism of ligand activation of a eukaryotic cyclic nucleotide-gated channel." Nat Struct Mol Biol **27**(7): 625-634.

Zheng, X., Hu, Z., Li, H. and Yang, J. (2022). "Structure of the human cone photoreceptor cyclic nucleotide-gated channel." Nat Struct Mol Biol **29**(1): 40-46.

Zhong, H., Molday, L.L., Molday, R.S. and Yau, K.W. (2002). "The heteromeric cyclic nucleotide-gated channel adopts a 3A:1B stoichiometry." Nature **420**(6912): 193-198.

Zhou, Y., Morais-Cabral, J.H., Kaufman, A. and MacKinnon, R. (2001). "Chemistry of ion coordination and hydration revealed by a K+ channel-Fab complex at 2.0 A resolution." Nature **414**(6859): 43-48.

Ziccardi, L., Cordeddu, V., Gaddini, L., Matteucci, A., Parravano, M., Malchiodi-Albedi, F. and Varano, M. (2019). "Gene Therapy in Retinal Dystrophies." Int J Mol Sci **20**(22).

Zinn, E., Pacouret, S., Khaychuk, V., Turunen, H.T., Carvalho, L.S., Andres-Mateos, E., Shah, S., Shelke, R., Maurer, A.C., Plovie, E., Xiao, R. and Vandenberghe, L.H. (2015). "In Silico Reconstruction of the Viral Evolutionary Lineage Yields a Potent Gene Therapy Vector." Cell Rep **12**(6): 1056-1068.

Appendix

Abbreviations

Abbreviation	Term
AAV	Adeno-associated virus
Ad	Adenovirus
AKT	Protein kinase B
AMPK	Adenosine monophosphate-activated protein kinase
AmpR	Ampicillin resistance
ANOVA	Analysis of variance
APS	Ammonium persulfate
arRP	Autosomal recessive RP
ATF6	Activating transcription factor 6
BAG2	BAG family molecular chaperone regulator 2
BGH	Bovine growth hormon
bp	Base pair
c	canine
cAMP	Cyclic adenosine monophosphate
CB	ChemiBLOCKER
CC	Connecting cilium
cDNA	Complementary DNA
cGMP	Cyclic guanosine monophosphate
CNBD	Cyclic nucleotide-binding domain
CNG	Cyclic nucleotide gated
CNGA1	CNG channel subunit A1
CNGB1	CNG channel subunit B1
DEP	Differentially expressed protein
DMEM	Dulbecco's Modified Eagle Medium
DNA	Deoxyribonucleic acid
dNTP	Deoxynucleoside triphosphate
DTT	Dithiothreitol
EDTA	Ethylenediaminetetracetic acid
EGTA	Ethyleneglycoltetraacetic acid
EIF2	Eukaryotic initiation factor 2

ER	Endoplasmic reticulum
ERAD	ER-associated protein degradation
ERG	Electroretinogram, Electroretinography
ERK	Extracellular-signal regulated kinases
FAT10	human leukocyte antigen-F adjacent transcript 10
FBS	Fetal bovine serum
FITC	Fluorescein isothiocyanate
GCL	Ganglion cell layer
GFAP	Glial fibrillary acidic protein
GNAT	Guanine nucleotide-binding protein G(t) subunit alpha
GRK	G protein-coupled receptor kinase
GSR	Glutathione reductase
GUCA	Guanylyl cyclase-activating protein
h	human
HK	Hexokinase
hRHO	Human rhodopsin promoter
hRHO194	Short human rhodopsin promoter (194 bp)
HRP	Horseradish peroxidase
Iba1	Ionized calcium-binding adapter molecule 1
IHC	Immunohistochemistry
ILM	Inner limiting membrane
INL	Inner nuclear layer
IPA	Ingenuity pathway analysis
IPL	Inner plexiform layer
IRE1	Inositol-requiring enzyme 1
IS	Inner segments
ITR	Inverted terminal repeat
KanR	Kanamycine resistance
kb	Kilobase
KO	Knockout
LB	Lysogeny broth
LC-MS/MS	Liquid chromatography-mass spectrometry/mass spectrometry
m	murine
MAPK	Mitogen-activated protein kinase
mRNA	Messenger RNA
mTOR	Mammalian target of rapamycin

n/a	Not altered
n/d	Not detected
NHP	Non-human primate
NRF2	Nuclear factor E2-related factor 2
OGDH	Oxoglutarate dehydrogenase
ON	Optic nerve
ONH	ON head
ONL	Outer nuclear layer
OPL	Outer plexiform layer
ori	Origin of replication
OS	Outer segments
OXPHOS	Oxidative phosphorylation
pA	Polyadenylation signal
PB	Phosphate buffer
PBS	Phosphate buffer saline
PBS-MK	PBS-$MgCl_2$-KCl_2
PCR	Polymerase chain reaction
PDB	Protein data bank
PDE6	Phosphodiesterase 6
PEG	Polyethylene glycol
PERK	R-like endoplasmic reticulum kinase
PFA	Paraformaldehyde
PI	*Post-injection*
PI3K	Phosphatidylinositol-3 kinase
PKM	Pyruvate kinase isoform M
PM	*Postnatal* month
PNA	Peanut agglutinin
PR+	Photoreceptor plus (combined thickness of photoreceptor OS and ONL)
PRPH	Peripherin
PTEN	Phosphatase and tensin homologue
qRT-PCR	Quantitative real-time PCR
rAAV	Recombinant AAV
RHO	Rhodopsin
RNA	Ribonucleic acid
ROM	Rod outer segment membrane protein
RP	Retinitis pigmentosa

RPE	Retinal pigment epithelium
rpm	Rounds per minute
RT	Room temperature
SAG	S-arrestin
SD-OCT	Spectral-Domain Optical Coherence Tomography
SDS	Sodium dodecyl sulfate
SDS-PAGE	SDS polyacrylamide gel electrophoresis
SV40	Simian virus 40
TBS-T	Tris-buffered saline with Tween-20
TCA	Tricarboxylic acid
TEMED	N, N, N', N' tetramethylethylene diamine
Tris	Tris(hydroxymethyl)aminomethane
UPR	Unfolded protein response
vg	Viral genomes
WPRE	Woodchuck hepatitis virus posttranscriptional regulatory element
WT	Wild type

Index of Figures

Index of Tables

Declaration of Author Contributions

Cloning of pGL2.1_hRHO-hCNGA1-mWPRE-BGHpA was performed at LMU by Dr. Victoria Splith (now ViGeneron GmbH). Production of rAAV2\GL.hCNGA1 was performed at LMU by the lab technicians Kerstin Skokann (Pharmacology for Natural Sciences, Department of Chemistry and Pharmacy, Ludwig-Maximilians-Universität München) and Tamara Gehringer (now ViGeneron GmbH). Production of rAAV5.hCNGB1/mod was performed at LMU by myself with support of Kerstin Skokann.

Preparation of *Pde6a*$^{-/-}$ dog samples was done by Prof. Simon Petersen-Jones and his group (College of Veterinary Medicine at the Michigan State University). Preparation of *Pde6a*^{MUT}*xCngb1*$^{-/-}$ mouse samples was conducted by Dr. Regine Mühlfriedel (Division of Ocular Neurodegeneration, Centre for Ophthalmology, Institute for Ophthalmic Research, Seeliger lab, University of Tübingen).

Jacqueline Bogedein (Department of Ophthalmology, University Hospital, Ludwig-Maximilians-Universität München) performed RoseTTAfold *in silico* modeling.
Proteomics analysis was performed by Dr. Pavel Kielkowski (Institute for Chemical Epigenetics (ICEM), Ludwig-Maximilians-Universität München).

Munich, 01.07.2022

Lena Isabelle Zobel

List of Publications

Wagner JE*, **Zobel L***, Gerhardt MJ, O'Riordan CR, Frederick A, Petersen-Jones SM, Biel M, Michalakis S. *In Vivo* Potency Testing of Subretinal rAAV5.hCNGB1 Gene Therapy in the *Cngb1* Knockout Mouse Model of *Retinitis Pigmentosa*. **Human Gene Therapy** (2021), **equal contribution*

Kandaswamy S, **Zobel L**, John B, Thyagarajan Santhiya S, Bogedein J, Przemeck GKH, Gailus-Durner V, Fuchs H, Biel M, Hrabě de Angelis M, Graw J, Michalakis S, Amarie OV. Mutations within the cGMP-Binding Domain of CNGA1 Causing Autosomal Recessive *Retinitis Pigmentosa* in Human and Animal Model. *Submitted to Cell Death & Disease*

Zobel L, Wagner JE, O'Riordan CR, Frederick A, Biel M, Michalakis S. Gene Therapy Successfully Restores Retinal Function and Delays Degeneration in a Mouse Model of CNGB1-linked *Retinitis Pigmentosa*. **The Association for Research in Vision and Ophthalmology** (2021), *Conference Poster*

Zobel L, Wagner JE, Occelli LM, Gerhardt MJ, O'Riordan CR, Frederick A, Biel M Petersen-Jones SM, Michalakis S. *In Vivo* Potency Testing of Subretinal rAAV5.hCNGB1 Gene Therapy in *Cngb1* Mouse and Dog Models of Retinitis Pigmentosa. **European Society of Gene & Cell Therapy** (2021), *Conference Poster*

Michalakis S, Occelli LM, **Zobel L**, Kielkowski P, Biel M, Petersen-Jones SM. Preclinical Testing of Subretinal Gene Supplementation Therapy for *PDE6A*-linked Retinitis Pigmentosa. **European Society of Gene & Cell Therapy** (2021), *Conference Poster*

Babutzka S, **Zobel L**, Diedrichs-Möhring M, Gehrke M, Wildner G, Ammer H, Michalakis S. Engineered AAV-based Vaccines against SARS-CoV-2. **European Society of Gene & Cell Therapy** (2021), *Conference Poster*

Meßner M, Schmitt S, Ardelt MA, Fröhlich T, Müller M, Pein H, Huber-Cantonati P, Ortler C, Koenig LM, **Zobel L**, Koeberle A, Arnold GJ, Rothenfußer S, Kiemer AK, Gerbes AL, Zischka H, Vollmar AM, Pachmayr J. Metabolic implication of tigecycline as an efficacious second-line treatment for sorafenib-resistant hepatocellular carcinoma. **FASEB Journal** (2020)

Acknowledgements

First of all, I would like to thank my supervisor Prof. Dr. Stylianos Michalakis for giving me the opportunity to pursue my PhD in his team. Stelios, thank you so much for all your guidance, support and encouragement over the years. I have learned so much and it was a pleasure to be part of your group.

A big thank you also goes to Prof. Dr. Martin Biel for welcoming me into his group and for all the great group experiences. I would also like to thank my thesis advisory committee, again Stelios, but especially Prof. Dr. Susanne Koch and Prof. Dr. Christof Osman for their advice and the great scientific discussions.

I also want to thank the LSM for admitting me to the doctoral program, for advancing my scientific education and for providing so many opportunities for embellishing my PhD.
Moreover, I thank the whole ViGeneron team, and especially Dr. Caroline Man Xu and Dr. Victoria Splith for welcoming me in the team and for supporting me in any way.
I would also like to thank Prof. Dr. Simon Petersen-Jones, Dr. Regine Mühlfriedel and Dr. Pavel Kielkowski for great cooperation, patience and scientific input.

More than one big thank you also goes to all my incredible colleagues who filled every day with fun and joy. Thanks for the great atmosphere in the lab, for all your help, the terrific celebrations, vodka-fizz-breaks and just the last almost 4 years together. Jacqueline and Sabrina, thank you so much for becoming such amazing friends, for all the wine-filled evenings and your loving support in every problem, professional as well as personal. I love you Powerpuff Girls.
In this context, I would also like to explicitly thank the animal keepers for helping me so much in the mousehouse. Thanks also to Johanna who taught me about life in the lab.
Another special thank goes to my very first student Ina for accompanying me on my journey as a PhD student. Ina, I have learned from you as much as I hope you have learned from me.

Zuletzt möchte ich mich bei meiner Familie bedanken. Liebe Mami, lieber Papi, ich danke euch so sehr für eure grenzenlose Unterstützung, euren Zuspruch und eure Liebe. Danke, dass ihr mir immer alles ermöglicht habt. Konsti, mein Herz, danke für deine Motivation, deinen Trost und deine Fürsorge und dass du immer für mich da bist. Ohne dich wäre ich wahrscheinlich beim Schreiben dieser Arbeit verhungert. Ich liebe euch!